The Mechanics and Control of Flexible Asymmetric Spinning

James Alexander Polyblank

Gonville and Caius College

June 2015

This dissertation is submitted for the degree of

Doctor of Philosophy

UNIVERSITY OF CAMBRIDGE
Department of Engineering

Preface

This dissertation is the result of my own work and includes nothing which is the outcome of work done in collaboration except as declared in the Preface and specified in the text. It is not substantially the same as any that I have submitted, or, is being concurrently submitted for a degree or diploma or other qualification at the University of Cambridge or any other University or similar institution except as declared in the Preface and specified in the text. I further state that no substantial part of my dissertation has already been submitted, or, is being concurrently submitted for any such degree, diploma or other qualification at the University of Cambridge or any other University of similar institution except as declared in the Preface and specified in the text

This dissertation is 50,834 words in length and contains 123 figures, which is within the limits set by the Department of Engineering.

James Alexander Polyblank

June 2015

Abstract

Metal spinning is a sheet forming process to produce axisymmetric products, but its commercial operation still depends on a dedicated mandrel which determines the shape of the product, and skilled craftsmen to control the working tool. In Flexible Asymmetric Spinning (FAS) the mandrel is replaced with three numerically controlled internal rollers, thereby removing the setup time and cost associated with producing the dedicated mandrel. However, if FAS could also be automated, the setup time and cost could be reduced further. This thesis focuses on three elements which need to be in place for the automation of FAS: the automation of the internal rollers; compensation for springback; and toolpath design to prevent failure.

Typically, automation requires a process model. To automate the internal rollers, a process model which predicts the effect of the internal roller position on the workpiece shape would be required – but as FAS is a novel process, no such models exist. To compensate for springback, a model of workpiece shape is required. To prevent failure, a model of the two modes of failure – wrinkling and tearing – is needed. For offline automation, these should be accurate models – but accurate models of both workpiece shape and failure are too slow to make this feasible. For online automation, fast, approximate models can be used – measurements of the product can be fed back in order to compensate for the model errors. However, a literature review showed that no models exist for workpiece shape or failure which are both fast enough for online use, and detailed enough to give information on how tool actions should be changed. This is why FAS has not yet been automated.

In previous work, the internal rollers were positioned through trial-and-error and only a straight-walled cup was successfully produced. In this work, a laser line scanner is installed to measure the workpiece shape online, and one of the internal rollers is positioned at the point where the workpiece just begins to diverge from the target shape. This prevents overlap with the target shape, and allows a greater range of products to be made.

Springback is typically prevented in conventional spinning by pressing the material hard against the mandrel. This is not possible in FAS due to the force limits on the internal tools. However, in FAS it is possible to move the working roller inside the target shape to compensate for springback. The laser line scanner is used to measure springback and calibrate a simple elastic cantilever model of springback online. By using this model to calculate how far to move the tool inside the target shape, springback errors are reduced by 75%.

Two approaches to toolpath design to avoid failure are investigated: Firstly, a finite horizon control system – where failure is checked for only for a short time into the future – is tentatively demonstrated using a slow but accurate finite element (FE) model, but this is too slow for industrial use. However, with a faster, linear-elastic model, the control system is too conservative and fails to produce the final product. Secondly, an empirical approach is investigated: a series of trials are carried

out with a parameterised toolpath. The result is a tentative set of rules for toolpath design which may provide the basis for a future control system.

Overall, this thesis makes steps towards the automation of internal rollers, compensation of springback, and design of toolpaths to prevent failure in FAS. With further work to extend the control system developed here to automate all three internal rollers and to verify the robustness of the springback compensation system, any conventional spinning machine could potentially be replaced by an FAS machine – with the toolpath of the working roller designed manually, as it currently is in conventional spinning. Yet the tentative sets of rules on toolpath design also open the door to a potential automatic toolpath generation system, and further work should begin by testing the robustness of these rules with changes in material and geometry. Then, with some likely extensions, they could be embedded into a working control system to fully automate FAS.

Keywords

Forming

Sheet metal

Flexible asymmetric spinning

Closed loop control

Acknowledgements

Firstly, I would like to thank my supervisor, Professor Julian Allwood. Without his hard work, support and advice, this research would not have been possible.

I gratefully acknowledge that this work was funded by Siemens Metals Technologies and the EPSRC Doctoral Training Account. I was also lucky enough to have support from my industrial supervisors at Siemens Metals Technology, Mick Steeper and Richard Cinderey, as well as their colleagues, in particular Nick Champion and Peter Walker.

My predecessor, Omer Music, designed and built the Flexible Asymmetric Spinning machine on which this research is based. His work is cited several times in this thesis, but I was not able to cite the thorough handover and extensive support he extended to me, for which I am grateful.

I am thankful to Professor Stephen Duncan at Oxford University for his input into the literature review into closed-loop control of product properties, as well as for his patience in helping me with my understanding of control theory.

I am thankful to Alistair Ross and those in the workshop here in the Cambridge University Engineering Department for their help, skill and speed in machining new parts for the FAS machine, and blanks for experiments. I am also thankful for the practical support of Martin Touhey and the technicians in the structures group.

I am thankful to those in the Low Carbon Materials Processing group and the Precision Guided Flexible Forming project, particularly Martin, Mark, Evros, Dan, David, Muiris, Vahid, Ed, Jeremy, Matt, Roger, Jianglin, Mr Chris and Dr Chris, for their technical discussions and practical support. I am also grateful to Ian in the Control group and Stefania and Eirini in the Construction Information Technology for their help with computer vision problems.

Finally, I am thankful to my wife, Natalie, and my parents for their unwavering love and support, and to all of my friends for making my time in Cambridge (and the trips away from Cambridge) a time I'll never forget.

Publications

Some of the material presented in this thesis has been published in journals and at conferences.

Journal papers (published)

J.A. Polyblank, J.M. Allwood, S.R. Duncan, 2014. Closed-loop control of product properties in metal forming: a review and prospectus. Journal of Materials Processing Technology, 214 (11), pp. 2333-2348

J.A. Polyblank, J.M. Allwood, 2015. Parametric toolpath design in metal spinning, CIRP Annals – Manufacturing Technology, Available online 16 May 2015, http://dx.doi.org/10.1016/j.cirp.2015.04.077 (In press)

Conference papers

J.A. Polyblank, J.M. Allwood, 2014. Support Roller Control and Springback Compensation in Flexible Spinning. In: International Conference on Technology of Plasticity, ICTP 2014, Nagoya, Japan, pp. 2499-2504

Table of Contents

Chapter 1 - Introduction

If we could imagine an ideal manufacturing process, it would probably be able to produce any product that we desire with perfect precision, no lead-time, no material waste and no defects. This would save manufacturers time and money, and allow designers greater flexibility to design without being restrained by the capabilities of current manufacturing processes. However, the evolution of metal forming technology over the past century seems to have moved further from this ideal rather than closer to it.

Metal forming – producing products by plastically deforming material into the shape we desire – dates back to the Bronze ages. Back then, and indeed until just about a century ago, metal forming was performed by a skilled craftsman with a hammer and anvil, and perhaps a furnace to heat the material up. His primitive tools only allowed him to produce parts which were approximate compared to those produced by today's techniques, but with almost no set up time he was able to produce a brand new shape according to his customers specifications. Furthermore, he could prevent defects by watching, feeling and hearing the material as he formed it, and adapting his approach accordingly.

Today's metal formers are able to produce very accurate products in large batches and very quickly using enormous forging presses of up to 80,000 tonne capacities with dedicated tooling. The problem, however, is that if a new shape is to be produced, large investments in new tooling are required – in both cash and time. Furthermore, the tooling might have to be redesigned several times in order to get it right – to make sure it forms the part accurately without defects. The cost and time of doing this means it is only economical if hundreds of thousands, if not millions, of the same part are to be made. Henry Ford famously said, referring to this new mass production approach: "You can have any colour you like, as long as it's black". Modern metal forming can produce accurate, high quality products – as long as you are willing to invest in the tooling.

1.1 Spinning as a flexible metal forming process

Metal sheet spinning offers a neat compromise between the ideal and this modern practice. It is a metal sheet forming process where a circular piece of sheet metal is spun about its axis while a tool is pushed into the sheet to form it onto a mandrel – a template of the part that is to be made (Figure 1-1a). It competes with deep drawing, where a circular blank is drawn into a die by a punch, with a blank holder used to prevent wrinkles forming as the material is drawn in (Figure 1-1b).

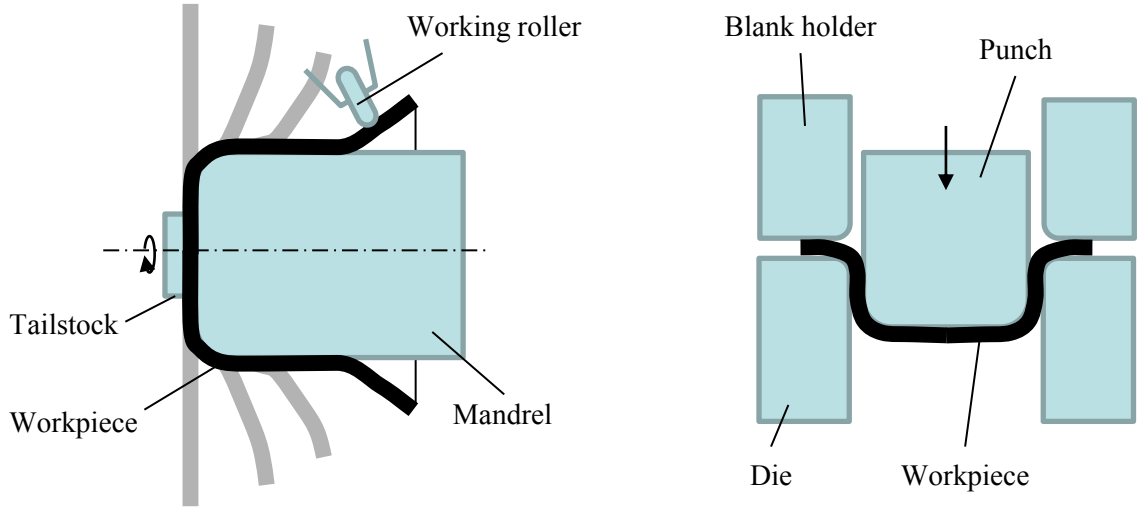

a) Conventional spinning **b) Deep drawing**

Figure 1-1 - Conventional Spinning

In deep drawing, a new punch and die, and possibly a blank holder, have to be made for new products, and the high tool forces mean that the lifetime of these tools can be low. In spinning, the mandrel is the only piece of dedicated tooling required and the tool forces are lower so that the lifetime of the mandrel is much higher than the punch/die set in deep drawing. This means that the fixed costs in spinning are much lower. However, because of the incremental nature of spinning, it is a much slower process – taking minutes for a product to be made – whereas deep drawing can produce several products per second. Spinning therefore typically takes the market for the high-value, low-volume products such as in aerospace (e.g. nose cones, turbine housings), healthcare (e.g. pressure vessel ends, centrifuges), and bespoke designer parts (lamps and light fittings etc.) – some examples of the latter are shown in Figure 1-2 – while deep drawing is used for high-volume parts such as beverage cans, pots, pans and containers and automobile panels.

Music (2011) moved metal spinning closer to our "ideal" manufacturing process by developing a flexible spinning process: he identified that the workpiece only makes contact with the mandrel in at most three distinct points, so was able to replace the mandrel with three numerically controlled internal rollers (Figure 1-3). He designed the Flexible Asymmetric Spinning (FAS) machine to exploit this technique - this is in fact the machine that was used in all of the experimental spinning work in this thesis, and is shown in Figure 1-4.

However, even with this additional flexibility, FAS is still some way from ideal. Like in conventional spinning, the tool motions are still defined by skilled craftsmen or by trial and error, adding to setup time and cost. The ultimate goal would be to make the whole process fast and automatic from a finished CAD (Computer Aided Design) file of the desired product to a spun product. This thesis focuses on three elements that need to be in place for this to happen, and to draw FAS closer to the ideal manufacturing process by reducing lead-time and increasing precision.

Figure 1-2 - Some bespoke spun parts and the mandrels used to make them (Photograph by Terry Tynan licensed under CC BY-SA 3.0)

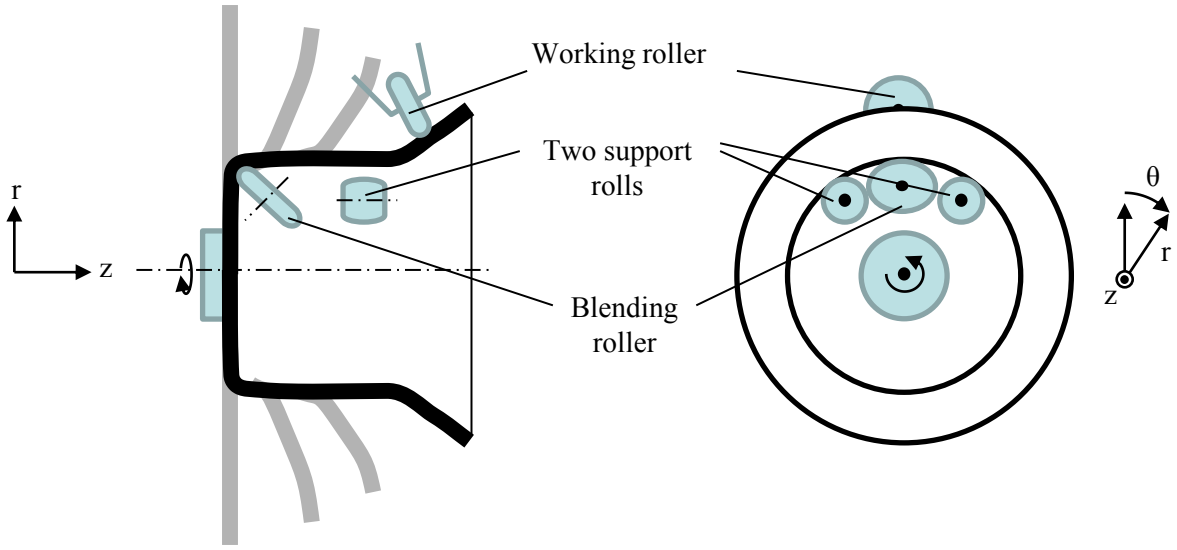

Figure 1-3 - Flexible Asymmetric Spinning

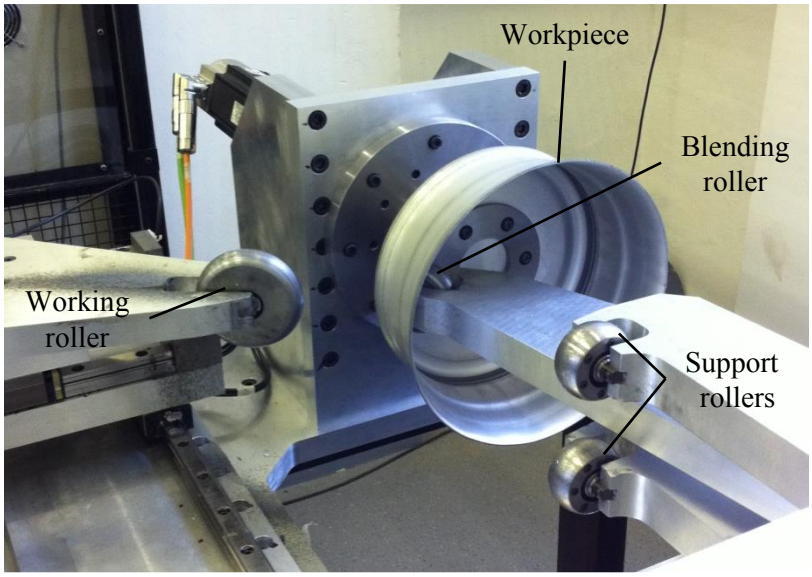

Figure 1-4 - The Flexible Asymmetric Spinning machine, as built by Music (2011)

Firstly, the three internal rollers add further degrees of freedom to FAS in comparison to conventional spinning. In previous demonstrations of the FAS machine, these have been positioned using trial and error, and were held stationary during spinning. However, to realistically replace any conventional spinning machine with an FAS machine, they must be automated – not all products can be produced by leaving the internal rollers stationary, and manually positioning the additional three rollers would result in cognitive overload for manual spinners.

Secondly, FAS presents an opportunity to improve precision over conventional spinning by compensating for springback automatically. There are two advantages that allow this to happen: firstly, the working roller can move inside the target shape without colliding with the mandrel (as long as the internal rollers are moved to allow this). And secondly, the internal rollers can be moved to effectively change the shape of the mandrel mid-process, allowing it to adapt and compensate for springback. However, the remaining challenge is working out exactly how to adapt the toolpath and the internal rollers in order to compensate for springback.

Thirdly, even if solutions to the above two problems allow perfectly accurate products to be made, the tool motions must not cause failure – either by wrinkling or tearing - in the workpiece. In conventional spinning, this is performed by skilled workmen, often with decades of experience of spinning. If products are to be produced in large batches or in mass, the motion of the tool under manual control is sometimes recorded and then played back with no operator intervention (apart from in exceptional circumstances). However, in order to reduce lead time and set up costs, this should be automated.

1.2 A framework for controlling Flexible Asymmetric Spinning

It might be possible to design and adapt these toolpaths offline using an offline process planning algorithm. The spinning machine then uses closed-loop control of the actuator positions in order to ensure that the tools follow the toolpath precisely – this is mature technology. This approach is shown in Figure 1-5. Because the process planning and the process itself are not included within the closed-loop actuator control, we refer to this as "open-loop" control of metal forming.

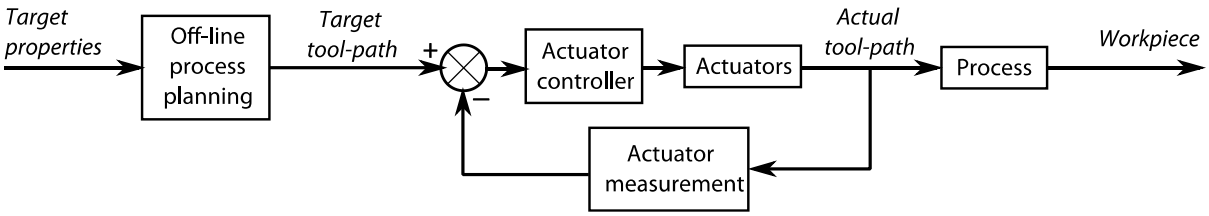

Figure 1-5 - A system diagram for open-loop control of metal forming

Offline process planning algorithms as shown in Figure 1-5 often use a model to predict the effect of control actions on the workpiece state.

$$\mathbf{q}_{k+1}(\mathbf{x}) = \mathbf{f}_k(\mathbf{q}_k(\mathbf{x}), \mathbf{u}_k); \quad \mathbf{q}_0(\mathbf{x}) = \mathbf{q}^i(\mathbf{x}) \tag{1.1}$$

where $\mathbf{q}_k(\mathbf{x})$ is the state of the workpiece at time t_k and position $\mathbf{x}$ in space – this will describe the shape of the workpiece, but may also include the residual stresses, material properties etc. if these were to be controlled as well. $\mathbf{q}^i(\mathbf{x})$ is the initial state of the workpiece. $\mathbf{u}_k$ is the control action taken – in the case of spinning, it is the increment of toolpath that occurs between t_k and t_{k+1}. Although toolpaths are continuous, toolpath commands are issued discretely to the machine controller at times $t_k = kT$, where $\{k = 0,1,2,\dots,K-1\}$, K is the total number of control actions applied during the process and T is the time between control actions.

The objective of the control system will be to minimise the difference between the final state, $\mathbf{q}_K(\mathbf{x})$, and the desired state, $\mathbf{q}^d(\mathbf{x})$, where the difference is usually expressed as the quadratic error

$$\left\|\mathbf{q}_K(\mathbf{x}) - \mathbf{q}^d(\mathbf{x})\right\|_2 \tag{1.2}$$

However, this only addresses achieving the right shape. Wrinkling or tearing, as well as any other constraints on the processes, must be included in the control system. These are expressed together as a vector inequality of the form

$$\mathbf{p}_k(\mathbf{q}_k(\mathbf{x}), \mathbf{u}_k) \leq 0 \tag{1.3}$$

Equations 1.1, 1.2 and 1.3 can now be combined to define open-loop tool-path planning as a standard optimization problem:

$$\begin{aligned} \min_{u_0 \ldots u_{K-1}} \quad & \left\| \mathbf{q}_K(\mathbf{x}) - \mathbf{q}^d(\mathbf{x}) \right\|_2 \\ \text{subject to} \quad & \mathbf{q}_{k+1}(\mathbf{x}) = \mathbf{f}_k(\mathbf{q}_k(\mathbf{x}), \mathbf{u}_k) \quad \text{for } k = 0,1,2, \ldots K-1 \\ & \mathbf{q}_0(\mathbf{x}) = \mathbf{q}^i(\mathbf{x}) \\ & \mathbf{p}_k(\mathbf{q}_k(\mathbf{x}), \mathbf{u}_k) \leq 0 \end{aligned} \qquad \textbf{1.4}$$

The solution to 1.4 will be a toolpath that should be followed to create the target product. In principle, if the process model is perfect, the optimal toolpath should achieve the desired final state, but in reality this is unlikely for three reasons:

- *Model uncertainty:* The model is, in practice, unlikely to predict the exact behaviour of the process, particularly if an approximate form of **f** is used to reduce solution times. In addition, some of the parameters in the model, such as material properties, may not be known exactly.
- *Disturbances*: External disturbances, such as variability in lubrication, tooling wear, variation in operating temperature, or eccentric loading of the blank, will cause variation in process performance compared with what is modelled.
- *Controllability:* The limitations of the spinning machine actuators mean that it is unlikely to be able to achieve all desired states perfectly. For example, it may not be able to create any arbitrary geometry anywhere within the workpiece.

It would therefore be helpful to find a different approach from that of Figure 1-5 for developing toolpaths – one that is more robust to modelling errors and disturbances. We might look back to the skilled manual spinner or the Bronze aged blacksmith, who did not plan his actions in advance, but developed them during production in reaction to feedback from his own senses. Learning from this approach, if we were able to install sensors within the forming process to monitor the state of the workpiece during processing, we can imagine a different form of toolpath design using closed-loop control, as illustrated in Figure 1-6. We refer to this as "closed-loop control of product properties" because now the product properties themselves are included within the closed-loop, and not just the actuator positions.

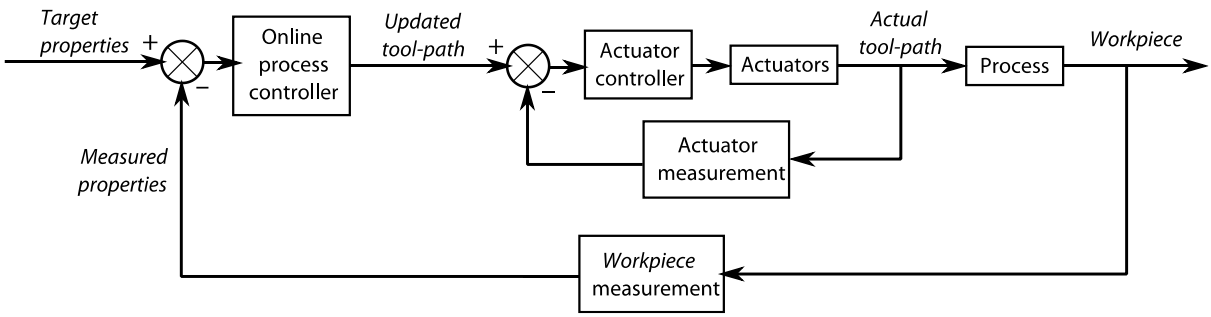

Figure 1-6 - A system diagram for closed-loop control of product properties in metal forming

Figure 1-6 introduces two changes to Figure 1-5: a means to measure the workpiece state during processing, and an online process controller in place of the previous offline process planning

expressed as equation 1.4. This leads to a closed-loop version of the open-loop optimisation statement of 1.4. The optimal toolpath can be determined iteratively using

$$\begin{aligned} \min_{u_{k'} \ldots u_{K-1}} \quad & \left\| \mathbf{q}_K(\mathbf{x}) - \mathbf{q}^d(\mathbf{x}) \right\|_2 \\ \text{subject to} \quad & \mathbf{q}_{k+1}(\mathbf{x}) = \mathbf{f}_k(\mathbf{q}_k(\mathbf{x}), \mathbf{u}_k) \quad \text{for } k = k', k'+1, k'+2, \ldots K-1 \\ & \mathbf{q}_{k'}(\mathbf{x}) = \widehat{\mathbf{q}}_{k'}(\mathbf{x}) \\ & \mathbf{p}_k(\mathbf{q}_k(\mathbf{x}), \mathbf{u}_k) \leq 0 \end{aligned} \qquad \textbf{1.5}$$

Although 1.5 has a similar form to the earlier statement in 1.4, this minimisation is different because it is applied to control actions over the period from $t_{k'}$ to t_{K-1} rather than the whole of the process, and the update of the process model uses the current state $\widehat{\mathbf{q}}_{k'}(\mathbf{x})$ obtained from the measurements rather than the modelled state. In applying this algorithm within the closed-loop system of Figure 1-6, having solved 1.5 to work out the optimal toolpath $\{\mathbf{u}_k : k = k', k'+1, \ldots, K-1\}$, only the first element of this sequence, $\mathbf{u}_{k'}$ is applied to the process, before taking another measurement of the state, $\widehat{\mathbf{q}}_{k'+1}(\mathbf{x})$. The minimisation is then repeated to give the optimal sequence of control actions over the (shorter) interval from $t_{k'+1}$ to t_{K-1}, where the new measurement of the state at time $t = (k'+1)T$ is used as the starting point for the process model. This idea of performing a repeated set of optimisations using an estimate of the current state is a discrete form of Model Predictive Control (MPC) (Maciejowski, 2000).

In this thesis, closed-loop control of product properties will be applied to spinning. However, in order to solve the minimisation of equation 1.5, a process model **f** and the constraint equations **p** are needed. The form of these equations in 1.5 is deceptively simple, but the modelling of spinning is not. In chapter 2, therefore, a review of modelling of spinning and its constraints will be presented in order to see if a suitable model exists – one which is fast and yet detailed enough to allow us to generate toolpaths online. A review of models used within closed-loop control of product properties in other processes will also be reviewed in order to see what level of approximation can be successfully applied within a closed-loop control system.

In chapter 3, the numerical and experimental methods will be described. In the remainder of the thesis, the application of closed-loop control of product properties to FAS will then be described, although only the axisymmetric spinning mode is considered (i.e. the asymmetric capabilities of FAS are not exploited here). Using closed-loop control of product properties to the position support rollers is discussed in chapter 4 and to control springback in chapter 5. Two attempts are made to apply closed-loop control of product properties to automatic toolpath generation to prevent failure in chapter 6 but the models created are either too slow for industrial use, or too conservative to create the final product successfully. In order to investigate automatic toolpath generation further, toolpath design is investigated parametrically in chapter 7. The outcome is a "first draft" control system to automate FAS spinning in its axisymmetric mode and a tentative set of rules to design toolpaths to avoid failure.

Both of these could be extended in the future in order to create an optimal control system for industrial applications and to eventually to exploit the asymmetric capabilities of FAS.

Chapter 2 - Literature Review

Metal spinning is a sheet forming process where sheet metal is spun and formed over a mandrel into an axisymmetric product. A comprehensive review of the mechanics of spinning was performed by Music et al. (2010), and a further review focusing specifically on non-axisymmetric, non-circular and tooth-shaped spinning was performed by Xia et al. (2014).

Metal spinning can be categorised into three groups based on the objective of the process. In two of these categories, the starting material is a flat sheet: conventional spinning, where the thickness of the sheet remains constant while the diameter is reduced (Figure 1-1a); and shear spinning, where the diameter ideally remains constant while the thickness is reduced according to the sine law (equation 2.1, Figure 2-1). The third category is tube spinning, where the starting material is a tube, and the process aims to reduce the thickness of the tube while increasing the length. Kalpakjian and Schmid (2008) also consider incremental sheet forming as a related process, with the tool moving in Cartesian coordinates rather than polar coordinates, and the sheet clamped around the edge, rather than in the centre as it typically is in spinning.

$$t = t_0 \sin(\alpha) \quad \textbf{2.1}$$

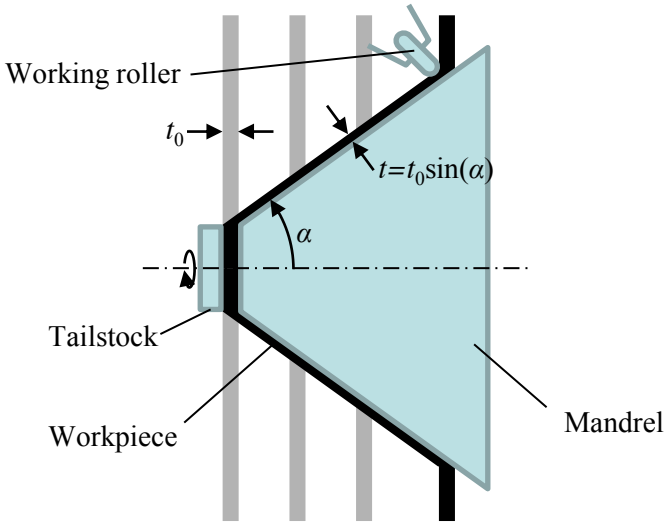

Figure 2-1 - Shear spinning

Xia et al. (2014) categorise the spinning process further based on whether the tool is on the inside or outside of the workpiece; whether a mandrel is used; whether the process is hot or cold; and whether the product is axisymmetric, non-circular, or even toothed.

Within this classification, the Flexible Asymmetric Spinning (FAS) process designed by Music and Allwood (2011a) sits within the cold, mandrel-less spinning processes and it can produce both circular and non-circular components depending on its mode of operation. It has so far only been used to

reproduce the mechanics of conventional spinning as the current machine cannot apply forces large enough to reproduce shear spinning, but the principle could be extended to this. In addition, it has so far only been used with the working roller on the outside of the workpiece, but the internal support rollers could in principle be used to form the workpiece from the inside, but again this has not yet been tried. By looking at other processes within the same categories, it is possible to see what challenges we might face in using FAS to produce accurate, defect free products.

Other *conventional spinning processes*, with or without a mandrel, have three failure modes, as stated by Lange (1985): wrinkling, circumferential tearing, and radial tearing. Lange states that to prevent wrinkling, the tool must gradually form the workpiece onto the mandrel with several passes. However, Hayama et al. (1970) found that the shape of these tool passes is important too.

Tearing is caused by high tensile stresses, and can also be prevented by careful design of the tool passes. Kegg (1961) and Hayama (1981) both identified that tearing occurs when the through thickness strain reaches the area reduction at fracture in a tensile test, suggesting that tearing could be prevented by controlling thickness rather than considering it as a separate problem.

Controlling thickness is a key concern across all categories of spinning process. Not only is control over the thickness required to produce the target thickness in the final product, but the thickness evolution can determine the mechanics of the process. Music et al. (2010) noted that the categories of conventional and shear spinning are idealisations and most spinning processes lie somewhere in between: It is difficult in conventional spinning to maintain the initial thickness exactly, and in shear spinning it is difficult to control the thickness according to the sine law, so in reality there will be some change in the outer diameter. Indeed, Music et al. (2010) define under spinning as where the resulting thickness is greater than the sine law suggests, and the diameter is drawn in slightly, and over spinning as where the resulting thickness is less than the sine law suggests and material builds up in front of the tool, folding the flange forwards.

In addition to these challenges, *mandrel-free spinning processes* can suffer from other shape errors. Music et al. (2010) identified four other mandrel-free processes, but only two of these were strictly spinning processes: Spinning with two rollers (Shima et al., 1997) and spinning with a general-purpose mandrel (Kawai et al., 2001), shown in Figure 2-2a and Figure 2-2b respectively. The other two were more similar to incremental sheet forming, with the workpiece clamped around the edge. In spinning with two rollers, an internal roller was placed opposite the working roller on the inside of the sheet in order to create a highly localised deformation similar to shear spinning. This process has only been used to make conical parts, and Shima saw errors of 18% in cone angle, but was able to reduce this by increasing through-thickness forces applied by the tool, and reducing the feed rate.

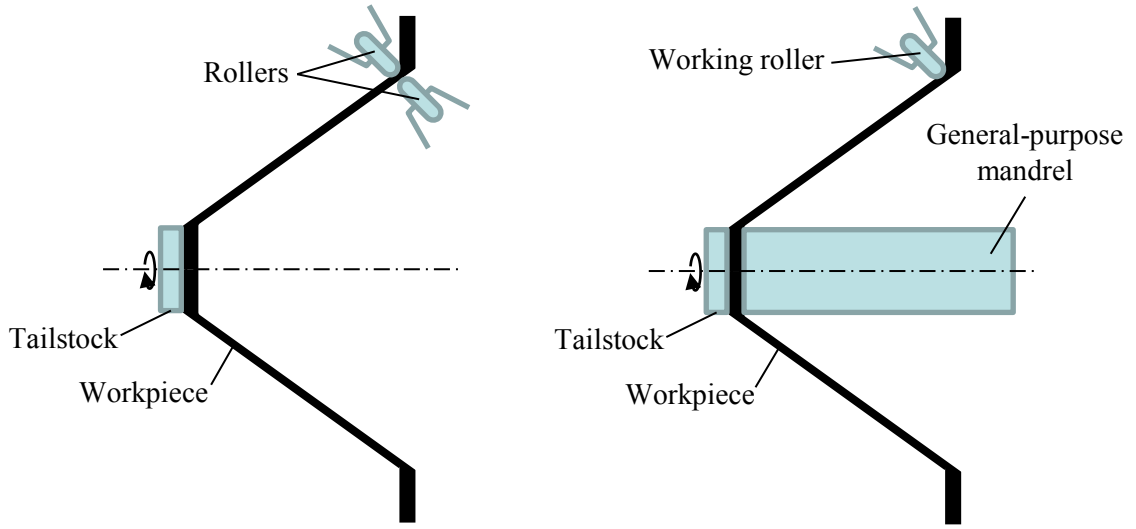

a) Spinning with two rollers (adapted from Shima et al., 1997)

b) Spinning with a simple cylindrical mandrel (adapted from Kawai et al., 2001)

Figure 2-2 - Spinning processes without a dedicated mandrel

Kawai attempted to reproduce conventional spinning with a general purpose, cylindrical mandrel, which was used the clamp the centre of the sheet while leaving the edges free. He used the general-purpose mandrel to produce conical (Kawai et al., 2001) and hemispherical parts (Kawai et al., 2007), and found that hemispherical products suffered from much more springback than in the conical products.

Springback is not seen as frequently in conventional spinning for two reasons: firstly, because the mandrel provides additional stiffness. Secondly, the tool can press the workpiece hard against the mandrel in order to force the workpiece to "lock on" to the mandrel; this is relatively easy in force-controlled or manual processes by increasing the forces, and can also be controlled through tapering the mandrel-clearance as the tool moves to the end of the pass in shear spinning (Kleiner et al., 2005). In FAS, the three internal rollers provide the same support as the mandrel, therefore increasing stiffness compared to spinning with a general-purpose mandrel, but the maximum tool forces are too small to force the workpiece to "lock on" to the mandrel.

An additional shape error that can be formed in mandrel-free spinning process is "overforming" – where the workpiece is formed beyond the target shape, while the mandrel would normally prevent this from occurring in conventional spinning. This error has been seen in early experiments with FAS (shown in Chapter 4, and published separately in Polyblank and Allwood, 2014), but was not seen in Kawai's experiments or any other literature. This is perhaps because of the smaller products that Kawai produced (~100mm diameter, compared to ~250mm diameter produced here) or it could just be hidden by his low-resolution measurements – He only measured the position of four points along the workpiece, compared to the up to 256 measured by the laser scanner in this thesis. Regardless, the problem highlights the importance of positioning the three internal rollers correctly in FAS.

Spinning *non-axisymmetric products* results in the same kinds of defects and shape errors as in conventional spinning, but with more circumferential variation, particularly in thickness. Amano and Tamura (1984), Awiszus and Meyer (2005) and Arai (2006) all use non-axisymmetric mandrels and different methods to fix the motion of the rollers to follow the mandrel: Amano and Tamura use a mechanism of cams and links; Awiszus and Meyer use a pair of spring-controlled rollers; and Arai uses force controlled rollers. These are therefore limited to one-pass spinning and the results are similar to shear spinning, but all of them experience poor control of thickness around the circumference, with errors of up to 23%, due to difficulties maintaining a constant roller-mandrel clearance.

Conventional, multi-pass non-axisymmetric spinning, like that which could be performed by the FAS machine, has been researched by Gao et al. (1999) and Sugita and Arai (2012). Gao et al. use an offset mandrel so that the contact-point between the working roller and mandrel is fixed in space while the workpiece rotates; however, he still experienced thickness errors of up to 10%. Sugita and Arai use numerically controlled rollers to synchronise the motion of the working roller to the mandrel. In a later paper they modified toolpaths designed for axisymmetric products to produce toolpaths for non-axisymmetric products and found the same failure modes - wrinkling and tearing – limited the range of path shapes that would work (Sugita and Arai, 2015). However, beyond the errors and constraints seen in axisymmetric spinning, there does not appear to be additional constraints in non-axisymmetric – just an increased challenge in modelling the asymmetric geometry.

In summary, in the same category of processes as FAS, there are challenges of shape errors, wrinkling, thinning and tearing, with the latter two being linked. Indeed, initial experiments with the FAS machine showed that all these problems occur in FAS without careful control of the machine, as will be seen in the experimental results presented in this thesis. However, it was shown in Chapter 1 that to control the process using closed-loop control of product properties, process models and constraint equations are needed. To apply closed-loop control of product properties to FAS, we require a process model of the shape evolution to control shape errors; a constraint model of wrinkling to prevent wrinkling; and a process model of thickness evolution combined with a constraint on the minimum thickness to control thinning and prevent tearing; The existing literature on each of these elements is reviewed respectively in sections 2.1, 2.2 and 2.3 of this literature review.

Then, in order to identify modelling techniques and approximations that could be made in order to generate new, fast models of spinning, a review on process models successfully used in closed-loop control of product properties in other metal forming processes is presented in section 2.4. Finally, the literature review concludes in section 2.5 by summarising the gaps in the literature and the objectives for this work.

2.1 Process models for workpiece shape

In the literature on spinning, there is very little work focusing on the geometry of the product. This is largely because, as Music et al. (2010) point out, the geometry is defined by the shape of the mandrel. However, this argument on its own is not enough to suggest that there would not be any springback – we might still expect the workpiece to elastically deform away from the mandrel when the tool is removed. However, it seems that in hand-spinning the workman is able to prevent springback by pushing the workpiece hard onto the mandrel in order to make sure it is "locked-on". They then knock the workpiece with a stick and, by listening to the resulting sound, tell whether the workpiece is indeed "locked-on".

Kleiner et al. (2005) confirm that this approach works, showing that by tapering the tool-die clearance towards the outer edge of the workpiece, springback could be reduced, but eventually at the cost of increased thinning. Shima et al. (1997) shows that this also applied to flexible shear spinning with two rollers – They were able to reduce springback by increasing the force between the two rollers. Both of these results would appear to be using the principle of stress superposition described by Kleiner et al. (2009) and Chatti et al. (2009) – By applying through-thickness stresses, the bending stresses and strains required to cause plastic deformation are reduced, and therefore the springback is reduced.

However, this stress superposition cannot be applied in spinning processes without a mandrel or internal rollers capable of applying large enough forces. This is why Kawai et al. (2007) experienced springback problems when attempting to spin a hemispherical shell with a general-purpose cylindrical mandrel. For controlling this springback error, and other shape errors such as overforming, a model of the shape evolution of the workpiece is needed.

Music and Allwood (2012) demonstrated an impulse response approach to modelling the geometry of conventional spinning. They showed, through experimentally verified FE models, that the impulse response was sensitive to the thickness of the sheet, the direction of motion, and the location of the tool, but after an initial transient stage the impulse response was approximately constant throughout the rest of the process (the "steady state stage"). This approach could potentially be used on line to predict the geometry of the workpiece – the impulse response could be measured online during the steady state stage and then used to predict the geometry after the next pass, for example. However, they did not demonstrate this, nor did they show whether convolution could be applied to sum up the impulse response over the rest of the process.

Other authors have turned purely to numerical methods to study spinning. Alberti et al. (1989) developed an axisymmetric FE model of shear spinning, suggesting that this was acceptable because the ratio of tool speed to mandrel speed is very small – but their analysis ignores the local, non-axisymmetric effect of the tool loading. They were able to calculate the springback, but did not verify

the results experimentally. Sebastiani et al. (2007) performed FE analyses of spinning and claim that springback is smaller later in the spinning process, when geometric stiffness of the workpiece is higher. However, this is little help in toolpath design. More recently, Li et al. (2014) developed an FE model of Kawai et al.'s (2001, 2007) spinning with a general-purpose mandrel, and performed a series of trials varying the shape of the toolpath from concave to convex. However, they did not vary the shape independently of the aggressiveness – the convex passes were more aggressive than the concave pass. They found that an aggressive convex toolpath resulted in less springback than a less aggressive concave pass.

However, even the simple axisymmetric FE models of spinning would be too slow to run online, given that even today they take several minutes to model just one tool pass, and the full three-dimensional models would certainly be too slow. Analytical models would be faster, but no analytical work has been performed to predict the springback or the overall geometry of the workpiece in spinning. This leaves the impulse response approach of Music and Allwood (2012) as the only promising existing geometry modelling option for online use in spinning.

2.2 Constraint models of wrinkle formation

Developing a model of wrinkling which allows us to form the constrain equation in the closed-loop minimisation is far more challenging, which is why generating toolpaths that avoid wrinkling remains a job for skilled craftsmen with years or even decades of experience. However, there is a great body of work in both spinning and beyond: wrinkling (or buckling) occurs in structural applications if the designer is not careful, and it can occur in other manufacturing processes such as stamping and deep drawing. Much of the work on wrinkling in spinning has developed from this work, so this review begins with a review of broadest work on the approaches to modelling wrinkling and buckling of shells. Then, the work on wrinkling in axisymmetric deep drawing is reviewed, before finally looking specifically at metal spinning.

2.2.1 Approaches to modelling wrinkling

In the published literature, three approaches to modelling and predicting wrinkles have been used: analytical, numerical and experimental methods. These three approaches will be reviewed here in turn.

Analytical approaches to wrinkling are documented by Timoshenko and Gere (1961). Although they begin their book by looking at models of the buckling of columns and bars of various shapes, they move on to models of thin plates, and then shells.

In particular, Timoshenko and Gere describe the energy method, which is a method of predicting when wrinkling will occur, as applied to linear-elastic material. A wrinkling deformation pattern, u^*, is assumed and the elastic energy stored by this deformation, $\Delta U(u^*)$, is calculated. This is compared

to the work that would be done, $\Delta T(P, u^*)$, by the actual applied force, P, if this deformation occurred. Then, the system will not wrinkle in this way if

$$\Delta U(u^*) > \Delta T(P, u^*) \quad \textbf{2.2}$$

but will be unstable if

$$\Delta U(u^*) < \Delta T(P, u^*) \quad \textbf{2.3}$$

Therefore, the critical load, P_{cr} for this deformation pattern can be found by forcing equality:

$$\Delta U(u^*) = \Delta T(P, u^*) \quad \textbf{2.4}$$

The wrinkling deformation pattern with the lowest critical force is the one that will occur first.

However, in spinning or deep drawing, it is not just the work done by the applied forces that must be calculated, but also the work done by the stresses resulting from prior deformation. Therefore, in order to use the energy method, an intermediate step is required to calculate the in-plane stress state caused by the applied load. Once these stresses are found, Kollár and Dulácska (1984) suggest that the work done by the applied load should be replaced by the work done by the pre-buckling compressive stresses.

Analytical methods for finding the pre-buckling stresses in shells are outlined in great depth, and with examples, by Timoshenko and Woinowsky-Krieger (1959) and Flugge (1973). Timoshenko and Woinowsky-Krieger use the differential equilibrium equations and, where necessary, compatibility equations to determine the stresses in plates taking the shape of a rectangle, circle, sector, annulus, ellipse or triangle with simple loading and support conditions. They also determine the stresses in axisymmetric shells with axisymmetric loading. Flugge's work extends this to look at axisymmetric shells with more general loading, and explores both exact and approximate methods for determining the stresses in these cases.

The work by Timoshenko et al. (Timoshenko and Gere, 1961; Timoshenko and Woinowsky-Krieger, 1959), Kollár and Dulácska (1984) and Flugge (1973) still continues to be referenced today in work on finite element methods, structural design and analysis, micromechanics and composites, and vibration and dynamics. However, all of the work is limited to linear-elastic problems, and therefore, it cannot be directly applied to metal forming, where plastic buckling is very likely.

Hill (1958) combined the energy method with plasticity theory to develop a formulation for plastic bifurcation (which includes both tensile and compressive instabilities), although this is difficult to solve analytically for more than very simple problems. Hutchinson (1974) applied the theory to plates and shells, by neglecting out-of-plane stresses, to write this formulation using resultant line-loads,

assuming proportional loading. More recently, Gonçalves and Camotim (2007) applied Hill's theory of plastic instability to generalised beam theory to develop a formulation for buckling in thin-shelled beams. However, in all of these problems, values of the stresses or stress resultants are needed in order to solve them. Finding these values analytically can be difficult or impossible in anything more than very simple systems.

The work by both Hill (1958) and Hutchinson (1974) used deformation theory to develop the formulations. Although deformation theory is generally considered less accurate than incremental flow theory, it was shown by Von Kármán (1910) and Shanley (1947) that it more accurately predicts elasto-plastic buckling.

The formulation derived by Hutchinson (1974) has been solved analytically for some simple systems, for which two examples follow: the wrinkling of a tube in hydroforming and the wrinkling of a doubly-curved shell. Examples relating to deep drawing are discussed in section 2.2.2.

Chu and Xu (2004) use Hutchinson's formulation to develop analytical expressions for critical wrinkling stress in hydroforming, noting that all prior work on tube hydroforming had been based on elastic theory, or used finite element methods. They assume that all prior deformation and stresses are axisymmetric, and that the axial stress is uniform along the tube. These simplifications allow them to solve the problem analytically.

Hutchinson and Neale (1985) used the work of Hutchinson to determine the largest principle stress (equation 2.5) and corresponding strain criteria (equation 2.6) for plastic buckling in a doubly-curved shell with radii of curvature r_1 and r_2. However, in order to solve the formulation, they assume that the principle stresses are in the same direction as the principle strain, and that the stress is uniform over the region of wrinkling.

$$\sigma_1^{cr} = \frac{2}{3}\frac{t}{r_2}\sqrt{E_s E_t} \qquad \textbf{2.5}$$

$$\epsilon_1^{cr} = \frac{\sqrt{n}}{2+\gamma}\frac{t}{r_2}, \quad \epsilon_2^{cr} = \frac{\sqrt{n}}{2+\gamma^{-1}}\frac{t}{r_1} \qquad \textbf{2.6}$$

Where σ_1^{cr} is the value of the largest principle stress at buckling; ϵ_1^{cr} and ϵ_2^{cr} are the values of the largest and smallest in plane principle strains at buckling, respectively; t is the sheet thickness; E_s is the secant modulus (the ratio of effective stress to effective strain), and E_t is the tangent modulus (the instantaneous gradient of the effective stress-strain curve); n is the hardening exponent in the Ludwik-Hollomon equation for hardening ($\sigma_y = C\bar{\epsilon}^n$); and $\gamma = \epsilon_2/\epsilon_1$ is constant, as proportional loading is assumed.

The assumptions that Hutchinson and Neale make in order to solve their problem analytically mean that they solve quite a specific problem. More recently, Kim and Son (2000) built on Hutchinson and Neale's work, with the added complexity of anisotropic material. This added complexity meant that they have to solve the problem numerically and plot the results on a wrinkling limit diagram. This highlights the difficulties in finding analytical expressions for wrinkling criteria in complex problems. For this reason, many authors have turned to numerical and experimental approaches to model wrinkling.

Numerical models can be used to find stresses and strains developed throughout a manufacturing process. FEM are a popular numerical method to model manufacturing processes; however, in their conventional form, they can only model wrinkling when the size of the wrinkles is much larger than the size of the elements. Nevertheless, Wang and Cao (2000) use finite element methods to find the effective dimensions of the compressive regions, and then comparing the developed stresses with the critical wrinkling stress for this region, which they work out using the energy method and an appropriate deflection shape. Lu et al. (2005) use a similar method, but then refine the mesh in the regions where wrinkling occurs in order to model the post-buckling behaviour. Gonçalves and Camotim (2007) use their formulation for modelling instability in general beam theory to make a beam element for use in FEM, and show, by a series of examples, that their results match experimental results well.

Despite the ease and low cost of numerical methods, they are approximations. Using the wrong type of element can lead to inaccuracies (for example, fully integrated elements can lead to shear locking, while reduced integration elements can lead to hourglassing). Using too coarse a mesh or applying stabilisation in order to ensure convergence can also result in inaccuracies. They must therefore be used with great care in order to ensure that they produce accurate results. Secondly, they are very slow to run, especially for non-linear, iterative manufacturing processes, and only give results for one case – to find out how the change in a particular parameter will effect wrinkling would mean re-running the model.

For a truly accurate indication of whether wrinkling will occur or not, experimental methods can be used. Kleiner et al. (2002) and Henkenjohann et al. (2005) performed 96 experiments to provide a way of understanding the effect of certain parameters (e.g. sheet thickness, material properties) on the occurrence of wrinkling. However, very little about the mechanics of wrinkling and the nuances of a particular problem is learnt by this method.

An understanding of how material properties effect wrinkling can be gained from the Yoshida buckling test. In this test, a square piece of material is clamped at opposite corners and stretched, causing compressive stress between the free corners, resulting in wrinkles parallel to the tension. This gives an understanding of the wrinkling formation tendencies of the material being tested, so that the

effect of material properties on wrinkling can be tested. However, Kim et al. (2000) note that, because the geometry is fixed, the stress ratio is fixed. They therefore propose a modified Yoshida buckling test where the geometry can be varied to gain an understanding of the effect of stress ratio on wrinkling. Nevertheless, the results can only be applied to a metal forming process if the stresses in that process are known.

In summary, analytical solutions are the easiest to generalise and learn from, and (once set up) can be used to predict wrinkling quickly, but they are not always achievable and simplifying assumptions are often made to derive them, often making them applicable to only very specific cases. Numerical solutions are cheap and easy to set up, but they must be set up carefully in order to ensure that they are accurate, they are slow at providing results and are generally too slow to run online, and the results are hard to generalise. Experimental methods can be used to accurately determine the effect of certain parameters, but are hard to generalise and are expensive to run due to material costs. These three approaches have all been applied to both deep drawing and in spinning, as will be seen in the following sections.

2.2.2 Wrinkling in deep drawing

Many of the models of wrinkling on spinning, particularly analytical models, are based on deep drawing (Figure 1-1b) because of the similarities between the two processes: they are both used to make axisymmetric parts, and the processes both induce compressive circumferential stresses in the flange of the workpiece. There are differences, however: In spinning the deformation is local to the tool and the loading is not axisymmetric. This generally acts to make wrinkling more likely in spinning, but it makes analyses much more difficult. Furthermore, in deep drawing, a blank holder can be applied to restrict the formation of wrinkling. This is not practical in conventional spinning.

Despite these differences, the similarities are enough that some of the results from deep drawing can be applied to spinning. For example, Siebel and Dröge (1955) used the tool forces found from deep drawing, and multiplied them by a parameter, C_d, to give an estimate for the tool forces in spinning. Kobayashi (1963), developed a theory of wrinkling in spinning based on deep drawing. It is therefore clear that looking at the analytical models of wrinkling in deep drawing will help towards the understanding of wrinkling in spinning.

Early models of wrinkling in deep drawing were developed by Geckeler (1928), and expanded on by Senior (1956). Senior modelled the flange in deep drawing as a series of rectangular plates in compression, each being the length of one half-wave of the wrinkles. He then used the energy method to predict the mean hoop stress, σ_h that would cause wrinkling:

$$0.46\left(\frac{t}{b-a}\right)^2 \leq \frac{\sigma_h}{E_0} \leq 0.64\left(\frac{t}{b-a}\right)^2 \qquad \textbf{2.7}$$

and the number of wrinkles that would form:

$$1.65\frac{a+b}{2(b-a)} \leq n \leq 2.33\frac{a+b}{2(b-a)} \quad \textbf{2.8}$$

Where a and b are the inner and outer radii of the flange, respectively, t is the thickness of the sheet and E_0 is the plastic buckling modulus, defined by Von Kármán (1910):

$$E_0 = \frac{4EE_t}{\left(\sqrt{E}+\sqrt{E_t}\right)^2} \quad \textbf{2.9}$$

Where E is the elastic Young's modulus, and E_t is the tangent modulus. Senior (1956) confirmed these experimentally by comparing the number of wrinkles and the reduction in outer diameter and showed reasonable agreement, with most experiments lying between the limits or close to them. However, some experiments showed 50% more waves than the upper estimate, and there are 20% errors on the predicted reduction in outer diameter at wrinkling.

Yu and Johnson (1982) improved on Senior's approximation of the flange as a series of rectangular plates. Instead, they modelled the flange as an annular plate, using Lame's equations, along with Timoshenko's work (Timoshenko and Gere, 1961; Timoshenko and Woinowsky-Krieger, 1959) on axisymmetric plates. Using the energy method, they found that the hoop stress that would cause wrinkling was similar to Senior's expression, but with an extra term which becomes significant for wider flanges. Their expression for the critical hoop stress, σ_c, became:

$$\frac{b-a}{b} = 0.67\sqrt{\frac{E_0}{\sigma_c}.\frac{t}{b}} + 1.2\frac{E_0}{\sigma_c}.\frac{t^2}{b^2} \quad \textbf{2.10}$$

and they show better agreement with the experimental results of Senior (1956).

Xiong and Xie (2002) built on Yu and Johnson's work, using the energy method to generate an expression for the critical wrinkling stress with the application of a blank holder, by applying an energy penalty to out-of-plane motion of the blank into the blank holder. However, Kim et al. (2003) argued that the contact conditions between the blank holder and the blank were more complicated than Xiong and Xie's model, because the thickening of the outer regions of the blank pushes the blank holder upwards, leaving a gap between the blank holder and other regions of the blank. They therefore used FEM to model this extra complication. However, their FEM model overestimates the critical punch stroke by up to 50%, but predicts the number of wrinkles to within 20%, which does not represent much of an improvement over the analysis of Senior (1956). Agrawal et al. (2007) were able to use an upper-bound approach to determine the thickening of the blank, and were therefore able to

develop an analytical predictor for wrinkling which showed improved agreement with Senior's (1956) experimental results compared to both Senior's (1956) or Yu and Johnson's (1984) models.

Senior (1956), Yu and Johnson (1982), and Xiong and Xie (2002) all determined circumferential hoop stresses at which buckling occurs. Finding the circumferential hoop stress in deep drawing is well documented (for example, by Hosford and Caddell, 2007), which means that wrinkling can be easily predicted in simple deep drawing.

Unfortunately, the complex, non-axisymmetric stress state in spinning means that the analysis is not so simple. Hayama et al. (1966) argued that because of the lack of symmetry in spinning, the cause of wrinkling is very different. This highlights that deep drawing theory cannot be applied directly to spinning. Nevertheless, the above works can be used as a starting point, or simply examples of the use of energy method, for developing an analytical model for wrinkling in spinning.

2.2.3 Wrinkling in spinning

Ideally, the constraint model within the closed-loop minimisation would be some kind of analytical expression, so that the minimisation could be performed, and a toolpath generated, quickly. An acceptable alternative would be a fast numerical model, but the key is that the model must be fast enough to run online. However, before reviewing analytical work, the conclusions from experimental and numerical work are reviewed, so that the analytical models can be evaluated in light of these conclusions.

Experimental work on wrinkling in spinning has had three approaches. Firstly, Hayama et al. (1966) and Hayama (1981) used strain gauges to measure the strains in the workpiece in spinning, in order to gain an understanding of the mechanics that cause wrinkling.

Secondly, von Finckenstein and Dierig (1990) proposed using tool force feedback in conventional to adjust the feed rate of the working roller to prevent wrinkling, as well as tearing. However, an initial tool path and a force path needed to be defined in advance, and this was only used to compensate for small changes in batches of materials. Arai (2003, 2005) used a similar approach in shear spinning, but just to ensure that the sheet was firmly pressed against the mandrel. However, in conventional spinning, this method has received very little further attention in the academic literature.

Thirdly, batches of experiments can be ran to gain an understanding of the toolpath shapes that reduce the chance of wrinkling. Hayama et al. (1970) performed experiments testing linear and involute toolpaths and found that involute toolpaths maximised that spinning ratio that could be achieved while avoiding wrinkling. Later Kawai (1989) performed a range of experiments, but rather than using it to create general rules, he created a searchable database of successful toolpaths for specific products. This has developed into statistical design of experiments methods by Kleiner et al. (2002) who run 96

experiments and manually grade wrinkles in their experiments from 0 (no wrinkles) to 6 (severe wrinkles). However, rather than developing a model or set of rules for online use, this was used within an offline toolpath planning algorithm to interpolate the existing parameter field and find the optimum path for a new problem (Henkenjohann et al., 2005). Auer et al. (2004) used a similar approach but considered wrinkling to be outright failure, rather than a measuring it on a scale to be minimised.

Numerical methods have also been used by Wang et al. (2011), Music and Allwood (2011b) and Watson and Long (2014) to gain an understanding of wrinkling in conventional spinning and design toolpaths. Wang et al. found that the severity of wrinkles increases as the tool feed rate increases and verify this experimentally. Music and Allwood designed toolpaths on a point-by-point basis, by modelling the workpiece as the tool is indented, and then as the workpiece rotated to see if wrinkling occurred. The tool indentation at that point was used to give one point of the toolpath. By doing this with the tool at a number of points along the workpiece, a toolpath was designed. By looking at the stresses, Watson and Long suggested that wrinkling was linked not only to compressive stresses in the flange, but also by plastic yielding at the tip of the flange.

Together, all of these investigations identified a number of operating parameters which have an effect on wrinkling, and the results are summarised in Table 2-1. In exploring the mechanics of wrinkling and explaining these results, Hayama (1966) found that wrinkling is caused by compressive stresses and circumferential curvature. This is similar to conclusions by Music and Allwood (2011b) who said that it is caused by a combination of compressive stresses and plastic hinges caused by the concentrated force applied by the tool. It is also similar to the conclusion of Watson and Long (2014) who showed through FE models that wrinkling was preceded by plasticity at the edge of the workpiece.

Once the geometry and material properties of the part to be made are defined, the only operating parameters that can be changed are the feed-rate, toolpath and roller nose radius. The effect of these on wrinkling are consistent with the conclusions made by Hayama (1966) and Music and Allwood (2011b): a decreased feed rate, less aggressive toolpath, or increase roller nose radius result in decreased curvatures and less severe stresses, leading to less likely wrinkling. This highlights the fact that the asymmetry in spinning makes wrinkling more likely when compared to deep drawing.

The experimental and numerical trials give a qualitative idea of how the operating parameters affect wrinkling. However, because they are difficult to generalise, their results cannot be directly used to generate the constraint equation in the closed-loop minimisation. Nevertheless, they give a starting point for evaluation the results of analytical models of wrinkling in spinning.

Table 2-1 – How the operating parameters should be changed ("-" means decrease, "+" means increase) in order to suppress wrinkling.

Parameter	To suppress wrinkling	Reference
Feed rate	-	Hayama et al. (1966), Wang et al. (2011), Music and Allwood (2011b)
Toolpath	Use involute toolpath	Hayama et al. (1970)
Roller nose radius	+	Siebel and Dröge (1955)
Sheet thickness	+	Hayama (1981), Kleiner et al. (2002), Xia et al. (2005)
Blank diameter	-	Kleiner et al. (2002)
Spinning ratio (diameter of blank to diameter of part)	-	Xia et al. (2005)
Roller-mandrel clearance	-	Arai (Arai, 2003), Xia et al. (2005)
Hardening exponent	-	Hayama (1981)

Kobayashi (1963) developed a basic analytical model based on Geckeler's (1928) and Senior's (1956) work on deep drawing. This model resulted in the wrinkling condition, that wrinkling occurs when:

$$\frac{a_0}{b_0} \leq \frac{a}{b}\sqrt{\frac{g}{1+g}} \tag{2.11}$$

Where

$$g = \frac{2C}{K\left(\frac{t_0}{a_0}\right)^2}(\delta - 1)\left[\frac{\left(\frac{1-\frac{a}{b}}{1+\frac{a}{b}}\right)^2}{1+(\delta-1)\left(\frac{a}{b}\right)^2}\right] \tag{2.12}$$

a and b are the inner and outer radii of the flange, subscript 0 means initial and f means final, t is the material thickness, $\delta = \frac{t_f}{t0}\sin\alpha$, α is the cone angle, C is a material constant and K is a constant (0.46 or 0.64).

However, this model is very simple, and ignores many of the operating parameters in Table 2-1 which have been shown to affect wrinkling. With no dependence on the tool commands $\mathbf{u}(\mathbf{x})$, the feed rate and toolpath shape for example, it is of little us when performing toolpath planning.

In order to make a true prediction of wrinkling in spinning, the pre-wrinkling stress distribution in the flange must be known, so that the energy method can be used. Although no further analytical works on wrinkling in spinning were found, there were other analytical works on spinning which provide a starting point for determining the stresses.

Sortais (1963) and Avitzur and Yang (1960) both take a work balance approach to determining the tool force. Sortais looks at the work done in one revolution of the workpiece, so that the deformation is axisymmetric, and equates this with the work done by the tangential tool force. Avitzur and Yang (1960) assumed purely plastic deformation, and calculated the strains from the velocity field, which they defined in relation to the geometry of the tool used, allowing them to calculate the work done in the region near the tool.

Quigley and Monaghan (2000) calculated the strains in spinning by assuming constant thickness. However, their experimental results show a large discrepancy with their theoretical results because the constant thickness assumption is rarely an accurate one.

Sortais's (1963) work only looks at the strains induced by one revolution, while Quigley and Monaghan's (2000) looks at the strains induced by the entire process. These do not give any insight on the local effects of the application of the tool, and do not consider the strain path, which would be needed to calculate the resulting stresses. Avitzur and Yang's (1960) work is more useful in the sense that it looks at the local strains around the tool, but it does not go as far as determining the evolution of compressive circumferential stresses in the flange.

Despite many decades of work trying to understand the wrinkling phenomenon in spinning, a model with the detail required to generate toolpaths still remains elusive. Numerical models exist but are too slow to be used online, and even if used in the offline toolpath planning were used, the minimisation would take months or even years to solve – a lead time which would be unacceptable in most industrial applications, even if the computational resources were available.

2.3 Process models of thinning and tearing

An understanding of the mechanics of tearing in spinning is sparse, but three papers in the published literature have linked tearing to the reduction in area at fracture in a tensile tests. Kegg (1961) performed shear spinning on an elliptical cone with a wall angle varying from 0 to 90°, so that the final percentage thinning according to the sine law would vary from 0 to 100%. He found that tearing occurred when the reduction in thickness is equal to the reduction in area at fracture in a tensile test. Hayama and Tago (1968) argued that this was not exactly valid because the forming forces were different to axisymmetric shear spinning, but later Hayama (1981) also linked tearing to the reduction of area at fracture in tensile tests.

Despite the lack of models of tearing, the link between thinning and tearing allows the possibility to control thinning, preventing it from reaching a critical value at which a tear can be expected. The academic literature on thinning is more abundant, given industrial demands not just to produce defect free parts, but also to produce parts of uniform thickness. As with the development of the understanding of wrinkling, the work in this area can be split in experimental, numerical and analytical work.

Experimental work in shear spinning has shown that, to achieve a uniform thickness, the sine law of thickness should be adhered to and the tool feed rate should be increased. Kalpakciolgu (1961) conducted experiments investigating the effect of deviation from the sine law, and found that in under-spinning (where the thickness was not reduced enough) thickness variations of more than 10% along the flange were measured in the final product. He found smaller variations when over-spinning (where thickness was reduced too much), but that the most uniform wall thickness was achieved when the sine law is achieved. Hayama and Murota (1963) found other working conditions could affect the strain distributions, and therefore the thickness, by up to 50%. They found that thickness was particularly sensitive to feed rate: a slower feed rate meant more thinning. Shima et al. (1997) confirmed that this also applies in the flexible two-roller shear spinning process, though at the expense of lower dimensional accuracy.

Sekiguchi and Arai (2012) showed that it was also possible to control thickness of a spun cone by oblique shear spinning methods – where the flange is inclined during forging (Figure 2-3). This allows a product to be produced with thickness greater than the sine law suggests, but only on one side of the cone – the cone is consequently thinner on the opposite side. This is therefore of limited use in producing products with uniform thickness, but is potentially useful in products where varying thickness around the circumference is required for structural purposes.

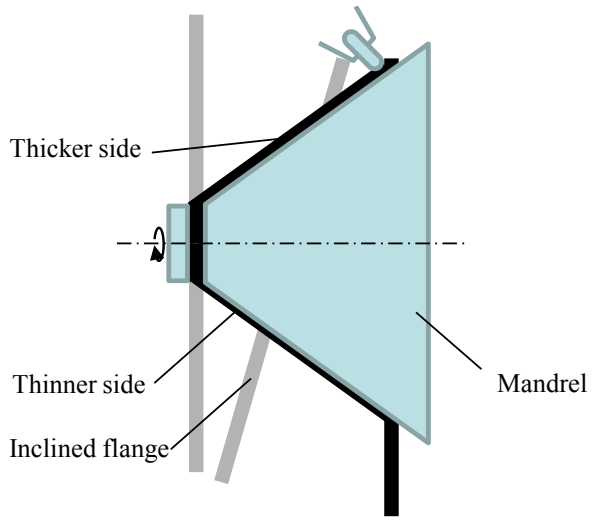

Figure 2-3 - Oblique shear spinning (Adapted from Sekiguchi and Arai, 2012)

Experimental work on thinning in conventional spinning has shown that the mechanics of thinning are different to that in shear spinning, and different parameters will affect the thickness. Kawai and Hayama (1987) point out that the toolpath geometry influences the final sheet thickness. Kang et al. (1999) studied just the first pass in conventional spinning, trying linear, concave and convex paths, but found that the first pass is in fact a shear spinning pass and the resulting thickness varies according to the sine law – suggesting that the first pass has a significant impact on the thickness of the final product. Wang and Long (2011) ran experiments and FE models of spinning with different toolpath shapes (concave, convex, linear and combined concave/convex - Figure 2-4) and found that a convex toolpath results in the least thinning and the lowest tool forces. Using a concave involute toolpath, Kawai and Hayama's experiments show that the number of passes and offset between passes determine the final sheet thickness, while El-Khabeery et al. (1991) report that low feed rates and a large roller nose radius gave the least and most uniform thinning. This is in contrast to the work in shear spinning, which showed that high feed rates led to more uniform thinning. No comment are made about this contrast in the literature, but it is possibly down to work hardening: in shear spinning a slow tool can lead to more work hardening, making the material progressively more difficult to work with and creating a non-uniformity in the thickness.

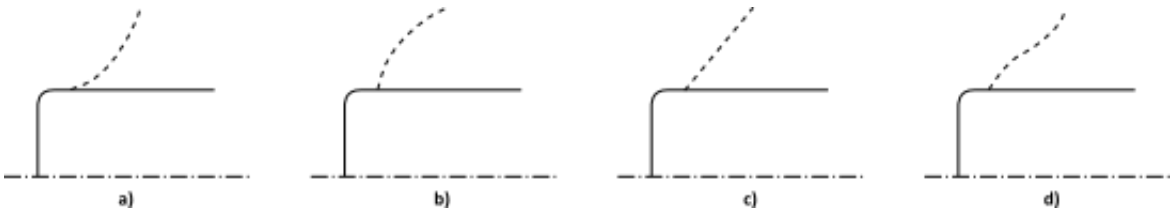

Figure 2-4 - Toolpath shapes: a) concave, b) convex, c) linear and d) combined concave/convex

The experimental work on force feedback and design of experiment methods used to prevent wrinkling were also successful in reducing thinning. Indeed, Reil (1993) used the tool force feedback system proposed be Von Finckenstein and Dierig (1990) and showed that it improved thickness uniformity by between 7 and 21%. As in wrinkling, this work evolved into the statistical design of experiments by Auer et al. (2004), who experimentally generated a database of toolpaths, and could then select toolpaths for a new part to minimise thinning and avoid either wrinkling or tearing. However, this is only possible within the parameter range that is tested experimentally.

To create models which can be more general, many authors have turned to numerical methods. Alberti et al. (1989) proposed using an axisymmetric FE model to model one-pass in conventional spinning. They use this model to predict geometry, thickness and tool forces in spinning, but give no validation. Liu et al. (2002) also use an axisymmetric model to study the first toolpass for different shapes of toolpath and find that an involute pass gives the lowest strains in the sheet. Mori and Nonaka (2004) extend the axisymmetric model to include circumferential shear, which allows them to model the build-up of material in front of the roller in shear spinning – although the amount of build-up agrees

with experiments, they do not verify any other metric (e.g. thinning) experimentally. Given the non-axisymmetric nature of the loading of the tool, it is unlikely that these models would be very accurate, and given the 20 minute computational time, they would also be too slow to run online.

In full, three-dimensional FE models, Quigley and Monaghan (2001) model just part of the first pass and show that strains and forces agree well with experiments, but at much higher computational cost than the axisymmetric models. They confirm the experimental results that the first pass is a shear spinning pass. Zhan et al. (2006) develop an explicit three-dimensional FE model of shear spinning to study stress, strain and thickness distribution and later (Zhan et al., 2007) use the model to confirm experimental results that high feed ratio produces more uniform thickness in shear spinning. Wang and Long (2013) use FE models of conventional spinning to model the first six tool passes, and find that most thinning occurs on the forwards passes. Furthermore, they find that, contrary to experimental results for conventional spinning, higher feed rates lead to more thinning, but less likelihood of tearing. They compare results with experiments at the end of the six passes, and find that the maximum amount of thinning agrees well, but the profile of thickness along the workpiece meridian is quite different in experiments and the model. Shi et al. (2014) use a similar FE model to test the response to uncertainties, and find that thinning is sensitive to tool feed rate.

Although the full three-dimensional FE models are more detailed than the axisymmetric models, they are even slower. They are likely, therefore, too slow even for offline control. Analytical models might provide a fast, even if approximate model, for online control. However, there are only two analytical models in the literature of thickness strains. Noyes (1983) create analytical models of the three dimensional strains in spinning. However, they make assumptions that in conventional spinning the thickness strain is zero, and in shear spinning the thickness follows the sine law. These assumptions then lead to estimates of the strain in the circumferential and radial directions. Quigley and Monaghan (2000) derive a similar model using the same assumptions and compare it to experiments, finding errors of up to 100% in some regions, which they attribute to the incorrect assumption on thickness strain. These assumptions on the thickness strains mean that these analytical models give no additional details on the thickness than the idealisations of the two categories of spinning process, and give no information on how the toolpath could be varied to produce the same product but with less thinning.

In summary, experimental work has shown that tearing and thinning are linked. There is a large body of literature on experimental investigations and numerical modelling of thinning, but very little on analytical models. Empirically based models will only work within the range they have been "trained" for. Three-dimensional FE models are too slow for online use, while axisymmetric FE models might soon be fast enough to run online, and although they have not been verified experimentally, closed-loop control of product properties can compensate for the approximations made. Analytical models

exist, but make idealised assumptions about the sheet thickness which means they are not useful for understanding either thinning or tearing.

2.4 Modelling techniques for closed-loop control outside of spinning

The above review on modelling in spinning has revealed that there are some models of spinning which might be appropriate for use within closed-loop control of product properties. For predicting the geometry, the impulse response approach is fast and general but it is not clear how the response might be summed up given the non-linearity of the process; and the axisymmetric FE models, although not experimentally verified, could still be good enough approximations to be used within the closed-loop control system, but may not be fast enough. The axisymmetric models could also be used to predict the degree of thinning, with a criteria on thinning used to prevent tearing. However, in wrinkling, no models were found which were detailed enough to be useful in toolpath generation, but fast enough to be used online. In all cases, detailed FE models could be used to accurately model the process, but would not be fast enough, either with today's computing power or for many decades, to be used online.

The reliance of FE is no surprise. The requirements in research and process design for accurate models has led to the continued development of modelling techniques for metal forming since the start of the 20th century. Osakada (2010) reviews the history of this development, noting a number of methods - such as slip-line fields, upper bound analysis and slab methods - that could be used to generate approximate analytical models. However, Osakada concludes that with the exponential increase in computing power since the 1970s, the Finite Element Method (FEM) has been dominant since the 1990s.

However, with today's computing power, FE models of spinning and indeed most metal forming processes are too slow for use within closed-loop control of product properties. The reliance on FE models has perhaps held back development of fast models, and therefore the application of closed-loop control of product properties. Hardt (1993) reviewed applications of closed-loop control of product properties published in the ASME Journal of Dynamic Systems, Measurement and Control and claimed that there was little focus from the dynamics and control community on manufacturing processes or process control – There were only 25 papers on the subject in the journal in the preceding 30 years, and only 2 of these related to metal forming, with the rest on machining, welding or casting. More recently, Lim et al. (2008) reviewed closed-loop of product properties in sheet metal stamping processes and found that a great deal of work had been done in this area, but concluded that there was still progress to be made in faster modelling and cost-effective sensors.

Despite this, our literature revealed that closed-loop control of product properties has been successfully applied to 12 metal forming processes to address geometric errors, defects and residual

stresses. Furthermore, Recker et al. (2011) has proposed closed-loop control of product properties as a solution to producing the desired material properties more accurately in incremental forging, but with no experiments yet carried out. This allows us to review the models used in each of these successful applications in order to identify how fast and approximate the models need to be in order to be successfully used in metal forming, so as to guide us in selecting suitable models for controlling metal spinning in the same way.

The fastest and most approximate models used in closed-loop control of product properties are linear, discrete-time, quasi-static, and assume that the process model is spatially and time invariant. In addition, the controller often uses a control horizon of one time step to minimise the computational cost of each minimisation – this means that rather than optimising the toolpath for the rest of the process, the toolpath is only optimised for the next time step, thereby reducing the computational load. For example, Hardt and Webb (1982) designed a closed loop control system for the shape of a part stamped with a matrix of punches (Figure 2-5). They use a conservative model of springback based on the difference between the tool shape and the resulting part shape. Thus, the control actions are given by

$$\mathbf{u}_k = \mathbf{u}_{k-1} - [\mathbf{q}_k(\mathbf{x}) - \mathbf{q}^d(\mathbf{x})] \qquad 2.13$$

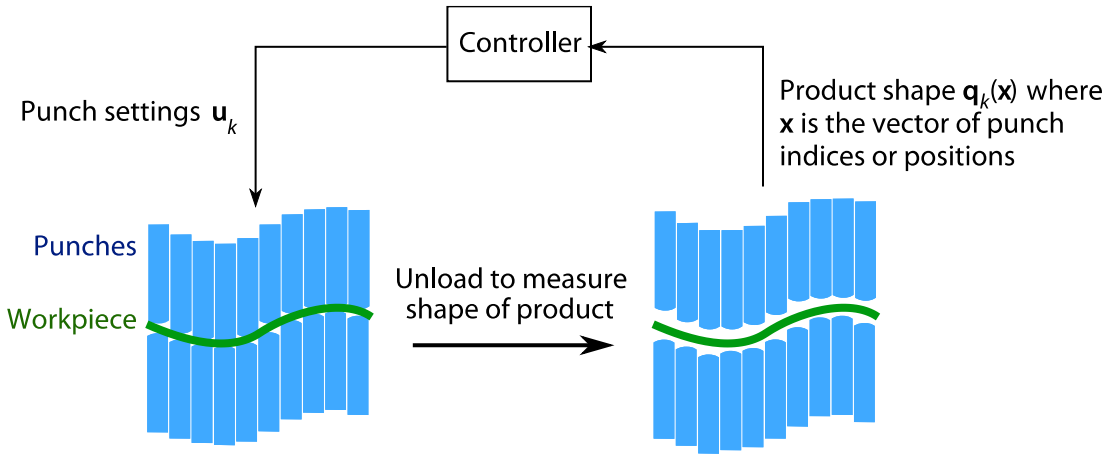

Figure 2-5 - Stamping with a matrix of punches (Adapted from Li et al. (2007))

Despite the conservative modelling of springback, as well as the implicit assumption that each punch has the same response, a reduction of error from 13% to 2% (a factor of 6.5) was achieved in 5 iterations. However, Li et al. (2007) reduced the error faster (from 4.2 to 0.25mm (a factor of 17) in the same number of iterations) by scaling the error term in equation 2.13 as:

$$\mathbf{u}_k = \mathbf{u}_{k-1} - \mathbf{c}_k(\mathbf{x})[\mathbf{q}_k(\mathbf{x}) - \mathbf{q}^d(\mathbf{x})] \qquad 2.14$$

For processes with mobile tools, in addition to actuator intensity, the tool path must be controlled. For example, Allwood et al. (2009) and Hao and Duncan (2011) applied closed-loop control to incremental sheet forming (ISF) of axisymmetric parts (Figure 2-6), restricting the tool path to a series

of circular contours with constant tool indentation along each contour. Allwood et al. (2009) determine the indentation in each step using an impulse response approach, having determined the impulse response experimentally at three stages in the process (early, middle and late). Hao and Duncan (2011) linearised the process model about a planned tool path, to create a fast online process model:

$$\mathbf{q}_{k+1} = \mathbf{q}^d_{k+1} + \left(\mathbf{q}_k - \mathbf{q}^d_k\right) + \mathbf{B}_k\left(\mathbf{u}_k - \mathbf{u}^d_k\right)$$
$$\text{with } \mathbf{B} \text{ defined so that } \mathbf{B}_k\mathbf{u}^d_k = \mathbf{q}^d_{k+1} - \mathbf{q}^d_k \qquad \textbf{2.15}$$

where the superscript "*d*" indicates the planned actuation and workpiece state. Using these simple models, they were able to reduce errors in the depth of a 25mm deep truncated cone from 3mm to 0.2mm.

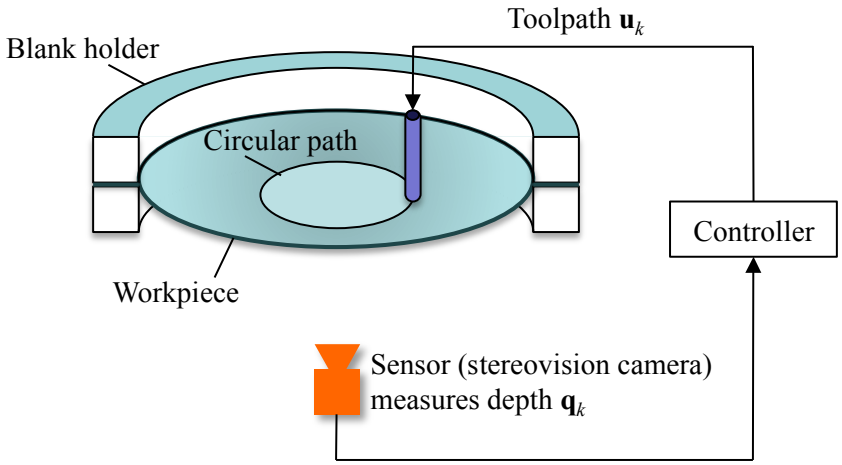

Figure 2-6 - Incremental Sheet Forming

In laser bending, Edwardson et al. (2004) took a similar approach for non-axisymmetric products, using contours of error between the target and measured product height as a path for the laser, with the same impulse response approach as above to determine actuation intensity. They were able to reduce the error in height from 8mm to 2.5mm in a 25mm deep cone.

These process models relate to discrete processes, in which a single part is made in a number of steps, with measurements and control updates between each step. However, closed-loop control of product properties has also been applied to continuous processes such as strip rolling (Figure 2-7). Indeed, strip rolling was the first process to have closed-loop control of product properties applied by Bravington et al. (1976), who showed a 40% reduction in flatness errors caused by residual stresses, compared to the uncontrolled process, with just two actuators. Duncan (1997) exploit the delay between the actuators and the sensors in strip rolling to determine the open-loop response of the actuators from small perturbations in their settings, and Duncan et al. (1998) use a zero-order-hold approach where the system waits after changing the actuator settings for a steady state to be reached

before taking another measurement and generating another set of control actions. Using this method, they were able to reduce the error to 5% of the uncontrolled value with 10 actuators.

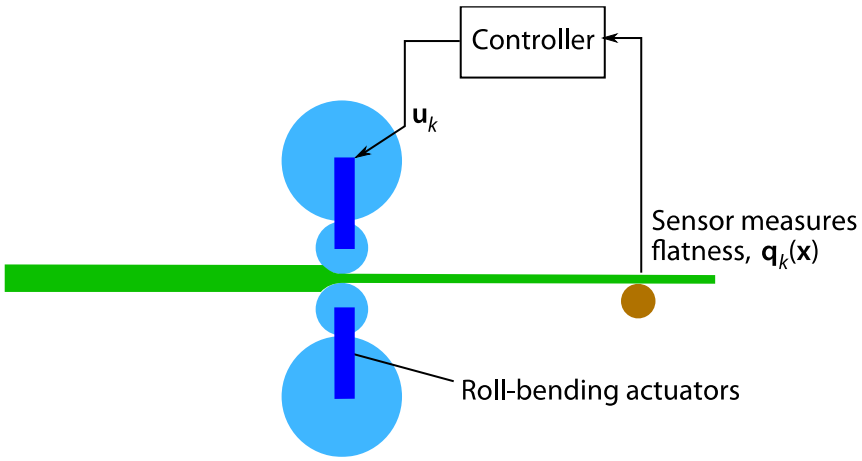

Figure 2-7 - Strip rolling

The discrete, zero-order-hold approach to controlling strip rolling neglects the dynamic effects of the changes to the actuator settings. Duncan (1995) justifies this assumption, pointing out that in many cases the dynamic effects and the steady state response are separable if all actuators have the same dynamic response and if, in the transient stage, the response retains the same shape but simply changes amplitude. For actuators with slower dynamic responses, such as those based on thermal expansion, the control system can be designed to compensate for the actuator dynamics (Duncan, 1989). Wellstead et al. (2000) show that in order to achieve high accuracy over small areas (i.e. constant thickness over small areas of sheet), then the delay in the response must be reduced by moving the actuators and sensors closer together and by increasing the response speed of actuators. However, by doing this, they show that often the process model can no longer be separated into steady-state and transient responses, and a full 2-dimensional model is required.

Luo et al. (1996) use a dynamic continuous process model to control the multi-axis beam bending process illustrated in Figure 2-8. They determine an approximate transfer function in Laplace space (transformed from the time-domain) based on classical beam theory with an elastic-perfectly-plastic material model. However, they note that with a dynamic model there is a chance that the system might become unstable.

Li et al. (2007) employed an adaptive model, to attempt to counter this instability by refining the process model using the history of inputs and outputs from earlier in the process. However, when Sun and Stelson (1997) used an adaptive process model to control multi-axis bending, they found that the resulting controller would be unstable. They therefore used a feed-forward controller to compensate for this instability, as proposed by Gross et al. (1994). Using this control system, they are able to reduce the errors in curvature from 50% to 10%.

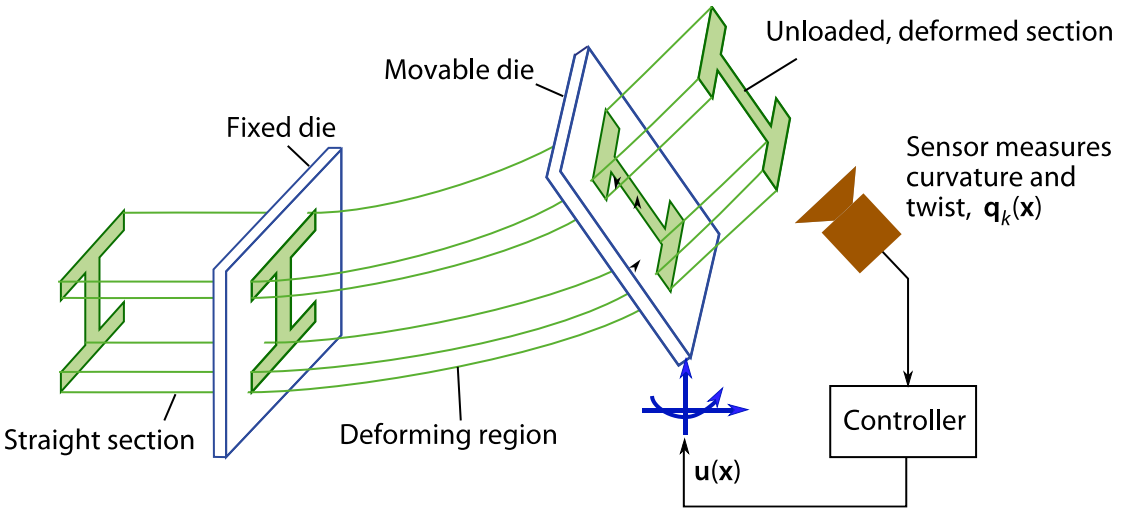

Figure 2-8 - Multi-axis bending and twisting (adapted from Sun and Stelson (1997))

The closed form process models given above are fast, but are not available for all metal forming processes. In order to take advantage of the flexibility and accuracy of FE modelling with the speed of these linear models, Prud'homme et al. (2002) ran (computationally expensive) FE models offline at different points in state space, and then interpolated between them online to provide real-time solutions. However, the interpolation is only valid over the region of state space modelled.

Some researchers, therefore, have used empirical process models to control metal forming processes. For example, Hardt et al. (1982) applied closed-loop control of product properties to a three-roll bending process, while Hardt and Hale (1984) did the same for three-roll straightening. Rather than explicitly using a process model to determine the evolution of the actuator settings, they used an integrator to control the actuator. This is a sub-set of proportional-integral-differential (PID) controllers, which are criticised by Desborough and Miller (2002) as they require retuning when process conditions change, but this is often neglected. They are often used, nevertheless, for their ease of set-up and use. Despite the simplicity, Hardt et al. (1982) reduce errors in curvature to less than 3% in roll bending, and Hardt and Hale (1984) reduce the lateral deflection by 53-91% in roll straightening.

In a more advanced example of an empirical process model, Yang et al. (1998) applied closed-loop control of product properties to a flexible L-bending process (Figure 2-9). By measuring the angle of the bend after the initial attempt at L-bending, the machine over-bends the workpiece in order to compensate for the springback. Rather than using a process model to determine the actuator controls they use a neural network. The network compares the input and state following the initial bend to results of previous experiments in order to determine the optimal actuator settings for the current workpiece. They reduce the error in bend angle from 4° to 0.5° in a 90° bend.

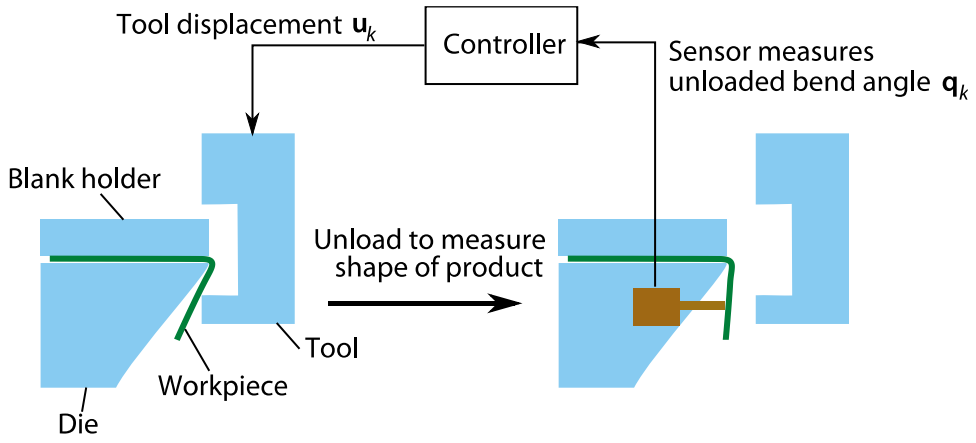

Figure 2-9 - L-bending (Adapted from Yang et al. (1998))

Despite extensive of work on developing fast process models for closed-loop control, few authors have focused on evaluating constraints – for example, to prevent wrinkling in spinning. The exception is in deep drawing (Figure 2-10), where the blank holder pressure must be set in order to avoiding failure due to wrinkling or tearing.

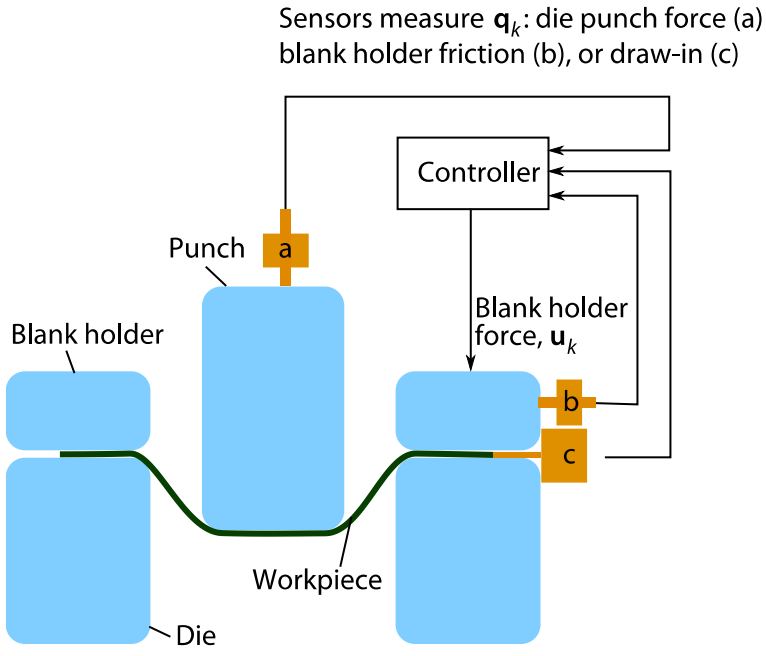

Figure 2-10 - Deep drawing

Siegert et al. (2000) and, more recently, Lim et al. (2008) reviewed the different approaches researchers have taken to predict such failures and found that in all approaches so far the blank holder force has been controlled to maintain a measured state variable within a given trajectory – in non-axisymmetric deep drawing the blank holder force distribution can be controlled with a segmented blank holder (Siegert et al., 2000) or draw beads. In the cases reviewed by Siegert et al. and Lim et al. the state was the punch force, blank holder friction or flange draw-in. More recently, Blaich and Leiwald (2008) measure the wall stress with a newly designed sensor and use this as the state. Successful trajectories of these states were found by experiment, so only some disturbances such as

changes in lubrication conditions and eccentric blank loading could be tolerated. Hardt and Fenn (1993) note that changes to the thickness and material properties of the blank must be known a-priori if trajectories of punch force or blank holder friction are followed, while following flange draw-in can tolerate these disturbances without prior knowledge.

In all the examples reviewed in this section, approximations have been used to speed up the solution of the process model and constraints. Even the uses of linear models have shown significant improvements in product quality. The use of empirical methods such as neural networks have also shown significant improvements, but they lack generality – they can only be used within the range of parameter space that they have been "trained for". However, even though it is clear that large approximations can be made, there is a clear trend: the models are all fast enough to be ran within a fraction of a second. This mostly rules out the use of FE models – even the axisymmetric models take several minutes to run with today's computing power – leaving only the impulse response approach as a feasible option as an online model for closed-loop control of product properties in metal spinning.

2.5 Conclusion

The goal of this thesis is to automate FAS. The automation problem is separated into three parts: automation of the internal rollers; compensation for springback; and designing toolpaths to avoid failure. The automation of the internal rollers is a novel one, because FAS is a novel process. However, the literature on processes related to FAS confirms that related spinning processes also suffer from springback errors, and the same modes of failure: wrinkling and tearing.

In order to solve these three problems, process models are needed. For offline control, such models must be very accurate in order to prevent errors in the model building up over time and resulting in errors in the toolpath. However, for online control, more approximate models can be used: in the literature, simple, linear models; empirically based neural networks; and simple PID controls have all been used within closed-loop control systems to produce significant improvements in product accuracy. However, models are still required - whether they are explicitly stated within the control system, or implicit in the way the control system works (e.g. in PID loops) – and they must be fast. Therefore, the literature was reviewed to see what models are available within the three areas of the automation problem in FAS.

For the automation of the internal rollers, a model of the effect of the internal roller positions on workpiece shape is needed. However, because the automation of the internal rollers is a new challenge in FAS, no work had focused specifically on this problem. FE models of spinning could be used, but these are too slow even for offline control, due to the large number of times that they would have to be run within the control system.

To compensate for springback, a model to predict springback and the resulting workpiece shape would be required. FE models are once again too slow even for offline use. The impulse response approach may be suitable for modelling the shape evolution, but it is unclear how the impulse response can be added given the non-linearity of the process, and it is also unclear how the impulse response might vary with the position of the internal rollers in FAS. Axisymmetric FE models are likely to be too approximate for offline use, while closed-loop control could correct for this approximation if the model were fast enough for online use.

To design toolpaths to prevent failure, a model to predict the two modes of failure – wrinkling and tearing – would be required. For modelling wrinkling, there are no suitable models that provide enough detail to generate toolpaths, but are fast enough to run online. Tearing can be prevented by limited thinning, but no suitable models exist for thinning either. Axisymmetric FE models can be used to predict thinning, but are too slow for online use and too approximate for offline use.

The lack of suitable models appears to be the key gap preventing the automation of both conventional spinning and FAS. Therefore, with the goal to automate FAS, this thesis aims to fill this gap by developing the models and applying these within closed-loop control of product properties in order to automate the internal rollers; compensate for springback; and design toolpaths to avoid failure.

This would represent a step forward in the development of FAS, and would allow it to automatically produce axisymmetric products. However, the FAS machine was also designed with the capability to produce non-axisymmetric products. Controlling the process in this way would require extending the models developed in this thesis to apply to non-axisymmetric spinning. Furthermore, the review into the categorisation of spinning processes revealed that some processes have a working tool on the inside of the workpiece rather than the outside – The internal support rollers on the FAS machine could be used to this effect to expand its range of operation. However, both of these possibilities will not be explored within this thesis, but could be the subject of further work.

Chapter 3 - Methodology

The investigations in this thesis primarily use two methods to build an understanding of the mechanics and control of flexible asymmetric spinning: Finite Element Methods (FEM) to model the process numerically and experiments to verify the control systems developed. Other methods are used in individual chapters, and are described in the relevant chapters. In this chapter, however, the implementation of these two primary investigative methods is discussed in detail and will be referred to in later chapters.

3.1 Finite element methods

FEM are a powerful tool for mechanical modelling. They enable complex mechanical problems to be modelled with relatively little manual effort (at least compared with setting up an analytical model or some form of bespoke approximate model). Furthermore, commercial Finite Element (FE) packages usually produce beautiful output. As a consequence, FE users are often so mesmerised by the output that they forget to maintain a healthy scepticism over the accuracy of the results. In this section, detailed investigations are carried out to ensure that the FE models used in this thesis are accurate and reliable.

The FE models developed here are designed to model the machine setup shown in Figure 3-1a, and this setup is replicated approximately in the FE modelling software, Abaqus as shown in Figure 3-1b. The model setup developed in this chapter is based on the tool following the first 12mm of a toolpath while the workpiece makes 10 rotations. Not all models used in this thesis model this setup exactly – some move the tool and workpiece in separate steps, and some model the process later, when the workpiece has already taken on some shape. However, all of the models used share a large degree of similarity in the broad dimensions and tools used, so it is assumed that if this setup can be modelled accurately, then the same FE model setup will work with slightly different physical setups where necessary in this thesis.

The common setup of these models is broken down here into four parts: The integration scheme and time incrementation in section 3.1.1; the assembly, boundary conditions and interactions in section 3.1.2; material modelling in section 3.1.3; and element selection and mesh design in section 3.1.4.

a) Physical machine setup

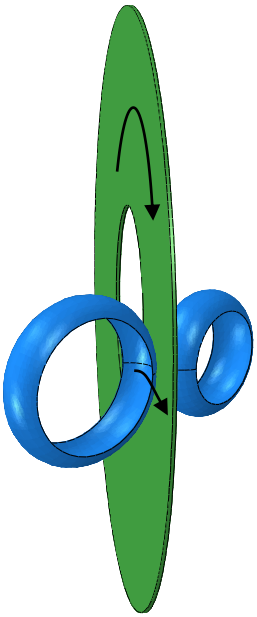

b) FE Model Setup

Figure 3-1 - The physical setup, and how it is represented in FE

3.1.1 Integration scheme and time increments

In FE models of non-linear processes, changes in the state (geometry, stress state etc.) of the system are predicted by ramping up the external load or boundary conditions over a period of time, and integrating over a series of small time increments in which the system is approximately linear. There are two schemes for integrating over the time increments: implicit integration and explicit integration. In explicit integration, the small changes in boundary conditions are applied at the start of the step. The equilibrium equations are solved to calculate the accelerations, which are integrated to find the state at the end of the step. In implicit integration, the equilibrium equations are solved at the *end* of each time increment in order to find the new equilibrium state after the small change in the boundary conditions.

Although implicit integration is more costly for each time increment, implicit integration is used in all FE models within this thesis as it offers two advantages over explicit integration. Firstly, implicit methods guarantee convergence or the analysis terminates, giving confidence in the model. Secondly, Abaqus adapts the time increment size, allowing larger time increments to be used in periods where the model is almost linear, but using small time increments to guarantee convergence when the model is very non-linear. In explicit analyses, there is a limit on the time increment size in order to prevent instability, and no convergence checks are performed to check that this time increment is still suitable.

However, Abaqus adapts the time increments quite aggressively: By default, Abaqus increases the time increment by 50% when two consecutive increments converge in fewer than 4 equilibrium iterations, and reduces the time increment by 75% when the solution appears to be diverging.

However, because the "optimum" time increment (that which reduces the chance of failure, but also reduces the total number of increments required) is approximately steady throughout most of the models, the default settings resulted in large oscillations about this optimal value as shown in Figure 3-2, and typically ~20% of increments failed to converge because they were too large. To reduce both the amplitude and frequency of these oscillations, and to keep the increment size closer to the optimum value, the increase was changed to just 3%, and the reduction to 25%. The resulting time increments are also plotted in Figure 3-2. Only ~4% of increments failed to converge, and the overall speed of the model was typically improved by 5%.

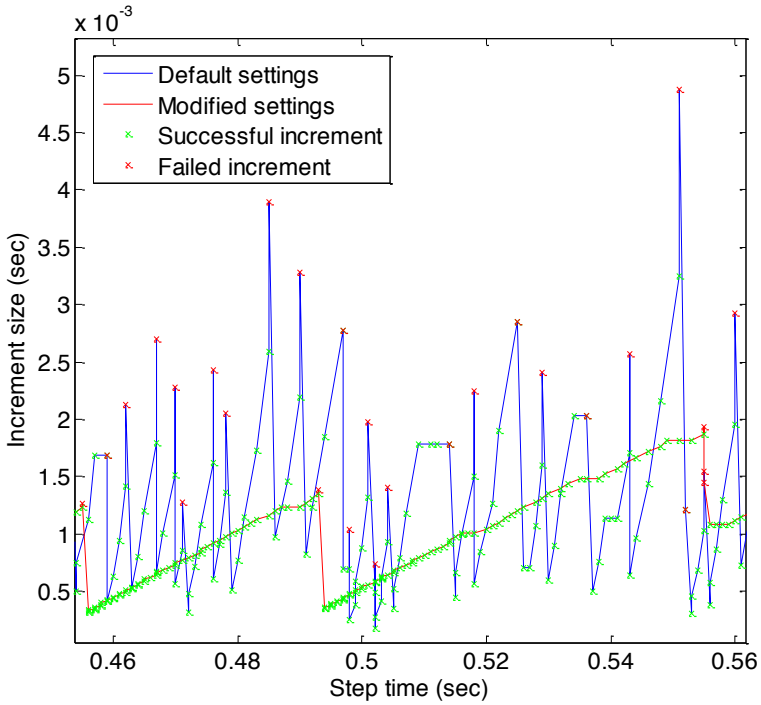

Figure 3-2 - Increment size for default and modified controls in Abaqus

Despite the incrementation of *time*, analysis is quasi-static – the measure of time is just used to ramp up the external loading. Inertial effects and strain-rate effects are ignored. This is acceptable because, in a literature review into the mechanics of metal spinning, Music (2010) found that the speed of the process had no effect on tool forces or spinnability. Furthermore, the flexible asymmetric spinning machine only runs at 200rpm – far slower than the typical 1,000-2,000rpm that industrial spinning machines run at.

3.1.2 Geometry and boundary conditions

The implicit solver is applied across the assembly according to the boundary conditions and interactions between parts within the assembly. However, the real world setup often cannot be modelled exactly, either due to limitations in model capability, or simply due to the computational complexity of modelling every physical aspect of the real world. For this reason, approximations are made in setting up the assembly, boundary conditions and interactions.

The assembly consists of the tools (working roller and internal rollers or mandrel, depending on the model) and the workpiece; none of the other machine components are included in the model. The tools are modelled as rigid analytical surfaces, as they are much stiffer than the workpiece due to their size (they are bulk metal, rather than sheet) and material (hardened tool steel). The workpiece is modelled as a deformable solid part, although the area attached to the spindle was not modelled (i.e. the workpiece was modelled with a 130mm diameter hole in, which is the diameter of the spindle clamping plate).

Displacement boundary conditions are used in order to model the motion of the machine tools and workpiece. A built-in boundary condition was applied to the edge of the hole in the centre of the workpiece, to represent the clamp on the spindle. The rotation of the spindle and workpiece was modelled by moving the tools around the workpiece leaving the workpiece stationary – this reduced the computational cost compared to rotating the workpiece, because the latter would mean moving thousands of nodes by small amounts as they rotate around the centre of the workpiece. Moving the tools around the workpiece typically increased the speed of the model by approximately 15% compared to rotating the workpiece and moving the tools only in the horizontal plane.

The interaction between the tools and workpiece was modelled through contact interactions. Contact between the tool and workpiece was modelled as frictionless, because, in practice, the tools were lubricated and free to roll, so friction forces are minimal. The tools were then controlled in the model using either displacement or velocity boundary conditions.

3.1.3 Material modelling

The mechanics of the deformable workpiece are defined by the material properties. However, within FE models, approximations also have to be made within material properties definitions, as often the precise yield surface cannot be modelled without both computational expense in the modelling, and experimental expense in calibrating the material properties.

The workpiece material used in the experiments in this thesis is commercially pure, half-hard Aluminium (AA1050-H14), and in the FE models, this is modelled using an anisotropic, elastic-plastic material which yields according to the Hill 1948 criterion (Hill, 1948) shown in equation 3.1

$$f(\boldsymbol{\sigma}) = \sqrt{F(\sigma_{22}-\sigma_{33})^2 + G(\sigma_{33}-\sigma_{11})^2 + H(\sigma_{11}-\sigma_{22})^2 + 2L\sigma_{23}^2 + 2M\sigma_{31}^2 + 2N\sigma_{12}^2} \qquad \textbf{3.1}$$

where F, G, H, L, M, N are constants to be calibrated by tests. They are defined as:

$$F = \frac{1}{2}\left(\frac{1}{k_{22}^2} + \frac{1}{k_{33}^2} - \frac{1}{k_{11}^2}\right), \qquad G = \frac{1}{2}\left(\frac{1}{k_{33}^2} + \frac{1}{k_{11}^2} - \frac{1}{k_{22}^2}\right), \qquad H = \frac{1}{2}\left(\frac{1}{k_{11}^2} + \frac{1}{k_{22}^2} - \frac{1}{k_{33}^2}\right)$$
$$L = \frac{3}{2k_{23}^2}, \qquad M = \frac{3}{2k_{13}^2}, \qquad N = \frac{3}{2k_{12}^2} \qquad \textbf{3.2}$$

where, for example, k_{22} is the stress ratio in the 22 direction, so that if σ_0 is the reference yield stress, the material will yield when loaded uniaxially in the 22 direction at $\sigma_{22} = k_{22}\sigma_0$. This is, therefore, an anisotropic version of the von Mises criterion. However, because there are more variables in this anisotropic yield criterion than in an isotropic one, more tests are needed to calibrate it.

In order to calibrate this material model, tensile tests were performed at a strain rate of 0.0003/second on dog-bone shaped specimens aligned parallel, perpendicular, and 45° to the rolling direction. The specimens were also unloaded part way through the tests in order to measure the Young's moduli. The measured moduli were:

$$E_0 = 62\text{GPa}, \qquad E_{45} = 56\text{GPa}, \qquad E_{90} = 62\text{GPa}$$

Where the symbol E is used to mean Young's modulus, and the subscript represents the angle from the rolling direction. A weighted average of these values was used to determine the through-thickness Young's modulus as in equation 3.3 – This may not be accurate, but the through-thickness properties are not critical. Indeed, often shell elements are enough to provide accurate results.

$$E_3 = \frac{E_0 + E_{90} + 2E_{45}}{4} = 59\text{GPa} \qquad \textbf{3.3}$$

The manufacturer's value of $\nu = 0.33$ was taken for the Poisson's ratio and a Mohr's circle analysis was performed to calculate the shear moduli:

$$G_{12} = 20\text{GPa}, \qquad G_{13} = G_{23} = 22\text{GPa}$$

This data was then compiled into an orthotropic stiffness matrix shown in equation 3.4, which could be entered directly into Abaqus.

$$\begin{pmatrix}\sigma_{11}\\ \sigma_{22}\\ \sigma_{33}\\ \sigma_{12}\\ \sigma_{13}\\ \sigma_{23}\end{pmatrix}[\text{MPa}] = \begin{pmatrix}90{,}300 & 43{,}700 & 42{,}100 & 0 & 0 & 0\\ 43{,}700 & 90{,}300 & 42{,}100 & 0 & 0 & 0\\ 42{,}100 & 42{,}100 & 85{,}400 & 0 & 0 & 0\\ 0 & 0 & 0 & 20{,}000 & 0 & 0\\ 0 & 0 & 0 & 0 & 22{,}000 & 0\\ 0 & 0 & 0 & 0 & 0 & 22{,}000\end{pmatrix}\begin{pmatrix}\epsilon_{11}\\ \epsilon_{22}\\ \epsilon_{33}\\ \gamma_{12}\\ \gamma_{13}\\ \gamma_{23}\end{pmatrix} \qquad \textbf{3.4}$$

The plastic material data was then considered. The stress-strain curve was smooth and did not show a clear yield stress, so the 0.2% proof stress was taken as the yield stress. The plastic region of the stress-strain curves measured is shown in Figure 3-3 for the rolling direction.

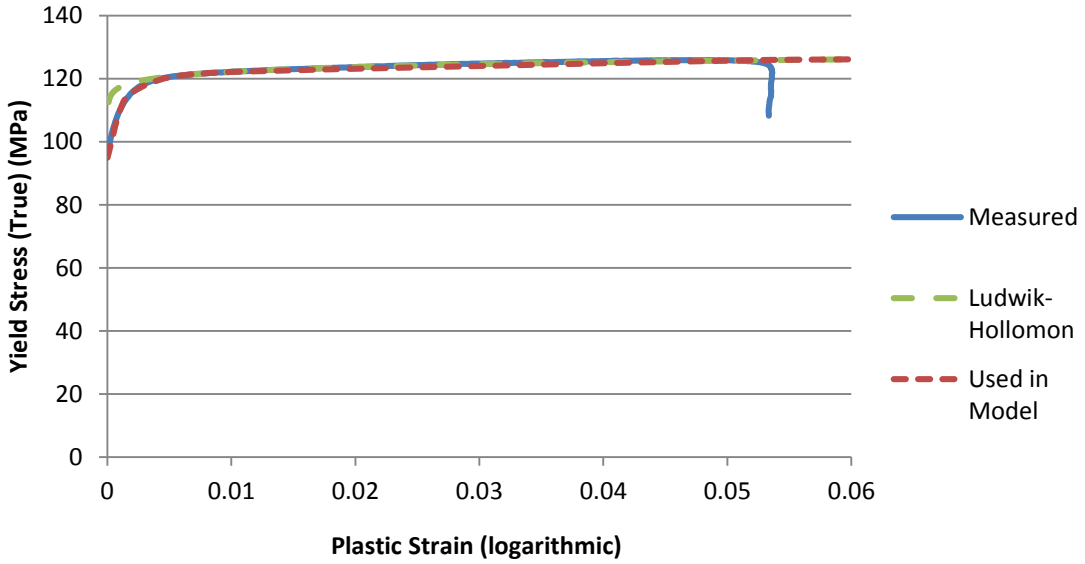

Figure 3-3 - Flow curve for AA1050-H14 in rolling direction

The plot is one of true-stress and true-strain, based on measured force and displacement. However, the conversion assumes that the deformation is uniform, so is only valid before necking occurs. In order to extrapolate the yield curve beyond the point at which necking occurs (as the material is much more ductile when loaded in opposite senses in two direction, as it typically the case in spinning), the Ludwik-Hollomon strain hardening equation is fitted as in equation 3.5 and plotted in Figure 3-3. There is a large disagreement between the measured flow curve and the Ludwik-Hollomon equation for low strains (<0.005), so the measured data is used in this region, and the Ludwik-Hollomon equation only used for plastic strains >0.005. The flow curved used in the Abaqus model is also plotted in Figure 3-3, showing a very close fit to the measured data until necking occurs.

$$\sigma = 132.7\epsilon^{0.0179} \tag{3.5}$$

To determine the stress ratios in the Hill 1948 criterion, the plastic stress-strain curves are needed in the other two directions. The plastic stress-strain curves for all three directions are shown in Figure 3-4. Best-fitting the scalar multiples gives:

$$k_{11} = 1, \qquad k_{22} = 1.078, \qquad k_{12} = 1.018$$

and the resulting flow curves in this direction are also plotted in Figure 3-4, showing good agreement with the experimental results until necking occurs.

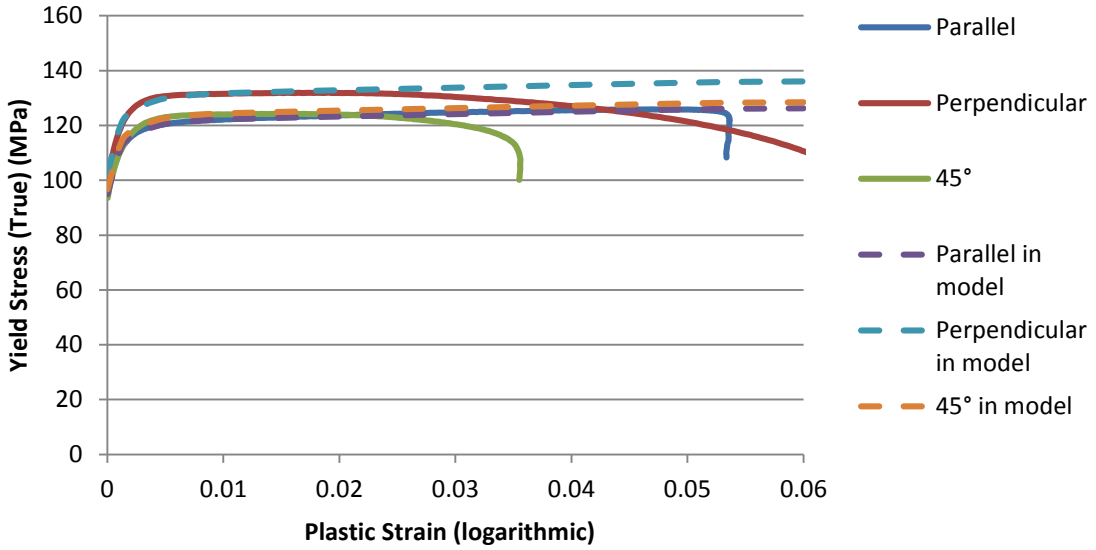

Figure 3-4 – Flow curve for AA1050-H14 in three different directions

These scalar multiples are then averaged to find the through-thickness and out-of-plane shear stress ratios:

$$k_{33} = \frac{k_{11} + 2k_{12} + k_{22}}{4} = 1.029$$
$$k_{13} = \frac{k_{11} + k_{33}}{2} = 1.015, \qquad k_{23} = \frac{k_{22} + k_{33}}{2} = 1.054 \tag{3.6}$$

3.1.4 Element selection and mesh design

Within the modelled assembly, the only part to be meshed is the workpiece, as the tools are modelled as analytical rigid parts. The design of the mesh can be broken down into two parts: the choice of element and the number of elements in the mesh.

The choice of element can be broken down further, given the vast number of options that Abaqus provides: firstly, whether to use continuum 3D stress elements, or one of the specialist structural elements Abaqus provides (e.g. shell, membrane etc.); secondly, the number of nodes on each element, which determines its shape (tetrahedral, wedge, hexahedral etc.) and order (linear, quadratic etc.); and thirdly, additional options such as reduced integration and incompatible modes.

The workpiece is a sheet product – its overall dimensions are much greater than its thickness and it can be considered "slender" and the through-thickness stresses are usually small. Therefore, shell elements could be considered, as well as continuum shell elements and full 3D stress continuum elements. However, in other FE models of spinning, Music (2011) and Wang (2012) both rule out shell elements in favour of continuum shell elements as continuum shell elements can model bending and contact more accurately, and can also be stacked to capture more detail of the through-thickness response.

However, at certain stages in the spinning process – particularly when the working roller is quite close to either the mandrel (in conventional spinning), or any of the internal rollers (in FAS) – the workpiece can no longer be considered slender. Out-of-plane shear and even through-thickness stresses can become significant and result in modelling errors. Large errors of over 200% in axial force and 700% on radial force could then be seen between experimentally measured and predicted forces, as seen in Figure 3-5. Continuum 3D stress elements must be used in order to model the out-of-plane shear and through-thickness stresses.

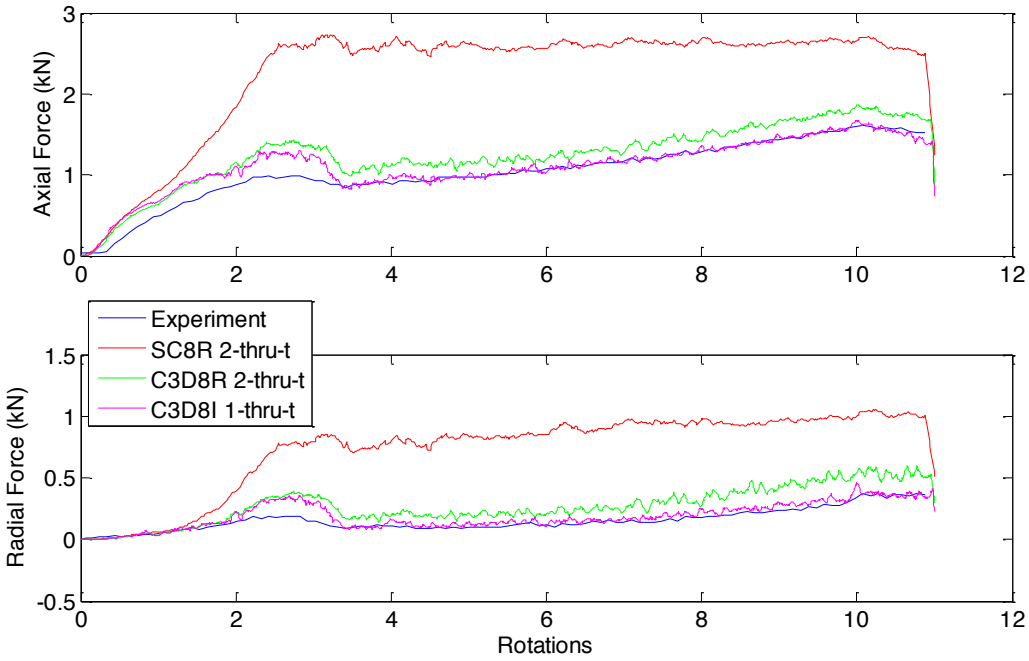

Figure 3-5 - The tool forces measured and predicted by FE (Note that a moving average has been applied to remove some noise to make the results easier to visualize)

Abaqus offers three different shaped continuum shell elements: tetrahedral, wedge, and hexahedral. However, tetrahedral and wedge elements have poor modelling accuracy, and are typically used to fill regions where the behaviour is not of interest to the user (*Abaqus 6.13 Online Documentation*, 2013). Within the remaining hexahedral elements, Abaqus offers 8-node linear and 20-node quadratic elements. However, the quadratic elements are too computationally expensive and are not considered here.

The final choice for element selection is the integration method. Abaqus uses Gaussian quadrature to integrate the strain energy across the elements for the purpose of the equilibrium calculations and offers two options for this: fully integrated elements (C3D8), using all 8 integration points needed to integrate exactly across the linear hexahedral element or reduced integration elements (C3D8R), using only 1 integration point. However, linear hexahedral elements cannot deform with uniform curvature, as would be expected when bending moments are applied (Figure 3-6a). Instead, they deform through a shearing mode (Figure 3-6b) resulting in parasitic shear stresses and overestimating the bending

stiffness of the element – This is called "shear locking". Therefore, fully integrated elements cannot be relied upon to model spinning accurately.

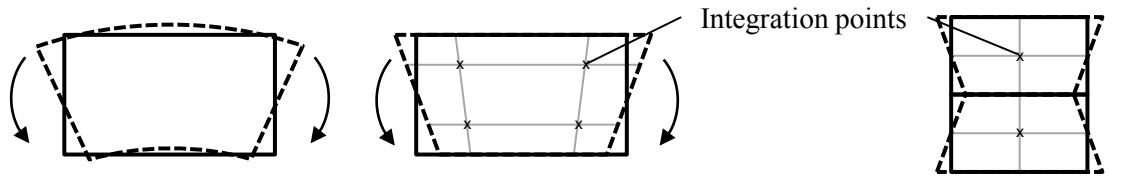

a) True bending deformation **b) Bending deformation approximated by linear element** **c) Hour-glassing mode**

Figure 3-6 - Deformation modes of linear elements

By using reduced integration, this problem of shear-locking is removed, but another is introduced. When only one integration point is used, an hour-glassing mode of deformation can occur freely (Figure 3-6c), as this mode results in no strain at the integration point and therefore no strain energy. Abaqus uses constraints to prevent this type of deformation occurring, which results in additional energy, "artificial energy", in the model. In an accurate model, artificial energy should remain small (typically less than ~1%) compared to the total internal energy in the model. Typically, the amount of artificial energy seen can be reduced by using more elements through the thickness of the sheet.

To prevent these problems in their models, Music (2011) used two reduced integration continuum shell elements through the thickness of the workpiece, while Wang (2012) used only one, but with enhanced hour-glassing control in order to prevent hour-glassing. These elements were found to result in good convergence and good agreement with experimental results – but they did not consider cases where the working roller was very close to the mandrel/internal rollers.

In our models, reduced integration elements resulted in large amounts of artificial energy when used to model the first 10 rotations of the spinning process. Figure 3-7 shows artificial energy with one element through-thickness growing as high as 95% of total internal energy before gradually dropping to 30%, which is suggestive of hour-glassing problems (the analysis then failed to complete due to divergence – probably caused by severe hour-glassing). With two elements, the artificial energy reaches approximately 25% very briefly before dropping to ~5%, but this is still too high. The resulting predicted forces with two C3D8R elements through the thickness is shown in Figure 3-5, showing much better agreement than with continuum shell elements, but still shows errors of up to 30% on axial force, and 100% on radial force.

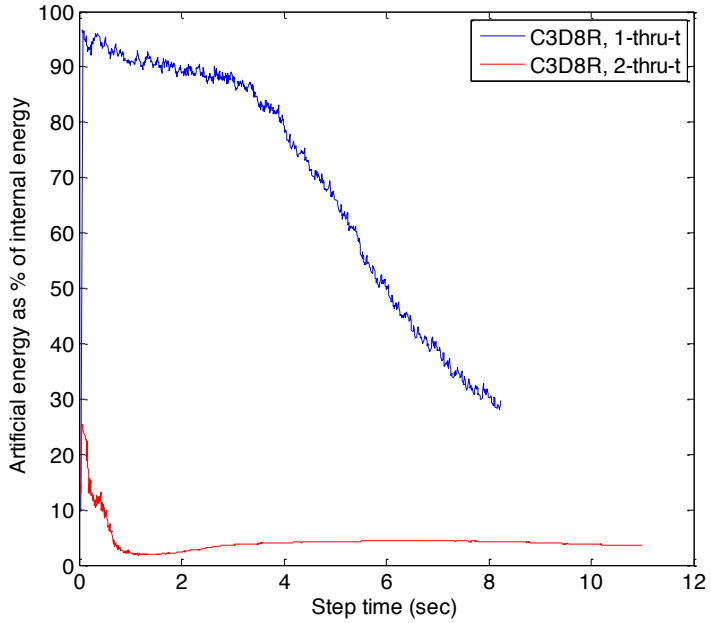

Figure 3-7 - Artificial energy as % of total internal energy with reduced integration continuum elements

Abaqus offers another method of removing the shear locking and hour-glassing problems, which is more efficient than increasing numbers of through-thickness elements in this case: Elements with incompatible modes (C3D8I). These are fully integrated elements, but with additional degrees of freedom independent of the displacement degrees of freedom in regular elements. These additional degrees of freedom eliminate parasitic shear stresses resulting from shear-locking. The additional degrees of freedom make them more expensive than reduced integration elements, but good results can be provided with one element through the thickness.

The result of using one C3D8I through the thickness is much more accurate force predictions, as shown in Figure 3-5. Although there are some large errors (25% on axial force, 80% on radial force) early on, after 3 rotations, a steady state is reached where the predictions show almost perfect agreement with experimental results, with some additional noise due to elements moving into and out of contact. Furthermore, with only one element through the thickness, the model runs twice as fast as the model with 2 reduced elements through the thickness. Therefore, C3D8I elements with one element through the thickness of the sheet are used in the FE models in this thesis (there are some cases where continuum shell elements are used, because these still provide accurate results when the roller is further away from the mandrel/internal rollers, but at a much lower computational cost).

With the C3D8I elements chosen, it remains to determine the optimum mesh size – a compromise between speed and accuracy of the model. Convergence tests are used to find the optimum, considering both the predicted tool forces, and the predicted workpiece geometry.

Figure 3-8 shows a comparison of the predicted forces with different mesh sizes, showing that the predicted forces converge very quickly with ~6,000 elements, and shows excellent agreement with

experiments once converged. There is some noise on the force predictions due to the discrete nature of node-to-surface contact, but this is acceptable in all but the coarse mesh (this is reduced by taking a moving average in the plots to make the plots clearer). The predicted shape, as illustrated by the meridian shape and axial displacement around the outer circumference of the workpiece in Figure 3-9, also converges and shows good agreement with experiments. Most importantly, the amplitude of oscillation converged to the experimental value.

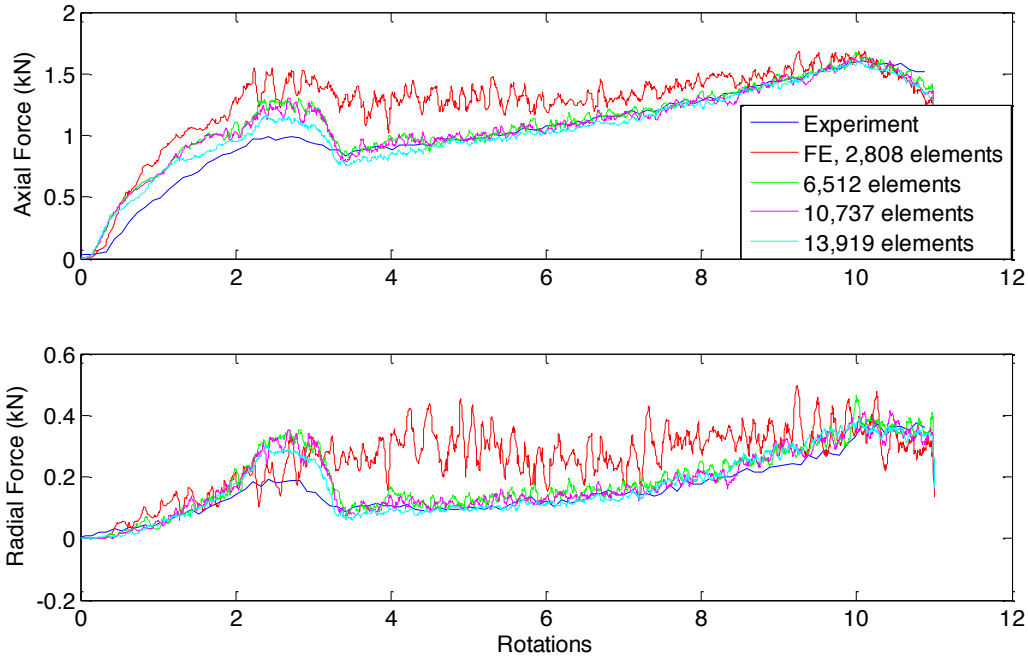

Figure 3-8 - The tool forces measured and predicted by FE (Note that a moving average has been applied to remove some noise to make the results easier to visualize)

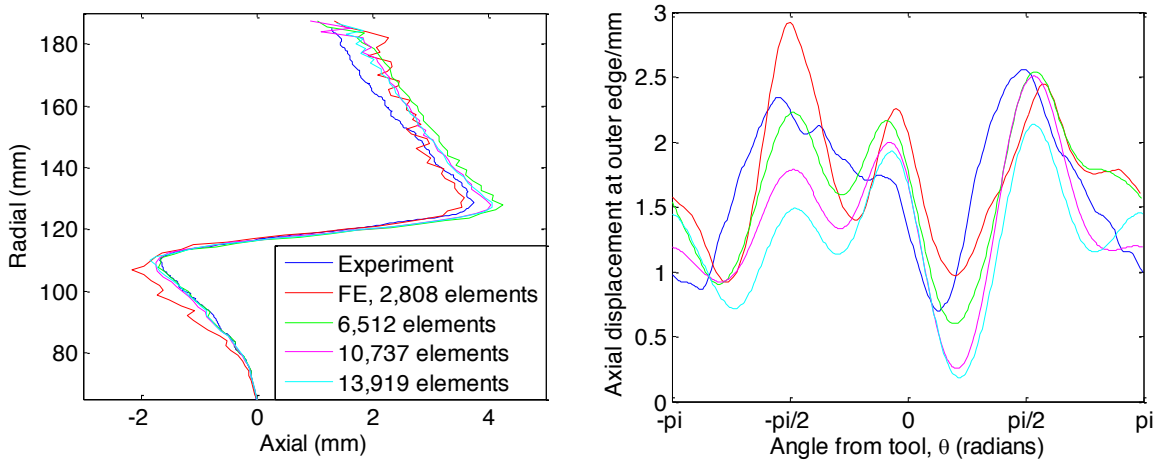

a) The workpiece meridian at θ=0 **b) Axial displacement around outer edge of workpiece**

Figure 3-9 – Measurement of the product shape (note that in a) the axial axis is enlarged to highlight differences)

Overall, the mesh with 6,518 C3D8I elements was chosen as the results show good agreement with experiments and convergence with other models, but is relatively computationally efficient (~2x faster than with 10,737 elements; ~4x faster than 13,919 elements). This corresponded to 10mm elements at

the centre of the blank, shrinking to 3mm towards the blending roller position (where contact modelling is critical), and growing to 5mm at the edge of the workpiece, giving the mesh shown in Figure 3-10. This mesh size distribution is then used in all models, although the exact number of elements will change depending on the shape and size of the workpiece.

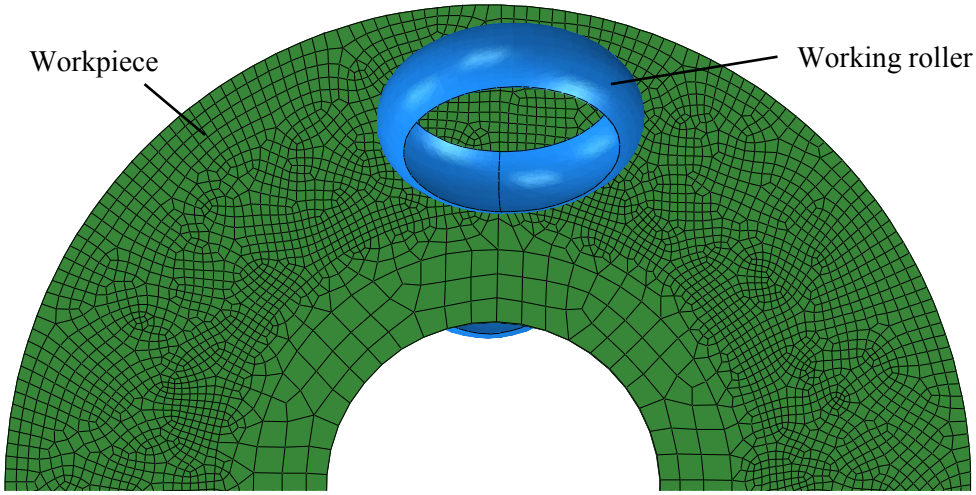

Figure 3-10 - FE mesh distribution

3.2 Experimental work

As well as FEM, this thesis contains experimental work on the FAS machine to understand the mechanics of the process and test the control systems. As described in chapter 1, the application of closed-loop control of product properties systems requires three elements: actuators, sensors and a process model.

The actuators to move the tools and rotate the workpiece were selected and implemented by Music (2011) within the design and development of the FAS machine. He also installed an NI (National Instruments) real-time controller to control the actuators and synchronise their motion.

For sensors, Music installed two load cells on the machine to measure the axial and radial load on the working roller. However, he suggested that in the future, a method of measuring the geometry of the workpiece should be added to the machine. Indeed, the implementations of closed-loop control of product properties used in this thesis require measurement of the geometry of the workpiece, and therefore a laser line scanner has been installed on the machine. Data from this laser is not only used for closed-loop control of product properties, but also to generate many of the plots in this thesis. The specification, selection and installation of this laser are described in section 3.2.1, along with a description of the plots generated using the output.

Finally, the process models will be developed and investigated throughout this thesis, but the application of these models to the control of the FAS machine presents a software development

challenge. The specification and high-level development of this software are described in section 3.2.2.

3.2.1 Addition of laser line scanner

Several commercially available laser line scanners were considered and evaluated according to 7 criteria described in Table 3-1. Ultimately, the Acuity AP620-300 laser was chosen, and the reasons for this choice are also shown in Table 3-1, alongside the evaluation criteria.

One concern with the Acuity AP620-300 was that it was Class 3B, which means that direct exposure to the laser is hazardous. However, three precautions were taken to protect against visual exposure in usual operation:

- The laser was fixed below eye level pointing downwards at the workpiece, so that it was not pointing towards operators or visitors should the workpiece break or otherwise not be present. This meant that the laser measured a meridian 90° from the point at which the working roller touched the workpiece – although the effect of loading on the measurement is minimal, in some cases it can be significantly affected.
- The laser was placed inside the existing cage of the machine and could only be turned on with the cage closed and locked, unless the override switch was on (only those trained to use the machine, familiar with the risk assessment, and having attended the laser safety training course may use the override key). The nominal ocular hazard distance (NOHD - the distance at which the power of the laser entering a 7mm pupil drops below 1mW) is 1m, and the laser would have to travel at least that distance to reach the cage.
- The laser was programmed to start up at the lowest power setting, and is not usually used at full power. It typically operators at 20% power, meaning the NOHD would be reduced to 200mm.

From time-to-time, it may be necessary to enter the machine with the laser on – for example, in order to align the laser. When this is done, either laser safety glasses, designed for the 660nm visible red laser, must be work, or the laser must be operated at a maximum 3% of full power and the operator must take care not to look directly at the laser.

Following the satisfaction of the laser safety officer, the laser was purchased and installed, and is shown working in Figure 3-12.

Table 3-1 - Specification for the laser line scanner and evaluation of AP620-300

Category	Criterion	Evaluation of AP620-300
Range	Must be able to measure the full range of shapes (including intermediate shapes) that can be produced on the machine	Measurement possible within a trapezium of width 165mm to 465mm, and depth 300mm. This range of measurements covers the full range of products produced on the FAS, as shown in Figure 3-11.
Materials	Must be able to measure Aluminium, Steel and Stainless steel, and cope shiny metallic surfaces – lubricated or otherwise.	Exposure is not automatically adjustable, as it was in some more expensive models, but could be manually adjusted to measure the current workpiece.
Speed	Scan frequency ~100Hz, therefore 30 measurements/rotation at top spindle speed. Spindle can be slowed down for more detailed scans.	Scan frequency of 250Hz.
Safety	Must be safe when installed – ideally Class 2 or safer.	Classified as Class 3B, which means direct exposure to the eye is hazardous. Precautions discussed below.
Accuracy	Comparable measurement accuracy to the position accuracy of tools (0.1mm)	Linearity of 0.3mm in the Z-axis (worst axis). Although poorer than the position accuracy, this is acceptable for proof-of-concept.
Compatibility/Ease of integration	Must be compatible/easily integrated into the existing LabVIEW software controlling the machine.	Not plug-and-play, but comes with DLL function library for controlling and communicating with laser.
Cost	<£7,000, including VAT plus internal labour	Total cost was £6,300, including cables and additional support structure.

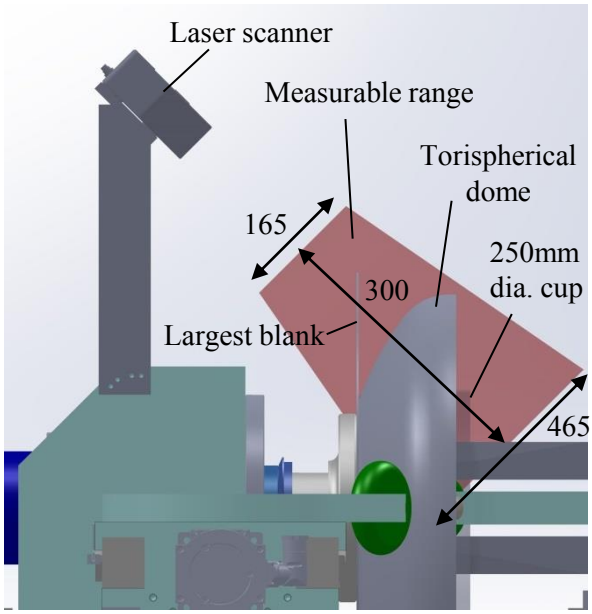

Figure 3-11 - The range of the Acuity AP620-300 laser, showing a range of shapes that it can measure

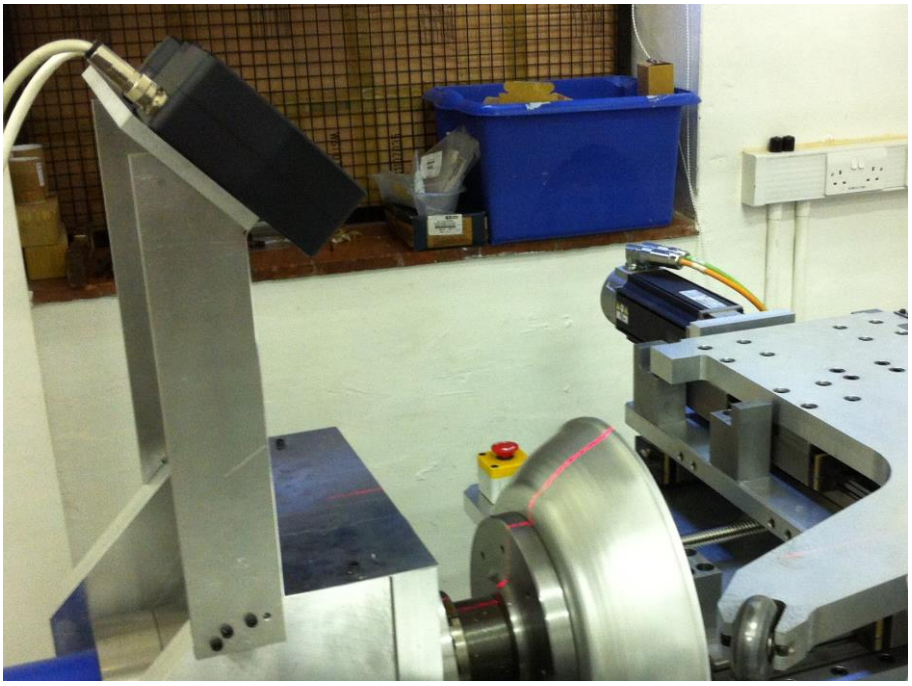

Figure 3-12 - The laser after installation, scanning a product

As well as enabling closed-loop control of product properties, the laser is also used to measure the final shape of the product after spinning. The laser takes 360 scans of the meridian, as the workpiece rotates by one revolution, giving the shape of the workpiece at intervals of 1° of rotation. The average meridian of these 360 profiles can then be plotted, along with the range of meridians in order to show any lack of axisymmetry. An example is shown in Figure 3-13a), when trying to produce a 316mm diameter cup with a 50mm corner radius.

From this data, two types of errors from the target shape can also be calculated: the "shape error", which is the distance from the average measured meridian to the target shape; and the "circularity

error", which is the range of radii along each circumference and therefore a quantitative measure of the lack of axisymmetry. These can then be plotted against the distance along the meridian of the workpiece, and an example is shown in Figure 3-13b). Many similar plots will be shown throughout this thesis in order to show the geometric accuracy of the parts produced.

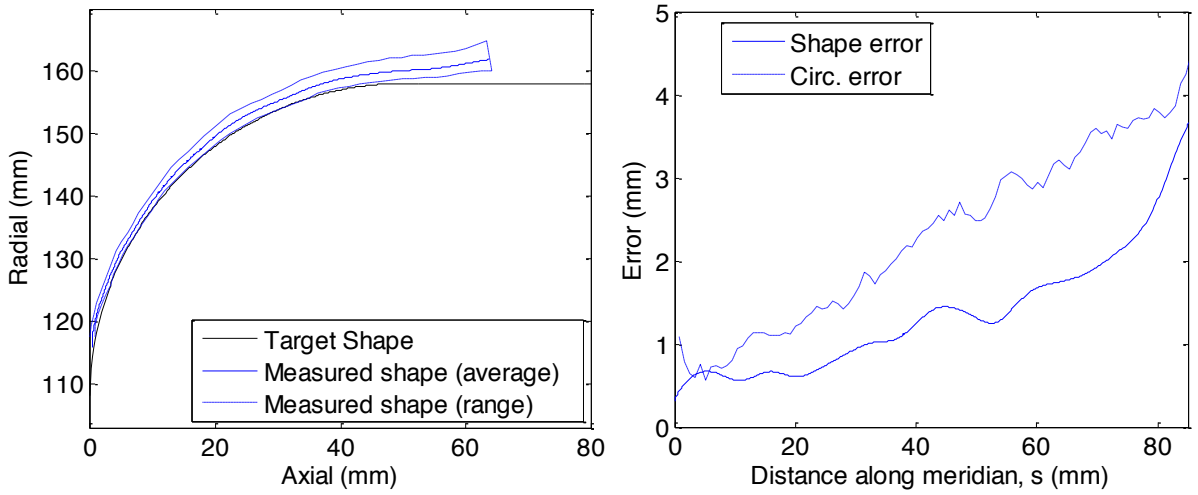

a) Workpiece meridian shape **b) Shape and circularity errors**

Figure 3-13 - Example measurements from laser line scanner

3.2.2 Design of software

With all of the hardware installed on the machine, software is needed to control it. Such software must be able to:

- Communicate with and control the machine
- Control the laser and take laser measurements
- Process and filter the laser measurements
- Run models – both FE and custom built, bespoke models
- Make decisions regarding tool motion

Having designed the FAS machine and performed some preliminary tests, Music (2011) had already developed the software to *communicate with and control the machine*. This was performed with LabVIEW, given the compatible NI real-time hardware used and the vast array of tools within LabVIEW to perform hardware control. LabVIEW is installed on the NI real-time controller to control the tool motion and synchronise their motion, and also on a Windows PC connected to the controller in order to perform the necessary processing and send motion commands back to the controller.

However, the Acuity AP620-300 laser line scanner was not directly compatible with LabVIEW, which meant that additional software had to be developed to *control the laser and take laser measurements*. The laser only came with a DLL function library for controlling it remotely. In order

to access this library, C++ functions were written, compiled into a DLL function library that was compatible with LabVIEW, and then embedded within LabVIEW code using a *Call Library Function Node*.

The laser measurements can be noisy and also include superfluous measurements such as the top of the spindle and the arms holding the internal rollers, so software is needed to *process and filter the laser measurements*. Because the laser measurements consist of 256 individual point measurements, MATLAB was used because it is optimised for the vector and matrix operations used to process these measurements. LabVIEW's *MATLAB script node* is used to call the MATLAB code from the LabVIEW code used to control the machine.

The laser scanner measurements are then used to create and *run the process models* developed and used within this thesis, including both custom models described in individual chapters, and FE models described in section 3.1. The custom models are developed using MATLAB, again due to its optimization for vector and matrix operations which allow it to do batch calculations very quickly, but also the range of tools it contains for modelling – the differential equation solvers, for example.

The FE models are ran using commercial FE software, Abaqus. However, neither LabVIEW nor MATLAB can call Abaqus directly. Instead, for running FE models, the MATLAB code generates a temporary input file and then uses a system call to prompt Abaqus to run the model defined by that input file. For reading the results, MATLAB uses a system call to run a Python script written using Abaqus' Python API. The Python script writes the results in a text file, which can then be read by MATLAB.

Finally, the software needs to *make decisions on motion commands* to send to the machine controller. Once again, this is performed using MATLAB code. The MATLAB code can either taken the output from the custom or FE model and use this to generate the next motion command; or it can generate a motion command from a predefined set of parameters defining involute curved. The former is "online" control as it responds to online measurements, and the latter is "offline" control as the toolpath is, in effect, predefined offline. The motion command is then passed back to LabVIEW through the output of the *MATLAB script node*.

The high-level system setup is summarised graphically in Figure 3-14.

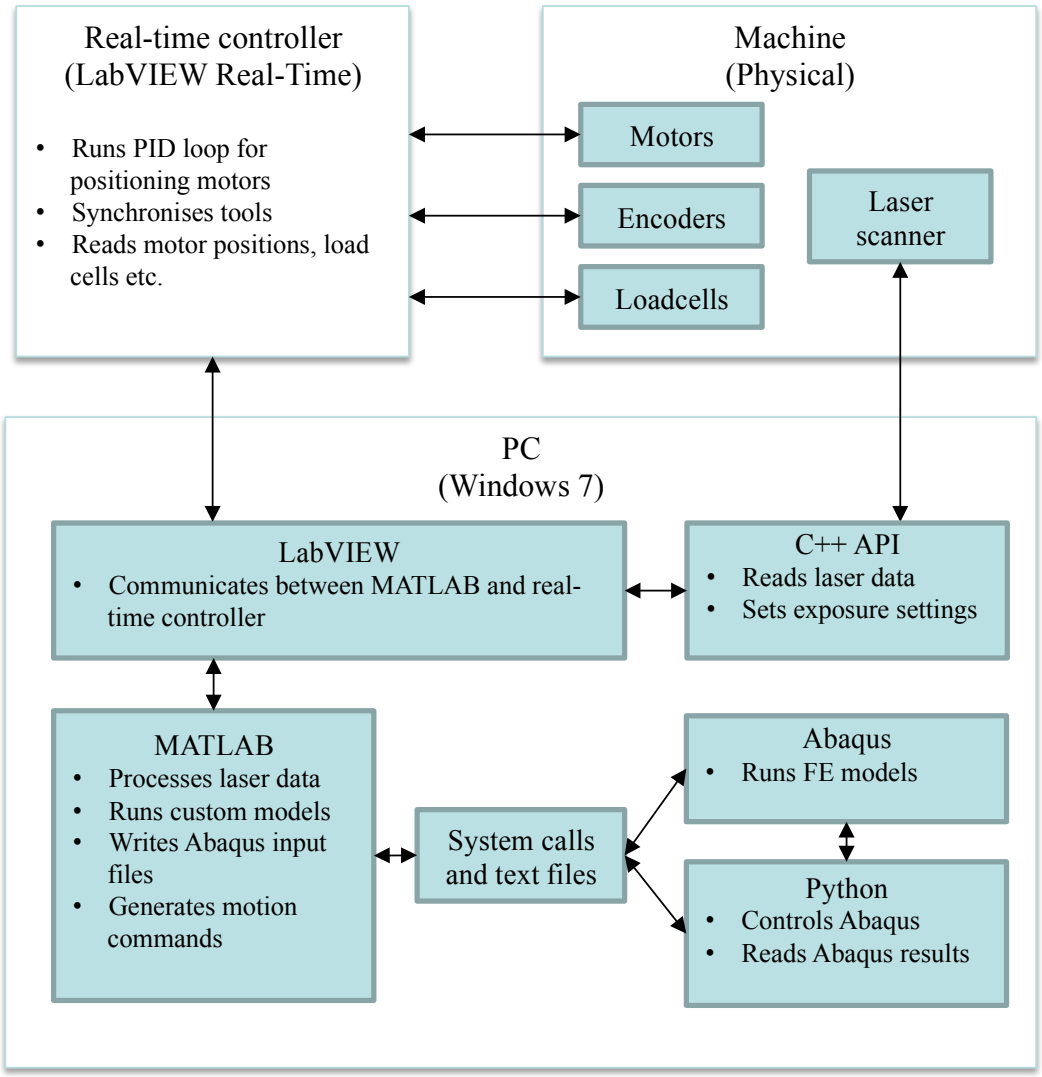

Figure 3-14 - High-level system setup

3.3 Conclusion and further work

The FE models developed in this chapter can be used to accurately and reliably model the spinning process. It will therefore help to provide a better understanding of the mechanics of both conventional spinning and FAS, and therefore to automate the process. In the future, particularly as computing power continues to increase, and as FE packages become more advanced, it may be possible to produce even more sophisticated and accurate models – For example, a more advanced material model may be included, modelling the microstructural evolution of the material being spun.

Software has been developed to control the machine either using models ran online, or using a set of involute parameters defined offline. The inclusion of MATLAB and Abaqus FE modelling software in the control system allows a range of automation approaches to be used. In this thesis, the software is used to control the internal rollers online; to modify the toolpath, both online and offline, to compensate for springback; and to generate the whole toolpath online.

In the future, the software could easily be modified and built upon in order to expand the range of automation techniques that can be applied. As the ideas developed in this thesis are developed further towards industrial standard, the software may even be rebuilt in one single software package, to simplify and reduce the overheads involved in multiple software packages communicating with each other.

Chapter 4 - Control of Internal Support Rollers

The FAS spinning machine designed and built by Music (2011) was designed to produce straight walled cups. The blending roller was positioned to provide support at the corner of the cup, while the two support rollers were positioned to provide support along the wall of the cup, as shown in Figure 4-1. After building the machine, Music successfully demonstrated the use of the machine to produce a 250mm diameter straight-walled cup. However, on using the machine further, two points were noted:

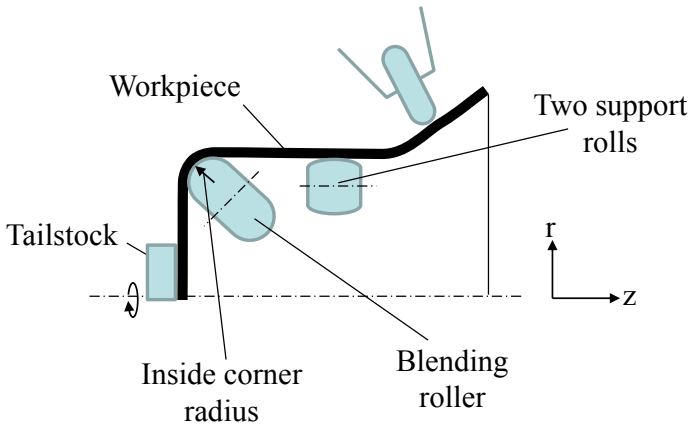

Figure 4-1 - The support set-up when spinning the straight-walled cup

Firstly, that it was still possible to make the straight walled cup even with only the blending roller used to provide the internal support (i.e. using one roller, rather than the three which Music proposed). Figure 4-2 demonstrates this, showing that the cup can be produced to within 0.5mm error both with all three internal rollers, or with just the blending roller – there is no significant effect on either the shape error (distance between the average meridian and the target shape) or the circularity error (the deviation in radius around the circumference of the product). This raised questions from potential industrial producers of the machine about whether all three rollers are needed after all.

Secondly, the machine was designed to produce straight walled cups with an internal corner radius equal to the blending roller nose radius, as highlighted in the example in Figure 4-1. For this reason, and to demonstrate the concept at minimal cost, Music fixed the blending roller axially – if the two radii were the same, support could be provided all around the internal corner without moving the blending roller axially. However, this axial constraint meant that shallow parts could not be produced.

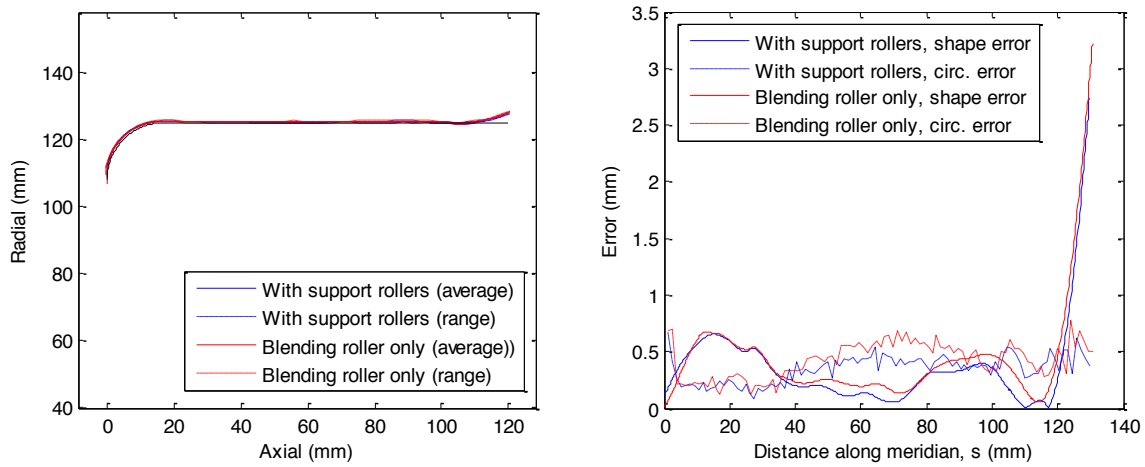

a) Workpiece meridian shape **b) Shape and circularity errors**

Figure 4-2 - The shape of the spun cup with all internal rollers and with only the blending roller (Note that these shapes are measured after springback is compensated for, as discussed in Chapter 5)

Figure 4-3 shows the achieved shape when attempting to spin a cup with a larger corner radius. The blending roller was axially fixed, so could not be moved to follow the inside of the target shape. Because of the design of the support rollers, they could not be moved into contact with the workpiece until the product was ~90mm deep (due to collisions with the blending roller) and nearly straight walled (due to the design of the rollers). Therefore, the workpiece continued to bend around the fixed blending roller, and become over-formed; something that would be impossible in conventional spinning due to the presence of the mandrel.

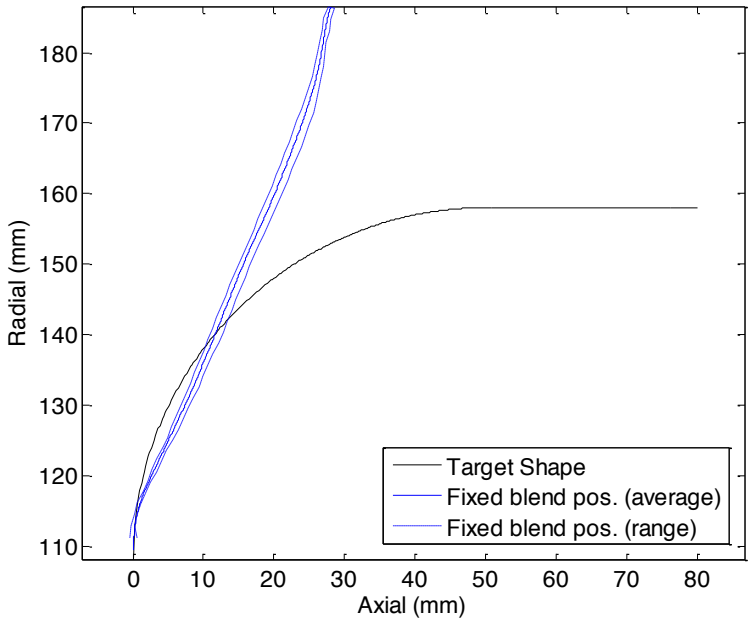

Figure 4-3 - The achieved shape when attempting to spin a straight walled cup with a larger corner radius

The aim of this chapter is to investigate these observations, to better understand the support requirements, and to attempt to redesign and automate the internal support rollers in order to enable the machine to produce a larger range of products. To achieve these goals, firstly, finite element

modelling is performed to identify the support requirements – this is the subject of section 4.1. Following these analyses, design changes to the machine are proposed, specified and implemented, and this is the subject of section 4.2. Finally, the automation of these internal support rollers is discussed in section 4.3. The solutions represent a step towards the industrial implementation of FAS, but there is still further work that could further improve the accuracy and stability of the process, and this is the subject of section 4.4.

4.1 Identifying the support requirements

That the 250mm diameter cup could be produced with only one internal roller, rather than three, does not discredit Music's initial work: It only shows that in the case of the cup, having three internal rollers is not the *only* way to reproduce the mechanics, although it may be that for other products three rollers are needed. To verify this, firstly, FEM are used to check that the same mechanics are indeed possible when producing the cup with just the blending roller used to provide the internal support. Then, different shapes are considered to check that in some cases three internal rollers are indeed necessary.

In this investigation, the FE models model just one rotation of the workpiece in order to investigate the impulse response – the deformation in the workpiece after one rotation. If the impulse response is the same in conventional spinning and FAS, then the mechanics are the same and the same product could be made. The workpiece starts with a shape that is either measured or assumed based on experimental observations, and is initially stress and strain free. This is a limitation of this approach: work hardening from spinning up to this point is neglected, yet may have led to different conditions in conventional spinning and FAS. However, modelling the whole process is computationally expensive, and would likely only lead to a small correction in the optimal position of internal rollers.

The model takes three steps: The tool indents the workpiece, the workpiece rotates once, and then the tool is removed. The FE models are set up as described in Chapter 3, although reduced integration continuum shell elements SC4R are used with two elements through-thickness. This is acceptable because through-thickness stress and out-of-plane shear are negligible in the cases modelled here and continuum elements would be too computationally expensive.

Figure 4-4 to Figure 4-6 show the assumed shape of the workpiece at three stages in the spinning of the 250mm diameter cup, as well as the contact forces between the mandrel and workpiece in conventional spinning. From these figures, it can be seen how the contact evolved: Early on in the process Figure 4-4, the contact is localised around the corner of the cup. In the middle (Figure 4-5) and late (Figure 4-6) stages of process, an additional two contact regions appear further up the wall of the cup – confirming the results of Music (2011), even though he demonstrated this for a larger, thinner cup.

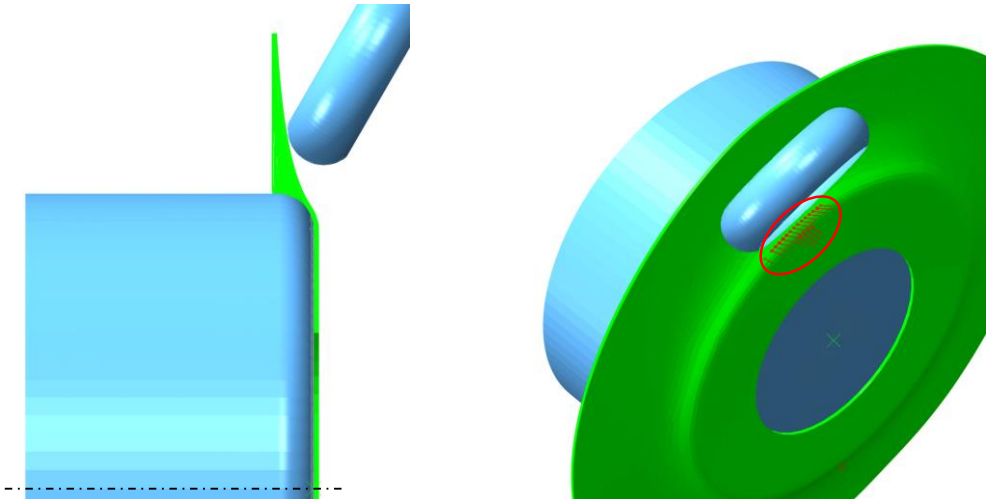

(a) (b)

Figure 4-4 - a) The shape and b) the contact region between mandrel and workpiece in the early stage of spinning a 250mm diameter cup

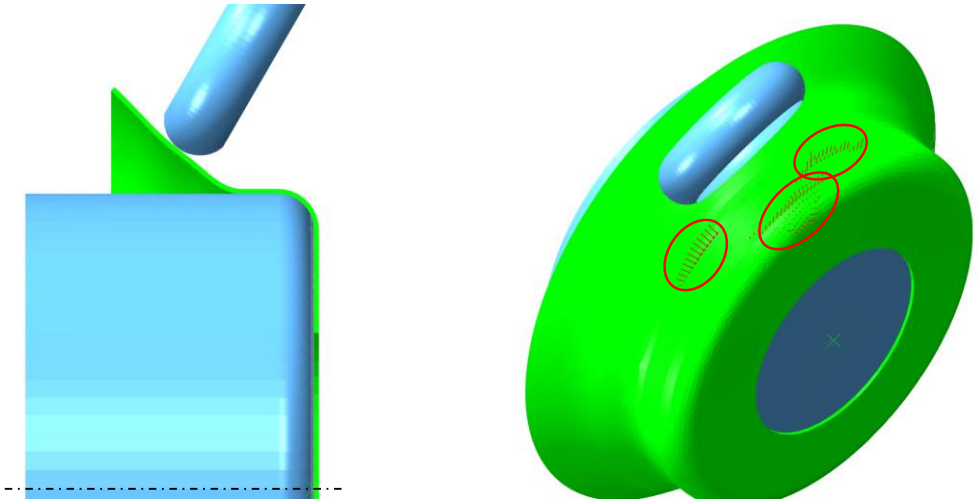

(a) (b)

Figure 4-5 - a) The shape and b) the contact region between mandrel and workpiece in the middle stage of spinning a 250mm diameter cup

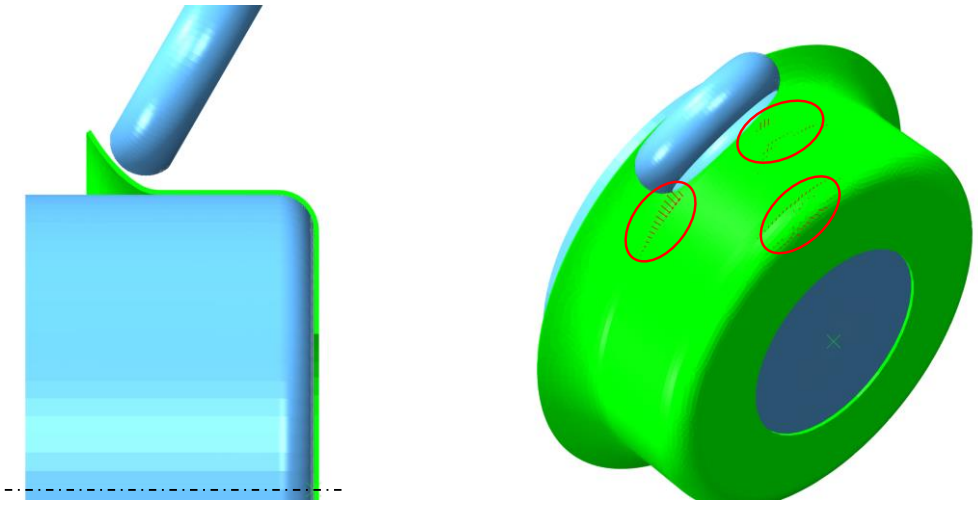

(a) (b)

Figure 4-6 - a) The shape and b) the contact region between mandrel and workpiece in the late stage of spinning a 250mm diameter cup

Although this does suggest that the mandrel could be replaced by three internal tools, as Music (2011) concluded, it does not suggest that this is the *only* way to reproduce the mechanics of metal sheet spinning – indeed the experiments suggest otherwise. To confirm this, further FE models were ran, but with the mandrel removed and replaced with either all 3 internal rollers (as Music suggested) or just the blending roller (as was successfully performed in experiments) – These two internal support configurations are shown in Figure 4-7, along with the conventional spinning setup. The plastic strains caused by one rotation of the workpiece at the three different stages of the process, and with the three different internal support configurations (mandrel, 3 support rollers and blending roller only) were recorded and compared.

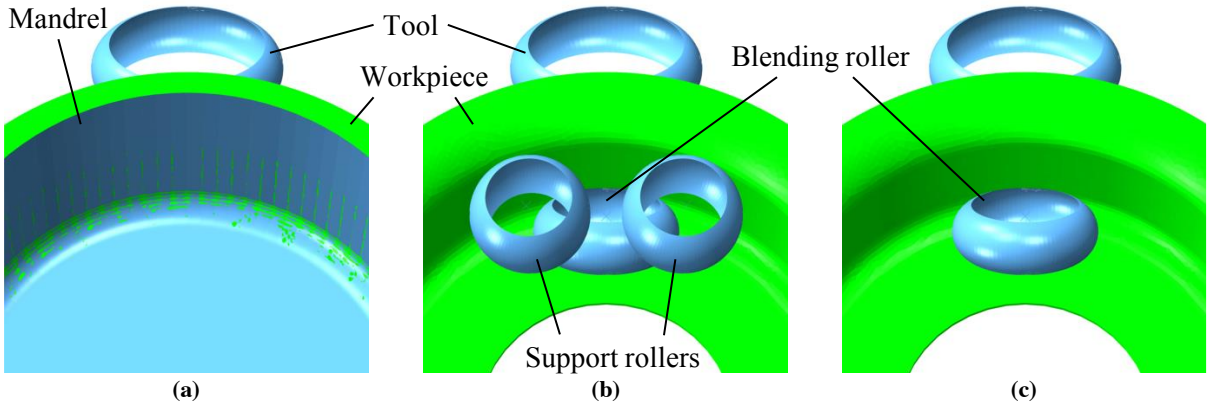

Figure 4-7 – Internal support configurations: a) conventional spinning; b) 3 internal rollers; c) blending roller only

Early in the process, the contact distribution of Figure 4-4 would suggest that only the blending roller is required. Indeed, in experiments where all three rollers were used, the workpiece would not have made contact with the additional two support rollers by this stage. Therefore, only the conventional case and the case with just the blending roller are considered. Figure 4-8 shows the plastic strain in these two cases, showing a very similar plastic strain distribution, suggesting that the mechanics are approximately recreated at this early stage with just the blending roller.

The plastic strain in the middle and late stages of the process are shown in Figure 4-9 and Figure 4-10 respectively. The plastic strain seen in conventional spinning is recreated almost exactly by the three support rollers, as Music showed. However, the plastic strain is also recreated approximately in the case where only the blending roller is used.

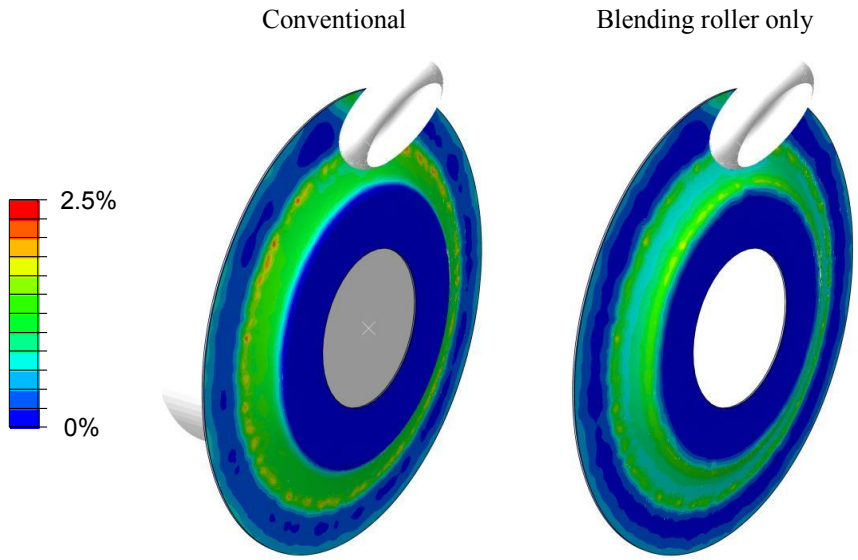

Figure 4-8 - The plastic strain after one rotation early in the spinning of a 250mm diameter cup

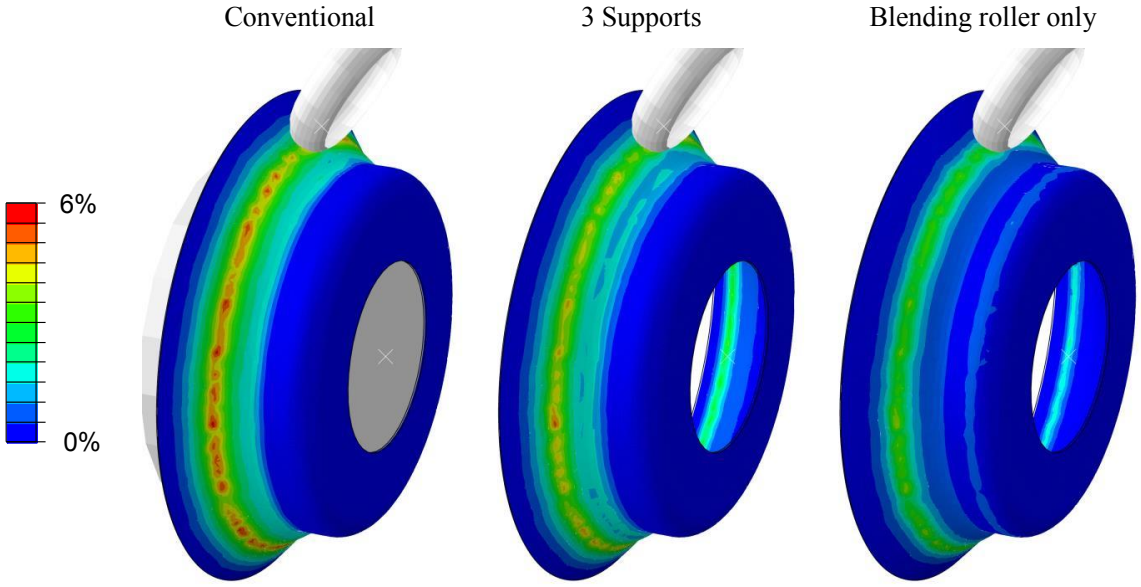

Figure 4-9 - The plastic strain after one rotation in the middle stage of spinning of a 250mm diameter cup

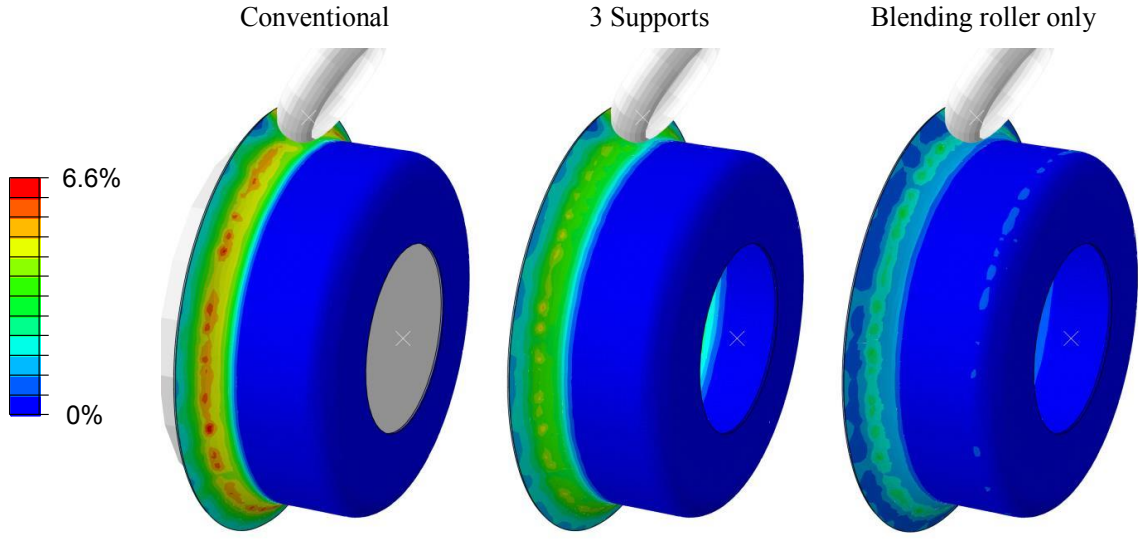

Figure 4-10 - The plastic strain after one rotation in the late stage of spinning of a 250mm diameter cup

There are two differences in the plastic deformations seen: Firstly, the absolute values of plastic strain observed are smaller with one internal roller than in conventional spinning, but this would only result in a larger springback error which could be compensated for (see Chapter 5). Secondly, there is some plastic strain around the corner of the cup, which could be problematic as the workpiece has already taken its target shape here, so further deformation would result in geometric errors and excess thinning. However, the strain is small compared to that seen in the unfinished regions of the workpiece (0.5% at the corner, compared with ~5% in the flange), suggesting that smaller tool displacements could reduce the plastic strain around the corner and reduce any geometric errors while still forming the unfinished regions of the workpiece. Therefore, even though these differences mean the mechanics of FAS with only the bending roller used are only approximately the same as those of conventional spinning, the same products could still be created by compensating the motion of the working tools, assuming that the slightly different mechanics did not contribute to failure through wrinkling or tearing.

The reason that the plastic strain can be recreated with only the blending roller is because of the geometric stiffness of the cup shape. Early in the process, when the workpiece has very little depth, it is only bending around the corner of the mandrel – the blending roller is enough to provide support here. Later in the process, when the walls of the cup are being formed, the workpiece has enough geometric stiffness to support itself from the corner (where the blending roller provides support), up the walls where, in conventional spinning, the mandrel would be in contact with the workpiece. Plastic deformation can therefore be created in the flange of the workpiece, without any in the "complete" areas which have reached the target shape.

From this preliminary investigation, it can be concluded from these FE models that the cup could be produced with only one internal roller, with some small geometric or thickness errors due to the extra plastic strain around the blend. This is consistent with earlier experiments where the cup was indeed produced with only one internal roller. The cup, however, is just one example of a range of shapes that is produced by spinning – and this cup is a special case in that the internal corner radius is the same as the nose radius of the blending roller. In order to demonstrate the full capabilities of the concept developed by Music, the production of different shapes should be demonstrated. For example, Cubberly and Bakerjian (1989) identified a range of different shapes which can be produced by spinning, shown in Figure 4-11.

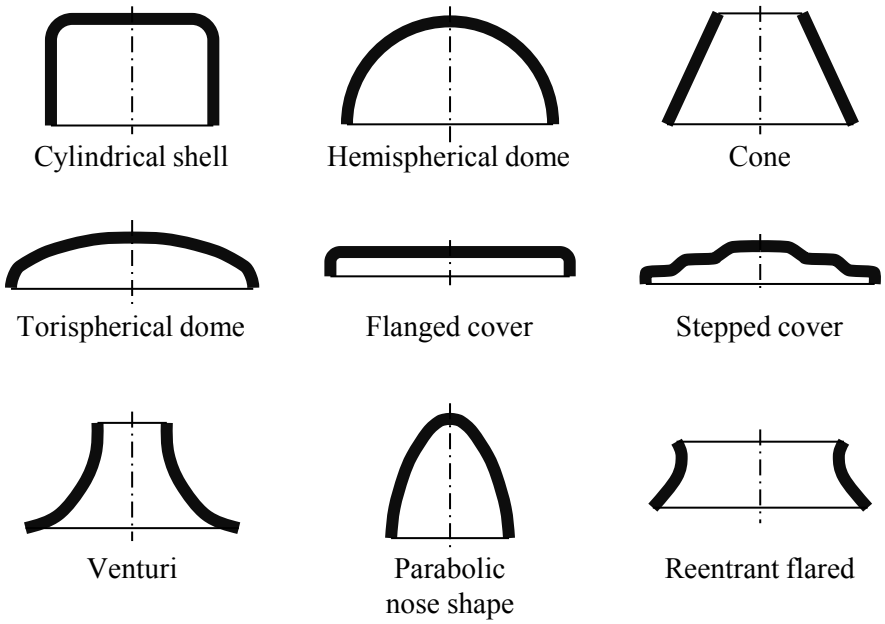

Figure 4-11 - Examples of shapes produces by spinning according to Cubberly and Bakerjian (1989)

To check whether three support rollers might be needed for other shapes, the same investigation that was carried out for the cup, was also carried out for two other shapes. Firstly, for a torispherical dome – this is a shape of spun shell that is frequently used on the ends of pressure vessels. The dimensions of this torispherical shell were chosen based on an approximate design for the end of a household hot water tank, and are shown in Figure 4-12 – Note that it is truncated so that it has a flat area that can be clamped to the spindle on the FAS machine. Secondly, for another straight walled cup, but with a 48mm inside-corner radius and an overall outer diameter of 316mm. The dimensions of this cup are shown in Figure 4-13.

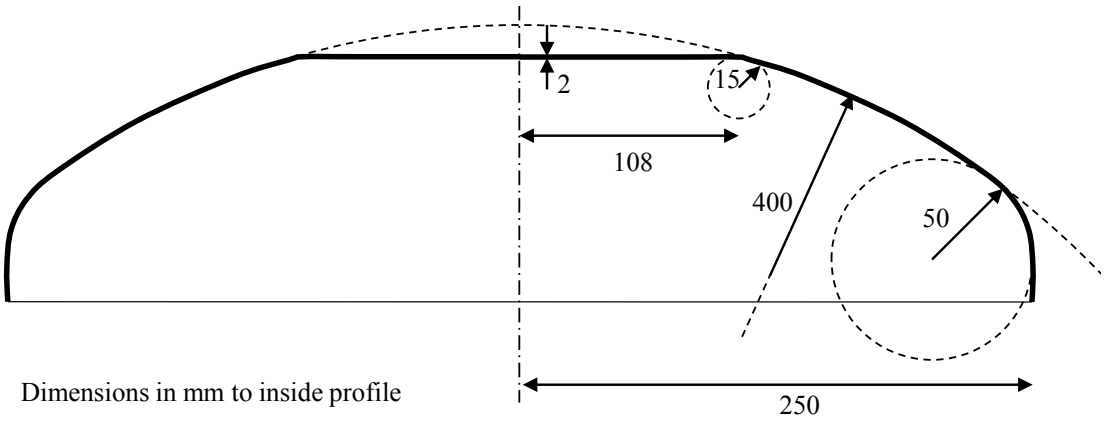

Figure 4-12 - Dimensions of the truncated torispherical dome

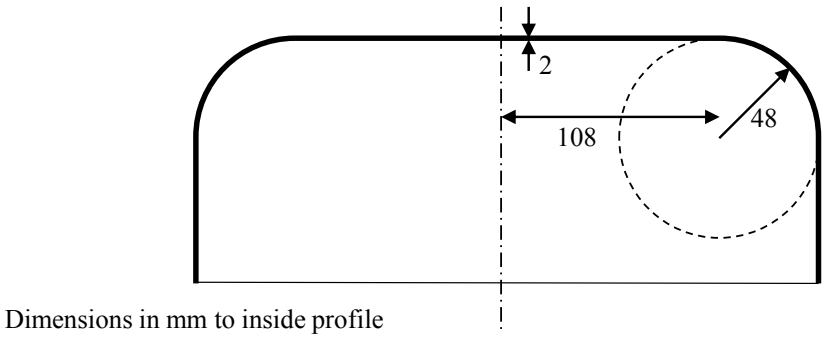

Figure 4-13 - Dimensions of the cup with a 48mm internal corner radius

Mid-way through the process of spinning the torispherical dome and the 316mm diameter cup, the workpieces are assumed to take the shapes shown in Figure 4-14a and Figure 4-15a respectively. The contact forces seen between the mandrel and workpiece in conventional spinning are shown in Figure 4-14b and Figure 4-15b. In both of these cases, three discrete contact regions are not seen. Instead, there are only two, with one wide contact region just where the workpiece stops conforming to the mandrel (where the two separate regions are seen in the spinning of the cup e.g. in Figure 4-5); and one smaller contact region closer to the base. Despite this inconsistency with earlier results, it was investigated whether the mandrel could still be replaced with three, or even just one, internal roller.

The internal rollers are configured differently when producing the shallow shapes and the 250mm diameter cup. Three different configurations are investigated for spinning shallow shapes: Just a blending roller, positioned to recreate the wide contact area seen in conventional spinning (Figure 4-16a); three internal rollers, with the two support rollers used to recreate the long contact area, and the blending roller positioned behind them to recreate the smaller contact area (or as close as possible if this results in a collision; Figure 4-16b); and three internal rollers, with the blending roller used to recreate the long contact area and the two support rollers used to recreate the smaller contact area (or as close as possible without collision; Figure 4-16c).

The plastic strain distributions for the different support configurations in spinning the torispherical dome are shown in Figure 4-17. The plastic strain is most similar in the configuration with three internal rollers, but with the support rollers in front of the blending roller. However, there is slightly more plastic strain at the base of the workpiece flange than is seen in conventional spinning (0.6% compared to 0.4%), suggested that the mechanics are similar, but not exactly the same. In contrast to the spinning of the 250mm diameter cup, the plastic strain cannot be recreated with just the blending roller – all three support rollers are required to reproduce the mechanics of conventional spinning most approximately when producing the torispherical dome.

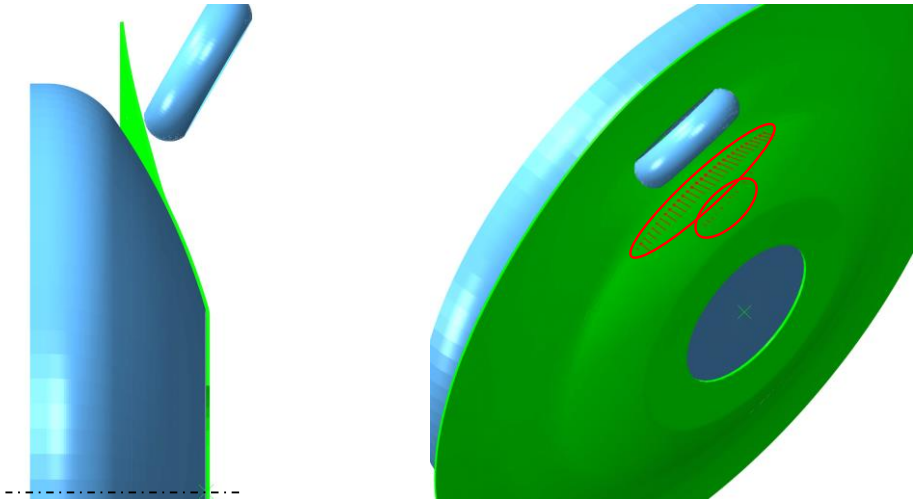

Figure 4-14 - a) The shape and b) the contact region between mandrel and workpiece in the middle stage of spinning the torispherical dome

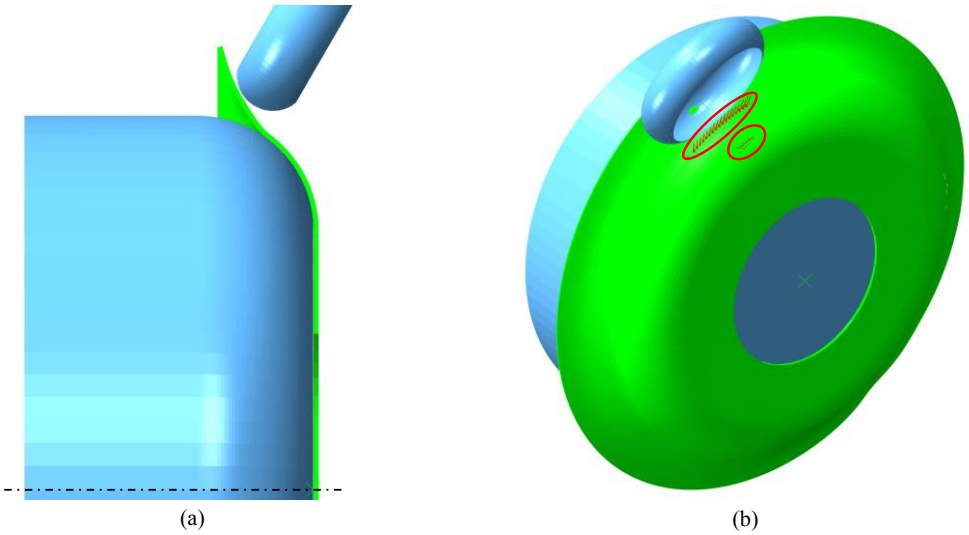

Figure 4-15 - a) The shape and b) the contact region between mandrel and workpiece in the middle stage of spinning a 316mm diameter cup

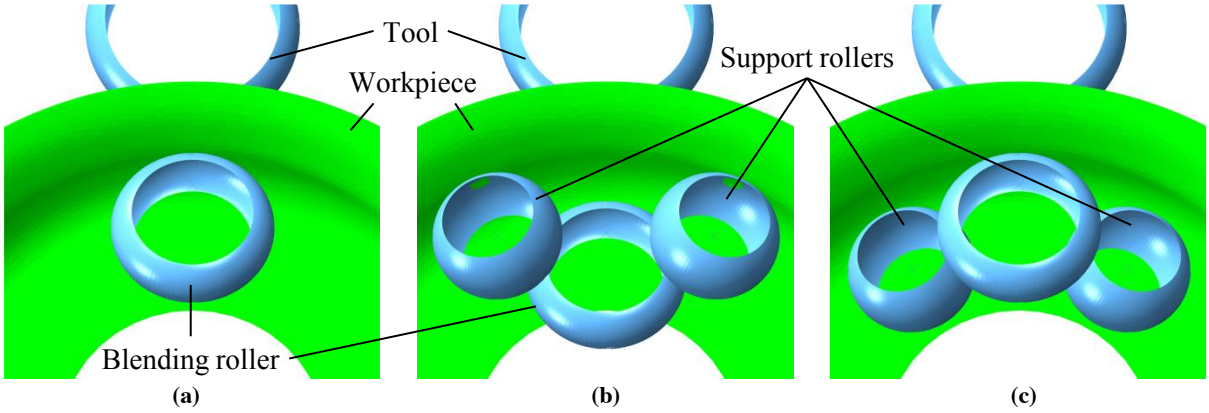

Figure 4-16 - Internal support configurations for shallow shapes: a) blending roller only; b) two support rollers in front of blending roller; c) two support rollers behind blending roller

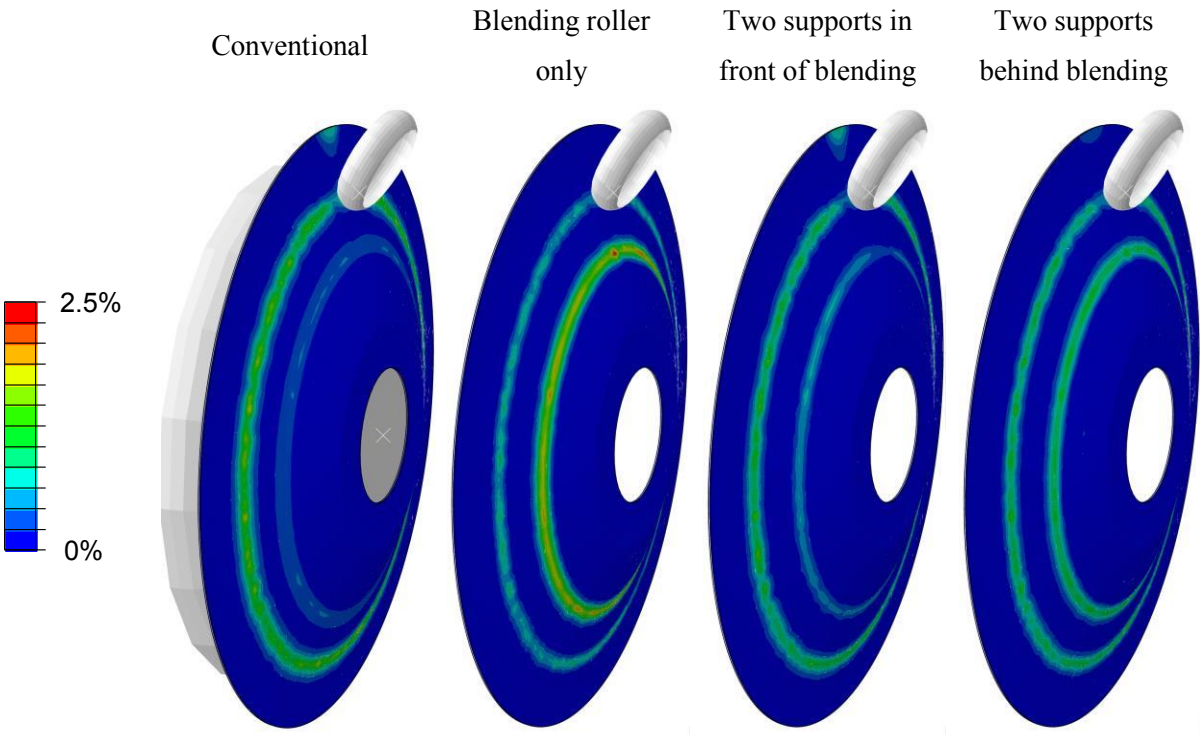

Figure 4-17 - The plastic strain after one rotation in the middle stage of spinning of torispherical dome

However, in spinning the 316mm diameter cup, a different support configuration is better at reproducing the mechanics of conventional spinning. The plastic strain distributions are shown in Figure 4-18, showing that, in this case, a better agreement when the two support rollers are placed behind the blending roller, although in this case there is a lot of plastic strain around the support rollers (5.5% compared to 3% in conventional spinning) due to their small curvature compared to the mandrel in conventional spinning. Bending at this point will not cause shape errors, as the workpiece flange can bend around this point without over-forming, but it may result in more thinning and a different failure mode. A similar plastic strain distribution is seen when only the blending roller is used, suggesting that the mechanics could be approximated almost as well with one blending roller as with all three internal rollers. This is only true, though, if the blending roller is allowed to move along the target profile of the cup, and cannot be recreated if the blending roller is fixed axially.

However, when the two support rollers are placed in front of the blending roller, the workpiece does not have the geometric stiffness to transfer the load to the three internal rollers without significant elastic deformation - the unsupported region between the three rollers, seen in Figure 4-16, is too large. Placing the blending roller closer to the working roller helps to provide support in this region. This could have been predicted by looking at the contact regions between the mandrel and workpiece in conventional spinning (Figure 4-14b for torispherical dome and Figure 4-15 for the 316mm diameter cup) – The contact region is much narrower in the case of the 316mm diameter cup than for the pressure vessel, suggesting that support should be provided over a much narrower region – e.g. by using one roller, rather than two circumferentially offset rollers.

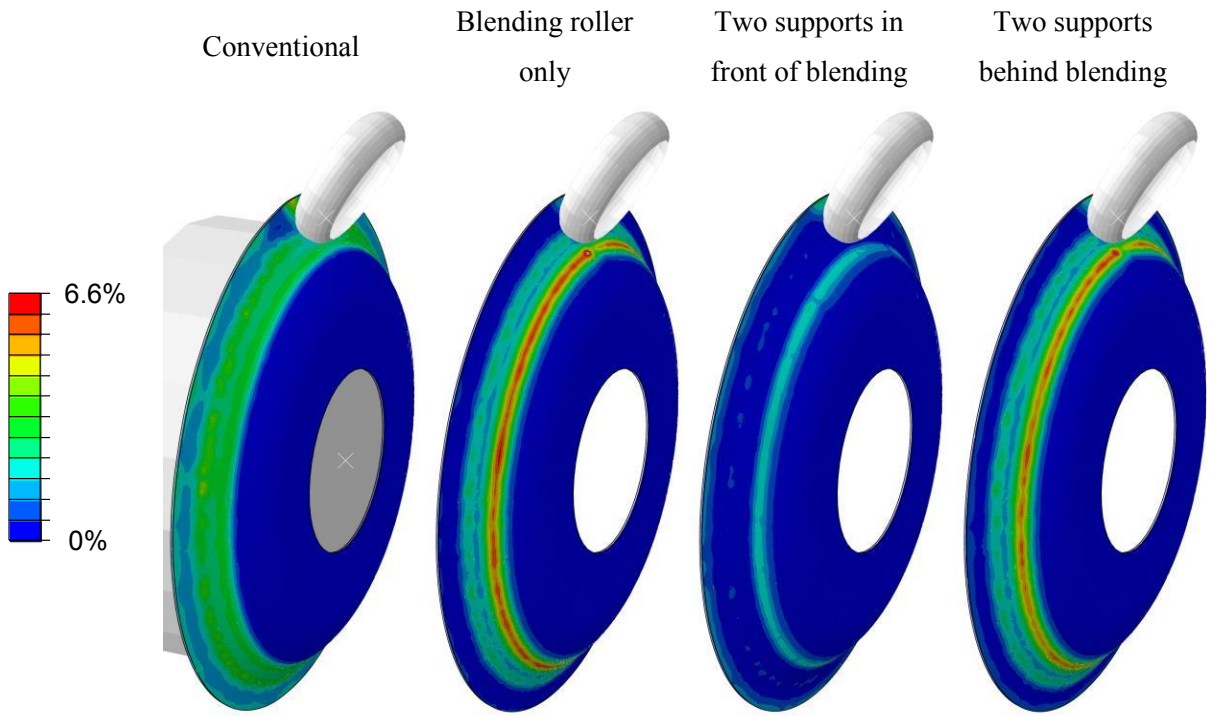

Figure 4-18 - The plastic strain after one rotation in the middle stage of spinning of a 316mm diameter cup

In conclusion, although in some cases using the blending roller alone is enough to provide sufficient internal support to approximate the mechanics of conventional metal spinning, in general, it seems that a further two support rollers are necessary to best approximate the mechanics. In some cases, the blending roller should be placed in front of the support rollers, while in others, it should be placed behind – in either case, both the blending roller and the support rollers should be able to move both axially and radially in order to follow the target shape.

Although it is not clear which support configurations will work for other product shapes, it will be some function of the geometrical stiffness of the workpiece, and the precise positioning of the support rollers will depend on the current shape of the workpiece.

In order to ensure that the correct support can be provided, some design changes were needed in order to improve the flexibility of the support rollers and allow them to provide a greater range of support configurations. The necessary design changes and the implementation of those design changes is the subject of section 4.2.

4.2 Modifications to internal rollers

The FAS machine designed by Music (2011) was designed to make the straight-walled cup described at the start of this chapter. The blending roller was axially fixed, and the support rollers were designed to make contact with the straight walls of the cup, so it was only possible to provide support in certain areas of the workpiece as shown in Figure 4-19. However, in section 4.1 it was concluded that to spin

a larger range of products, for example the toroidal shell, it must be possible for all three internal rollers to make contact anywhere on the inside of the workpiece in order to provide sufficient support.

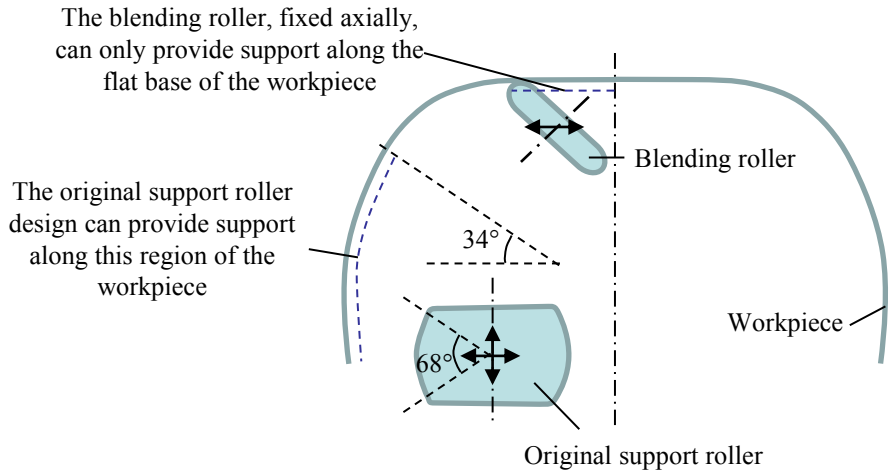

Figure 4-19 - The limited regions inside the workpiece where the original internal rollers were able to provide contact (Not to scale)

To achieve this, two design changes were proposed: Firstly, the blending roller needed to be actuated axially in order to follow the profile of the target shape in the early stages of spinning – this is the subject of section 4.2.1. Secondly, the support rollers needed to be redesigned so that they could provide support at an earlier stage of the process, and not have to wait until the wall of the product became almost parallel with the axis – this is the subject of section 4.2.2. These design change would allow the blending roller to move along the shape of the product and provide the necessary support until a later stage of the process where the support rollers could provide additional support.

4.2.1 Actuating the blending roller axially

The first step in design is to produce a specification. This step is made somewhat easier due to the existing specification of the machine from Music (2011) – He already calculated that the axial force on the blending roller was 2.5kN, but applied this purely through structural elements as he did not actuate this axis. Additionally, and conveniently, linear guides in the axial direction were already fitted to allow the blending roller to be released after the production of a part, so the part could be removed. The only remaining work was to design the actuation and mechanical drive system.

In order to aid this, the specification in Table 4-1 was produced.

Table 4-1 - Specification for blending roller axial axis

Geometry	Must fit in existing space allocated for the FAS machine
Loading	Axial force on blending roller: 2.5kN
Kinematics	Speed: 30mm/s (consistent with other axial axes) Range of motion: 0-200mm Must be able to move roller within sheet thickness of the spindle in order to provide support from the earliest stages of spinning.
Structural design	The structure already exists and modification should be kept to a minimum
Actuator	Servo motor and ball screw to be consistent with existing design principals on the machine.
Sensors and control	2 limit switches (including one for reference search) All components should be compatible with existing software in order to allow smooth integration.
Safety	No additional hazards. Existing enclosure and stop switches will be sufficient. This should be reviewed following design.
Manufacture	All components should be simple to manufacture, and the number of new components minimised by utilising, where possible, existing components.
Assembly	Assembly does not need to be simple as it will only need to be done once. However, consideration should be given to ensure that assembly is possible with tools available.
Cost	< £5,000

In order to ensure compatibility with existing components the same design principals were used – that is, the use of a servo motor and ball screw to deliver linear motion. Given that the power output of the axis is 75W (2.5kN x 30mm/s), a 220W servo motor should be sufficient (this is the smallest motor of the same make as the existing motors). However, this solution required a gearbox to allow the correct force/speed operating point to be reached. An alternative solution was to use a larger motor with no gearbox. These solutions are compared in Table 4-2.

Table 4-2 - Design options for drive mechanics on blending roller axial axis

Option 1: 220W motor + gearbox	**Option 2: 630W motor, no gearbox**
Emerson Servo Motor (220W)	**Emerson Servo Motor (630W)**
Torque: 0.7Nm	Torque: 3Nm
Speed: 3,000rpm	Speed: 2,000rpm
Wittenstein LP Gearbox, ratio = 4	**No gearbox**
Efficiency: 97%	
Output torque: 2.7Nm	
Output speed: 750rpm	
NSK Precision Rolled Ball Screw, lead = 5mm	
Output force: 3.4kN (>2.5kN design load)	Output force: 3.8kN (Nb: ball screw support rated load: 3.4kN, but still >2.5kN design load)
Output speed: 62.5mm/s (>30mm/s design speed)	Output speed: 167mm/s (>30mm/s design speed)

On receiving quotes from suppliers, option 2 (without the gearbox) turned out to be cheaper (the increase in price on the motor was smaller than the cost of the gearbox). In addition, a gearbox would add additional backlash and torsional compliance, reducing the position accuracy. Therefore, on the basis of both cost and accuracy, option 2 was chosen. In addition, a torque limiter was added between the motor and ball screw to prevent damage to the machine components in the event of an overload or collision.

The machine was already controlled by a National Instruments (NI) Compact RIO 9022 controller running a real-time operating system, but there was no space for an additional NI 9514 drive interface – the 8 slots were used up with the 7 existing drive interfaces, and the NI 9237 data acquisition module for the load cell. A National Instruments 9144 8-slot Ethercat extension chassis was purchased and the data acquisition module moved into the new chassis so that the new drive interface could be placed on the same chassis as the other drive interfaces (this is optimal for synchronising all 8 axes). Finally, a servo amplifier was required to drive the motor. The overall system diagram for the machine is shown in Figure 4-20, with the modifications highlighted (The laser scanner discussed in chapter 3 is also shown).

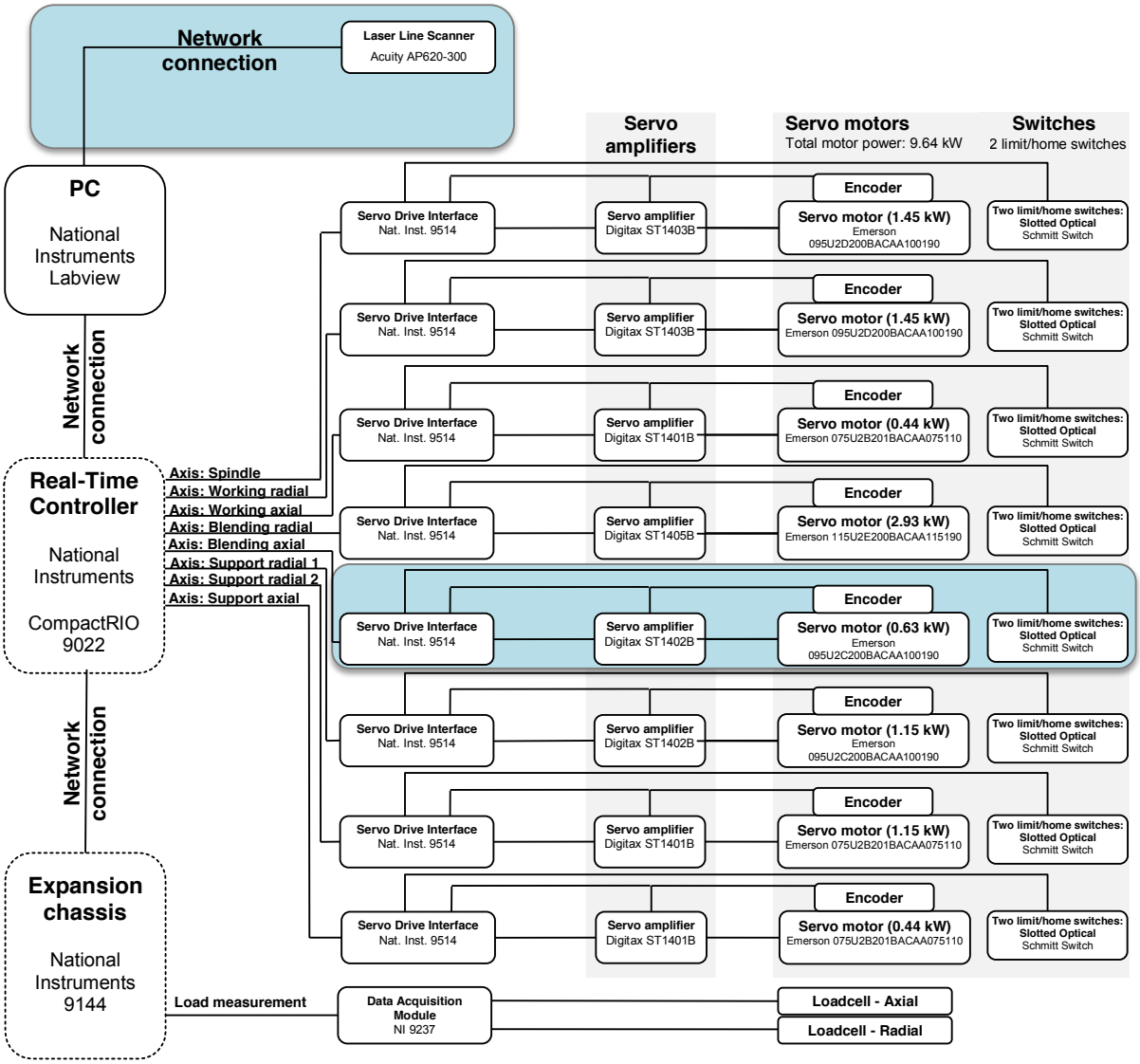

Figure 4-20 - System diagram, with the modifications highlighted in blue.

4.2.2 Redesigning the support rollers

The original support rollers were unable to provide support all the way around the inside of the workpiece because the arc length of the roller nose is only 68°, as highlighted in Figure 4-19. Support could be provided around the whole workpiece if an additional degree of freedom were added to allow the support roller to rotate around a vertical axis (perpendicular to the page in Figure 4-19), however, this was ruled out quickly due to the expense of additional equipment. The only other option is to change the arc length of the support roller nose as in Figure 4-21.

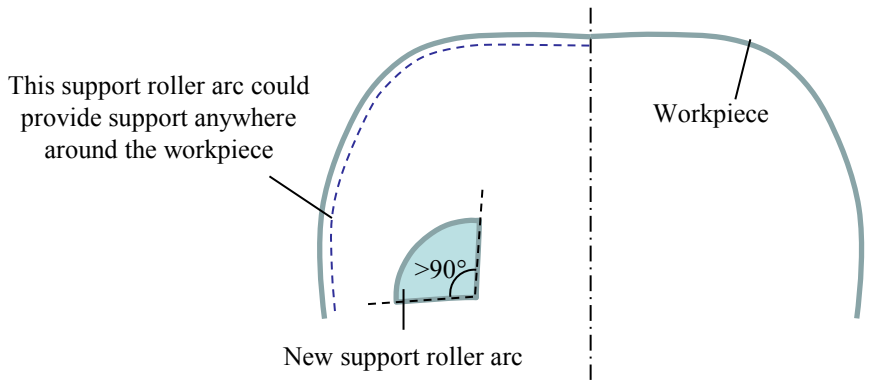

Figure 4-21 - The arc length of the support roller required to support the workpiece anywhere

Three design options were considered and evaluated according to the following criteria:

- Slip between the workpiece and roller must be minimized, as this can cause poor surface finish as well as unpleasant noise;
- The roller must still be able to withstand the forces specified by Music (2011): 1.25kN radially, 1kN axially and 0.2kN tangentially;
- The rollers must be able to get as close as possible to the blending roller;
- The rollers must still be able to move over the blending roller arm without colliding.

The three design options are shown schematically in Figure 4-22. Design option 1 is to replace the roller with a truncated spherical roller, which is only supported at one side, as shown in Figure 4-22a. However, in order to maintain the same stiffness in the axel as in the original design (which is supported at both ends), the axel would need to be wider, the bearing larger, and then the whole roller larger. However, the larger roller would collide with the blending roller arm.

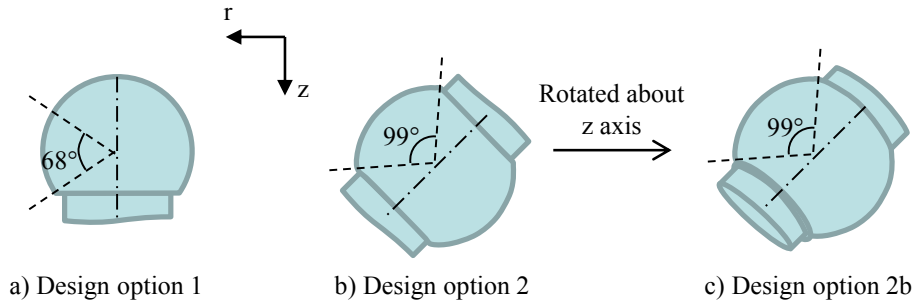

Figure 4-22 - Design options considered for new support roller

Design option 2 is to make the roller a little wider (in order to make the arc length greater than 90°), and to rotate the roller by 45° about the vertical axis, as shown in Figure 4-22b. However, because the axis of the support roller is no longer parallel to the axis of the workpiece, this may result in slip between the workpiece and support roller – the surface of the support roller would have velocity component in the axial direction, while this would never be the case with the workpiece.

Design option 2b is therefore a small modification on design option 2: The roller is rotated about the axial direction as shown in Figure 4-22c. With this method, it is only possible to reduce the slip to zero at one radius. However, by picking a typical radius at which support is provided (175mm – the midpoint between the radial position limits of ~100mm to 250mm), and designing to reduce slip to zero here, a value of rotation of 16° is arrived at. At the extreme radial positions, the maximum slip angle would be 10.2°, compared to 24.9° maximum without any rotation (i.e. in design option 2). The noise and surface finish created due to this slip angle was investigated by performing experiments, moving the working roller across the lubricated workpiece while the workpiece rotates at a speed to recreate the 10.2° slip angle. However, only a quiet gliding noise was produced, and the surface finish was not affected. An additional advantage of this design option was that it allowed the end of the support roller arm to be chamfered, so that it could be moved closer to the blending roller, as shown in Figure 4-23.

Design option 2b was therefore chosen and commissioned as shown in the photograph in Figure 4-23.

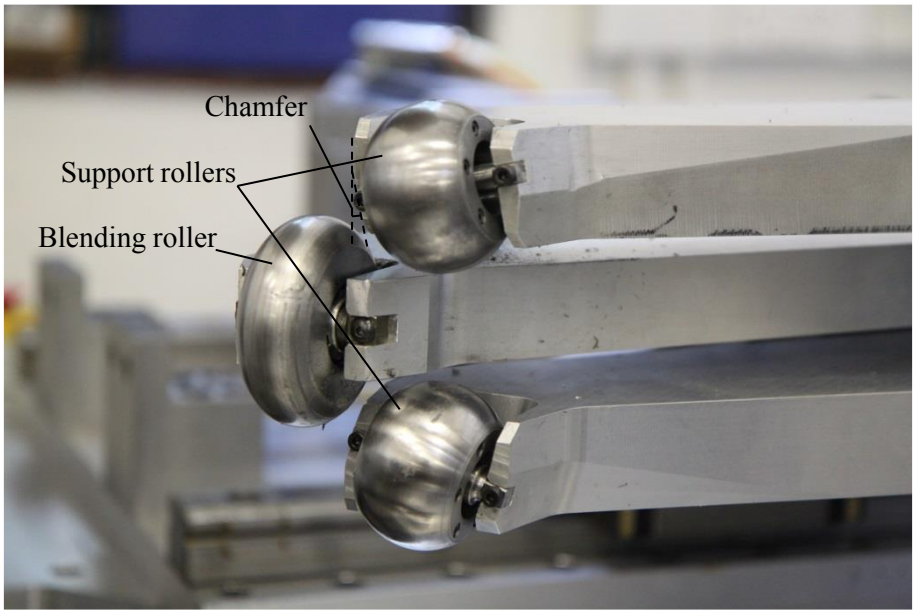

Figure 4-23 - The support rollers, as commissioned, highlighting the chamfer

4.3 Control of internal support rollers

In FAS, placing the blending roller and support rollers in the right position is critical to producing the part accurately. Figure 4-3 has already shown the effect of not allowing the blending roller to move at all, and in section 4.1, it became clear that either the blending roller or the support roller should be placed at just the point where the workpiece stops conforming to the mandrel. This position could in principle be calculated from knowledge of the toolpath – For example, using FEM to model the process and predict the shape of the workpiece at every point during the process. Because this requires no feedback from the workpiece, it is referred to here as “offline” positioning. An alternative is to measure the workpiece and use this feedback to determine the support roller positions.

With offline positioning, at least with today's computational power, FEM of the whole process would be too slow. An alternative is to use a simplifying assumption: to neglect springback and assume that, at the end of each toolpass, the workpiece takes the exact shape of that toolpass. The implication is that the blending roller remains in the same position for each pass, until the working roller reaches the base of the pass. At this point, the blending roller then moves to a position just opposite the working roller, as shown in Figure 4-24.

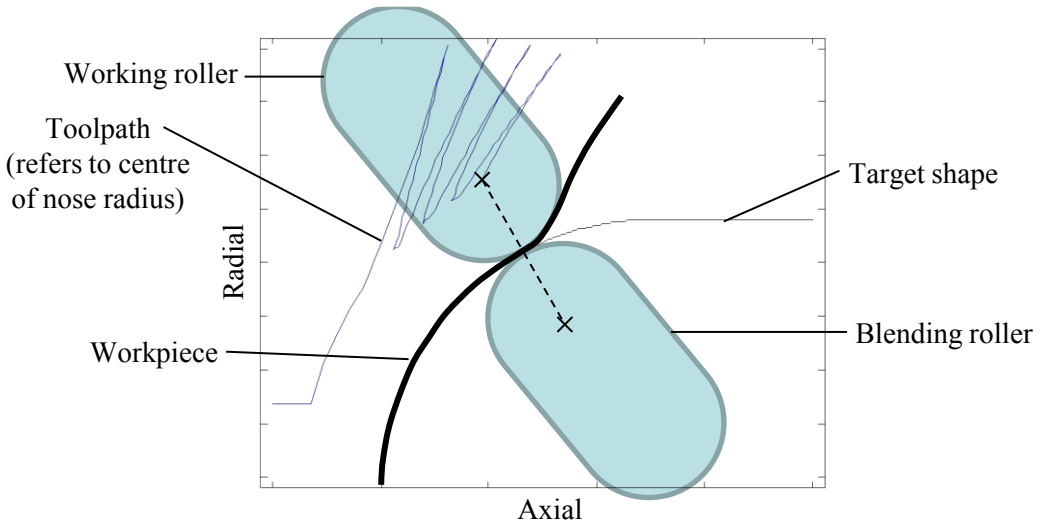

Figure 4-24 - Positioning the blending roller offline

However, in reality there is some springback, and this results in a gap between the blending roller and the workpiece. This led to a large unsupported area of the workpiece, so the workpiece was bent around the clamping plate, rather than the blending roller. This has three effects: larger geometric errors at the base, which becomes no longer flat; increased springback as the effective stiffness of the workpiece is reduced; and a lack of stability leading to earlier wrinkling. Figure 4-25 shows the shape of product produced using this strategy, showing large errors in the achieved shape when attempting to produce the 316mm diameter cup of Figure 4-13. Although this part completed successfully, albeit with large errors, larger parts with larger springback wrinkled before completion. This is likely to also be the case with harder materials with more springback (e.g. stainless steel).

With accurate modelling too slow, and approximate modelling too inaccurate, it is clear that the use of the laser scanner is necessary to measure the workpiece shape and to position the blending and support rollers correctly. With the shape of the workpiece measured, three algorithms are considered to position the internal rollers: near-real-time positioning; twice-per-pass positioning; and a hybrid positioning approach – The development and testing of these algorithms are discussed in this section.

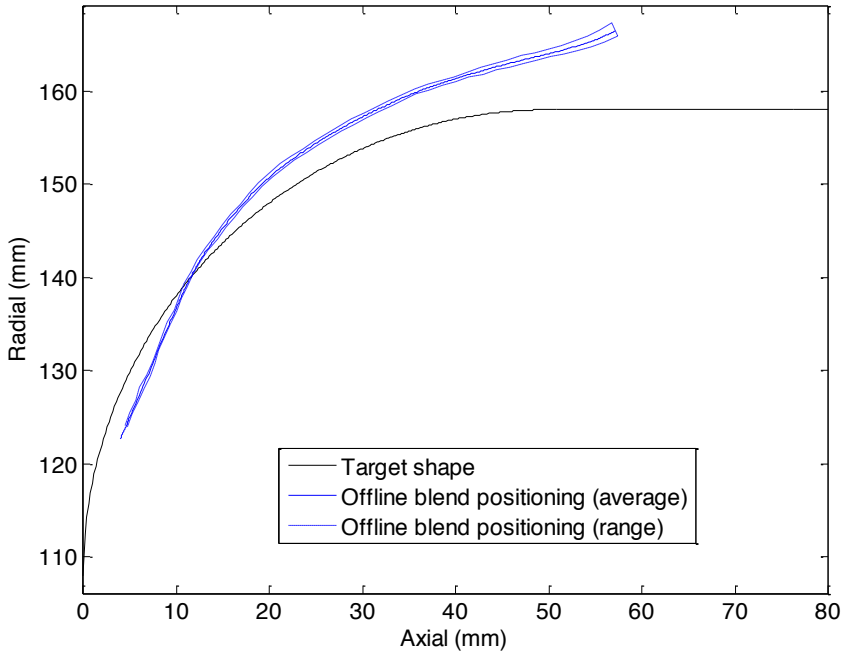

Figure 4-25 - The shape of product produced when using offline blending roller positioning

4.3.1 Near-real-time positioning

In the near-real-time positioning approach, the blending roller is repositioned every time a new motion command is issued from the PC to the real-time controller (typically every 3 mm of motion of the working roller). It is not exactly real-time, because the blending roller is repositioned at these discrete points, and in any case there is a delay between measuring the workpiece, performing the calculations on the PC, and delivering to command to the real-time controller.

The algorithm works by measuring the workpiece shape and comparing it with the target shape. Working from the spindle outwards, it looks for the last measurement point on the workpiece that is inside the target shape – it is trying to find the point where the workpiece just stops conforming to what would be the mandrel in conventional spinning. This point is used as the tip of the blending roller, and the position of the centre of the nose of the blending roller is found by simply offsetting this by the nose radius. An example of this being applied is shown in Figure 4-26.

However, sometimes the measured workpiece shape is significantly affected by the loading of the working roller, particularly when the working roller is nearer the edge of the workpiece. The blending roller position was therefore based on the loaded shape. The blending roller sometimes moved to far around the target shape and did not provide sufficient support to the workpiece, leading to bending around the clamping plate. Additionally, when the working roller moved along the workpiece or unloaded it all together, the measured shape would change and the blending roller would move abruptly. Both of these led to increased instability and the workpiece wrinkled before the process completed.

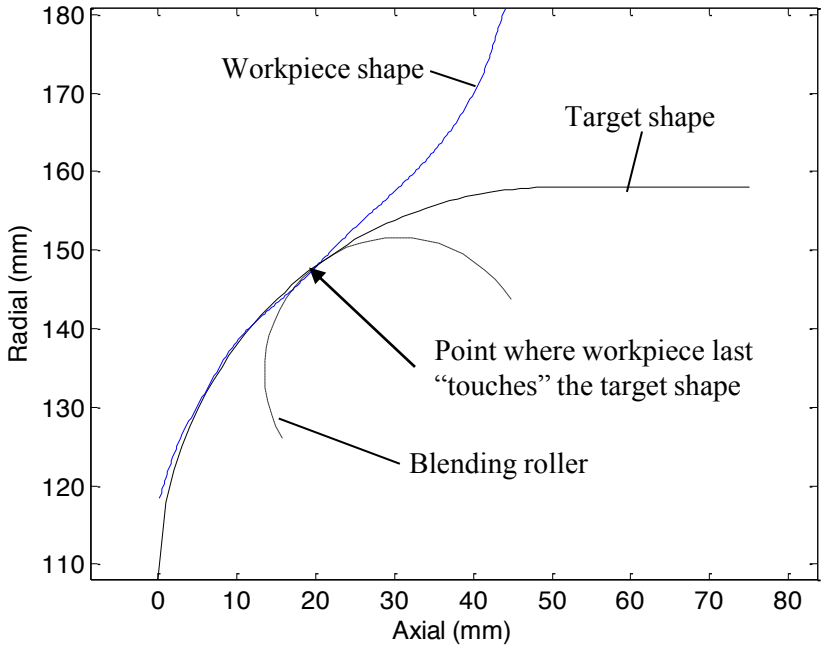

Figure 4-26 - The blending roller positioning algorithm

There are two possible ways to overcome this: To unload the workpiece before measuring, or to measure the loaded workpiece and use a fast model to calculate to unloaded shape. However, measuring the unloaded shape would mean unloading the workpiece after every small motion of the working roller, significantly slowing down the spinning process. Calculating the unloaded shape from the loaded shape is not trivial, and would require a great investment in developing a model, or using another FE model, which would be too slow to run online in anything near real-time. Nevertheless, the latter approach could be the subject of future work. In this thesis, as a compromise, a twice-per-pass positioning approach is considered.

4.3.2 Twice-per-pass positioning

In the twice-per-pass positioning approach, the blending roller is only positioned twice in each pass: Firstly, when the working roller is at the base of the workpiece. In this position, the effect of the loading on the measured shape is negligible, so the laser scanner effectively measured the unloaded workpiece. Secondly, when the working roller reaches the outer edge of the workpiece, it is unloaded and then a measurement of the unloaded workpiece is taken and used to position the blending roller.

The blending roller is positioned according to a similar algorithm described in section 4.3.1. However, it was found that the algorithm was more stable if the target shape was offset by a small amount (in this case, 1mm) when looking for the last "overlap" between the mandrel and workpiece. The blending roller was then positioned by offsetting this point by the nose radius *plus* the offset. This algorithm is demonstrated in Figure 4-27. The extra offset is thought to work because, if the blending roller positioning algorithm works correctly, there would be no overlap with the target shape in most regions, so the offset provides a more stable way of determining which regions of the workpiece are

"on the mandrel". In addition, it moves the blending roller slightly further around the target shape in order to allow for some more of the workpiece to be laid onto the target shape before it is repositioned again.

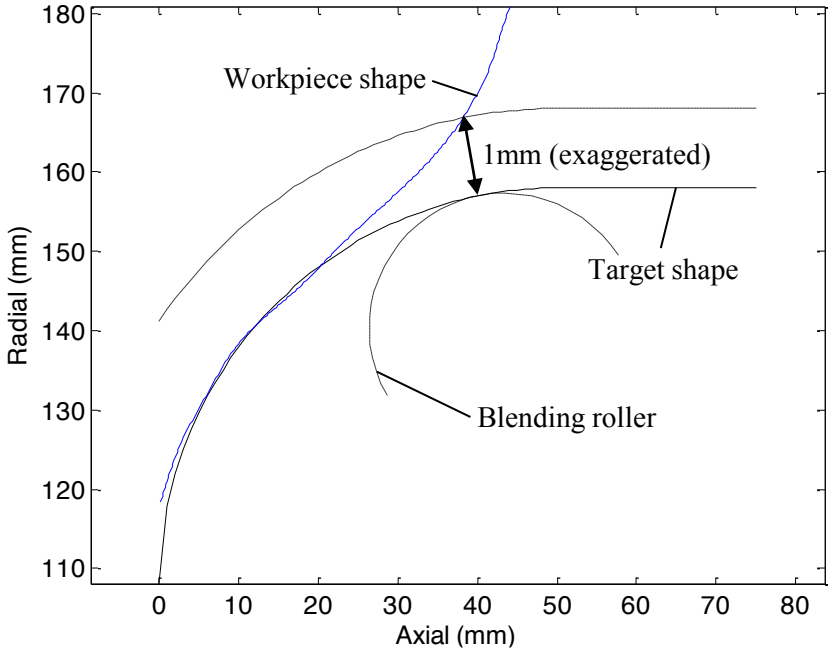

Figure 4-27 - Blending roller position algorithm with 1mm offset

The product shape produced using this approach is shown in Figure 4-28a, compared to offline blending roller positioning; the errors are shown in Figure 4-28b. The product was successfully produced without wrinkling, and the achieved shape error around the 50mm radius corner is reduced from 2mm to 1.2mm, and the maximum shape error reduced from 8.4mm to 5.3mm. However, near the base of the cup (towards the left of the plots), there is still a 1.2 mm overlap with the target shape, and a hybrid approach to blending roller positioning is therefore proposed to overcome this.

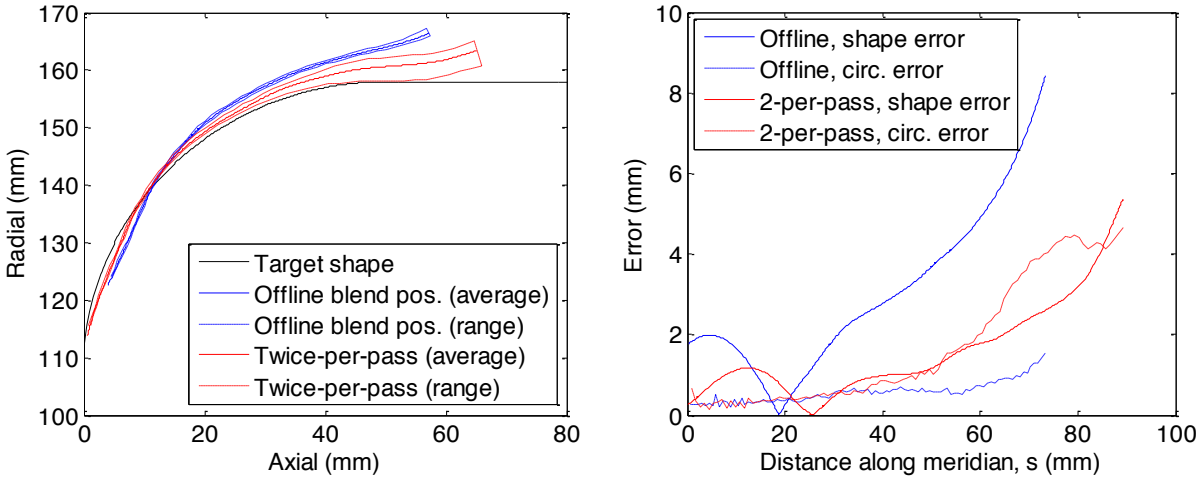

a) Workpiece meridian shape

b) Shape and circularity errors

Figure 4-28 – Workpiece measurements after offline and twice-per-pass blending positioning

4.3.3 Hybrid positioning approach

It was found that most of the over-forming around the base is produced during the first toolpass, which is typically the most aggressive pass. Therefore, a hybrid approach is proposed, where the near-real-time positioning approach is used for the first forward tool pass, and the twice-per-pass positioning is used in subsequent passes.

The resulting product shape is shown in Figure 4-29a alongside results from the twice-per-pass approach, and the errors are plotted in Figure 4-29b. The achieved shape has better agreement with the target shape – The 1.2 mm error around the corner of the cup has been reduced to 0.6 mm, while the error remains similar elsewhere.

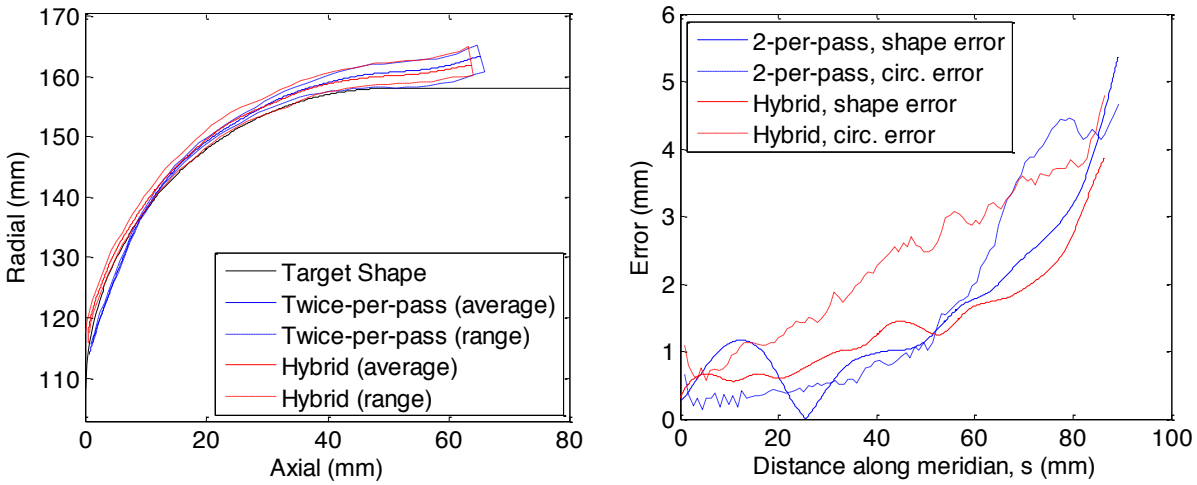

a) Workpiece meridian shape **b) Shape and circularity errors**

Figure 4-29 – Workpiece measurements after twice-per-pass and hybrid blending positioning

4.4 Conclusion and further work

Early experiments showed that the spinning of a 250mm diameter Aluminium cup could be spun with just one internal roller fixed axially, despite the FAS machine being designed with three. However, in this chapter, FE modelling showed that this was a special case: in general, three rollers may be needed - this was demonstrated for a torispherical shell - and usually the blending roller should be able to move axially. The FE modelling also showed that the optimal position of the internal rollers depends on the shape of the workpiece, and that either the two support rollers or the blending roller should sit just where the workpiece just begins to diverge from the target shape.

Design changes were made to enable the blending roller to be moved axially, and for the other two support rollers to provide support for a greater range of shapes. The laser scanner was used to measure the shape of the workpiece, and an algorithm was designed to use the measured shape to position the blending roller at the point where the workpiece shape just begins to diverge from the target shape.

Experiments showed that a hybrid approach – where the blending roller is positioned in near-real-time on the first pass, and then twice in each subsequent pass – allowed the product to be made successfully with very little overlap with the target shape.

This work demonstrates that simple models can be used within closed-loop control of product properties to position supporting or guiding tools, and not just working tools as was seen in the literature review of chapter 2. The approach could therefore be extended to other sheet forming processes where dedicated dies are replaced by supporting tools, such as two-point incremental sheet forming.

With further work, the automation of the internal rollers could allow any conventional lathe to be replaced by an FAS machine. Rather than machining a new mandrel for each new product, only the target shape would need to be given to the machine control system. Once this is done, the control of the working roller could be passed to a skilled workman, while the internal rollers would be positioned to recreate the support that a mandrel would provide. However, because the skilled workman operates based on real-time information the internal rollers should be positioned in real-time; and because the workman might want to create a full range of products, all three internal rollers should be automated.

In order to enable real-time positioning of the internal rollers, the *unloaded* shape of the workpiece should be calculated. It is not feasible to measure this directly, so further work could look at developing an observer model that can use the measured loaded shape along with the tool positions and forces to calculate the unloaded shape. This may produce an even more accurate positioning system for the internal rollers, and with a skilled workman, would allow the workman to feel the effects of the "mandrel" in real-time, as they would in conventional spinning.

The FE modelling in this chapter showed that three support rollers are required to approximate conventional spinning for the production of a wider range of shapes including the torispherical shell. However, this chapter has only shown successful algorithms to position the blending roller in the 316mm diameter cup. Controlling just the blending roller is sufficient to carry out investigations into springback control and toolpath generation in subsequent chapters, but further work could look at expanding the algorithms developed in this chapter to enable the selection of the optimal support configuration, and the correct positioning of the support rollers – perhaps by considering the geometrical stiffness of the current workpiece shape.

Chapter 5 - Springback Compensation

The initial flexible asymmetric spinning machine design did not have online geometry measurement, so Music (2011) was not able to compensate for geometric errors online. Subsequent measurements of the 250mm diameter cup demonstrator are shown in Figure 5-1a, showing errors of over 7mm from the target shape. Measurements of the 316mm diameter cup with a larger blend, used as a demonstrator of blending roller positioning in chapter 4, are shown in Figure 5-1b, showing errors of 4mm.

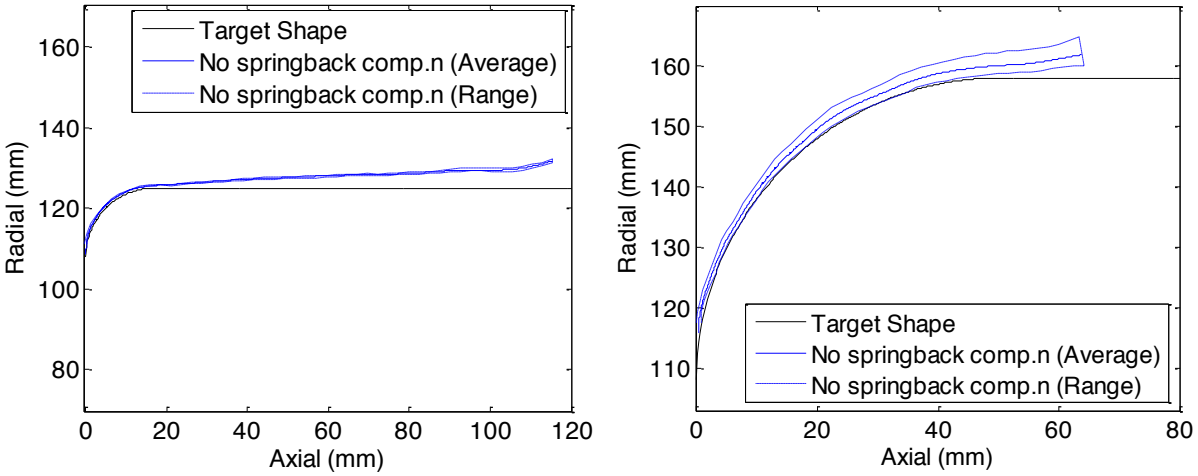

a) 250mm diameter cup with 15mm internal corner radius

b) 316mm diameter cup with 48mm internal corner radius

Figure 5-1 – Product shapes with no springback compensation

The primary reason for this error is that the toolpaths used in each of these cases did not compensate for springback. The toolpaths were generated by moving the tool so that it uses the target shape as a "base" - in each pass the tool would move from this base to the edge of the workpiece, and then back to the base to push a small amount more material into the desired shape. An example toolpath is shown in Figure 5-2, demonstrating how the target shape is used as a base. However, when the tool moves away from the base shape, or is unloaded altogether, elastic unloading causes the material to move away from the base again so that the target shape is not actually achieved.

A unique advantage of FAS is that the working roller can be moved inside the target shape in order to compensate for this springback error. In conventional spinning, this is not possible as the tool would then collide with the mandrel; it is possible to redesign and remachine the mandrel, but this might take several iterations and increases the lead time of the product. (An alternative method which some hand spinners utilise is to heat up the workpiece so that it expands and then spin it on to the mandrel as much as possible. As the workpiece cools it will shrink onto the mandrel, but this is approximate and not for precision manufacturing).

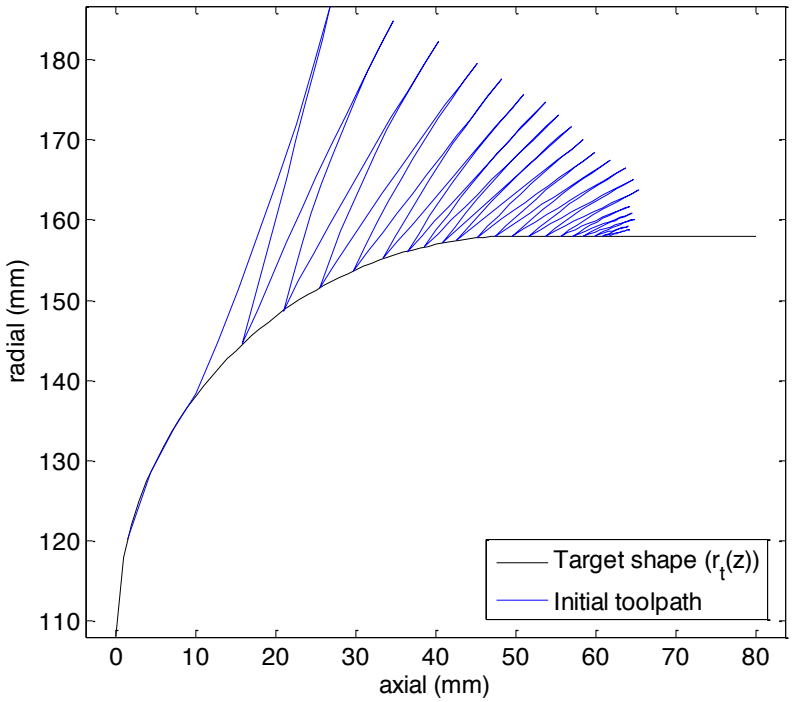

Figure 5-2 - A toolpath for the 316mm diameter cup with no springback compensation

The challenge in compensating for springback is working out how far inside the target shape to move the tool in each pass. Although open-loop control with an offline model could be used, this would be difficult if the blending roller is positioned online as this will have a large effect on the degree of springback and the amount of compensation required. In addition, accurate modelling would be prohibitively slow – the exact shape would need to be known in order to model the springback, and this would require a very slow finite element model. Any fast, approximate model would suffer from a large degree of model uncertainty resulting in large errors. Here, we therefore choose to use a closed-loop control system to compensate for springback.

In this chapter, three different closed-loop control approaches to compensating for springback will be discussed: A part-by-part approach, where the compensation for each part is calculated based on the error in the previous part, is described in section 5.1. A final corrective pass approach, where the springback is measured at the end of the process, just before a final pass is used to attempt to correct for it, is described in section 5.2. Online compensation of springback, where springback is measured in each pass, and then predicted for the next pass using a simple model, is described in section 5.3. Finally, the three approaches are evaluated together and further work is proposed in section 5.4.

5.1 Part-by-part springback compensation

Part-by-part compensation is where springback is compensated for in the next part, $k+1$, based on the measured springback in the previous part, k. The initial toolpath for the first part ($k=0$) is generated assuming no springback, using the target shape as the base shape as described in the introduction to chapter 5 and equation 5.1.

$$r_{b,0}(z) = r_t(z) \quad \textbf{5.1}$$

where $r_{b,k}(z)$ is the radius of the base shape for part number k at axial position z, and $r_t(z)$ is radius of the target shape at axial position z. The part is then measured, and the base shape for generating toolpaths for subsequent parts is given by:

$$r_{b,k}(z) = r_{b,k-1}(z) - \left(r_{k-1}(z) - r_t(z)\right) \quad \textbf{5.2}$$

where $r_k(z)$ is the measured radius of part k at axial position z. The resulting base shape for the second part is shown in Figure 5-3a. This new base shape is then used to generate a compensated toolpath, as shown in Figure 5-3b.

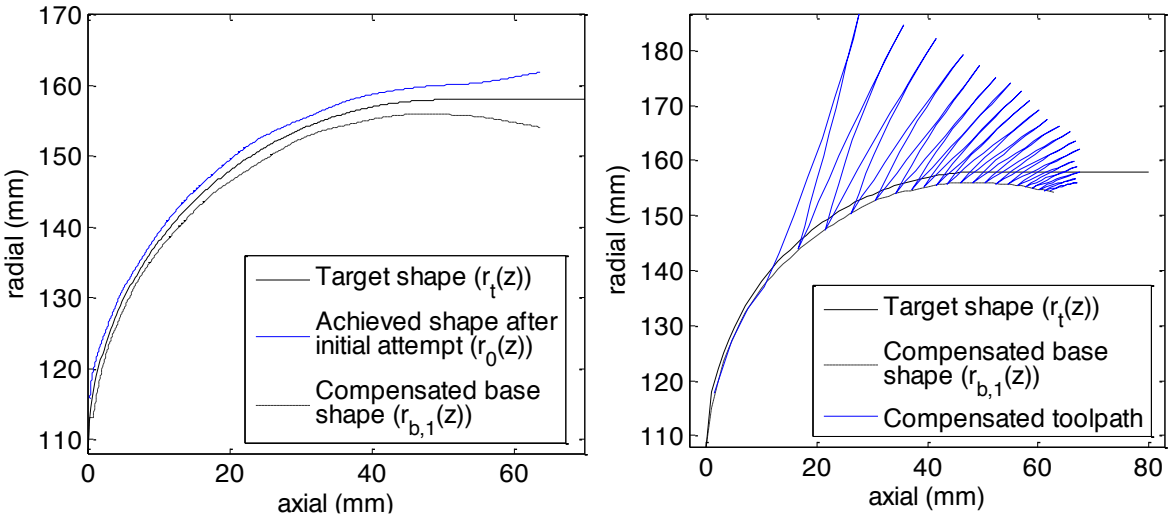

a) Compensating the base shape **b) Toolpath generated from compensated base shape**

Figure 5-3 - Part-by-part springback compensation

The shape achieved after only one iteration of this approach is plotted in Figure 5-4a, and the shape error (distance between average meridian and the target shape) and circularity error (the deviation in radius around the circumference of the product) in Figure 5-4b. The product errors are reduced significantly: the shape error from 3.9 mm to 1.5 mm suggesting that springback has been reduced as expected. Furthermore, the circularity error has been reduced from 4.8 mm to 2.3 mm, suggesting that this compensation has improved the stability and circularity of the cup. This is probably because the workpiece makes contact with the internal rollers further along the meridian, providing more stability as the size of the free region of the workpiece is reduced.

The disadvantage of this approach is that the first part goes to waste. However, the broad objective of this work, as described in Chapter 1, is to be able to produce an accurate, successful part, first time and with no lead time – the wasted part not only adds cost, but also lead-time. Further iterations of this compensation method would no doubt further reduce error, but at increased costs – instead, alternative compensation methods which do not waste parts are considered.

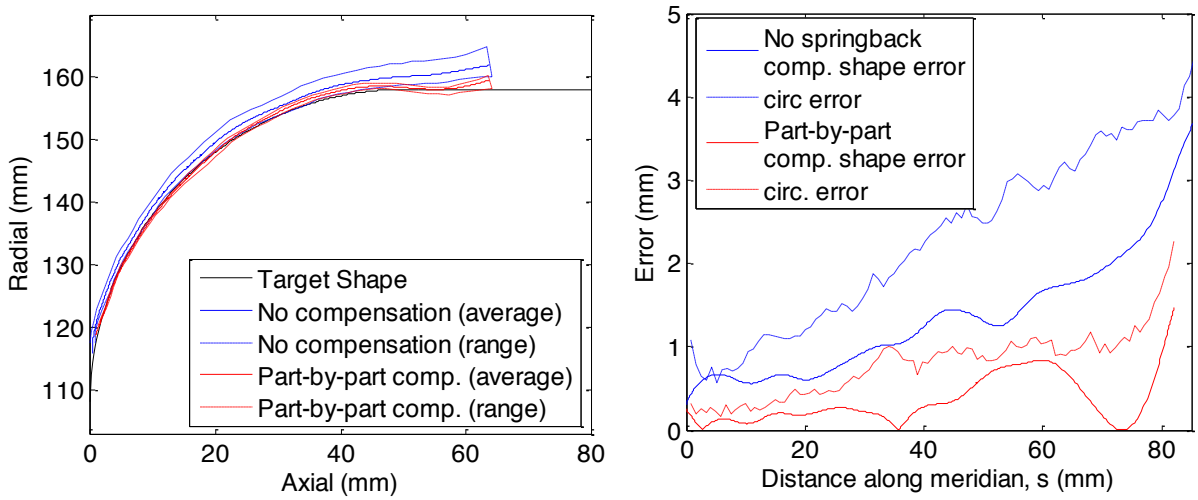

a) Workpiece meridian shape **b) Shape and circularity errors**

Figure 5-4 - The achieved shapes with no springback control and after one iteration of part-by-part compensation

5.2 Final finishing pass

An alternative is to design a final pass to remove the springback from each part made, independently of previous parts. This final pass is designed in the same way as the compensated base shape for the first compensated iteration ($k = 1$) in section 5.1. That is, the coordinates for the tip of the tool are given by:

$$r_w(z) = r_t(z) - \left(r_0(z) - r_t(z)\right) \qquad \textbf{5.3}$$

where $r_w(z)$ is the radial position of the tool at axial position z. The base shape shown in Figure 5-3a) is therefore the same as the final toolpass. The blending roller follows the same path on the other side of the sheet, but with a gap between the blending roller and working roller 0.2mm less than the thickness of the sheet. This aims to simulate the through-thickness compression that would be achieved by squeezing the material between the tool and mandrel in conventional spinning, and to attempt to reduce the amplitude of wrinkles by "squashing" them.

The achieved shape is shown in Figure 5-5a and the errors in Figure 5-5b. The shape error is only reduced slightly from 3.9 mm to 2.8 mm, which is a much smaller improvement than that from part-by-part compensation.

The circularity error is also reduced from 4.7 mm to 3.2 mm, but it can be seen from Figure 5-5b that this reduction is all towards the outer edge of the workpiece in the region where $s > \sim 60$mm. This is consistent with where the force is largest, as shown in a plot of the tool force in Figure 5-6. This suggests that this squeezing force of 0.4-0.5kN is effective at reducing the amplitude of wrinkles. However, this could not be explored further as the machine is position controlled, rather than force controlled. Further work could, however, explore the possibility of using a force-controlled final pass to reduce wrinkles.

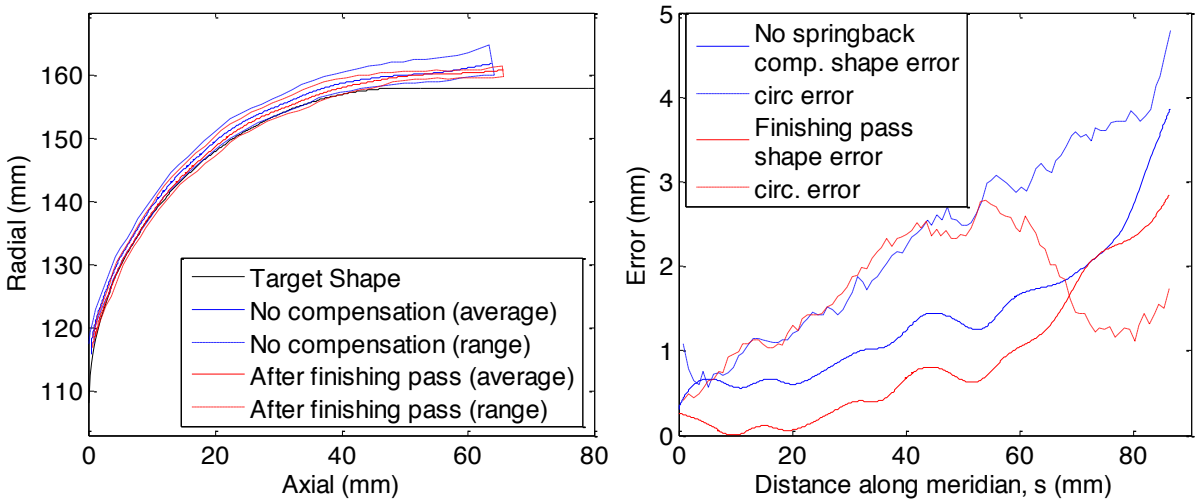

a) Workpiece meridian shape **b) Shape and circularity errors**

Figure 5-5 - The achieved shapes with no springback control and after the finishing pass

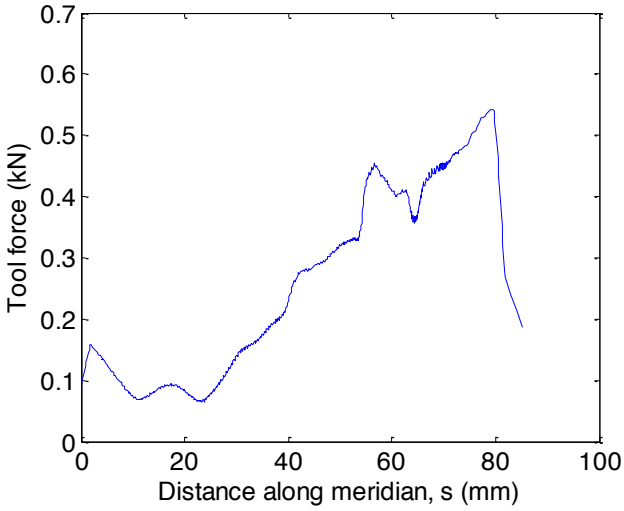

Figure 5-6 - Tool force along the finishing pass

Overall, the reduction in error is smaller than with part-by-part compensation. Although the advantage of this approach is that a part is not wasted, the additional finishing pass adds to the time to produce a part.

5.3 Online compensation

Springback could be compensated for in each toolpass by moving the tool inside the "target shape". This distance should be calculated so that, when the tool is removed, the area of the workpiece that it was in contact with springs back to the target shape. In both section 5.1 and 5.2, this distance was calculated based on the geometric error at the end of the production of the part, therefore requiring the current part to be wasted, or for additional processing time to be added to correct for it.

If the springback could be calculated prior to starting each pass without needing information from previous parts, neither additional attempts nor additional processing would be required to compensate for springback. However, because of the changing shape of the workpiece, and the changing position

of the tools along the workpiece, the amount of springback will vary throughout the toolpath and indeed each tool pass. In order to estimate how much springback will occur each time the tool reaches the target shape, a model is required.

On one extreme, a full, elastic-plastic finite element model could be used. It would be able to calculate the evolution of the shape and material properties perfectly, and it would be able to calculate the springback at any point. However, it would be extremely slow – it might take months for the model of the process to run, never mind the optimisation.

Instead, a fast, approximate model could be used. Here, the workpiece is modelled as simple, elastic, 1-dimensional, cantilever as shown in Figure 5-7. The clamping plate clamping the workpiece to the spindle is modelled as the built-in cantilever base. The blending roller is modelled as a simple support, and the working roller as a point load. The springback is calculated by working out the displacement that would need to be applied by the working roller to cause first yield, which is given by equation 5.4.

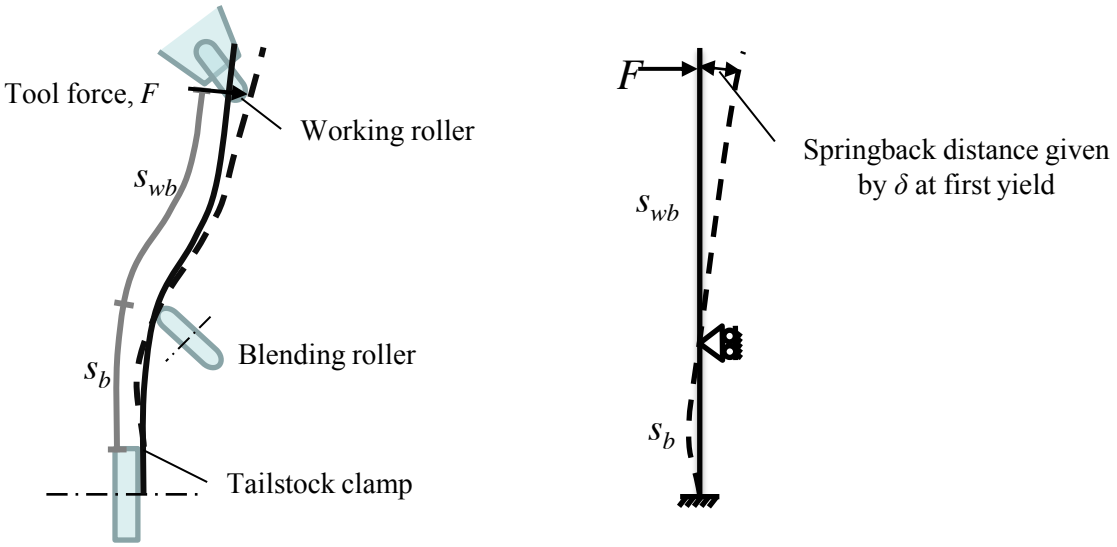

Figure 5-7 - The workpiece being modelled as a simple elastic cantilever

$$\delta = \frac{M_p}{EI}\left(\frac{s_{wb}s_b}{4} + \frac{s_{wb}^2}{3}\right) \qquad \textbf{5.4}$$

where δ is the springback, M_p is the plastic moment per unit width at first yield, and EI is the bending stiffness per unit width, s_b is the meridional distance from the spindle clamp to the tip of the blending roller, and s_{wb} is the meridional distance from the blending roller to the working roller.

However, this model would not predict springback very well for several reasons, in rough order of their effect:

- The axisymmetry of the workpiece will change the stiffness significantly;

- The displacement at first yield is not a good indicator of springback because, in reality, there will be more plastic deformation in both the material closer to the centre of the sheet and the material elsewhere in the workpiece;
- The workpiece is not straight - it usually has some curvature along the meridian;
- There may be other uncertainties, e.g. in the material properties. But these are likely to be negligible errors compare to those above.

Therefore, rather than taking the result of equation 5.4 directly, it could be calibrated by measured experimental data. To do this, a constant multiplier, c_g, is added in equation 5.5 to compensate for some of the errors introduced due to the reasons listed above.

$$\delta = \frac{c_g M_p}{EI}\left(\frac{s_{wb}s_b}{4} + \frac{s_{wb}^2}{3}\right) \qquad \textbf{5.5}$$

The constant is recalculated from the elastic springback distance measured each time the tool reaches the edge of the workpiece on its forwards pass. By changing the values of s_b and s_{wb}, equation 5.5 can then be used to predict the springback distance, δ, when the tool reaches the base of the toolpass on the backward pass. This then allows the backwards pass to be designed with this distance as the overlap with the target shape. M_p and EI are assumed to remain constant, so they can be included in the calibration factor and do not need to be known a priori.

Even as the working roller moves inside the target shape based on this online compensation, the blending roller continues to be positioned based on the uncompensated target shape, to ensure that it still makes contact with the workpiece after unloading, and not just when fully loaded. No final finishing pass is applied.

The achieved shape is shown in Figure 5-8a and the errors in Figure 5-8b. The dimensional error is reduced: the shape error from 3.9 mm to 1.5 mm; and the circularity error from 4.8 mm to 0.8 mm. The improvement in shape accuracy is the same as in part-by-part compensation, but with the advantage that no part goes to waste – the first part is made to this degree of accuracy. However the circularity error is significantly improved compared to both of the previously considered compensation methods. This is thought to be because the compensation is done throughout the part, so that the workpiece is placed onto the blending roller further around the workpiece, resulting in greater stability as the working roller works on the remaining area of the flange. This is consistent with experience gained from hand spinning – The hand spinner usually tries to remove springback and get as much of the workpiece laid onto the mandrel as early as possible to increase stability.

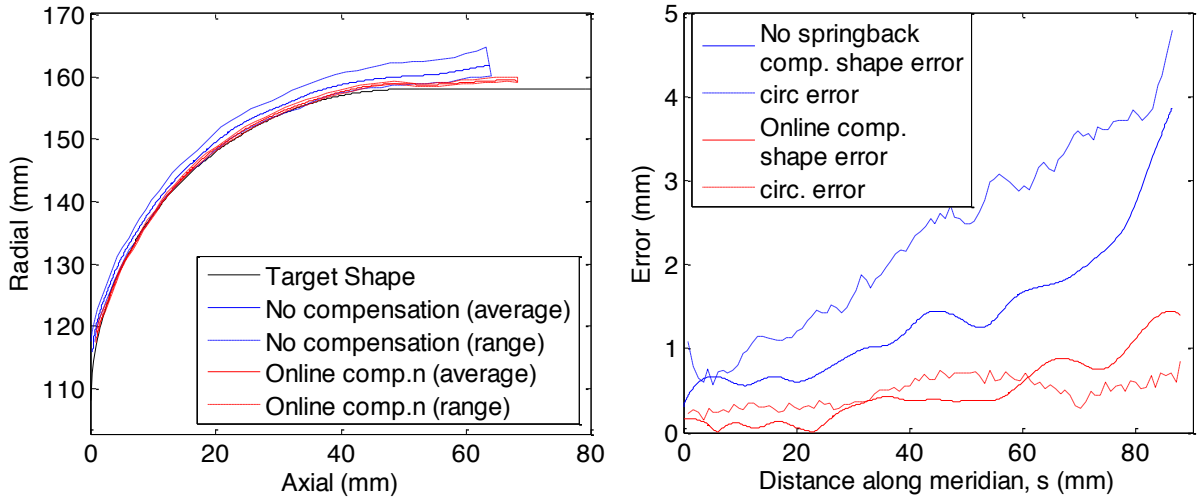

a) Workpiece meridian shape **b) Shape and circularity errors**

Figure 5-8 - The achieved shapes with no springback control and with online springback control

5.4 Conclusion and further work

Three different methods of closed-loop springback compensation have been investigated: part-by-part compensation; compensation with a final finishing pass; and online compensation with a simple cantilever model. The shape and circularity errors with these three approaches are shown in Figure 5-9, compared to those with no compensation.

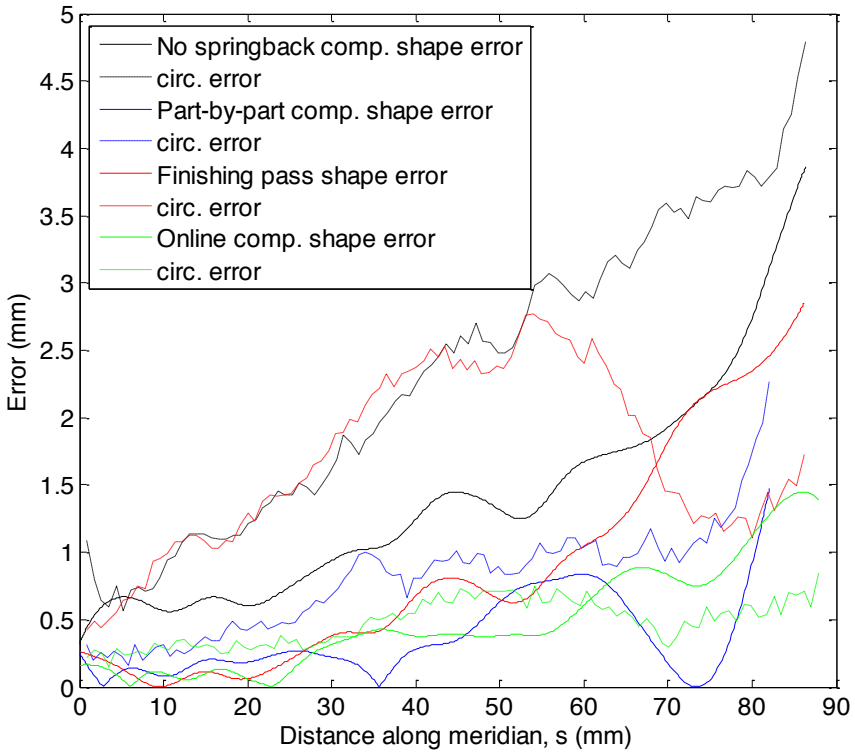

Figure 5-9 - The shape and circularity errors with no springback compensation and with the three compensation approaches

All of the compensation methods reduce the shape error significantly, showing that they are all, to some degree, effective at reducing springback. However, online compensation is the most effective,

reducing the maximum shape error from 3.9mm to 1.5mm even with only a very approximate model. A further advantage of online compensation is that it does not need to produce a waste product or add additional processing time.

All of the methods also reduce the circularity error, particularly part-by-part compensation and online compensation. This is because, as springback is reduced during the process, the workpiece makes contact with the blending roller further along the meridian, increasing the stability of the region of the workpiece remaining to be formed. Again, the improvement was most effective in the online compensation model, with a reduction in circularity error from 4.8mm to 0.8mm.

This chapter therefore adds to the growing body of literature showing that closed-loop control of product properties can be used with simple and approximate models to significantly improve the accuracy of parts produced using metal forming processes. It could also be directly extended to other flexible spinning processes which suffer from springback problems, such as Kawai et al.'s (2001) spinning with a general purpose mandrel, and Shima et al.'s (1997) spinning with two rollers.

Even without further work on toolpath generation, the springback compensation methods developed here could be applied to FAS with a manually controlled tool. In numerically controlled conventional spinning, the skilled workman controls the tool with a joy-stick. The control system prevents damage due to collisions between the mandrel and roller either by limiting the force, or limiting the motion of the tool with knowledge of the mandrel. In FAS with online compensation, the control system could allow the workman to move the tool slightly inside the target shape in order to compensate for springback. The workman would be unaware of the correction, and would therefore be able to effortlessly avoid springback while not thinning the sheet by applying large through-thickness forces.

However, despite significant improvements to the accuracy of FAS, the achieved shape errors of 1.5mm and circularity errors of 0.8mm are still greater than typical industrial demands for tolerances of less than 0.1mm. Furthermore, the approach has only been tested on commercially pure Aluminium, so further tests need to be performed to see whether the system also works with more challenging materials such as steel, stainless steel and titanium etc. – although this will also require an upgrade to the force capacity of the tools. Two pieces of further work could reduce these errors and ensure the system works well for other materials: Improving the model to further reduce shape errors and exploiting the flexible mandrel to reduce circularity errors.

The use of a simple, 1-dimensional cantilever to model the workpiece is quite a stark assumption. With further modelling effort, this could be extended to assume an axisymmetric workpiece (perhaps with axisymmetric loading initially, and then further extended to assume non-axisymmetric loading), and to use something more advanced than displacement at first yield to estimate springback. In addition, the model could be calibrated from more than just one measurement at the end of the

workpiece – perhaps the model could be best-fitted to a number of data points measured throughout the previous pass in order to reduce the effect of noise and ensure that model is better fitted to reality.

Secondly, the improvement in circularity could be exploited further. FAS has the advantage that the effective mandrel can not only change shape quickly for each new part, but can also change quickly during the part. The internal rollers could therefore be used to recreate the effect of replacing the mandrel frequently throughout the spinning of a part, enhancing the stability of the workpiece throughout the process, not just once some regions of the workpiece have reached the ultimate target shape.

Chapter 6 - Toolpath Generation to Avoid Failure

Toolpath generation remains an open challenge in metal spinning: Where should the working roller be moved in order to produce the desired product without causing the workpiece to wrinkle or tear? Indeed, the same questions could be applied to all processing parameters in spinning, such as the feed rate and the dimensions of the tools used, but a qualitative, if not quantitative understanding of these parameters has already been developed in the literature, as discussed in Chapter 2 (and summarised in Table 2-1). Toolpath design remains the biggest challenge in spinning, and therefore is the focus of the discussion here.

Historically, toolpath design has been carried out manually. A skilled craftsman can feel and see the effects of the forces they apply to the workpiece, and adapt their motion accordingly. Even on more modern CNC spinning machines, toolpath design is performed by a skilled craftsman, but is recorded and then repeated automatically.

In a more structured approach to toolpath design, Hayama et al. (1970) compared linear, quadratic and involute toolpaths and found that an involute toolpath profile, described by parametric equations 6.1 and 6.2, gave the highest spinning ratio. Liu et al. (2002) suggested that this was because an involute profile generated the lowest radial and tangential stresses in the workpiece.

$$z = a(\cos\theta + \theta\sin\theta) + c_1 \quad \textbf{6.1}$$

$$r = a(\sin\theta - \theta\cos\theta) + c_2 \quad \textbf{6.2}$$

In the development and demonstration of the flexible spinning machine, toolpaths for demonstrator parts were made by trial and error. Using the results of Hayama et al. (1970) and Liu et al. (2002), involute toolpaths were used, and five parameters for each pass (toolpass length, L_t, and start angle, α_1 and end angle, α_2 of the forward and backward pass (subscript *f* and *b* respectively), as shown in Figure 6-1) were varied in each trial until a working toolpath was found. An example of a working toolpath (designed by Music, 2011) to produce a 250mm diameter cup with a 15mm corner radius is shown in Figure 6-2. However, due to the effort of designing toolpaths in this way, only four products have been successfully made on the spinning machine: a cup with 15mm corner radius, a similar cup with 50mm corner radius, a cone, and a dome.

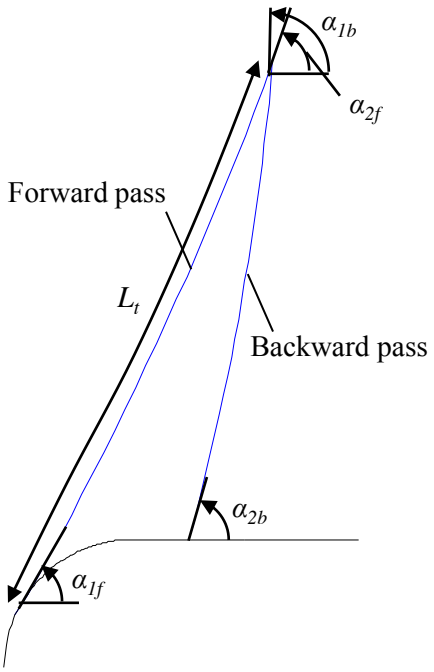

Figure 6-1 - Parameters of the involute toolpath

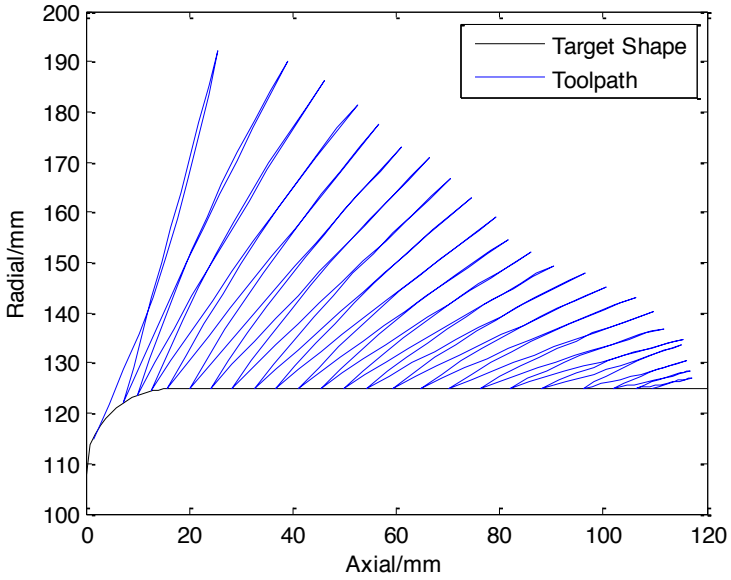

Figure 6-2 – A working toolpath for a 250mm diameter cup with a 17mm corner radius.

All of these forms of manual toolpath generation are both time consuming and costly. If toolpath design could be automated, the lead time and labour costs would be reduced. Furthermore, it is a necessary part of achieving the objective of creating a fast CAD to CAM solution with FAS.

As described in chapter 1, the challenge of designing toolpaths lies in developing process models, $\mathbf{f}_k$, and constraint models, $\mathbf{p}_k$, in the open-loop minimisation of equation 1.4 (repeated here as equation 6.3).

$$\begin{aligned} \min_{u_0 \dots u_{K-1}} \quad & \left\| \mathbf{q}_K(\mathbf{x}) - \mathbf{q}^d(\mathbf{x}) \right\|_2 \\ \text{subject to} \quad & \mathbf{q}_{k+1}(\mathbf{x}) = \mathbf{f}_k(\mathbf{q}_k(\mathbf{x}), \mathbf{u}_k) \quad \text{for } k = 0,1,2, \dots K-1 \\ & \mathbf{q}_0(\mathbf{x}) = \mathbf{q}^i(\mathbf{x}) \\ & \mathbf{p}_k(\mathbf{q}_k(\mathbf{x}), \mathbf{u}_k) \leq 0 \end{aligned} \qquad \textbf{6.3}$$

Although it is the objective of constraint model, $\mathbf{p}_k$, to prevent wrinkling and tearing, an accurate process model, $\mathbf{f}_k$, is also needed in order to calculate the current state of the workpiece, $\mathbf{q}_k(\mathbf{x})$, as an input to the constraint model. In the closed-loop minimisation (equation 1.5, repeated here as 6.4), $\mathbf{q}_k$ is measured directly, allowing an approximate form of the process model, $\mathbf{f}_k$, to be used, while the constraint can still be calculated accurately.

$$\begin{aligned} \min_{u_{k'} \dots u_{K-1}} \quad & \left\| \mathbf{q}_K(\mathbf{x}) - \mathbf{q}^d(\mathbf{x}) \right\|_2 \\ \text{subject to} \quad & \mathbf{q}_{k+1}(\mathbf{x}) = \mathbf{f}_k(\mathbf{q}_k(\mathbf{x}), \mathbf{u}_k) \quad \text{for } k = k', k'+1, k'+2, \dots K-1 \\ & \mathbf{q}_{k'}(\mathbf{x}) = \widehat{\mathbf{q}}_{\boldsymbol{k}'}(\mathbf{x}) \\ & \mathbf{p}_k(\mathbf{q}_k(\mathbf{x}), \mathbf{u}_k) \leq 0 \end{aligned} \qquad \textbf{6.4}$$

However, the challenge of constraint modelling still remains, and the model must now be fast enough to be run online. Yet, in the review of modelling in spinning, no fast model of wrinkling exists which can be used for toolpath generation. FE models could be used, but are too slow: the FE model presented in chapter 3 would take over a year to model the whole toolpath of Figure 6-2, and this model might run hundreds of times in the minimisation 6.4. As highlighted in chapter 2, the lack of fast models of thinning and wrinkling which can be used for toolpath generation is the key reason why automatic toolpath generation has not been achieved.

The aim of this chapter is to explore whether the computational load of the optimisation in 6.4 can be reduced in order to make feasible the automatic, online generation of toolpaths which do not cause wrinkling or tearing. Two approaches will be considered:

Firstly, by using a *finite horizon approach*. The minimisation of 6.4 is ran from the current time, $t_{k'}$ to the end of the process, K. Instead, it could just be performed for the next K_c increments, where K_c is known as the control horizon. The minimisation should therefore be faster because there are fewer control actions to model and optimise each time it is ran. However, there is a risk that optimising only the next K_c time steps does not lead to overall optimisation. The resulting toolpath might lead into a trap, creating an intermediate shape that cannot be formed into the target product without failure. In order to test this, in section 6.1 an accurate but slow FE model is used within a closed-loop, finite horizon control system to see if failure can be avoided. This allows the finite horizon approach to be tentatively tested, but the resulting control system is too slow for industrial applications.

The second way of reducing computation load is by using a *faster, more approximate constraint model* in place of $\mathbf{p}_k$. It has already been shown that fast, approximate process models can be used

within a closed-loop control system to produce accurate results – there were several examples presented in the literature review in chapter 2, and indeed in order to control the blending roller in chapter 4 and to overcome springback in chapter 5. However, these examples made approximations within the process model, $\mathbf{f}_k$, not the constraint model. Any error in the process model can be compensated for by measuring the state of the workpiece after the control actions have been implemented. However, if a modelling error in the constraint model, $\mathbf{p}_k$, results in control actions which result in failure, these errors cannot be compensated – the process model, therefore, can be approximate, but only if it is conservative. In section 6.2, a very fast and approximate stress-based criterion is developed, applied online and evaluated, in order to explore what degree of approximation can be applied while still producing a successful toolpath.

6.1 Finite horizon toolpath design by finite element analysis

In order to evaluate the possibility of using a finite horizon approach to generate toolpaths online separately to evaluating the possibility of using a fast approximate constraint model, an accurate constraint model must be used. Therefore, in this section, the very slow but accurate FE models described in chapter 3 are used within the closed-loop minimisation of equation 6.4 in order to create a so-called "FE-in-the-loop" control system.

Equation 6.4 is deceptively simple in its abstract form, so detailed design work is needed to develop a working FE-in-the-loop control system. This design work will be described in section 6.1.1 to develop a control system to prevent wrinkling. The resulting control system will be evaluated in section 6.1.2. The results will be used to develop a thinning criterion in section 0, and then the improved control system evaluated in section 6.1.4.

6.1.1 Developing an FE-in-the-loop control system

The minimisation equation 6.4 is deceptively simple, and needs some development beyond its abstract form to design a working control system. In this section, more details about its precise implementation will be described.

Rather than strictly running the minimisation of 6.4, this control system will only seek to find the limiting value of the control actions, u_k, and will then apply the largest possible value. In effect, we are solving a modified version of 6.4, written as equation 6.5. In future, it could be combined with the work of chapter 5 in order to limit springback – but the aim here is only to test the constraint modelling approach.

$$\begin{aligned} \max \quad & u_{k'} \dots u_{K-1} \\ \text{subject to} \quad & \mathbf{q}_{k+1}(\mathbf{x}) = \mathbf{f}_k(\mathbf{q}_k(\mathbf{x}), \mathbf{u}_k) \quad \text{for } k = k', k'+1, k'+2, \dots k'+K_c-1 \\ & \mathbf{q}_{k'}(\mathbf{x}) = \widehat{\mathbf{q}}_{k'}(\mathbf{x}) \\ & \mathbf{p}_k(\mathbf{q}_k(\mathbf{x}), \mathbf{u}_k) \leq 0 \end{aligned} \qquad \textbf{6.5}$$

In order to define the toolpath as a series of control actions which are to be optimised, the toolpath will be split into a series of linear sections. The control action, u_k, defines the angle of inclination in space of the kth linear section. The length of each of these linear sections is equal to the distance the tool travels during 5 revolutions of the workpiece, and the tool will move along each of these sections at a feed rate of 1.2mm/revolution (so the length is $5\text{revs} \times 1.2\text{mm/rev} = 6\text{mm}$).

The finite horizon approach is then applied by only optimising for the next $K_c = 1$ line segment of the toolpass. In practice, this means that the FE model developed in chapter 3 will be used to model only the next 5 rotations of the workpiece to see if failure occurs (The exception is for the first increment in which the first 10 rotations are modelled, as it was found that after 5 rotations the workpiece is still quite unstable resulting in modelling errors which settled down after 10 rotations).

In order to determine the limiting angle, $u_{k,max}$, three to four FE models are ran in parallel with the tool moving at different angles. These angles are chosen by human judgement, usually at the same angle as the previous toolpath segment and then one slightly higher and one slightly lower – this was usually successful as the limiting angle was relatively steady, but at some points more attempts were needed in order to find the limiting angle. The selection of trial angles could be automated in a full, commercial application of this toolpath generation system, but currently the limitation is the speed of the FE model.

After the 5 rotations with the tool moving along the trial toolpath segment, an assessment is performed to see whether failure has occurred and the constraint inequality breached (i.e. if $\mathbf{p}_k(\mathbf{q}_k, u_k) > 0$). Firstly, a final rotation is carried out in the FE model with the tool held stationary in order to reduce the asymmetry. This is to attempt to remove any of the effects of the asymmetric path of the tool around the workpiece, which might look like wrinkles. The tool is then unloaded and Python is used to extract the results into a text file. MATLAB is then used to analysis the results, and judges the toolpath angle to have failed if:

- The *amplitude of wrinkles* - defined as the maximum Fourier component of the axial displacement around the outer circumference of the workpiece - exceeded 0.5mm *unless* the amplitude of wrinkles had been attenuated compared to the start of the model. 0.5mm was chosen as this was found to be an acceptable level of wrinkling amplitude which might be seen due to anisotropy, noise, and the inherent asymmetry in the way to tool is applied.
- The *tool forces* exceeded their design load.
- The tool *penetrated the target shape* (this was checked before running the FE model) – This is the way in which the target shape is achieved, assuming no springback. In future we could use the results of chapter 5 to compensate for springback here.

In order to complete the closed-loop, a toolpath file was generated and the same tool motions were performed physically using the spinning machine. The full 3D shape of the workpiece was measured using the laser. This measured data is used to update the positions of the nodes from the previous FE model to create the starting point for a next set of FE models. In addition, the work hardening strains, residual stresses and the thicknesses at each node in the previous FE model are used as the initial conditions for the nodes in the new FE model, so that here the workpiece state $\mathbf{q}_k$ includes more than just the workpiece shape.

These subsequent FE models start with two more analysis steps than the FE model for the first increment: Firstly, they start with an "equilibrium" step, in which the solver allows the workpiece to come into equilibrium with the residual stresses that have been applied – this is necessary because the change in nodal positions with the same residual stresses from the previous analysis may cause the system to no longer be in equilibrium. In practice, however, this only results in a very small change to the workpiece geometry, as demonstrated by the plot in Figure 6-3 of axial displacement at the outer edge of the workpiece before and after the correction after a total of 50 rotations, compared to at the end of the following 5 rotations. This shows that the changes in geometry due to the correction and equilibrium step are very small compared to the change from the subsequent deformation.

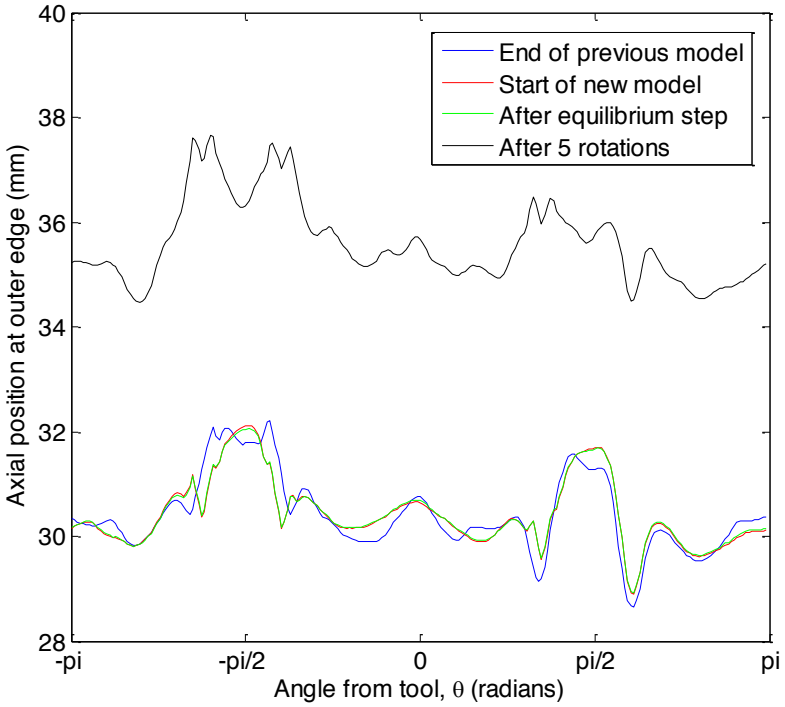

Figure 6-3 - The axial position of the outer circumference of the workpiece after 50 rotations, plotted before and after correction, after coming to equilibrium with the residual stresses, and after the subsequent 5 rotations.

In the second additional step, the tool reloads the workpiece to move to the same position it was in before it unloaded the workpiece at the end of the previous toolpath increment. After this, the process

of optimising for the toolpath angle is repeated for the next 5 rotations, before the tool is unloaded once more.

This closed-loop control system is demonstrated in Figure 6-4.

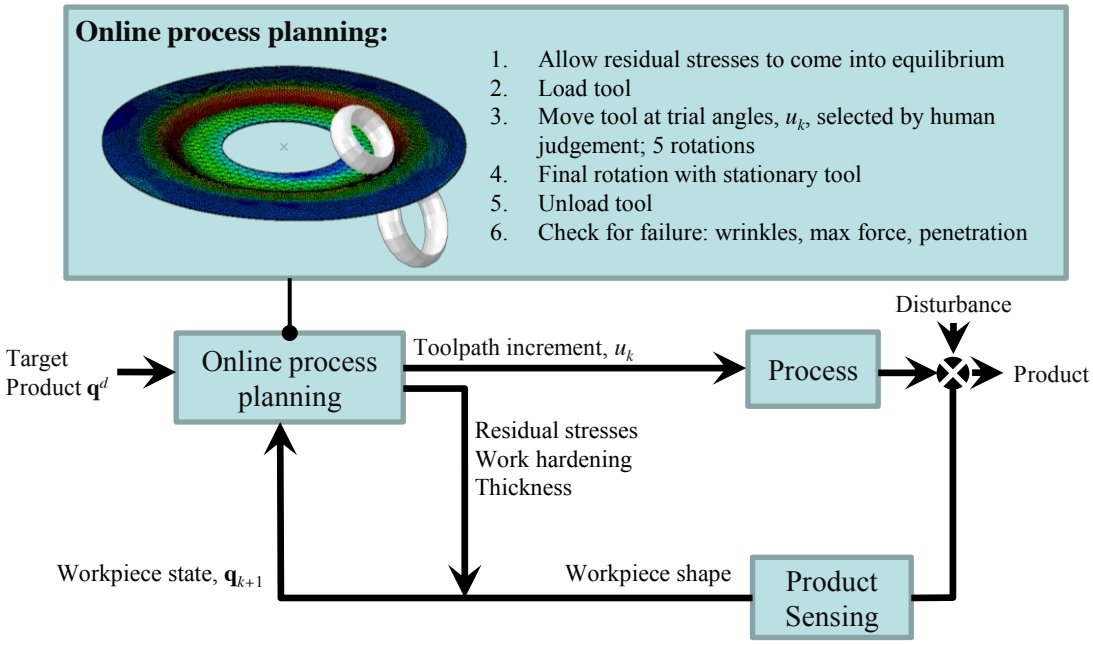

Figure 6-4 - A system diagram of the FE-in-the-loop control system

It was already shown in chapter 3 that the models were accurate for the first 10 rotations of the workpiece. To check that the closed-loop control prevents errors in the model from ballooning by correcting the geometry every 5 rotations, the same comparisons are performed as in chapter 3 but after 50-55 rotations (Nb: The final rotation in each increment is not included in the total rotation counts): between the predicted and experimentally measured forces and workpiece geometry. The forces are shown in Figure 6-5, the meridian shape after 55 rotations in Figure 6-6a, and the axial displacement around the outer circumference of the workpiece in Figure 6-6b.

Some small errors have built up in the force, but the error is still less than 10% on axial force – this is likely due to the very simple material model (The Hill-1948 criterion is one of the simplest ways of modelling anisotropy). There are also small absolute errors on the radial force, but as these forces are very close to zero, the relative force is misleadingly high. On the shape of the workpiece, the agreement is good, especially on the meridian, with some small qualitative disagreement on the circumferential shape. Overall, it is still comforting to see that, even after so many rotations of the workpiece, the error is still manageable.

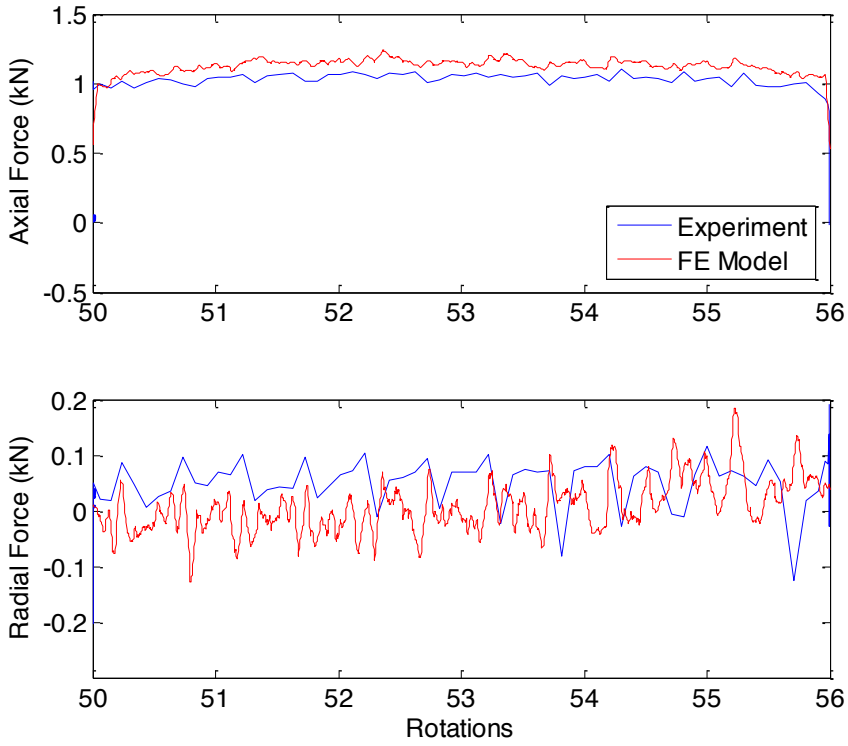

Figure 6-5 - Comparison of tool forces between experiment and FE model after 50-55 rotations of the workpiece, plus the final rotation with the tool stationary.

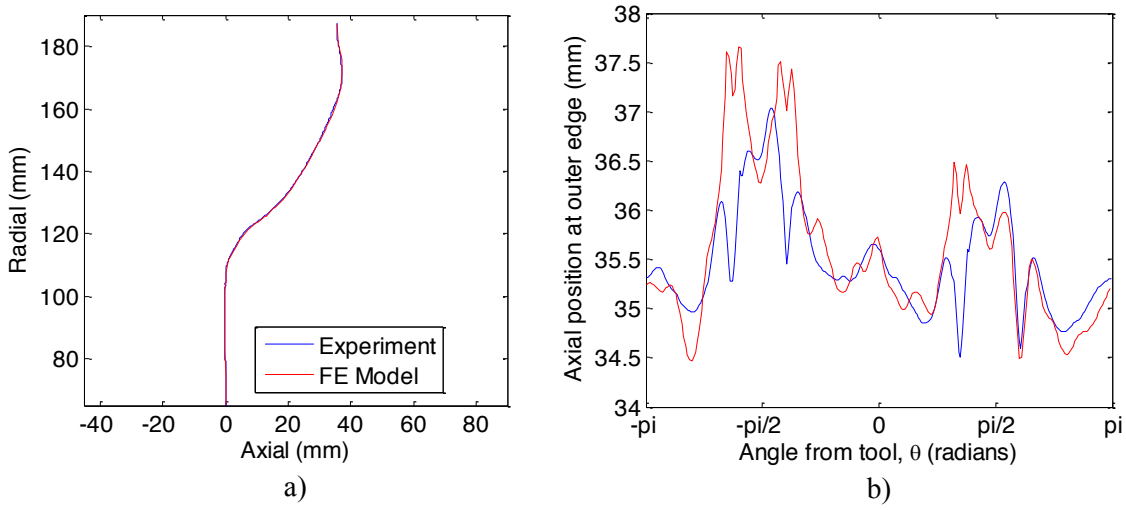

Figure 6-6 - Comparison of a) the meridian shape and b) the circumferential shape after 55 rotations of the workpiece

6.1.2 Evaluating the FE-in-the-loop control system

The toolpath generated by the FE-in-the-loop control system described in section 6.1.1 is plotted in Figure 6-7, compared with the trial and error toolpath. The toolpath designed by the FE-in-the-loop control system is much more aggressive than the trial and error toolpath. Despite the aggressiveness, wrinkling is successfully prevented, although the workpiece failed by tearing before the whole of the first toolpass was generated.

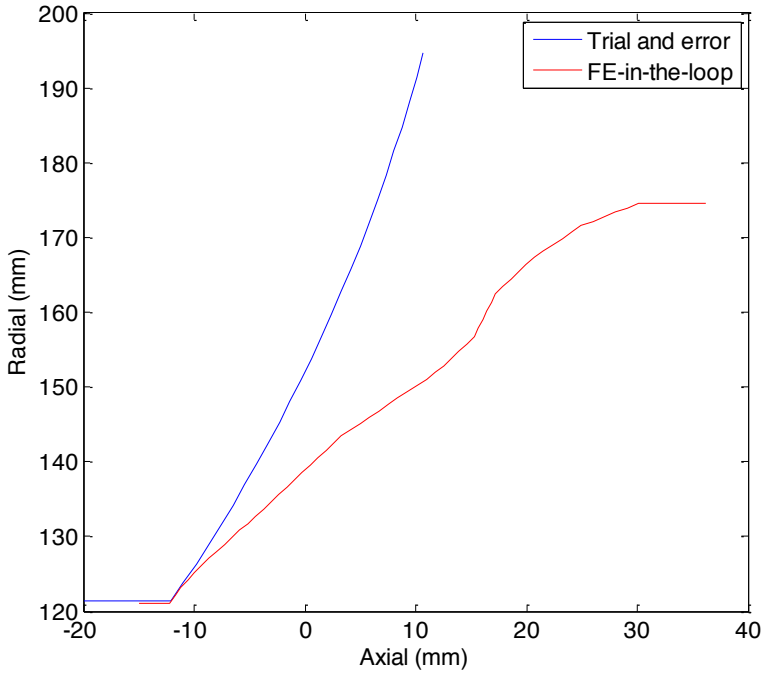

Figure 6-7 - The toolpath generated by the FE-in-the-loop control system, compared to a working trial and error toolpath

This suggests that, at least in the first pass in spinning the Aluminium cup, tearing limits the aggressiveness of the first toolpass. Certainly, it means that tearing must be included in a successful toolpath design strategy. Fortunately, on removing the workpiece from the machine and measuring the thickness after failure, it seems that FE model predicts thinning very well in all regions other than where the tear occurred, as shown in the plot of thickness along the workpiece meridians in Figure 6-8. The FE model does not predict tearing (this would require a ductile fracture criterion), but the tear occurs soon after the thickness drops below ~0.8mm. Even if the minimum thickness is not a suitable criterion for tearing, this is far more thinning than would be acceptable in industrial production. A thinning criterion should therefore be developed to prevent not just tearing, but an unacceptable degree of thinning.

6.1.3 Developing a thinning criterion

The difficulty in setting a thinning criterion is that thinning occurs progressively, unlike wrinkles which grow very quickly but can be controlled if detected early enough. Therefore, to ensure that the minimum allowable level of thickness is not exceeded, we would need to increase the control horizon to model the process to the end. This is not feasible as it would take months or years to run the FE model – we would much prefer to use a control horizon $K_p = 1$ which only takes 1 day to optimise.

However, an incremental thinning criterion then needs to be set – how much thinning can occur in the next time increment in order to ensure that the ultimate thinning criterion is not breached? Or equivalently: how much of the total allowable thinning can happen in the next toolpath increment?

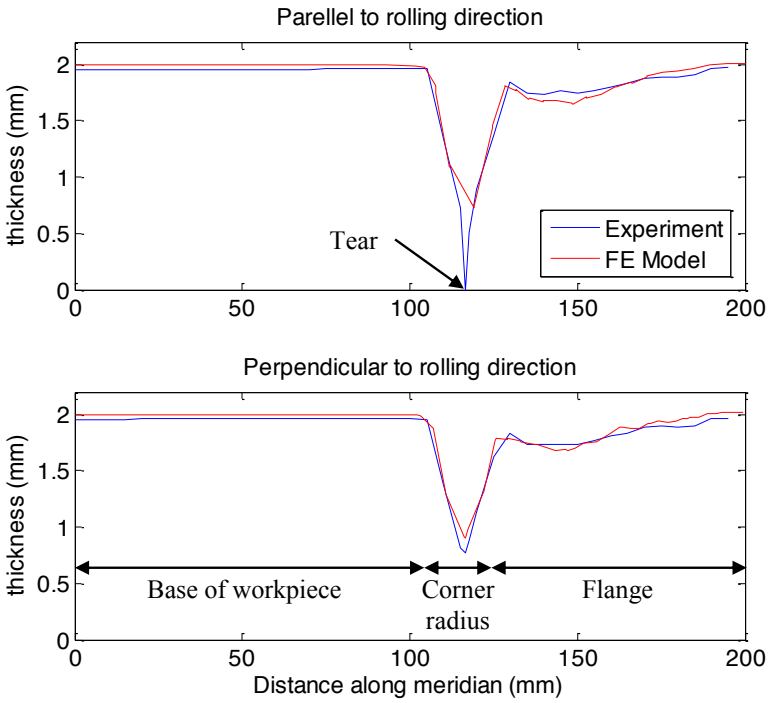

Figure 6-8 - Thickness along the workpiece meridians in the rolling direction and perpendicular

We chose to assume that thinning would happen at a constant rate with respect to workpiece rotations in developing the thinning criterion. This is backed up by the history of minimum thickness in the workpiece in the initial FE-in-the-loop experiments with no thinning criterion, shown in Figure 6-9 (Note that it was not possible to measure this experimentally online, so the history had to be taken from the FE models). This shows that thinning occurred at an approximately constant rate.

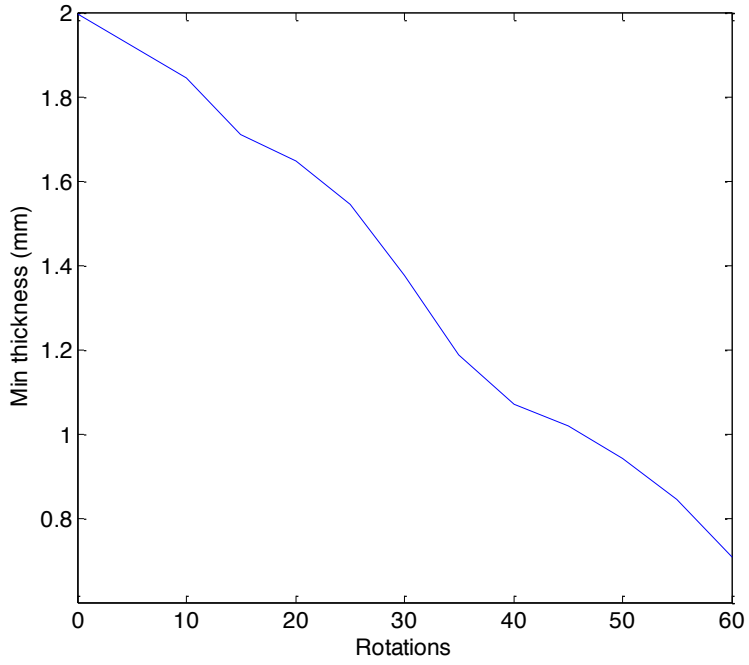

Figure 6-9 - The thickness history in the FE-in-the-loop experiment with no thinning criterion

The thinning criterion is demonstrated in Figure 6-10. The difficulty is that it is not known a-priori how many rotations the toolpass will require, as the length of the toolpass depends on the precise path that it takes. Therefore, an estimate is made based on the meridional distance from the tool to the edge of the workpiece, and this is updated in each toolpath increment. The allowable thinning per increment is also varied depending on the *actual* thinning that occurred (according to FE model) in the previous increments. This is demonstrated by the updated thinning trajectory shown in Figure 6-10.

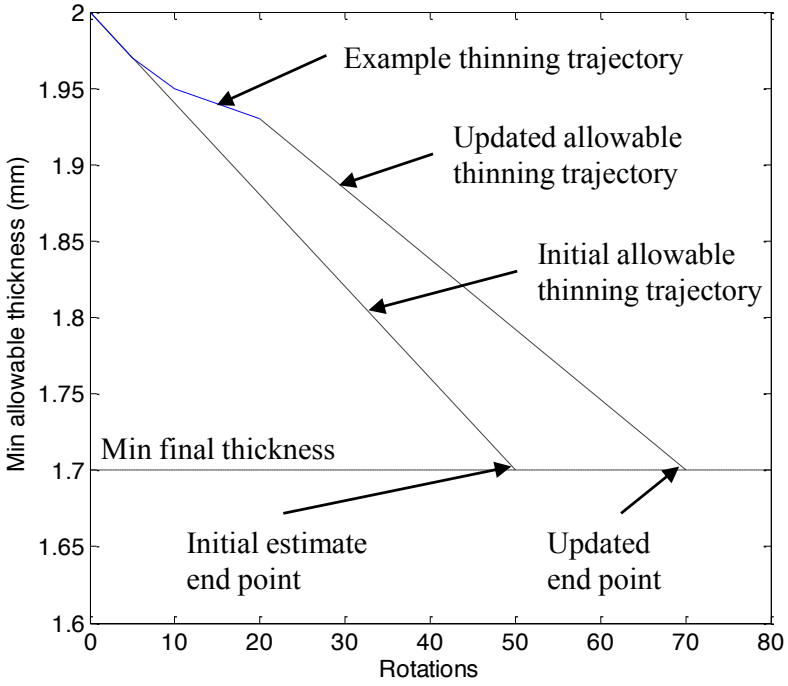

Figure 6-10 - Demonstration of the updating of the thinning criterion

The control system remains exactly the same as in section 6.1.1, but with the addition of this criterion – if the thickness drops below the allowable minimum thickness, the toolpath angle is judged to have failed.

6.1.4 Evaluation of FE-in-the-loop control with a thinning criterion

The toolpath generated by the FE-in-the-loop control system with the thinning criterion described in section 0 is plotted in Figure 6-11, compared with the trial and error toolpath. It is striking that the toolpath is much less aggressive than both the FE-in-the-loop with no thinning criterion and the trial and error toolpath. The difference is apparent right from the start of the toolpath – where the trial and error toolpath and the FE-in-the-loop toolpath with no thinning criterion both indent the workpiece all the way to the target product before moving radially outwards, the FE-in-the-loop toolpath with a thinning criterion moves radially outwards before hitting the target shape.

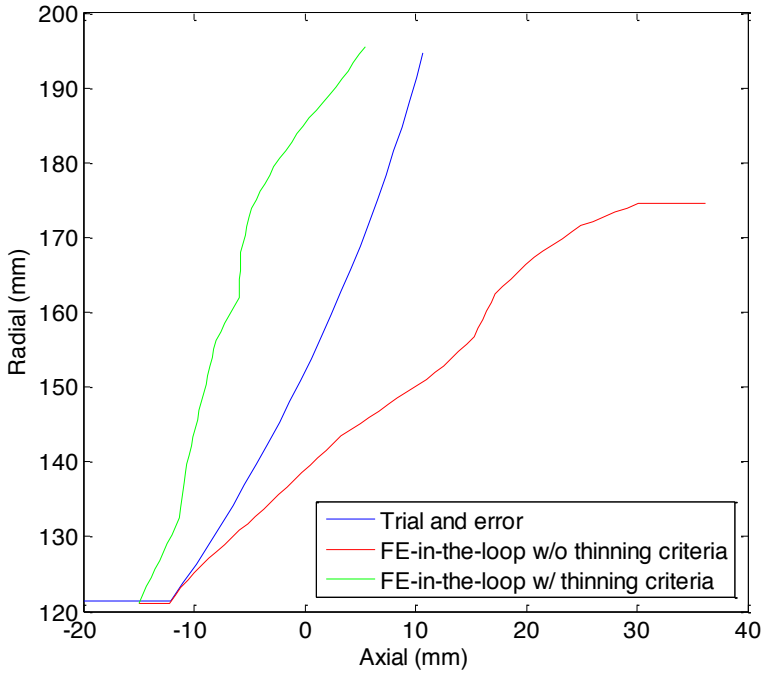

Figure 6-11 - The toolpath generated by the FE-in-the-loop control system with and without a thinning criterion, compared to a working trial and error toolpath

However, even though the addition of the thinning criterion resulted in a much less aggressive toolpath, the thinning criterion only limited the toolpath angle in the very first toolpath increment – the very first 10 rotations. The thickness history is plotted in Figure 6-12, showing that following the first 10 rotations, very little thinning occurs – the workpiece only thins by 3.3%, much less than the allowable 15%. Instead, it is wrinkling that limited the aggressiveness of the workpiece following the first 10 rotations.

The trial and error toolpath – which does not result in either wrinkling or excessive thinning – is proof that it is possible to use a more aggressive toolpath and still meet the ultimate wrinkling and thinning criteria. However, with the full FE-in-the-loop toolpath, the path diverges from the trial and error toolpath in the first toolpath increment because of the thinning criterion.

This result suggests that the tool should be more aggressive in the first increment of the toolpath. One explanation for this is that it "locks" the workpiece onto the mandrel – or in this case the blending roller – providing the stability that the workpiece needs in order to prevent wrinkling from occurring later in the workpiece. This is consistent with the first move of the skilled hand spinner – he would typically move the tool quite aggressively into the workpiece at the very base in order to lock the workpiece down onto the corner of the mandrel. This is both for the stability of the workpiece, and for safety (it reduces the chances of the workpiece slipping between the mandrel and tailstock). However, in order to allow this aggressive initial move, the thinning criterion would have to be relaxed in the first increment – with the current thinning criterion, the tool does not touch the target shape before moving radially outwards, as was seen in Figure 6-11.

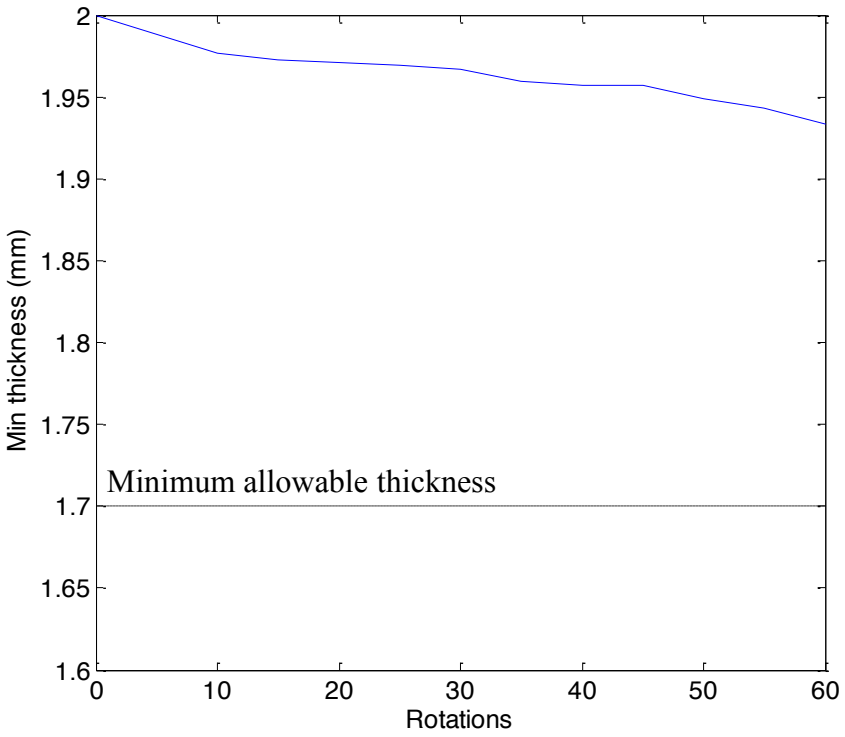

Figure 6-12 - The thickness history in the FE-in-the-loop experiment with a thinning criterion

If a finite horizon control system is to be used, the thinning trajectory is therefore critical to the success of the toolpath generator. A linearly decreasing thickness trajectory results in very conservative actions to start with, while wrinkling limits the aggressiveness later on and prevents much further thinning. A thickness trajectory which allows much more thinning earlier on, but then compensates by tightening the thinning criterion later on, would produce a more aggressive path which meets the ultimate criterion.

Nevertheless, despite the fact that there were alternative toolpaths which would have been successful, in both the FE-in-the-loop trials, the toolpaths generated led to a workpiece which did not wrinkle. This provides some evidence – although limited – that the finite horizon approach to toolpath generation can successfully generate toolpaths, as long as the thickness trajectory is set correctly. To the question posed at the start of this chapter, therefore, we tentatively conclude that a finite horizon approach can be used to reduce the computational load of the toolpath generation problem.

Still, the control system proposed in this section is too slow for commercial use. Indeed, that fact that each of the single toolpasses in this section took 2 weeks to generate, suggests that a research project to conclusively determine whether the finite horizon approach could be used would take decades – it would take over a year to fully design a single toolpath for a single product and a single material. A much faster model is needed in place of the FE model to make further research feasible, and indeed to make industrial application feasible. Therefore, in section 6.2, a fast, approximate model will be explored in place of the FE model used in this section.

6.2 Toolpath design using a fast, approximate model

The second approach to reducing the computation load of the toolpath generation problem was to use fast, approximate models in place of the constraint model. In the introduction to this chapter, it was noted that such an approximate model would still have to be conservative in order to prevent failure. However, in this section, we will begin to explore how approximate and conservative a model can be used and still generate a successful toolpath.

A review of chapter 2 showed that no models of either thinning or wrinkling existed that were fast enough to run online, yet contained enough detail to be useful in toolpath design. Therefore, in this section, a new approximate model will be developed and evaluated online to generate toolpaths. At this stage, the model will only consider wrinkling. Such a model will still have to be conservative in order to prevent wrinkling, and in being conservative it is hoped that other failure modes can be avoided. Still, fast models of thinning and tool forces should be the focus of future work in order to *guarantee* that these failure modes can be avoided when generating toolpaths.

The fast model of wrinkling is developed in two stages: In section 6.2.1, a stress-based for criterion for wrinkling will be developed. However, a fast model for predicting the stresses caused by a given control action will still be needed in order to calculate the limiting control actions. The development of such a fast model is the subject of section 6.2.2. This model will be used within a closed-loop control system to generate toolpaths online, and the design of this control system is the subject of section 6.2.3. Finally, this model and control system will be evaluated in section 6.2.4. The results highlight a problem not yet considered: foldback, and modifications to the control system to address this are discussed in section 6.2.5.

6.2.1 Identifying a stress-based criterion for wrinkling

The inspiration for the stress-based wrinkling criterion here is provided by a previous attempt at automatic toolpath generation by Music and Allwood (2011b). They investigated wrinkling and began to design a toolpath using FE models that consisted of two simple steps: In the first step, the tool indented the stationary workpiece. Then, in the second step, the workpiece rotated while the tool was held stationary. Recording the amount that the tool could indent the workpiece in the first step without wrinkling occurring in the second step generated a single point on the toolpath – a single control action, u_k. A toolpath was generated by repeating such a test with the tool at three points along the meridian. Examples early in the process and mid-stage are demonstrated in Figure 6-13.

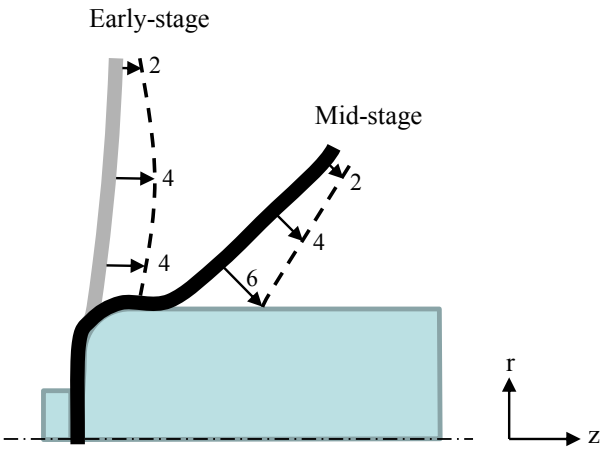

Figure 6-13 - The limiting tool indentations predicted by Music and Allwood (2011b) at an early and mid-stage of production

However, Music and Allwood's models still took 2-3 hours to run, and several models needed to be run with different tool indentations to determine the limiting indentation. These models are therefore too slow to run online. Most of this modelling time, however, was spent on the second step – rotating the workpiece. Therefore, if wrinkling could be predicted by looking at the stresses present at the end of the first step – simply indenting the tool into a stationary workpiece – then the limiting control action could be calculated much faster. In order to investigate this hypothesis the mechanics of this "indent-then-rotate" process will be examined using FE models and assessing the tool forces, plastic strains and stresses.

Music and Allwood themselves highlighted that the tool indentation varies throughout the process as the workpiece shape changes. In order to generate an accurate picture of the mechanics of the indent-then-rotate process, the FE models here were based on "real" workpiece shapes, by using the laser scanner to measure the evolving shape of the workpiece throughout the spinning of the cup using the toolpath in Figure 6-2. Six of these shapes, measured at different points throughout the production, were then imported into FE software Abaqus to produce a 2mm thick, axisymmetric workpiece. These shapes are plotted in Figure 6-14, along with the position of the tool.

The setup of the FE models here is different to that in chapter 3 and in section 6.1. This is simply due to the order in which the work was carried out: the FE work here was carried out before the material tests in chapter 3. It is still commercially pure Aluminium and is modeled as isotropic elastic-plastic material with Ludwik-Hollomon strain hardening law, but with the coefficients shown in equation 6.6, a Young's Modulus of 71GPa and an initial yield stress of 85MPa – approximate data given by the manufacturer. However, this should not invalidate the results, as the aim is to produce a wrinkling criterion which works for a wide range of different materials – and certainly across small changes in Aluminium alloy.

$$\sigma = 151\epsilon^{0.071} \qquad \textbf{6.6}$$

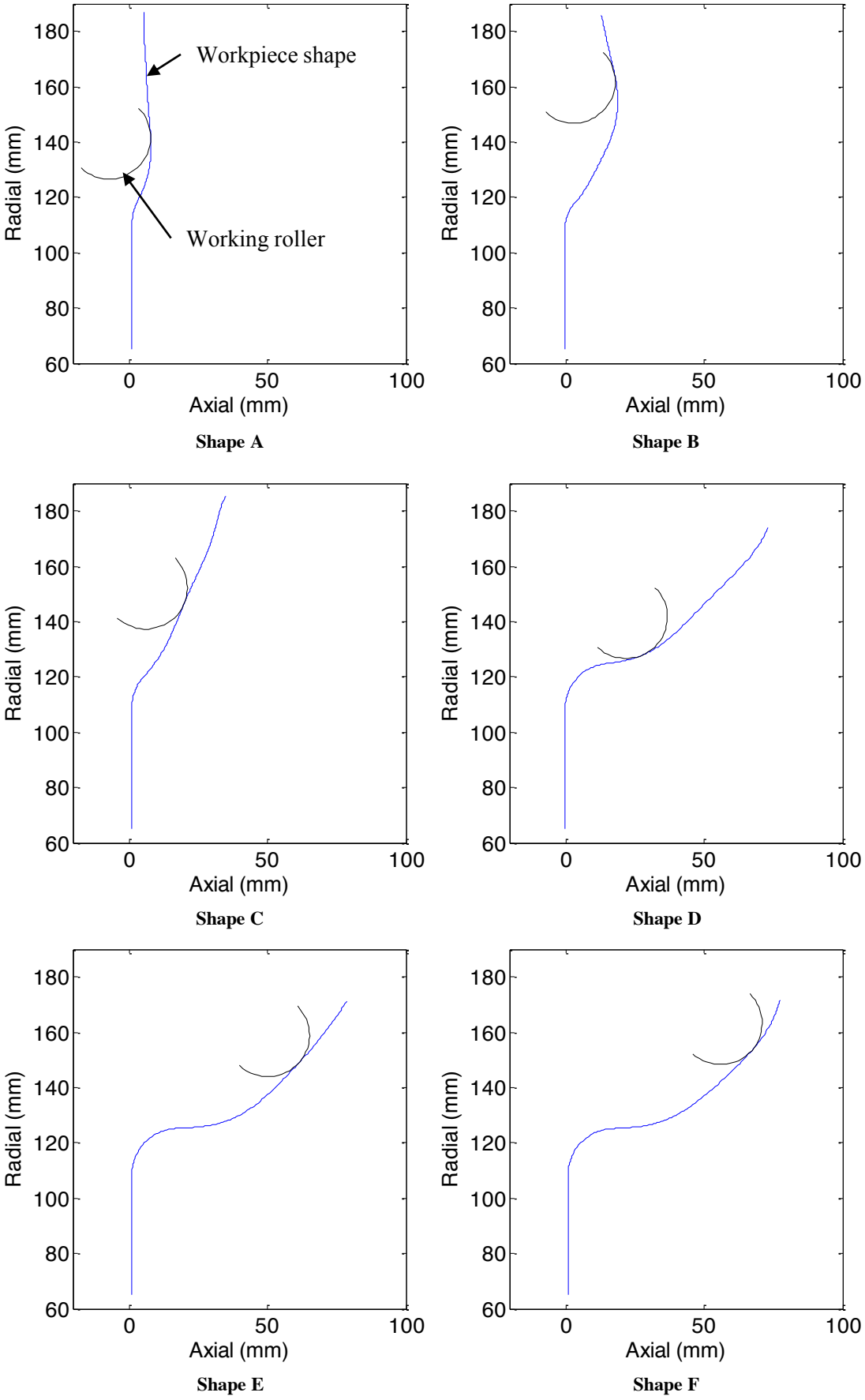

Figure 6-14 – The measured workpiece shapes and tool positions used to investigate the mechanics of spinning

With these FE models, the indent-then-rotate procedure is ran, and the tool forces and plastic strains examined, particularly at the indentation where wrinkling subsequently occurs in the rotation step.

The tool forces predicted by the FE model when indenting workpiece measured early in the process (shape C) and late in the process (shape E) are shown in Figure 6-15. The indentation at which wrinkling occurs is also highlighted. In these examples, the force peaks and then drops off at a tool indentation approximately 1-2mm smaller than that at which wrinkles become visible in the rotation step. This might be expected, as such a drop in force would normally be indicative of some kind of instability, as the instantaneous stiffness becomes negative. However, this drop off in force is not seen in all examples (it is not seen, for example, in indenting another shape early in the process (shape B), with the tool forces also shown in Figure 6-15), but some tapering off of stiffness is still seen before wrinkling occurs.

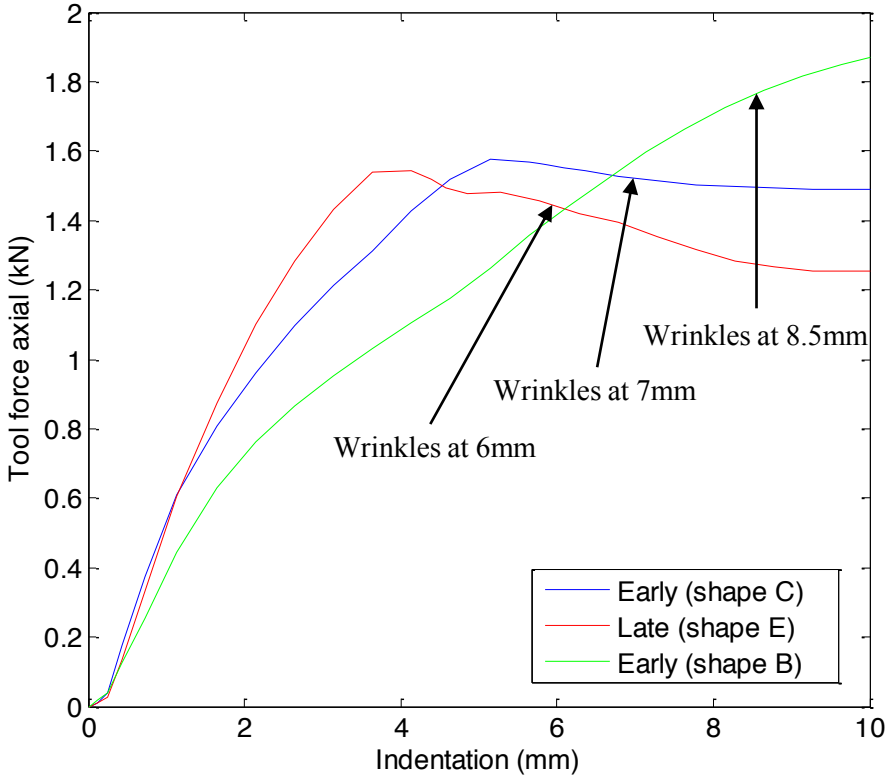

Figure 6-15 - The axial tool force when indenting the workpiece at different stages of the process

To investigate this drop off in force or stiffness further, the distribution of plastic strain as the tool indents the workpiece was assessed. For shape C, the force peak occurs at a tool indentation of approximately 5mm, and wrinkling occurs at 7mm. The plastic strain distribution on the inside of the workpiece as the tool gradually indents the workpiece from 4mm to 7mm is therefore shown in Figure 6-16.

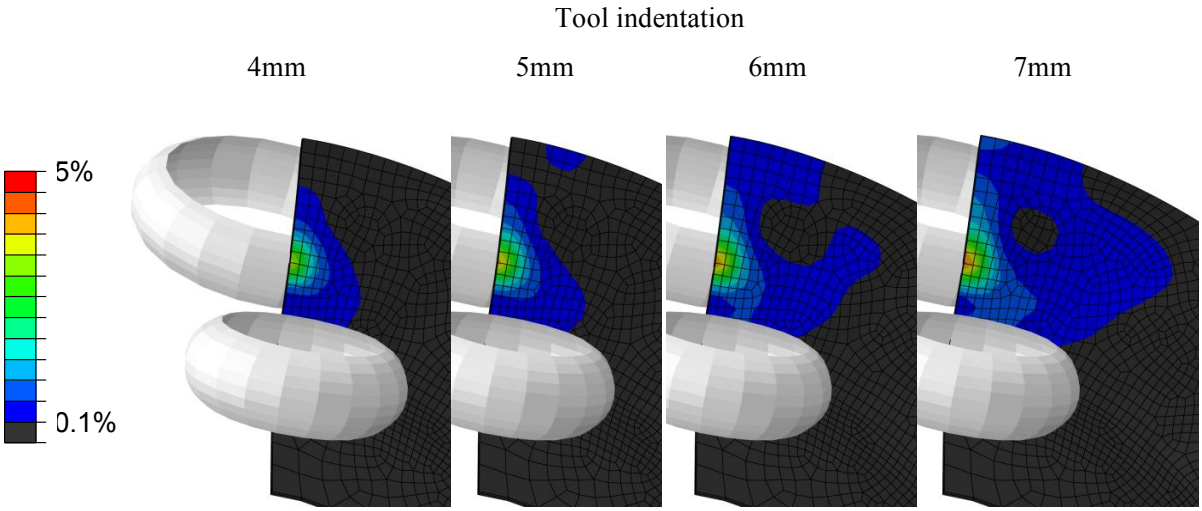

Figure 6-16 - The plastic strain distribution as the tool indents the workpiece defined by shape C

The plastic strain is seen to be local to working and blending rollers, and gradually extends towards the edge of the workpiece as the tool indentation increases. In this case, the drop in force or stiffness coincides with the plastic strain reaching the edge of the workpiece – this was consistent across all of the shapes in Figure 6-14. This plastic strain at the edge of the workpiece allowed a plastic hinge to form, which would explain the sudden drop in stiffness, but also allows a mechanism by which a plastic wrinkle can develop as the change in shape at the edge of the workpiece becomes dominated by bending rather than compression and shrinkage of the diameter.

This observation provides a way of predicting whether wrinkling will therefore happen in the rotation, just be looking at whether the stresses at the edge of the workpiece yield in the indent step. This is consistent with the conclusions of Music and Allwood (2011b) who noted that wrinkling was due to a combination of plastic hinge formation as well as compressive stress; and the observation has been more recently confirmed by work independently carried out by Watson and Long (2014), who modelled the conventional spinning process more dynamically and identified that the onset of wrinkles coincided with yield at the edge of the workpiece.

In order to test that this criterion is conservative – as is necessary for an approximate form of the constraint model – the criterion is tested using the FE models generated from the measured shapes in Figure 6-14. Figure 6-17 plots the tool indentation at which this approximate criterion is met against the indentation at which wrinkling is first observed in the rotation step. The results don not show a perfect agreement – far from it – but they do show enough of a correlation to suggest that this criterion could be calibrated and further developed in order to create a fast and approximate, yet still conservative, model for the generation of toolpaths online.

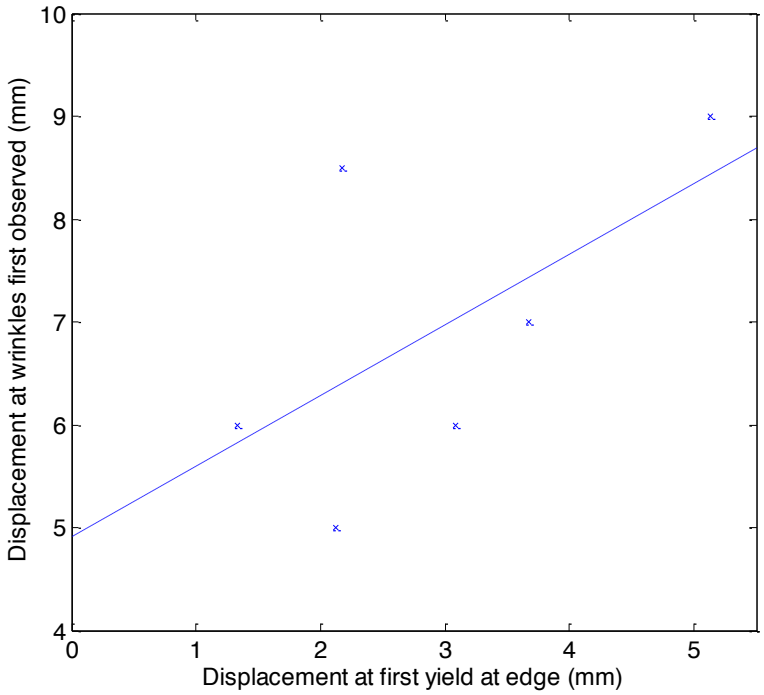

Figure 6-17 - The predicted displacement with the approximate criterion against the actual displacement at which wrinkles are first observed, showing the straight line of best fit.

6.2.2 Developing a fast model to predict stresses

Although we have now found a possible way of predicting whether wrinkling will occur in the "rotate" step of Music and Allwood's (2011b) indent-then-rotate models based on the stresses at the end of the "indent" step, the indent step still takes ~1 minute to run in an FE model. This is still too slow to run online: in 1 minute, the working roller on the existing spinning machine would typically move ~200mm – more than the entire radius of the 250mm diameter cup produced with the example toolpath in Figure 6-2. In this section, the aim is to find the fastest possible model to determine the maximum tool indentation based on the criterion developed in section 6.2.1.

There are two reasons why the elastic-plastic FE model was so slow: Firstly, because the model is non-linear. Therefore, in section 6.2.2.1, the possibility of using a linear FE model by making series of approximations is explored, and then the predicted tool indentations are compared with the non-linear model to ensure that this is still conservative.

Secondly, the use of Abaqus as a solver within a LabVIEW control system introduces a large amount of overheads in opening Abaqus, creating the model, and extracting and processing the results. MATLAB offers a neat solution, firstly because it can be connected directly to LabVIEW, reducing overheads (as described in chapter 3); and secondly, because, through the MATLAB ODE solvers it offers the opportunity to use a bespoke model which performs the same analysis as Abaqus but more efficiently. The derivation of the ODEs for the bespoke model is presented in section 6.2.2.2. In section 6.2.2.3 a number of optimisations are discussed in order to further speed up the solver. Finally,

the model results are compared to the linear FE model in section 6.2.2.4 in order to check that the bespoke model is still reliable, but is also faster.

The result of this section will therefore be a fast model which can be used to replace, the very slow but accurate model used in the FE-in-the-loop control system of section 6.1 – with some modification to the control system, as will be described later in section 6.2.3.

6.2.2.1 Creating a linear FE model

The non-linear FE model is slow because solver must gradually increment the tool displacement whilst updating the strains and stresses so that they are in equilibrium. If the model was linear, the FE solver would only need to run the equilibrium analysis once, and could use the results to extrapolate to the tool displacement that caused plastic yield at the edge of the workpiece. Here, the approximations required in order to make a linear FE model are presented, and then the limiting tool indentations predicted by the linear FE model are compared to those predicted by the non-linear FE model in order to check the validity (or more specifically, the conservativeness) of such approximations.

There are three sources of non-linearity in the non-linear FE of section 6.2.1: plasticity, large displacements and contact. In order to produce a linear model, the following approximations are therefore made in the linear FE model to remove these non-linearities:

- The material is modelled as linear-elastic material with a Young's modulus equal to 70,000MPa. Because plasticity tends to reduce the stiffness of a part, this approximation would tend to make the workpiece stiffer, reducing the tool indentations, making it more conservative.
- The model assumes that displacements are small. Because large displacements tend to stiffen the workpiece, this approximation would make the model less conservative. However, both the very conservative approximations made until now should allow this approximation to be made without resulting in too aggressive tool indentations.
- The working roller is approximated as applied a point-load directly to the workpiece.
- The blending roller is approximated as applying a no-normal-displacement boundary condition around a circle concentric with the workpiece. (The reason it is applied around a circle, rather than just at a point, is to simplify the Fourier-style solution, which is described later).

None of these approximations would be justified if we were aiming to produce an accurate solution. It would be extremely difficult to justify using an elastic model to model a plastic metal forming process, and small displacement approximations typically start to deviate as the displacement becomes comparable with the thickness of the sheet. However, once again, we do not seek an accurate solution

– merely an approximate but conservative model that could be calibrated to generate toolpath commands which do not result in wrinkling.

To check that the results with these approximations still generate indentations that correlate with those given by the more accurate, plastic, large-displacements model, the two models are used to generate indentations from all of the measured shapes when producing a part with the toolpath in Figure 6-2. The indentations generated are plotted in Figure 6-18, showing that the two models correlate well, although (as hoped) the linear model *generally* gives more conservative results. There are some exceptions – large spikes in the predicted displacement. This was found to be caused by some special shapes where there is very little stress at the edge of the workpiece due to the indentation of the tool in the linear elastic FE model, when this is not seen in the more non-linear FE model.

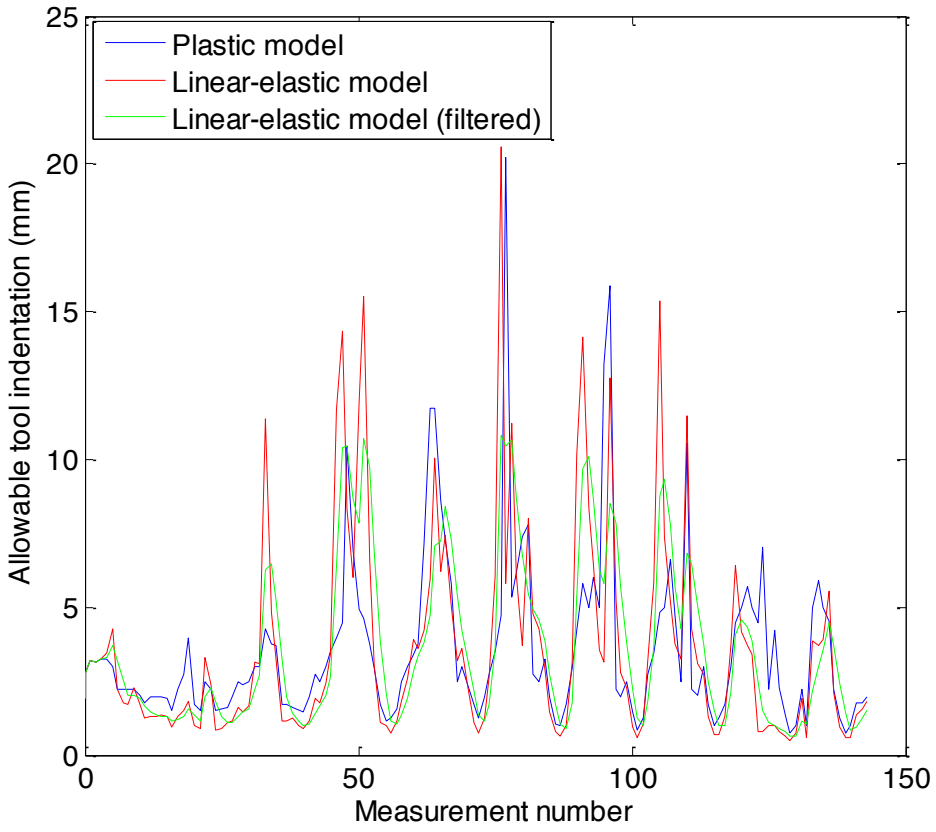

Figure 6-18 - Indentations generated by the plastic, large-displacement model and the elastic, small-displacement model with simplified boundary conditions. The filtered indentations are also plotted.

To ensure that the linear model always generates conservative indentations, and not just on average, the indentations are filtered. This will also help to smooth the toolpath generated, and prevent large swings in tool motion commands. A Gaussian filter which filters over the previous five indentations is applied to smooth the results, and the filtered indentations are also plotted in Figure 6-18, showing that this produces a smooth and conservative set of indentations when compared with the slower but more accurate plastic large-displacement model. However, the linear-elastic model is faster, taking only ~40 seconds to run, compared to typically over 1 minute with the plastic model – this is an

improvement, but only a modest one because the majority of this time (~25 seconds) is spent on the overheads of opening Abaqus, and running the model pre-processor. It is is still too slow for online use. In the remaining subsections of 6.2.2, we will therefore explore how to improve the speed of this model through a different *implementation* of such a linear-elastic model.

6.2.2.2 Deriving the differential equations for a fast, bespoke model

In order to improve the speed of the linear model for calculating the limiting tool indentation, a bespoke model will be designed and implemented in MATLAB. In this section, the focus is on the design: can we create a simplified set of differential equations to make a bespoke model, specific to the case at hand: the indentation of an (approximately) axisymmetric shell? By simplifying the differential equations, the number of degrees of freedom in the problem can be reduced compared to the FE models of section 6.2.2.1, and the solution should therefore be much faster. The derivation of such a set of differential equations is presented here, and the implementation of a fast solver will be discussed in the subsequent section 6.2.2.3.

The differential equations are derived starting with a set of partial differential equations (PDEs) from Flugge (1973), describing an element of a shell forming a surface of revolution (i.e. an axisymmetric shell, but not necessarily axisymmetric loading). The element is shown in Figure 6-19 and the equilibrium equations given by Flugge are:

$$\frac{\partial}{\partial s}(rN_s) + \frac{\partial N_{\theta s}}{\partial \theta} - N_\theta \cos\phi - k_1 r Q_s = -r p_s \tag{6.7}$$

$$\frac{\partial}{\partial s}(rN_{s\theta}) + \frac{\partial N_\theta}{\partial \theta} + N_{\theta s} \cos\phi - Q_\theta \sin\phi = -r p_\theta \tag{6.8}$$

$$N_\theta \sin\phi + k_1 r N_s + \frac{\partial Q_\theta}{\partial \theta} + \frac{\partial}{\partial s}(rQ_s) = r p_r \tag{6.9}$$

$$\frac{\partial}{\partial s}(rM_s) + \frac{\partial M_{\theta s}}{\partial \theta} - M_\theta \cos\phi = rQ_s \tag{6.10}$$

$$\frac{\partial}{\partial s}(rM_{s\theta}) + \frac{\partial M_\theta}{\partial \theta} + M_{\theta s} \cos\phi = rQ_\theta \tag{6.11}$$

$$N_s = D\left[\frac{\partial v}{\partial s} + k_1 w + \nu\frac{\frac{\partial u}{\partial \theta} + v\cos\phi + w\sin\phi}{r}\right]$$

$$N_\theta = D\left[\frac{\frac{\partial u}{\partial \theta} + v\cos\phi + w\sin\phi}{r} + \nu\left(\frac{\partial v}{\partial s} + k_1 w\right)\right]$$

$$N_{s\theta} = N_{\theta s} = D\frac{1-v}{2}\left[\frac{\partial u}{\partial s} + \frac{\frac{\partial v}{\partial \theta} - u\cos\phi}{r}\right]$$

$$M_s = K\left[\frac{\partial^2 w}{\partial s^2} + \frac{\nu}{r}\left(\frac{1}{r}\frac{\partial^2 w}{\partial \theta^2} + \frac{\partial w}{\partial s}\cos\phi\right)\right]$$

$$M_\theta = K\left[\frac{1}{r}\left(\frac{1}{r}\frac{\partial^2 w}{\partial \theta^2} + \frac{\partial w}{\partial s}\cos\phi\right) + \nu\frac{\partial^2 w}{\partial s^2}\right]$$

$$M_{s\theta} = M_{\theta s} = K(1-\nu)\left[\frac{1}{r}\frac{\partial^2 w}{\partial s \partial \theta} - \frac{1}{r^2}\frac{\partial w}{\partial \theta}\cos\phi\right]$$

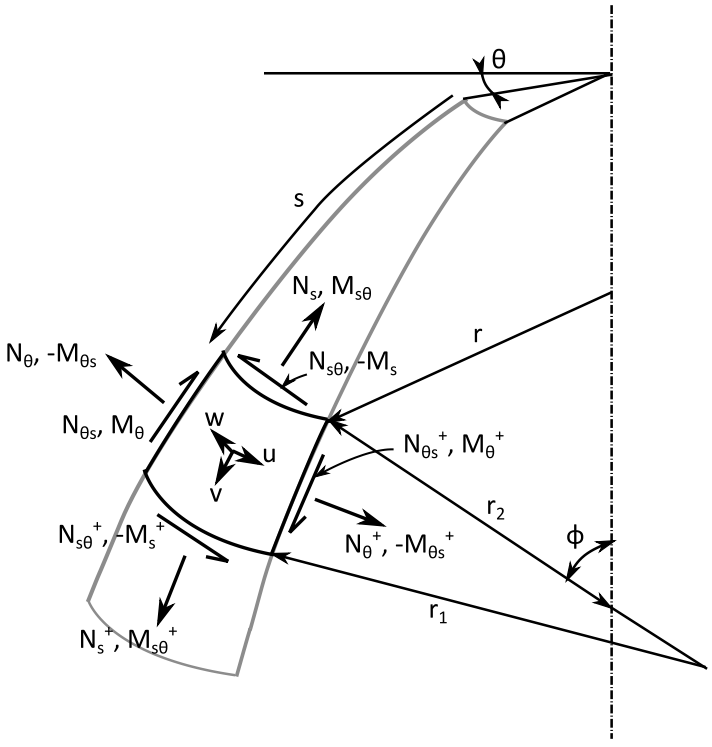

Figure 6-19- An element from a shell of revolution.

And the elastic laws:

$$N_s = D\left[\frac{\partial v}{\partial s} + k_1 w + \nu\frac{\frac{\partial u}{\partial \theta} + v\cos\phi + w\sin\phi}{r}\right] \quad \textbf{6.12}$$

$$N_\theta = D\left[\frac{\frac{\partial u}{\partial \theta} + v\cos\phi + w\sin\phi}{r} + \nu\left(\frac{\partial v}{\partial s} + k_1 w\right)\right] \quad \textbf{6.13}$$

$$N_{s\theta} = N_{\theta s} = D\frac{1-\nu}{2}\left[\frac{\partial u}{\partial s} + \frac{\frac{\partial v}{\partial \theta} - u\cos\phi}{r}\right] \quad \textbf{6.14}$$

$$M_s = K\left[\frac{\partial^2 w}{\partial s^2} + \frac{\nu}{r}\left(\frac{1}{r}\frac{\partial^2 w}{\partial \theta^2} + \frac{\partial w}{\partial s}\cos\phi\right)\right] \quad \textbf{6.15}$$

$$M_\theta = K\left[\frac{1}{r}\left(\frac{1}{r}\frac{\partial^2 w}{\partial \theta^2} + \frac{\partial w}{\partial s}\cos\phi\right) + \nu\frac{\partial^2 w}{\partial s^2}\right] \quad \textbf{6.16}$$

$$M_{s\theta} = M_{\theta s} = K(1-\nu)\left[\frac{1}{r}\frac{\partial^2 w}{\partial s \partial \theta} - \frac{1}{r^2}\frac{\partial w}{\partial \theta}\cos\phi\right] \quad \textbf{6.17}$$

where N are line normal forces, M are line moments and Q are line shear forces with directions defined by the subscripts according to the right hand rule. p are applied pressures. u, v and w are displacements in the in-plane circumferential, in-plane meridional and out-out-plane directions. $k_1 = \frac{1}{r_1}$ is the curvature in the meridional direction, and is used in preference to r_1 because r_1 goes to infinity in straight regions, causing problems with the solver. D is the normal stiffness defined as $\frac{Et}{1-\nu^2}$ where E is the Young's modulus, t is the material thickness and ν is the poisons ratio. K is the bending stiffness defined as $\frac{Et^3}{12(1-\nu^2)}$.

Within these equations, there are only three independent unknowns, so all of these equations can be reduced to just three. This was performed by substituting equations to into 6.10 and 6.11; then equations 6.10 and 6.11 were substituted into equations 6.7 to 6.9 to give just three equations with three unknowns: u, v and w. However, these are still both functions of both the meridional distance, s, and the angle, θ. To simplify these PDEs into ordinary differential equations (ODEs), a Fourier type approach is taken. As the tool indents the workpiece at $\theta = 0$, the workpiece is symmetric about this plane. u, v and w therefore take the form:

$$u = \sum_{n=0}^{\infty} u_n(s) \sin n\theta \tag{6.18}$$

$$v = \sum_{n=0}^{\infty} v_n(s) \cos n\theta \tag{6.19}$$

$$w = \sum_{n=0}^{\infty} w_n(s) \cos n\theta \tag{6.20}$$

Ultimately, this leads to three ODEs which can be solved for each value of n. The complete solution will be dominated by low-frequency terms, so that it is expected that the solution will converge with increasing, n, at which point the solver terminates.

$$\begin{aligned}
&\frac{u_n Dn}{r}\left(-\frac{3}{2}\cos\phi + \frac{\nu}{2}\cos\phi\right) + \frac{du_n}{ds} D \frac{n}{2}(1+\nu) \\
&\quad + v_n D\left(\frac{1}{2}\frac{n^2}{r}(\nu - 1) - \frac{1}{r}\cos^2\phi - k_1 \nu \sin\phi\right) + \frac{\partial v_n}{\partial s} D \cos\phi \\
&\quad + w_n\left[D\left(k_1\cos\phi - \frac{1}{r}\sin\phi\cos\phi + r\frac{dk_1}{ds}\right) - K\frac{2n^2 k_1}{r^2}\cos\phi\right] \\
&\quad + \frac{\partial w_n}{\partial s}\left[D(rk_1 + \nu\sin\phi) + Kk_1\left(\frac{n^2}{r} + \frac{1}{r}\cos^2\phi + \nu k_1 \sin\phi\right)\right] \\
&\quad - \frac{\partial^2 w_n}{\partial s^2} K k_1 \cos\phi - \frac{\partial^3 w_n}{\partial s^3} K r k_1 = -\frac{\partial^2 v_n}{\partial s^2} Dr
\end{aligned} \tag{6.21}$$

$$\begin{aligned}
&\frac{u_n D}{2}(rk_1 \sin\phi\,(1-\nu) - \cos^2\phi\,(1-\nu) - 2n^2) + \frac{\partial u_n}{\partial s}\frac{D}{2} r\cos\phi\,(1-\nu) \\
&\quad + v_n D \frac{n}{2}\cos\phi\,(\nu - 3) - \frac{\partial v_n}{\partial s}\frac{Dn}{2} r(1+\nu) \\
&\quad + w_n n\left[-D(\sin\phi + \nu r k_1) + K\sin\phi\left(\frac{k_1}{r}\sin\phi\,(1-\nu) - \frac{n^2}{r^2}\right)\right] \\
&\quad + \frac{\partial w_n}{\partial s}\frac{Kn}{r}\cos\phi\sin\phi + \frac{\partial^2 w_n}{\partial s^2} Kn\sin\phi = -\frac{\partial^2 u_n}{\partial s^2}\frac{Dr^2}{2}(1-\nu)
\end{aligned} \tag{6.22}$$

$$u_n Dn(\sin\phi + vrk_1) + v_n D(\sin\phi + vrk_1)\cos\phi + \frac{\partial v_n}{\partial s} Dr(rk_1 + v\sin\phi)$$
$$+ w_n \left[D(\sin^2\phi + r^2 k_1^2 + 2vrk_1 \sin\phi) \right.$$
$$\left. + \frac{Kn^2}{r}\left(\frac{n^2}{r} + k_1(v-3)\sin\phi - \frac{4}{r}\cos^2\phi\right)\right]$$
$$+ \frac{dw_n}{ds} K \left[\frac{2n^2}{r}\cos\phi + \frac{1}{r}\cos^3\phi + 2k_1 \sin\phi\cos\phi \right. \quad \textbf{6.23}$$
$$\left. - vr\left(\frac{dk_1}{ds}\sin\phi + k_1^2\cos\phi\right)\right]$$
$$- \frac{d^2 w_n}{ds^2} K(2n^2 + rk_1\sin\phi\,(1+v) + \cos^2\phi) + \frac{\partial^3 w_n}{\partial s^3} 2Kr\cos\phi$$
$$= -\frac{\partial^4 w_n}{\partial s^4} Kr^2$$

These equations are second order in u_n and v_n, and fourth order in w_n, so there should in total be eight boundary conditions in each region over which the ODEs are solved. There will be boundary conditions (BCs) applied at the spindle, at the blending roller, at the working roller, and at the free edge. In addition, there will be a discontinuity in the curvature, k_1, in the transition from the flat base to the curved region of the workpiece around the blending roller. This causes a spike in $\frac{dk_1}{ds}$, which appears in equations 6.21 and 6.23, and initially caused problems with the solver. A further split was added at this discontinuity, resulting in a total of four regions and 32 boundary conditions. These BCs will be:

- Built in at the spindle, $s = 0$: Four BCs
- Compatibility base-blend at split: Four BCs
- Equilibrium of $N_s, N_{s\theta}$, M_s and Q_s at split: Four BCs
- No out-of-plane displacement around the circle on which the blending roller sits. This is an approximation to the effect of the blending roller because a point support cannot easily be applied in this type of analysis: One BC
- Compatibility at blending roller: Four BCs
- Equilibrium of $N_s, N_{s\theta}$ and M_s at blending roller: Three BCs
- Compatibility at application of tool force: Four BCs
- Equilibrium of $N_s, N_{s\theta}$, M_s and Q_s at application of tool force: Four BCs
- Equilibrium at free edge: Four BCs

These BCs are written in mathematic form in appendix A. The result is a series of equations that can be solved using MATLAB's ODE solvers.

6.2.2.3 Implementing the fast, bespoke model with the MATLAB solvers

The ODEs derived in 6.2.2.2 cannot be solved analytically, especially when the geometry is measured discretely, rather than analytically. Fortunately, MATLAB has some fast numerical tools for solving ODEs, and the implementation of these tools to solve the ODEs quickly is the subject of this section.

Because there are boundary conditions applied on each side of four different regions, MATLABs boundary value problem solver *bvp4c* is used, rather than the simple ODE solvers which are designed for a set of initial conditions – boundary conditions just applied at one end of a single region. However, in using the *bvp4c* solver, a number of options exist to take advantage of MATLAB's optimisation for vector or matrix calculations. In addition, the code can be edited to allow further optimisation. Five of the optimisations are highlighted within a simplified schematic of how the *bvp4c* solver works in Figure 6-20.

Firstly, if a good initial solution can be found, this will reduce the number of iterations the *bvp4c* will take to find a final solution. Given that the solution does not change wildly as the frequency increases gradually, the solution from the previous value of n was used as the initial solution for $n + 1$.

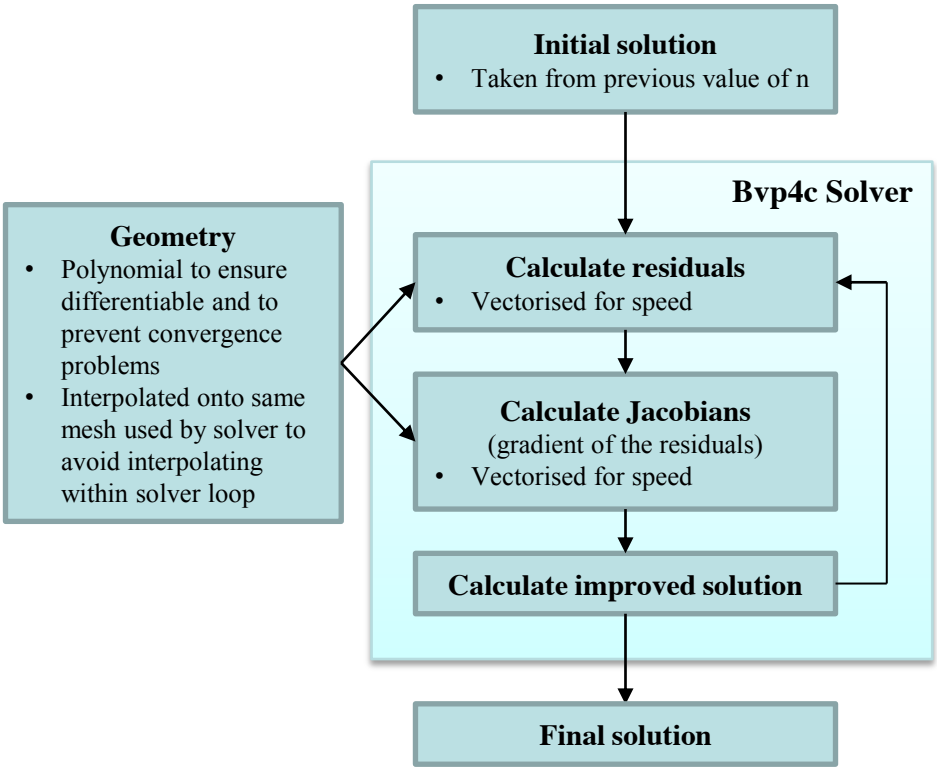

Figure 6-20 - A simplified schematic of the bvp4c solver, highlighting where improvements are made to increase speed

Secondly, the *bvp4c* solver has the option to use vectorised equations for the ODEs and BCs. This allows the residuals to be calculated for any number of points with one call to the ODE/BC functions.

Given MATLABs optimisation for vector/matrix calculations, this was one of the first optimisations applied.

However, the *bvp4c* solver does *not* have the option to vectorise the calculation of the Jacobian. Instead, it calls the Jacobian function once for each point that it wants the Jacobian for. To change this, the original code for *bcp4c* was copied and edited into a new function *bvp4cJVec*, which supports a vectorised Jacobian.

The geometry of the workpiece appears in all of the ODEs and BCs. Every time *bvp4c* calls the ODE or BC functions for a series of mesh points, the geometry of the workpiece must be known at the mesh points. If the mesh points did not coincide with the points at which the geometry was defined at, an interpolation would be required within the *bvp4c* loop, which would be slow. To avoid this, the interpolation was carried out with prior knowledge of the mesh before the *bvp4c* solver was called. If remeshing is required, the interpolation is carried out again at the same time that the remeshing is performed, rather than every time the ODEs/BCs are called.

Any noise on the geometry can also cause problems with the solver, especially as the ODEs refer to differentials of the geometry (the laser measures *r*-*z* coordinates, ϕ is the first derivative, k_1 is the second derivative, $\frac{dk_1}{ds}$ which also appears is the third derivative). Any high frequency noise is amplified during differentiation and can cause convergence problems within the solver. In order to prevent this noise building up, a polynomial was fitted to segments of the *r*-*z* laser measurement. The polynomial guaranteed smooth differentiation and prevented convergence problems due to noise.

With all of these optimisations, as well as some smaller ones, the model typically took 1 second to perform 22 iterations of n on a 2.66GHz dual-core Intel Core 2 Duo processor. This was usually enough iterations of n to cause convergence, although sometimes more were needed where the deformation was particularly "narrow" resulting in large higher frequency terms, in which case up to 70 iterations might be needed, taking ~3seconds.

6.2.2.4 Evaluation of the bespoke model vs. the linear FE model

To check that the MATLAB model worked correctly, given the possibility of error introduced throughout the derivation of the ODEs, the BCs and the implementation of this in MATLAB, the results were compared with the linear FE models making the same approximations (linear elastic, small displacements etc.) and using the same boundary conditions, as described in section 6.2.2.1.

These checks were performed on all six shapes shown in Figure 6-14. For brevity, however, only the results for a shape in the early stage (shape C) and late stage (shape E) are shown here.

For shape C, a contour plot of stresses predicted by the MATLAB model is shown in Figure 6-21, and the equivalent plot according to the FE models is shown in Figure 6-22. This shows good qualitative

agreement, but it is difficult to assess the quantitative agreement from these plots. Therefore, the out-of-plane displacements along the meridian for three different Fourier components are shown in Figure 6-23, showing excellent agreement across most of the shape. Some small errors do build up in regions of large curvature, and this is because the MATLAB model assumes that the curvature is much greater than the thickness – in reality, around the blending roller and working roller, where the radius of curvature is 15mm (compared to a thickness of 2mm), this is borderline. But the error is, nevertheless, very much acceptable given the approximations made and discussed in section 6.2.2.1.

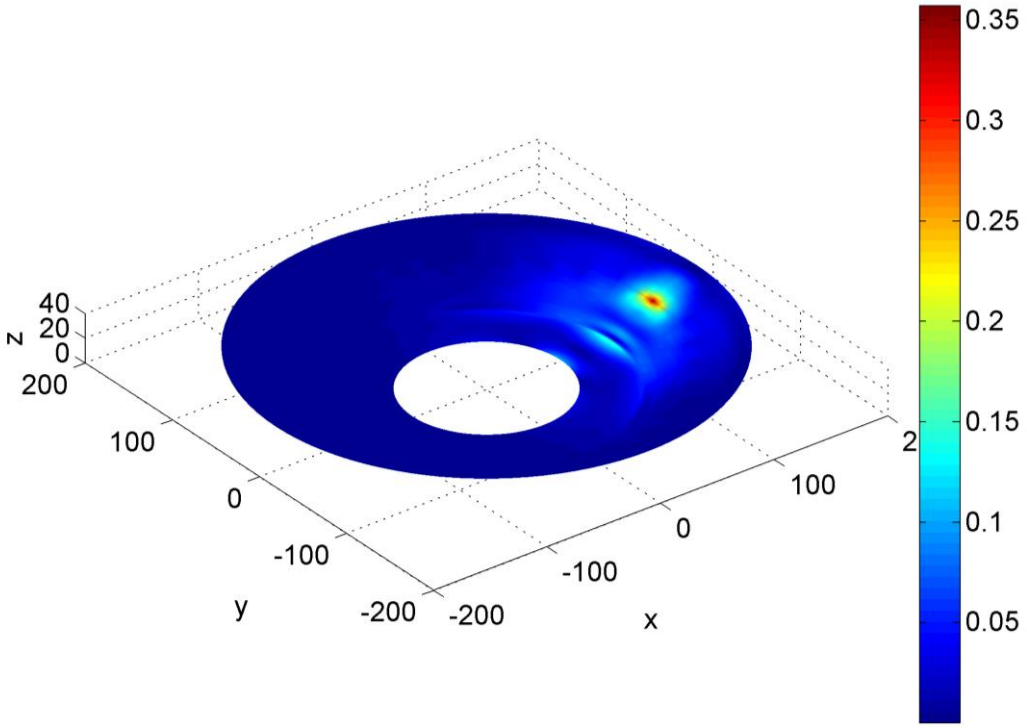

Figure 6-21 - Stresses in shape C according to MATLAB model

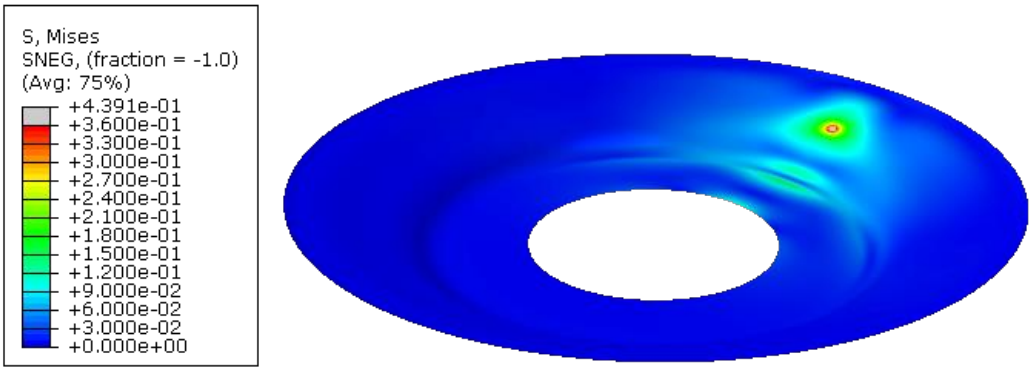

Figure 6-22 - Stresses in shape C according to FE model

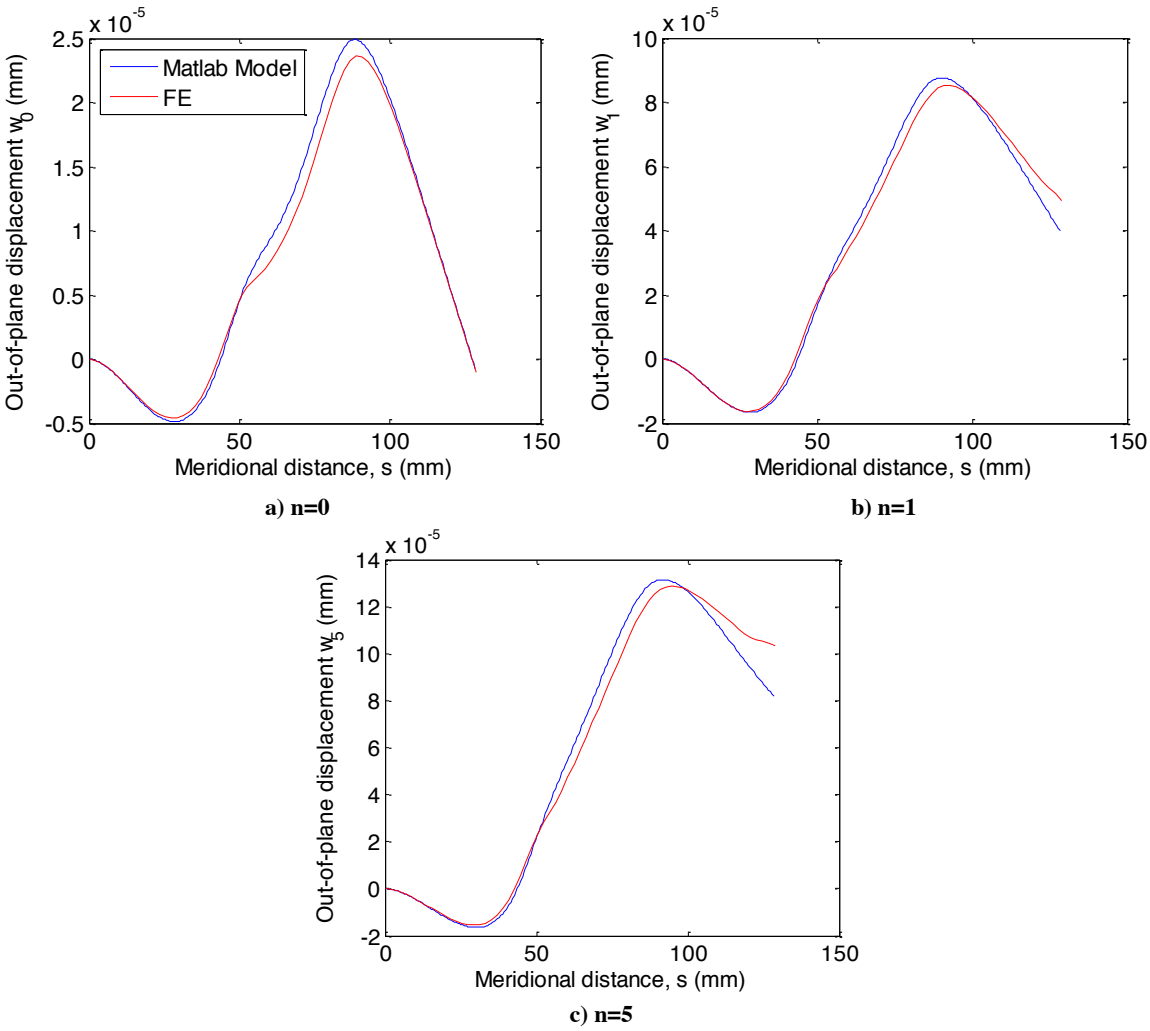

Figure 6-23 - Three Fourier components of the out-of-plane displacements in shape C

Similar levels of agreement are seen in the analysis of shape E. The contour plot of stress from the MATLAB model is shown in Figure 6-24, and from the FE model in Figure 6-25. The out-of-plane displacements are shown in Figure 6-26. Once again this shows excellent agreement over most of the workpiece.

The comparison of the MATLAB and FE results show good agreement in the predicted stresses and displacements. However, the objective of using a MATLAB model was to improve the processing speed. The comparison of the elapsed time to run the models is shown in Figure 6-27. It shows that the timings are consistent across models, taking ~40 seconds to run the FE model, and ~1.5 to run the MATLAB model. This represents a significant improvement, although note that much of the FE model timing is due to overheads: it takes about 15 seconds to run the solver, 10 seconds to run the input file processor, and the rest of the time is for starting up Abaqus itself, running the Python script to build the model and extracting the results. Perhaps a more efficient program could reduce these overheads, but it would require significant changes to the model setup to reduce it substantially below the ~15 seconds required for the input file processor and the solver. The MATLAB model therefore

offers a significant performance enhancement over the FE model with very little trade-off in accuracy. The MATLAB model is therefore fast enough to be used to generate toolpaths online.

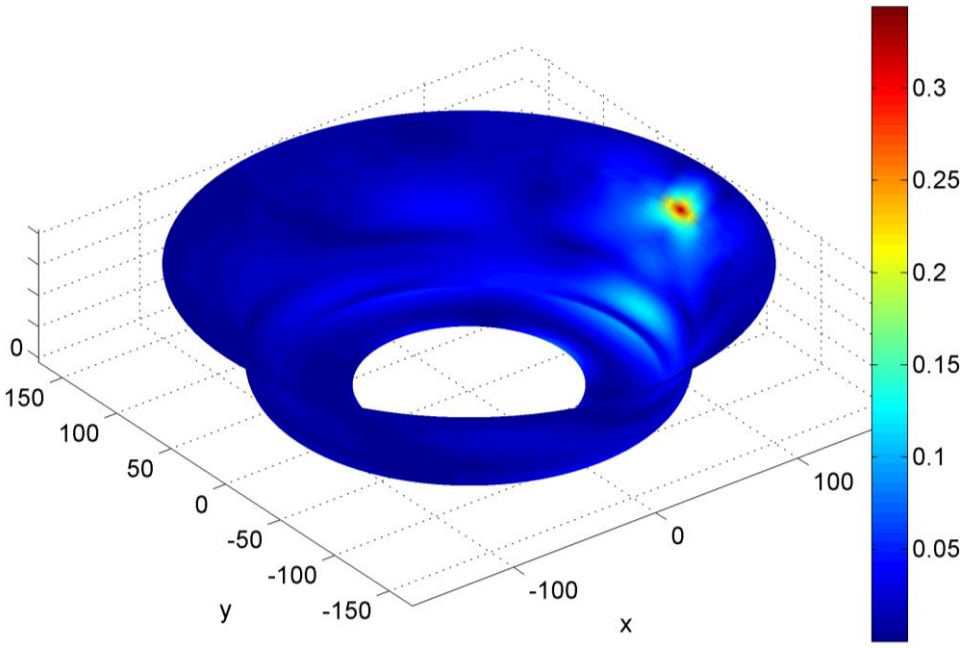

Figure 6-24 - Stresses in shape E according to MATLAB model

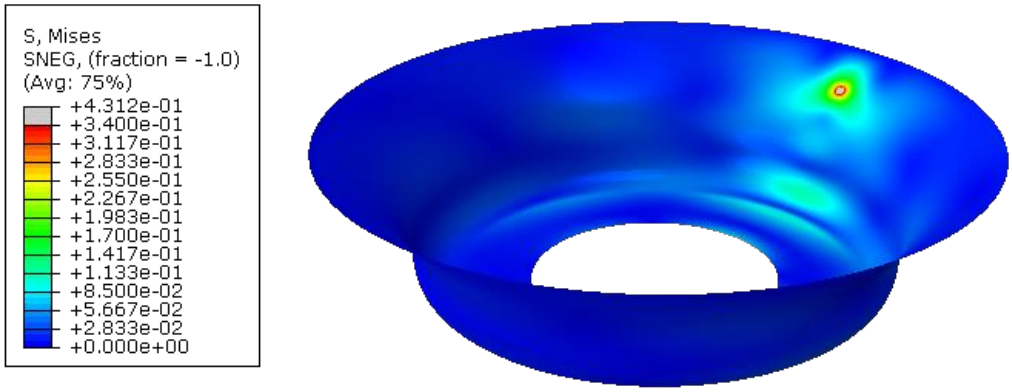

Figure 6-25 - Stresses in shape E according to FE model

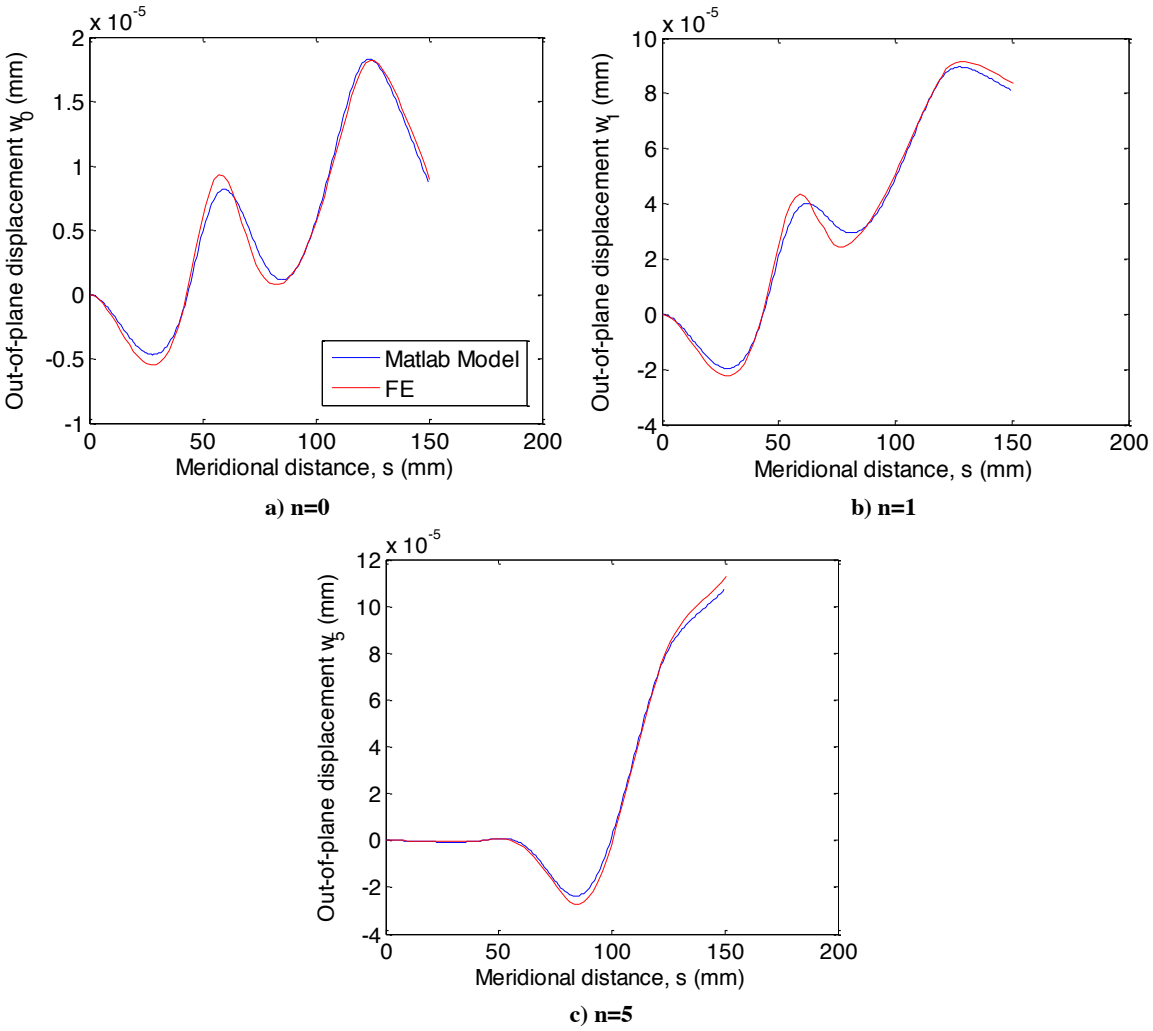

Figure 6-26 - Three Fourier components of the out-of-plane displacements in shape E

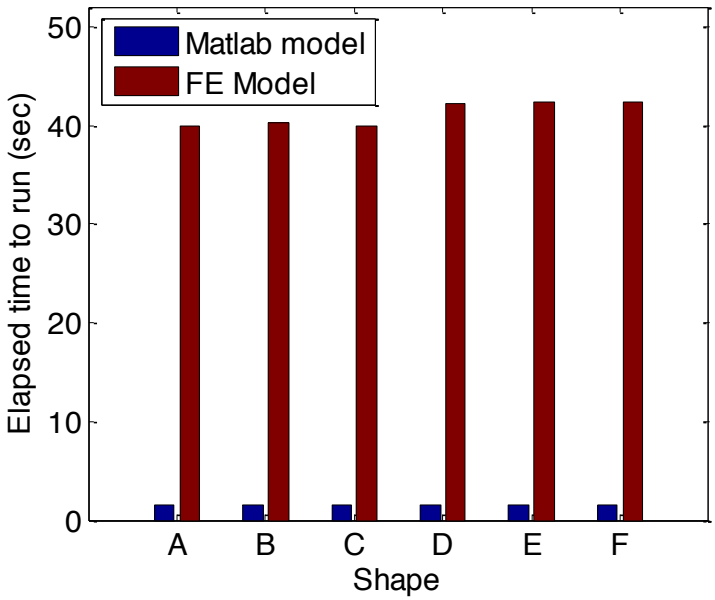

Figure 6-27 - Elapsed time to run the FE and MATLAB models

6.2.3 Developing a control system with a fast, approximate model of wrinkling

The fast, approximate model developed in sections 6.2.1-6.2.2 is to be used in the simplified closed-loop minimisation of equation 6.5 – where the maximum control actions are calculated, and then applied until the target shape is reached. However, there are too key complications in replacing the slow and accurate FE model used within the FE-in-the-loop control system of section 6.1, with the fast and approximate model developed in sections 6.2.1-6.2.2: Firstly, while the FE-in-the-loop system used the angle of linear sections of the toolpath as the control action, u_k, the fast, approximate models simply give a tool indentation relative to the current shape of the workpiece. Some work is needed to translate this into a tool motion command – this turns out to be equivalent to calibrating the model, and is discussed in section 6.2.3.1. Secondly, the differential equations 6.21, 6.22 and 6.23 refer not only to the workpiece shape (through the radial coordinate, *r*, and the meridional coordinate, *s*), but also to up to the third derivative of this (through the derivative of curvature $\frac{dk_1}{ds}$). This means that the measured state of the workpiece, $\hat{\mathbf{q}}_k(\mathbf{x})$, must be passed to the model in a smooth and differentiable form, and this is the subject of 6.2.3.2.

The result is a closed-loop toolpath generation system which can take the measured shape of the workpiece and use the model described in sections 6.2.1-6.2.2 to generate motion commands.

6.2.3.1 Generating motion commands from control actions

The control actions generated by the fast model described in sections 6.2.1-6.2.2 are different to those generated by the FE-in-the-loop control system developed in section 6.1. The FE-in-the-loop control system in section 6.1 defined the control action, u_k, as the *angle* at which the tool travelled in space. In each time increment, the tool moved from its starting position, along this angle, to an end position. In the next time increment, the tool started from the end position of the previous time increment. However, in the fast model of sections 6.2.1-6.2.2, the control action is given by the indentation of the tool normal to the surface of the workpiece – not an angle. If this motion *into* the workpiece is not coupled with some motion *along* the workpiece, then the next motion command will drive the tool further into the same point. This could be repeated endlessly, leading to a toolpath where the tool simply drives straight into the workpiece, as demonstrated in Figure 6-28a. Attempting this on the machine quickly led to workpiece wrinkling.

The solution to this would be to move the tool some distance, s_{step}, along the workpiece at the same time as moving u_k into the workpiece, as shown in Figure 6-28b. However, the choice of s_{step} affects the ultimate aggressiveness of the toolpath. As s_{step} increases, the same predicted indentation *into* the workpiece will occur as the tool moves a greater distance *along* the workpiece, reducing the angle of the toolpath relative to the workpiece and so reducing the aggressiveness. Therefore, s_{step} can be considered a calibration factor, or perhaps more aptly, a "conservatism factor", as it can be varied to

adjust the conservativeness of the ultimate toolpath. Calibrating the value of s_{step} will be the subject of the rest of this section.

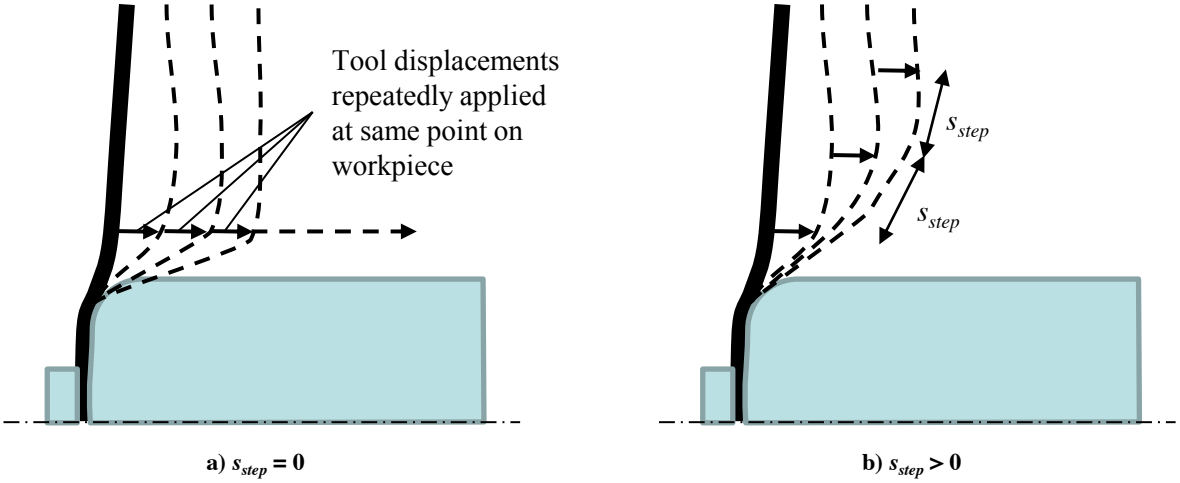

Figure 6-28 - a) The toolpath designed when the tool is not moved along the workpiece b) the toolpath evolution at a finite value of s_{step}

To calibrate s_{step}, the first toolpass was generated offline with varying values of s_{step}. A value of s_{step} was then selected based on which generates a toolpath closest to the trial and error toolpath shown in Figure 6-2, because this was known to work well.

In order to generate such toolpaths *offline* an offline geometry predictor was needed (effectively taking the place of the process model, $\mathbf{f}_k$, in the offline minimisation of equation 1.4). This geometry predictor assumed that there was no springback, and that the effect of the tool was entirely local (i.e. that it did not change the shape of the workpiece anywhere else). The shape of the workpiece was therefore defined by the (smoothed) toolpass shape, and was assumed to remain flat in regions where the tool had not yet deformed. This offline geometry predictor is demonstrated in Figure 6-29. It is designed specifically for the first pass, but this is because only the first pass is to be designed offline here – using such an approach for subsequent passes would lead to a continued build-up of errors due to the assumptions made here.

The first toolpass generated with this offline geometry predictor and the fast model of sections 6.2.1-6.2.2 are shown with s_{step} = 5mm, 7mm and 10mm in Figure 6-30. A value of 7mm gives the best agreement with the trial and error toolpath, and is therefore used as the calibrated value of s_{step} in subsequent experiments.

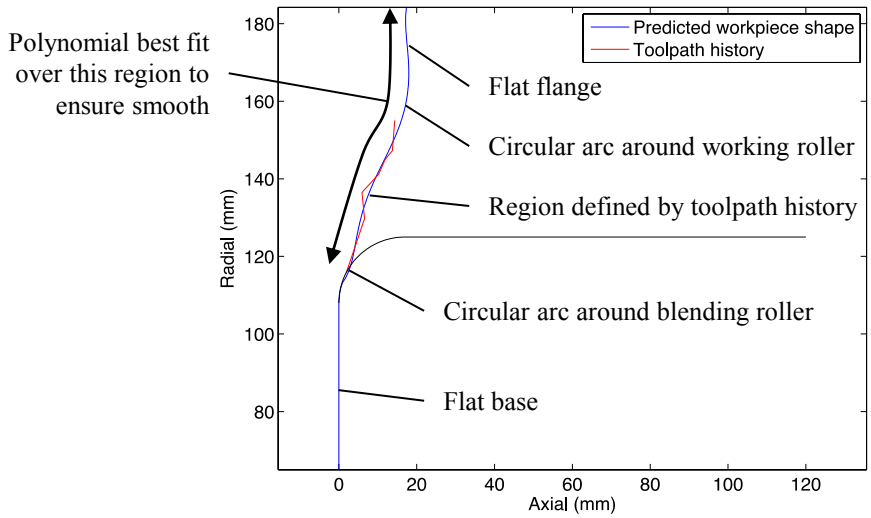

Figure 6-29 - The geometry predictor

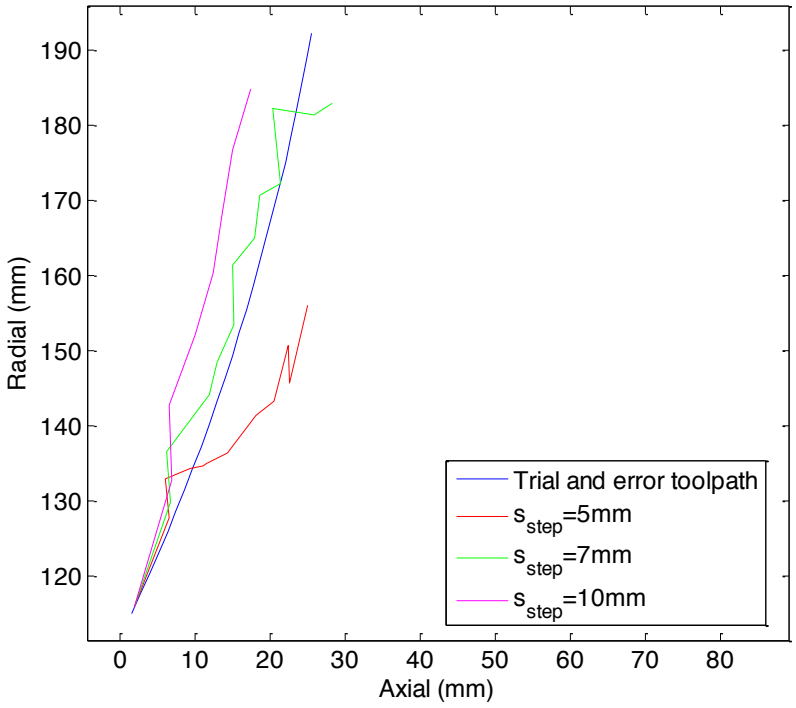

Figure 6-30 - The toolpaths created offline for different values of s_{step}, compared to the trial and error toolpath

However, this calibration applies specifically to producing a 250mm diameter cup from a 375mm diameter blank from 2mm commercially pure Aluminium using a tool with a 15mm nose radius. If the material, or the tool dimensions change, it is likely that s_{step} will change too. 7mm is conveniently about the width of the plastic strain band left by the tool as the workpiece rotates, so we hypothesise that the two might be linked. This would make sense, as after forming this region of the material, the tool should be moved to "fresh" material 7mm away before the model can be re-ran. However, this is just conjecture, and should be investigated in future work, along with the possibility of allowing s_{step} to vary according to data gathered online (as the calibration factor did in springback control in chapter 5).

6.2.3.2 Online measurement of workpiece geometry

Introducing online measurements into the control system can improve accuracy because the inputs to the constraint model are no longer based on an assumed process model (as they were in section 6.2.3.1, for example). However, the additional difficulty is that these real measurements contain noise. There will be a small amount of noise on the r, z coordinates measured by the laser line scanner in measuring the workpiece shape. This noise was small enough that basic filtering allowed FE models to be built based on them in the FE-in-the-loop controller of 6.1. However, in order for these measurements to be used in the model developed in section 6.2.2, these must be differentiated three times in order to find ϕ, k_1 and $\frac{dk_1}{ds}$. This differentiation amplifies high frequency noise and causes problems in the ODE solver.

Therefore, the laser measurements must be processed carefully in order to ensure that they can be used within the fast model to produce a sensible control action. The following measurement processing procedure was introduced in order to prepare the measured shape for the ODE solver:

- Measurement points outside a "region of likely measurements", which is calculated from the toolpath history, are removed. This removes erroneous points often caused by reflections, glare, and sunlight etc.
- A Gaussian filter is applied to the remaining points to remove some high-frequency noise.
- An edge detection algorithm detects and removes points that appear to measure the edge of the workpiece, rather than the surface.
- A feature detection algorithm detects the centre and radius of the corner of the cup. The corner of the cup was then replaced by a perfect circular arc.
- The region radially inside the corner of the cup is replaced by a perfectly flat region.
- A fifth order polynomial is fitted to the s, ϕ coordinates in the region outside of the corner of the cup. This was found to give the best agreement with measured data while removing high-frequency noise and ensuring the data is differentiable.
- The polynomial coefficients are then used directly to differentiate to find k_1 and $\frac{dk_1}{ds}$, before evaluating the polynomial and integrating back to z, r coordinates.

An example workpiece measurement mid-way through the spinning process is shown in Figure 6-31, highlighting some of the above steps.

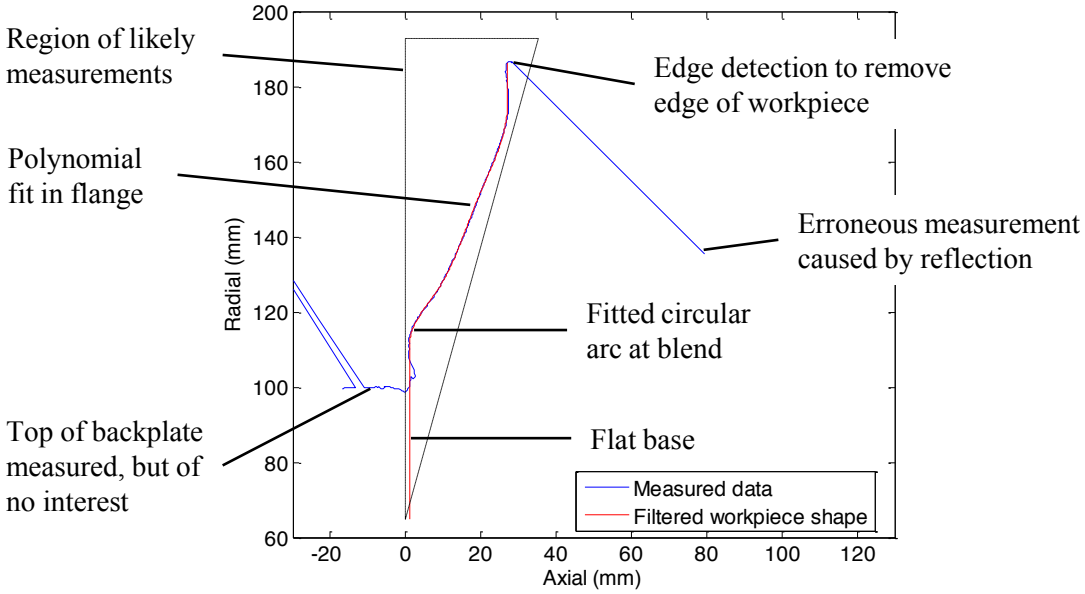

Figure 6-31 - An example of the workpiece measurements being filtered and fitted

The result is a measurement of the workpiece shape which can be used in the model described in section 6.2.2 to calculate the tool indentation, u_k, which can then be used in the way described in section 6.2.3.1 to generate a motion command. Once executed, the workpiece shape is measured again and the closed-loop repeats. It only remains to evaluate this control system.

6.2.4 Evaluation of toolpath generator

The aim of section 6.2 was to explore whether a fast, approximate model of wrinkling could be used within a finite-horizon closed-loop control system to generate a successful toolpath online. A fast, approximate model was developed in sections 6.2.1 and 6.2.2, and a control system was designed to use this model to generate a toolpath in section 6.2.3. In this section, this online toolpath generator is evaluated.

The toolpath ultimately produced by this online toolpath generator is shown in Figure 6-32, compared with the trial and error toolpath from Figure 6-2. Towards the base of the workpiece, the toolpath generator produces a toolpath which looks similar to the trial and error toolpath. However, as the tool moves towards the outer edge of the workpiece, the toolpath generator generates increasingly conservative tool points. This happens for two reasons: the first is because the edge of the workpiece folds axially back as the tool is pushed into the workpiece closer to bottom of the flange – this effect we term "foldback". As the tool moves out, the toolpath indentation is relative to this folded back shape, meaning that the tool might (and indeed does) move axially back as it moves towards the edge of the workpiece.

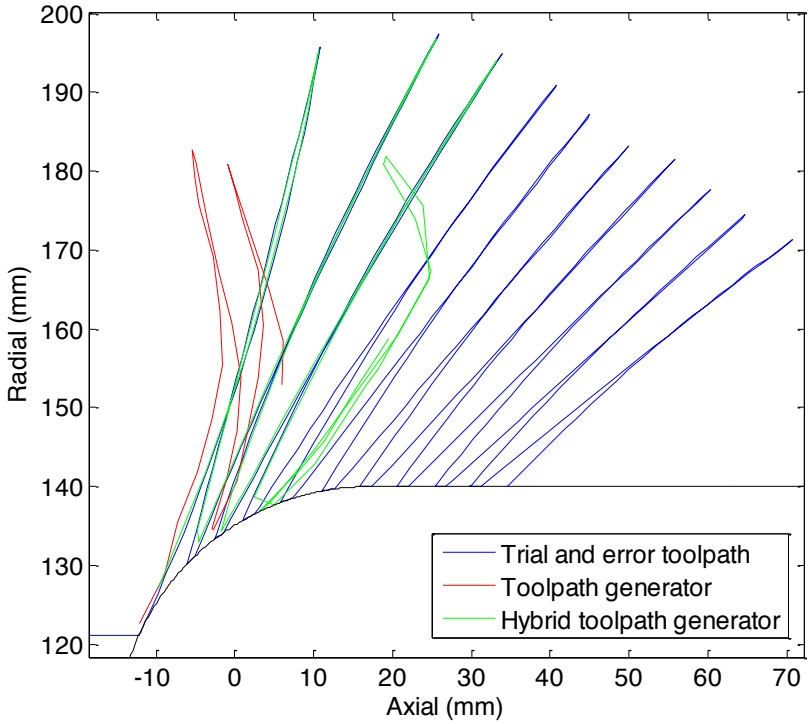

Figure 6-32 - Toolpaths generated by elastic toolpath generator and the hybrid toolpath generator, compared to the trial and error toolpath for reference.

The second reason is that the limiting tool indentations predicted by the toolpath generator become increasingly conservative as the tool moves toward the edge. This appears to be because the yield criterion at the edge of the workpiece is reached due to plastic region local to the tool, rather than the sprawling hinges seen in Figure 6-16. This conservatism towards the edge means that the folded back shape of the workpiece is perpetuated.

Ultimately, the folded back edge of the workpiece collided with the arm holding the working roller (Figure 6-33) and the process had to be terminated before any damage to the machine could result.

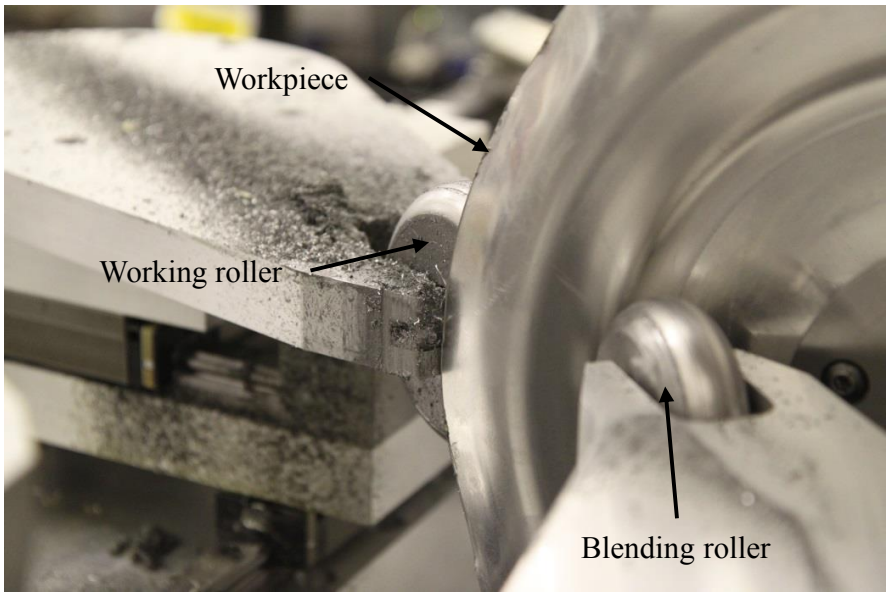

Figure 6-33 - Photograph of foldback causing workpiece to jam in between working roller and roller arm

Even if the machine could be redesigned to rotate the tool and avoid collision (at considerable expense of design effort and build cost), the problem of foldback would still appear later in the process. To confirm this, an experiment was performed where the tool followed the trial and error toolpath for three passes, before the closed-loop toolpath generator started generating the motion commands – a so called "Hybrid toolpath generator", because the toolpath is partly generated by trial and error. The resulting toolpath is also shown alongside that generated entirely automatically in Figure 6-32, showing that foldback begins to occur immediately, even at this later stage of the process.

We therefore conclude that this toolpath generator does not work in its current form: it is too conservative and would continue to perpetuate the folded back shape which is difficult to then draw in to the target shape. Some modification to the controller is therefore needed to prevent or eliminate the folded back shape, and some initial attempts will be described in section 6.2.5.

6.2.5 Modifications to the toolpath generator to address foldback

It is possible that the proposed toolpath generator may still work with some modifications to prevent foldback. In this section, three such modifications are attempted in order to investigate this possibility: firstly, by using forward passes only and not introducing backward passes until later in the process; secondly, using a slightly more accurate, less conservative, model of wrinkling; and thirdly, by extrapolating the first few points of each toolpass in order to attempt to "drive through" the foldback.

Following discussions with a professional hand spinner, it was suggested that the backward pass could increase foldback. His strategy, therefore, was to avoid backward passes until the flange had reached a critical angle at which foldback would not cause problems. The resulting toolpath is shown in Figure 6-34 compared with the toolpath generator with backward passes. The tool passes curve backwards slightly less, and foldback is reduced to a level which prevents the workpiece getting jammed in between the working roller and the arm. However, although the jamming does not occur, foldback does still occur and perpetuates, causing the workpiece to collide with the working roller arm (although because the collisions only occur on the forward pass, the workpiece does not get jammed between the roller and the roller arm, as seen in Figure 6-33, so the experiment could continue for longer).

In order to generate more aggressive toolpath points, even when the workpiece folds back, we look back at Figure 6-18 which showed that the slower but more accurate plastic model with large-displacement generated slightly more aggressive tool indentations. Although this model is slow (taking around 60 seconds to generate each point), it is possible to run this model online running the machine at a slower speed. However, at this slower speed the machine took 15 minutes to complete one toolpass, whereas with the earlier model and the trial and error toolpath it would typically take 15

minutes to produce the entire product, so a much faster model would be needed in an industrial application.

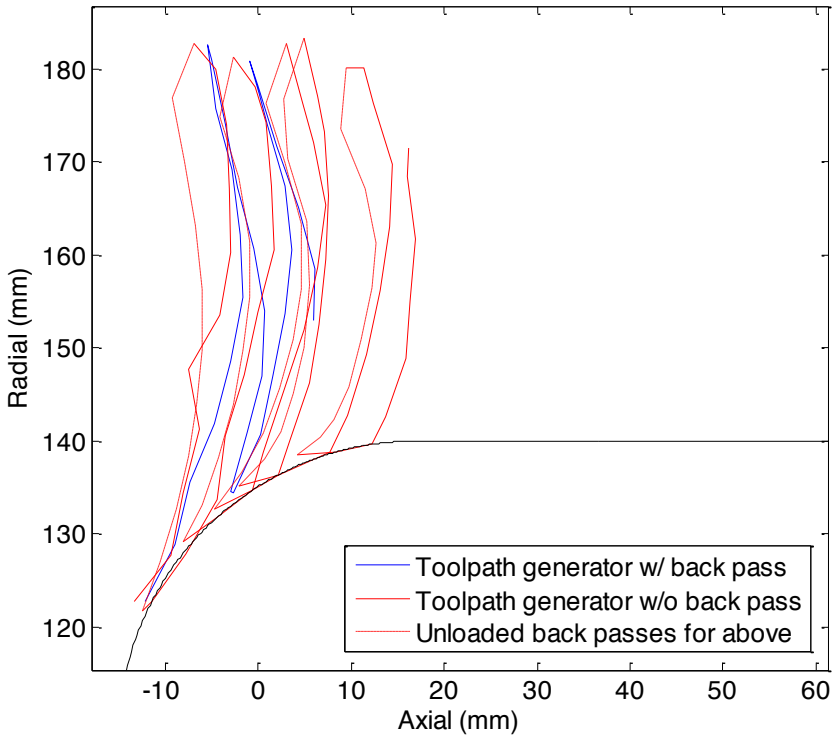

Figure 6-34 – The toolpaths generated by the elastic generator with and without back passes (The unloaded back passes are shown as dashed lines)

Nevertheless, the resulting toolpath is shown in Figure 6-35 alongside the toolpath generated with the elastic model. In the first pass forward, it is slightly more conservative, but this is compensated by a more aggressive first backward pass and second pass. The result, however, is still a very similar toolpath and the same problem occurs: the workpiece folds back and gets jammed between the working roller and roller arm.

Finally, in order to overcome the toolpath generator becoming conservative towards the edge of the toolpath, the first four points of the pass (which typically agreed well with the trial and error toolpath) were extrapolated to form the rest of the forward pass. The resulting toolpath is shown in Figure 6-36, with two different trials. Despite the same set-up in each of the two trials, the results vary wildly. A small amount of variation or noise on the first four points in the forward pass resulted in huge variations in the rest of the pass. Even though many of the passes look sensible when comparing them to the trial and error toolpass, eventually a very aggressive pass was produced which resulted in the workpiece tearing.

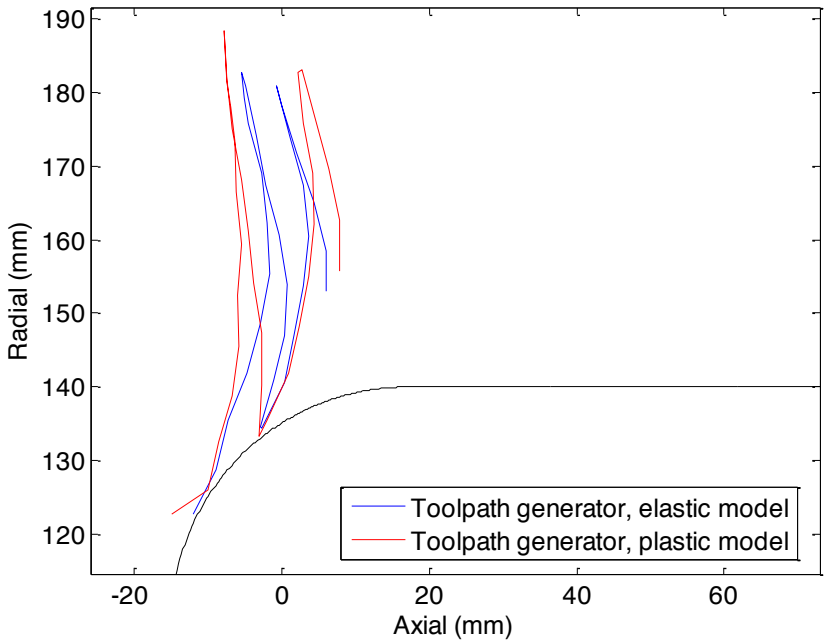

Figure 6-35 - Toolpaths generated with the linear-elastic approximations and with the full, plastic, large-displacement FE model

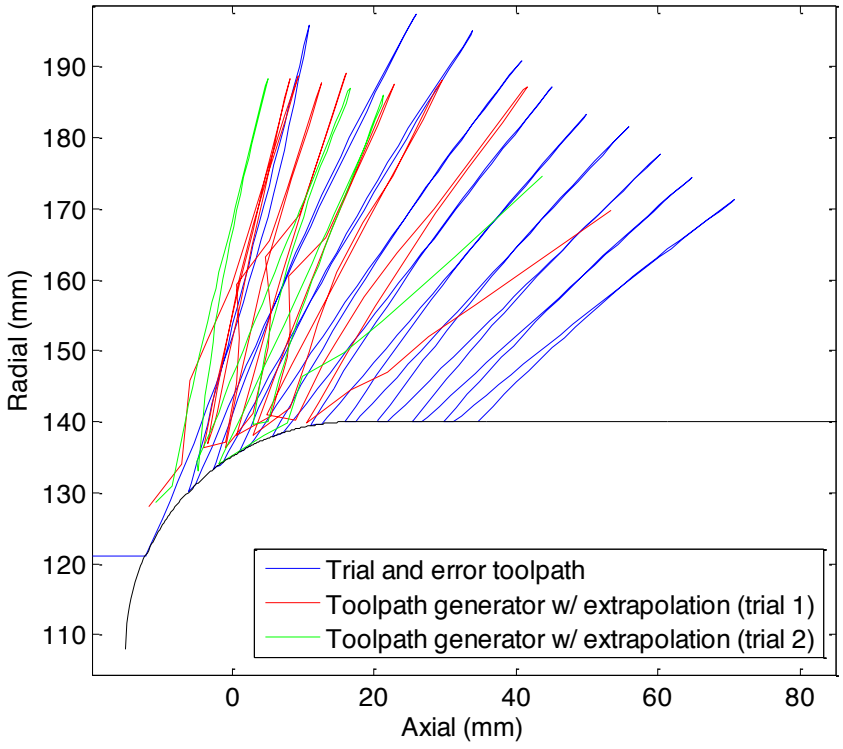

Figure 6-36 - Toolpaths generated with linear extrapolation, compared with the trial and error toolpath for reference

These three basic workarounds have therefore failed to overcome the foldback problem. A more advanced method of preventing foldback: either by using a different model or control system that is not conservative toward the edge of the workpiece, or by using a constraint on foldback. This could be the subject of further work, along with the development of a thinning/tearing and force constraint.

6.3 Conclusion and further work

Currently, the computational expense of modelling the spinning process from start to finish is too high to make online or even offline toolpath generation feasible. Therefore, in this chapter, we sought to investigate two methods of reducing this computational expense: through a finite-horizon control approach, and by using a fast, approximate model.

By using an accurate but slow FE model, an FE-in-the-loop control system was designed and implemented in order to demonstrate the finite-horizon approach. Although the resulting control system was too slow for industrial applications, the control system successfully generated a first pass of the spinning process that avoided wrinkling, and also avoided tearing by setting a criterion on thinning. The results showed tentatively that a finite-horizon approach could successfully be used to prevent failure in spinning, although the chosen trajectory of the evolution of thickness can have a significant effect on the resulting toolpath. More tests are needed to make this conclusive: by designing more tool passes, and also using different material, but the time required to design these toolpaths makes such a research project extremely unlikely.

The speed of the control system was determined by the speed of the FE model. To reduce the computational cost further, a fast and approximate model of wrinkling was tested within a similar control system. This model was based on a fast, linear elastic model to calculate the stresses resulting from indenting the workpiece, and wrinkling was assumed to occur at the tool indentation that caused the edge of the workpiece to yield. However, on testing this toolpath generator online, it became very conservative towards the edge of the workpiece, producing a folded back shape which resulting in a collision with the roller arm. Some simple improvements and workarounds were attempted, but with limited improvements.

In order to see the successful automation of toolpath generation using closed-loop control of product properties, one of two things needs to happen:

Firstly, a more suitable model must be developed. The accurate FE model used within this thesis is far too slow for industrial use – it would take over a year to produce a full toolpath. Industrial applications would require a toolpath to be generated in several minutes if it were to be performed online – Even a decade of computational power improvements will not be able to speed the model up by the five orders of magnitude required. The linear-elastic model with the stress-based criterion was, although fast enough for online use, too approximate – in particular, it was too conservative towards the outer edge of the workpiece, creating a folded back shape. Something faster than the FE model, but more advanced than the linear-elastic model needs to be developed.

Secondly, or alternatively, a more sophisticated control system could be developed. In this chapter, the control loop was closed by passing the measured workpiece shape to the toolpath generation

model, in order to calculate the next tool motion. However, a more sophisticated system may also pass on information about whether wrinkles *actually* occurred, and in what amplitude. The control system could then use this information to adapt the model, by changing the calibration factors (e.g. s_{step}, or some multiple of the tool indentation) in real-time, and thereby perhaps allowing the very fast, linear-elastic model to be used online.

Chapter 7 - Parametric Toolpath Design

Given the clear complexity of creating a constraint model that is fast enough to use online, but detailed enough to be useful in generating toolpaths that do not result in wrinkling or tearing – or the foldback problem found in chapter 6 - many authors have turned to empirical methods rather than theoretical based models.

In the literature review of chapter 2, we saw that several authors have performed experiments to determine the optimum shape of the toolpath in order to minimise the chances of wrinkling or fracture occurring. Hayama et al. (1970) tried a range of linear and involute toolpaths, and recommended involute paths. Liu et al. (2002) found a similar result through FE analyses: that involute toolpaths minimised the stresses and strains that lead to wrinkling and thinning in the workpiece. Wang and Long (2011) compared linear, convex, concave and combined toolpaths and found that convex toolpaths minimised both tool forces and thinning. Li et al. (2014) parameterised the first tool pass using Bezier curves and used FE models to investigate how the curvature of these passes effects thinning and springback – but they did not vary the parameters individually. Their key result was to show that a more aggressive convex pass resulted in higher tool forces and more thinning compared to a less aggressive concave pass. No published work looked at foldback in spinning, although interviews with skilled hand spinners revealed that it can cause collisions with the tool and prevent its continued outward motion. Their strategy to prevent it was partly reactive: if it begins to happen, to be less aggressive while close to the mandrel, and to push the foldback forward as the tool reaches the edge of the workpiece. However, while these results provide some suggestions about toolpath generation they are still insufficient to design a complete toolpath for a specific component.

For this reason, Kleiner et al. (2002) and Auer et al. (2004) used the statistical design of experiments approach to design toolpaths for specific materials and products. They both assumed that a toolpass took a circular shape with a variable radius of curvature, but used different approaches to optimising the parameters. Kleiner et al. used human judgement to grade the severity of wrinkles from 1 to 6, and optimised the first forward and backward pass to minimise the severity. Auer et al. considered wrinkling to be outright failure, creating a window of acceptable toolpaths, and then optimised the whole path within this window to minimise thinning, rather than considering tearing.

However, rather than developing a set of rules for online toolpath modification, the work evolved into an offline toolpath planning algorithm which interpolates the existing parameter field to find the optimum set of parameters for a new problem (Henkenjohann et al., 2005). This is a practical approach to generating a toolpath, but is limited to the parameter region in which experiments have been carried out.

The academic literature on toolpath design therefore lacks a clear and practical set of rules for modifying toolpaths in order to prevent or minimise both wrinkling and thinning in parallel, and that can be applied in general. Furthermore, although Music (2011) noted that the mechanics of spinning varied from early in the process to the end of the process, it is unclear how this change in mechanics alters the way toolpaths should be designed or modified.

Therefore, in this chapter, similar to the work of Hayama et al. (1970) and Wang and Long (2011), a set of experiments is performed with a parameterised toolpass to explore how the design of the toolpath influences product geometry, tool forces, wrinkling, thinning and foldback. These experiments are performed early and late in the process and with both forwards and backwards passes in order to see how the mechanics vary. The methodology is presented in section 7.1. The results are presented in 7.2, with an immediate discussion of the effects of each of the parameters. However, in section 7.3, a more thorough analysis and discussion of the over 10GB of data generated through these experiments is presented.

7.1 Methodology

Each experiment in this investigation consists of three steps: firstly, the initial geometry was created as described in section 7.1.1. After producing the initial geometry, the parameterised toolpass is followed, as described in section 7.1.2. Measurements are taken both throughout and at the end of the production of the spun part, as described in section 7.1.3.

7.1.1 Creating the initial workpiece geometry

The mechanics of spinning change significantly as the workpiece shape evolves during the process, and in particular the mechanics of the early stages (where the workpiece is flat so has very little membrane stiffness) are quite different from later stages. Accordingly two initial workpiece geometries were used: a flat blank at the very beginning of the process and a 45° cone. The trials were all limited to a single material (commercially pure, half-hard aluminium sheet, AA1050-H14) with constant (2mm) thickness and an initial blank diameter of 375mm.

The 45° cone was produced using a trial and error toolpath, using the blending roller positioning system described in chapter 4, and the springback compensation system described in chapter 5 to produce a working toolpath. After the cone was produced the first time, the exact toolpath was repeated at the start of each experiment late in the process.

7.1.2 Parameterising the toolpass

The toolpass is parameterised as a quadratic Bezier curve shown in Figure 7-1. The quadratic Bezier curve is fully defined by three points: a start point, $\mathbf{p}_0$, an end point, $\mathbf{p}_2$, and a "stretch point", $\mathbf{p}_1$. A point on the Bezier curve is given by the parametric equation:

$$\mathbf{B}(t) = (1-t)^2\mathbf{p}_0 + 2(1-t)t\mathbf{p}_1 + t^2\mathbf{p}_2, \qquad t \in [0,1] \tag{7.1}$$

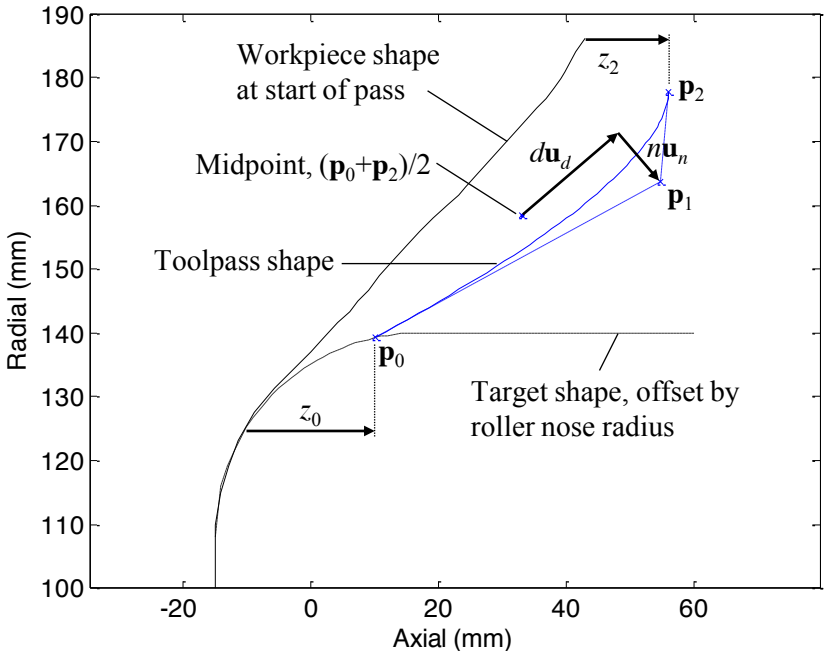

Figure 7-1 - A quadratic Bezier curve used to define a toolpass

The starting point, $\mathbf{p}_0$, is defined relative to the point at which the workpiece shape at the start of the parameterised path leaves contact with the target shape prior to this toolpass. $\mathbf{p}_0$ must nevertheless be on the target shape, so its radial component is determined by its axial coordinate, z_0. The end point of the pass, $\mathbf{p}_2$, must be at the outer edge of the workpiece, so can be defined solely by its axial coordinate, z_2, measured relative to the workpiece edge prior to this parameterised toolpass (as demonstrated in Figure 7-1).

The position of the "stretch point", $\mathbf{p}_1$, is defined relative to the mid-point between $\mathbf{p}_0$ and $\mathbf{p}_2$ and by the coordinates d along the unit vector, $\mathbf{u}_d$, from $\mathbf{p}_0$ to $\mathbf{p}_2$, and n along the unit vector, $\mathbf{u}_n$, normal to $\mathbf{u}_d$ (equations 7.2-7.4). Increasing n leads to a more concave toolpath, while a negative value of n leads to a convex toolpath. Changing d moves the larger curvatures towards the mandrel (d<0) or the perimeter (d>0).

$$\mathbf{p}_1 = 0.5(\mathbf{p}_0 + \mathbf{p}_2) + d\mathbf{u}_d + n\mathbf{u}_n \tag{7.2}$$

$$\mathbf{u}_d = \frac{\mathbf{p}_2 - \mathbf{p}_0}{|\mathbf{p}_2 - \mathbf{p}_0|} \tag{7.3}$$

$$\mathbf{u}_n = \begin{bmatrix} 0 & -1 \\ 1 & 0 \end{bmatrix} \mathbf{u}_d \tag{7.4}$$

The four parameters of Figure 7-1 allow considerable flexibility in toolpath design. However, to vary each parameter in parallel and plot the measured results would require a 5-dimensional graph (4

dimensions for the parameters, and 1 for the resulting metric) – which would be very difficult to interpret, even if such a graph could be produced. Instead, a sequential approach is taken. Starting from a straight-line tool path with n=0 (and d=0, although this has no effect while n=0), a first set of trials considers straight line paths with increasing rotation – by increasing z_2. The most promising value of z_2 is chosen, and a second set of trials then explores variation in z_0. The best value of this parameter is chosen also, allowing in turn a similar approach for the remaining two parameters.

Following advice from craftsmen, for the flat blanks, only forwards passes were tested, but for the 45°cone, both forwards and backwards passes were possible. For backward passes, z_2 was determined by the tool position at the end of the toolpath used to produce the cone, so only three parameters are varied. In all, 74 components were produced and the resulting set of toolpaths is shown in Figure 7-2.

7.1.3 Measuring the output

To draw as much information from the trials as possible, we seek to take some measure of the proximity of failure of the workpiece – by wrinkling, tearing or foldback - as well as anything that might be of interest to a skilled manual spinner. Informal discussion of toolpath design strategies with skilled craftsmen has revealed a variety of means to describe the process: some operators refer to the tool force – the feeling in their hands as the process evolves; others refer to the shape of the path; others monitor the evolution of the product geometry – which defers from the toolpath due to the marked elastic loading and unloading that occurs as the tool traverses the workpiece, and due to the continued plastic deformation at the base of the workpiece even as the tool moves towards the edge.

Therefore in the sequence of trials in this work, product geometry was monitored throughout each trial by the laser line scanner whose output could be processed to show shape deviation (the difference between the toolpath and workpiece profile arising from elastic loading and unloading during the pass) which was calculated as a function of the distance along the meridian, s (Figure 7-3a), the maximum "foldback" angle during the toolpass (Figure 7-3b), and the wrinkling amplitude at the end of the toolpass (defined by the mean amplitude of deviation of the workpiece profile from the mean profile around the workpiece).

Tool forces were monitored in each pass by load cells, so that the effect of parameters on the tool force magnitude and distribution could be investigated, as well as the effect of the tool forces on the outcome of the product.

Thinning was measured as a precursor to tearing. Component thickness was measured after each trial by placing the workpiece between a calibrated dial gauge and the tip of a fixed ball (Figure 7-4). The thickness was measured every 5mm along meridians perpendicular and parallel to the rolling direction. To create a single scalar value, the minimum thickness was taken and divided by the initial thickness (2mm) to give the maximum nominal percentage thinning.

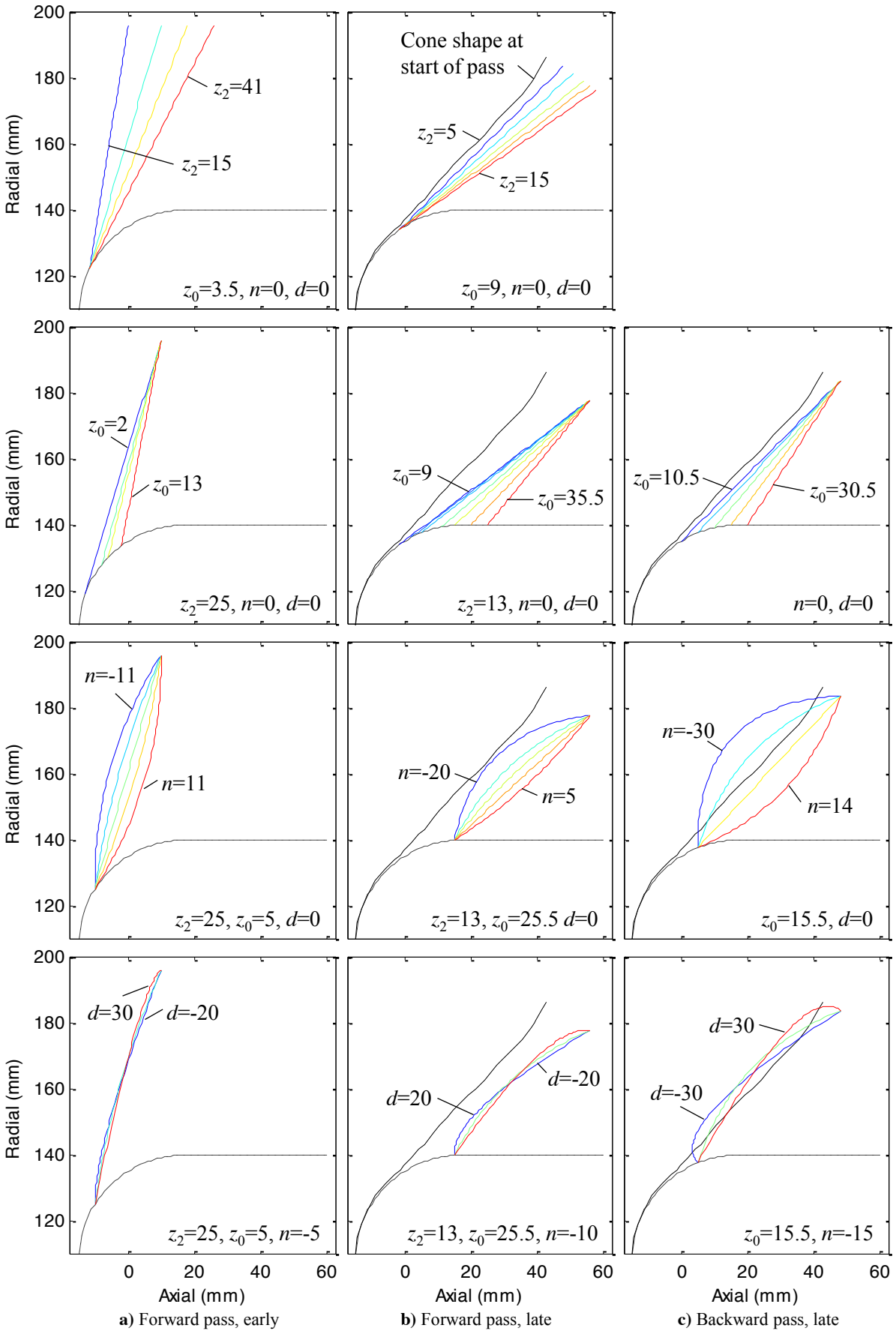

a) Forward pass, early **b)** Forward pass, late **c)** Backward pass, late

Figure 7-2 - The range of toolpasses used in experiments

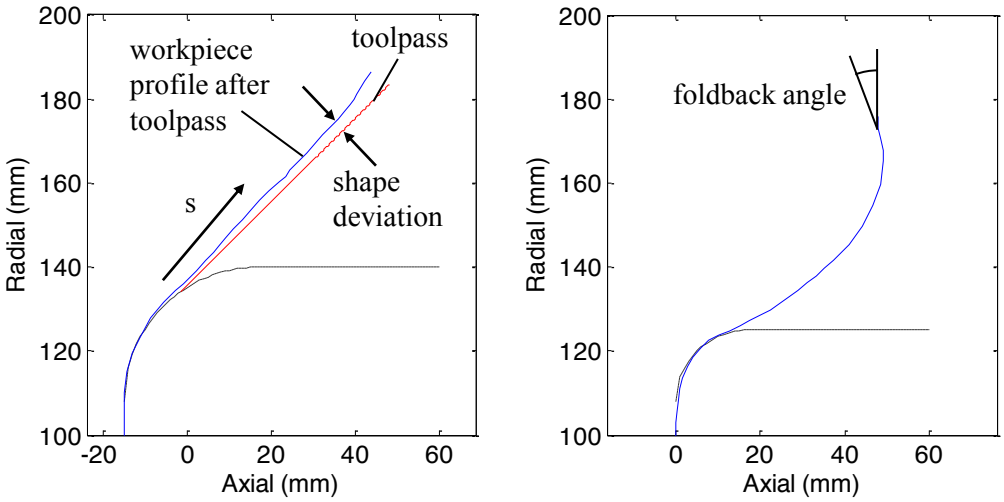

a) Shape deviation measurement **b) Foldback angle measurement**

Figure 7-3 - Workpiece measurements

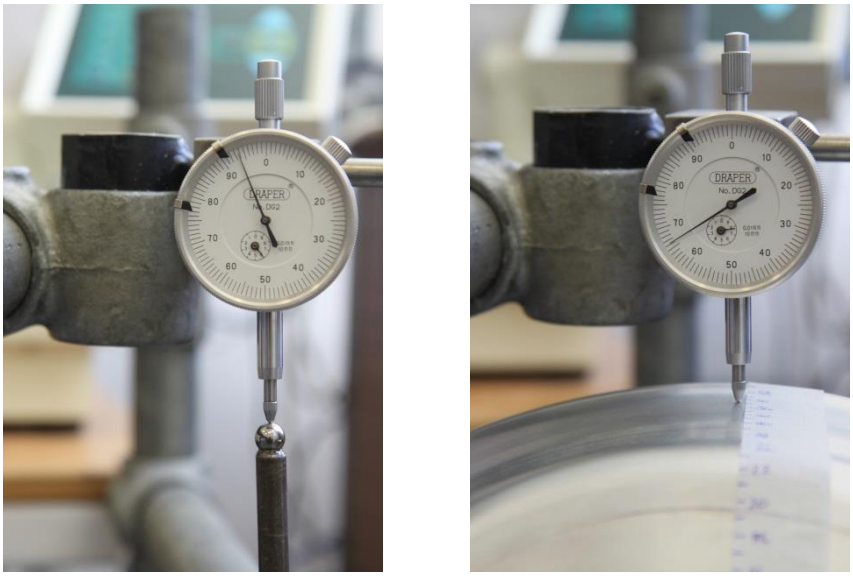

a) With no workpiece **b) Measuring workpiece thickness**

Figure 7-4 - The thickness measuring equipment

Generally the measurements are repeatable, but important experiments (defined as those which appear "optimum" or those which present counter-intuitive results) were repeated and error bars on the thickness, wrinkle and foldback measurement plots in section 7.2 show the range of measurements taken.

7.2 Results

The results of these experiments are shown across all of the figures in this section: The total tool forces are shown in Figure 7-5. Shape deviation is shown in Figure 7-6. The complete thickness profiles are shown in Figure 7-7. Wrinkle amplitude and the maximum thinning seen in each product are shown in Figure 7-8 early in the process and Figure 7-9 late in the process. The maximum foldback angle seen in the process is shown in Figure 7-10. The implications of these results are discussed here, and the underlying data is interrogated more rigorously in section 7.3

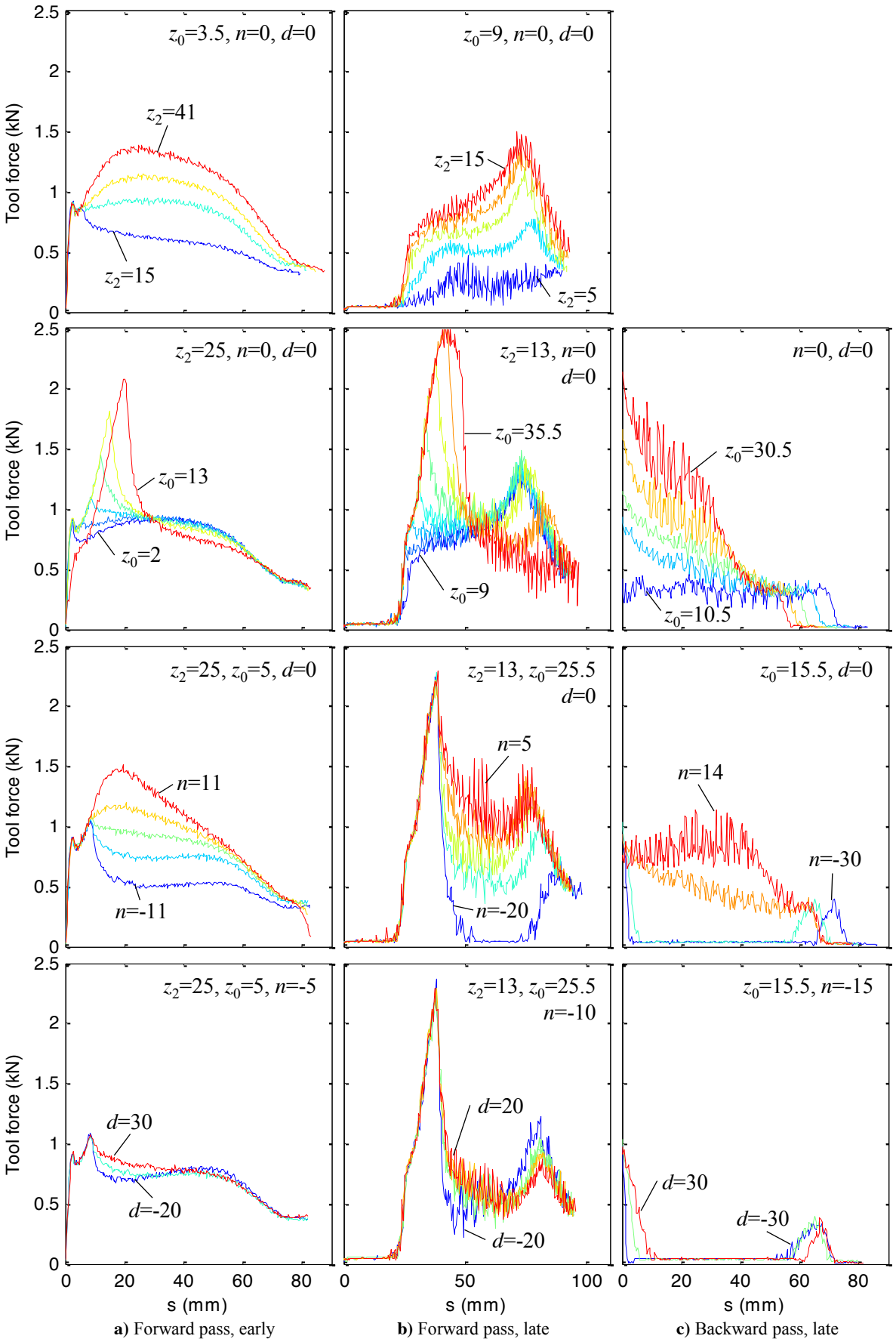

a) Forward pass, early **b)** Forward pass, late **c)** Backward pass, late

Figure 7-5 – The total tool forces

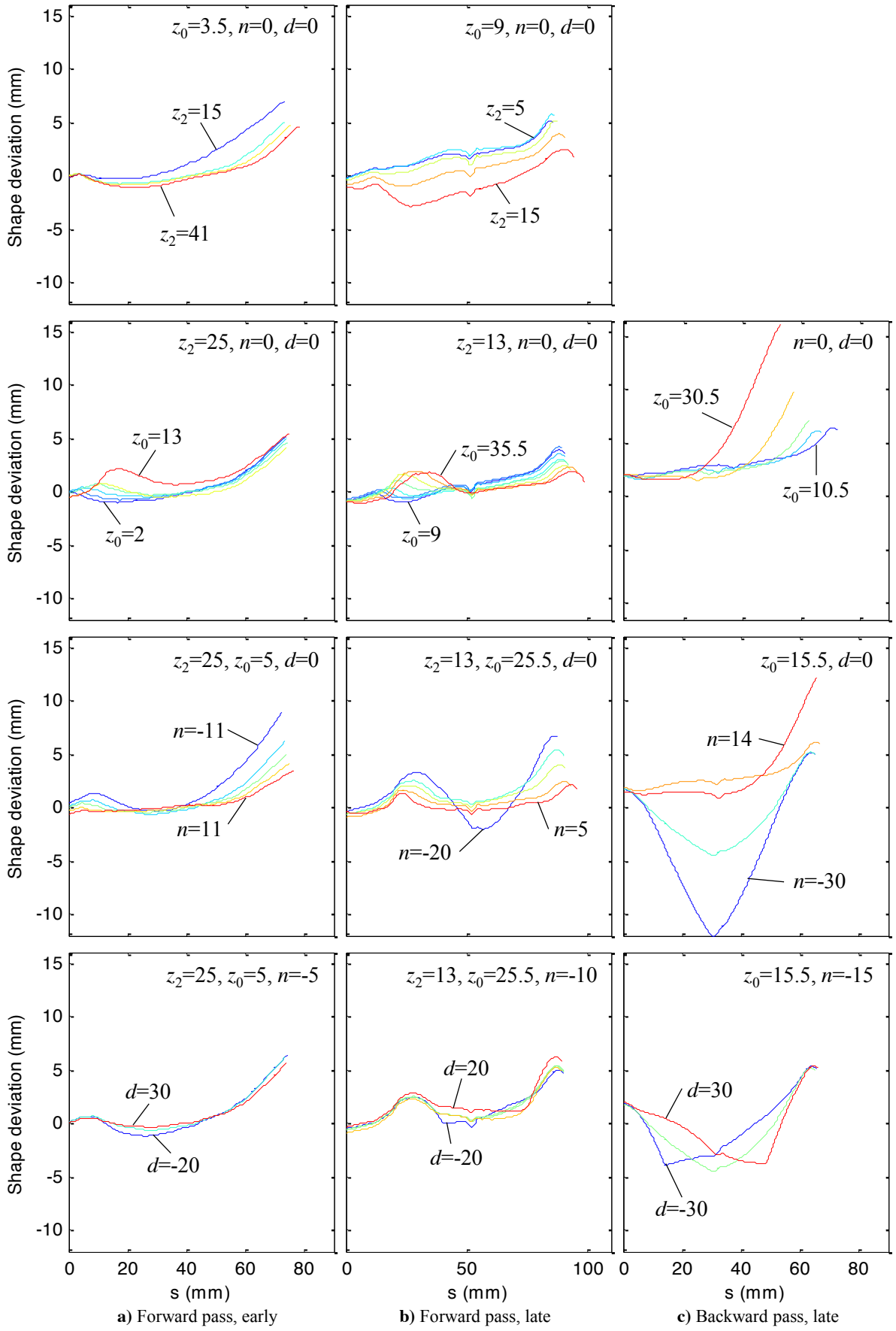

a) Forward pass, early **b)** Forward pass, late **c)** Backward pass, late

Figure 7-6 - Shape deviation - the difference between the toolpath and the workpiece shape

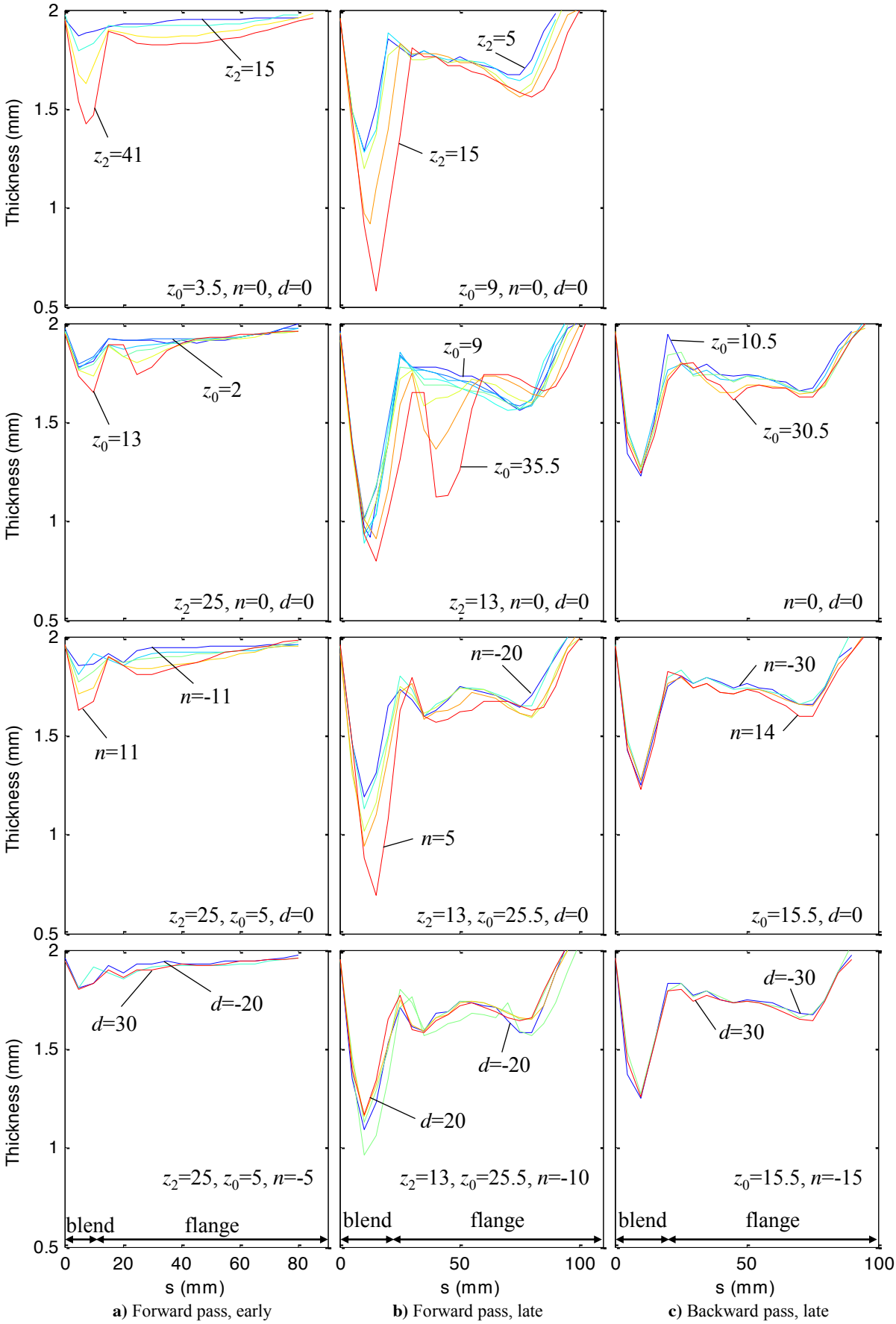

a) Forward pass, early **b)** Forward pass, late **c)** Backward pass, late

Figure 7-7 - Thickness profile after parameterised pass

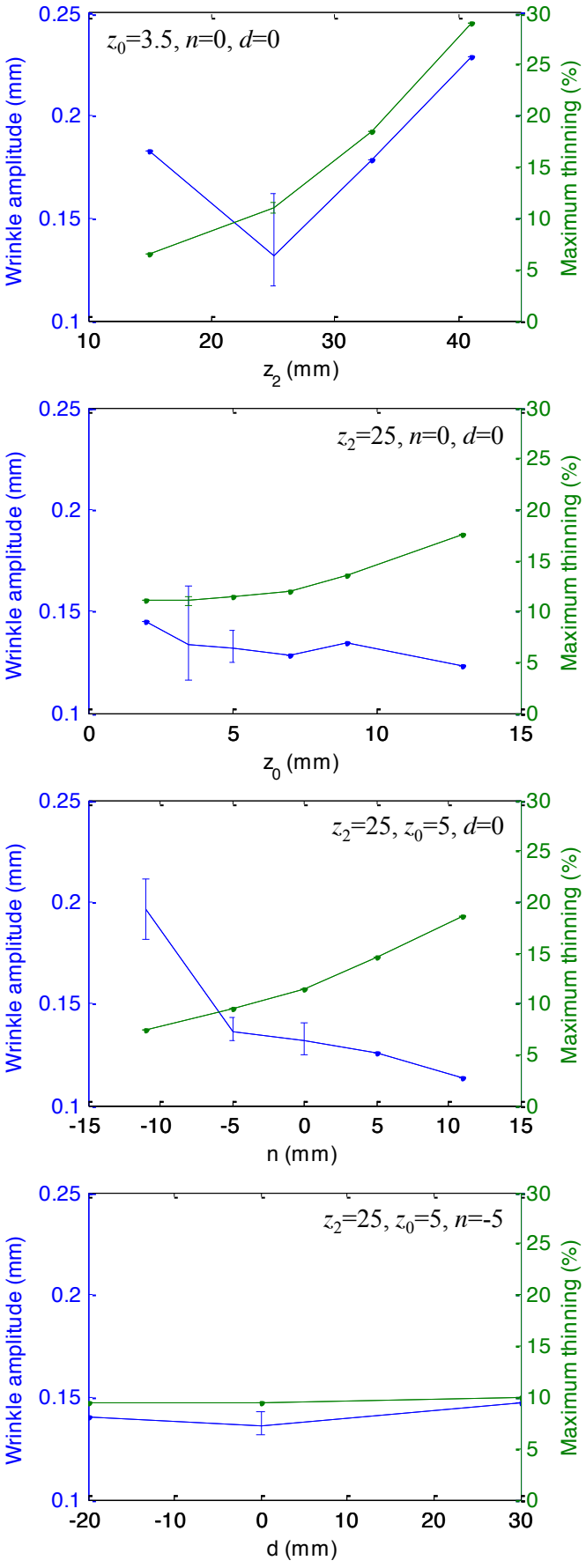

Figure 7-8 - Wrinkling and thinning early in the process

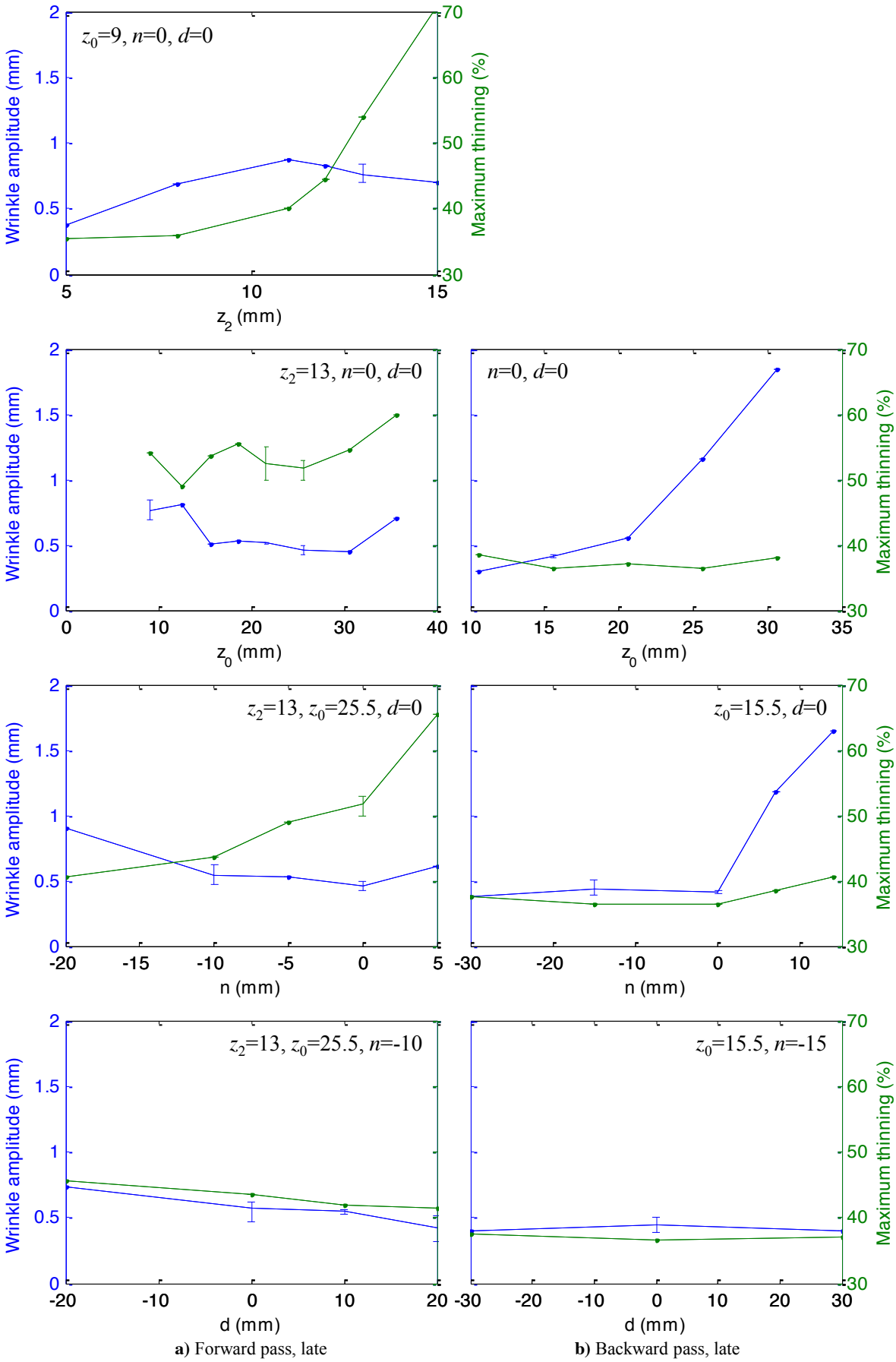

a) Forward pass, late **b)** Backward pass, late

Figure 7-9 - Wrinkling and thinning late in the process

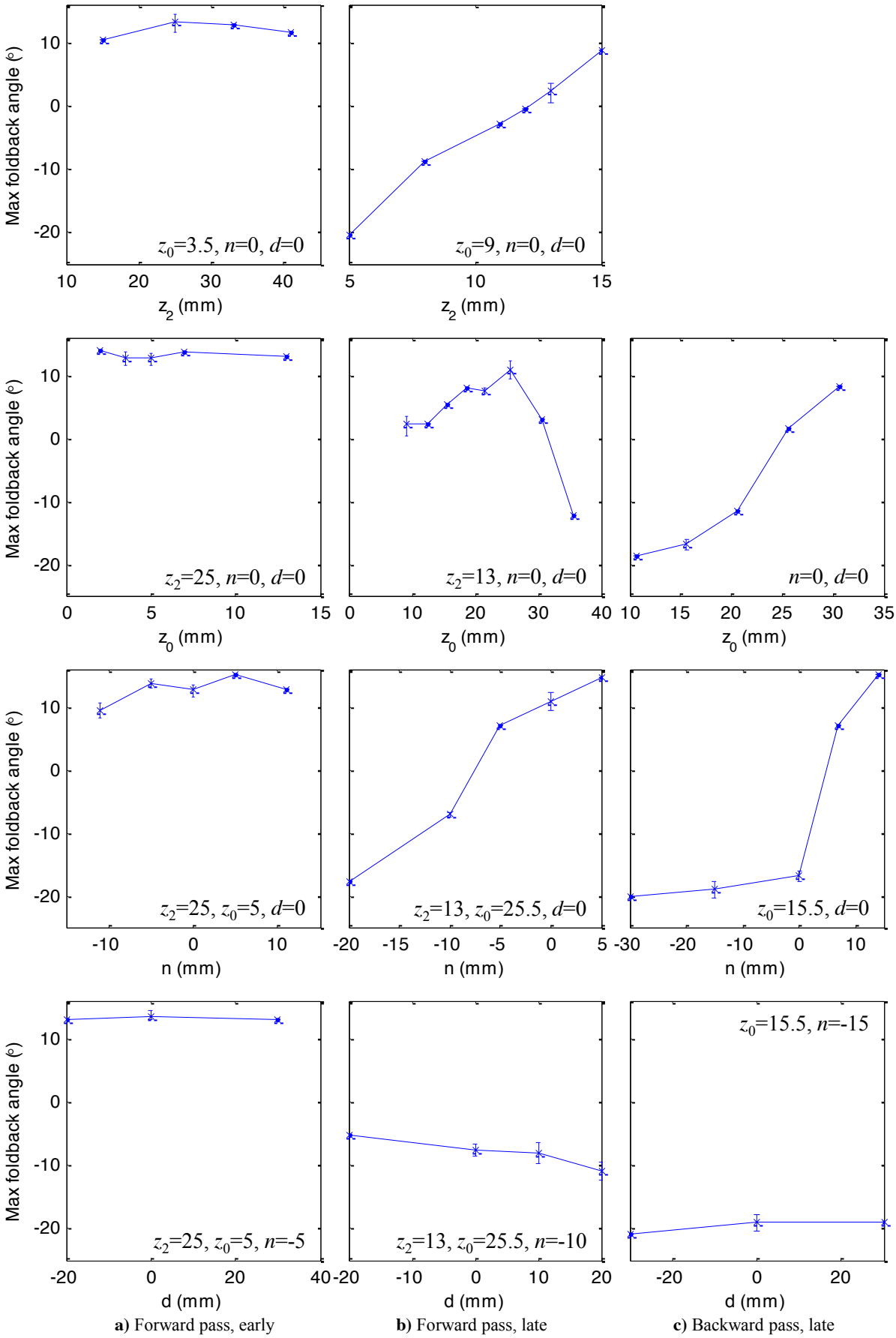

a) Forward pass, early **b)** Forward pass, late **c)** Backward pass, late

Figure 7-10 – Foldback

7.2.1 Early in the process

The value of z_2 represents the overall aggressiveness at the end of the toolpass. Figure 7-5a shows that, as expected, increasing z_2 leads to increased forces – particularly, and perhaps surprisingly, in the middle of each pass, suggesting that most of the deformation occurs in the middle of the pass rather than at the end. Equally, it is initially counter-intuitive that a larger aggressiveness and larger forces lead to less shape deviation – less difference between tool path and eventual profile – because normally this would mean more elastic loading and unloading. However, this may reflect the increase in geometric stiffness as z_2 increases and the blank is deformed further from its initially flat state – resulting in *less* elastic loading and unloading.

The maximum thinning on this first pass is surprisingly high – up to 30%, and increases with increased z_2. This is consistent with the observations of Kang et al. (1999) from experiments and Quigley and Monaghan (2001) from FE models that most thinning occurs in the early passes of spinning – although they suggest that they are like shear-spinning passes, while the results of Figure 7-7a suggest that thinning is concentrated at the blend due to the severe bending here. Still, this is a clear signal to avoid too much deformation early on as it considerably raises the danger of subsequent circumferential cracking. However, the tendency to wrinkle also increases with increasing deformation, although the minimum of this tendency occurs when at least some deformation has occurred – this is likely to be because the workpiece is increasingly stiff and therefore stable, as it is deformed away from its initial flatness. The foldback angle at this first pass seems to have little significant sensitivity to any of the parameters, varying only between 10 and 15°, which is small compared to the variations seen later in the process. Overall, the value of z_2=25mm selected from these trials was chosen as it produced the minimum amplitude of wrinkling.

Craftsmen believe in the importance of "locking on" the workpiece to the mandrel early in the process – which suggests a preference for a high value of z_0. This is partly for safety (as it immediately reduced the chance of the product slipping out from between the mandrel and backplate), but is also supposed to improve the stability of the workpiece. However, the latter is not reflected in the results of Figure 7-8, which shows that any variation in the wrinkle amplitude with z_0 is smaller than the natural variation, or noise, in repeated experiments. However, increasing z_0 results in an increase in maximum thinning around the blend, arising from the sharp spike in tool force as the tool initially pushes so far into the workpiece – indeed further increases in z_0 beyond 13mm resulted in the maximum force capacity of the machine axis being reached. Therefore, a value of z_0=5mm is chosen as thinning did not increase until z_0 was larger, while the interviews with manual spinners did suggest some advantage of a larger value.

An increasingly concave toolpath (n>0) seems to be clearly beneficial in reducing wrinkling: as n increases, the tendency to wrinkle is reduced, although this comes at the cost of a significant increase

in the average tool force – particularly at the middle of the pass where the tool moves further into the workpiece with increasing n – and the consequent increase in thinning, consistent with the results of Wang and Long (2011). However, the increased stiffness of the workpiece produced as n increases results in less shape deviation. Overall, a value of n=-5mm selected mainly to minimise thinning before further decreases act to significantly increase wrinkles. For this modest value of n, the trials of d (the offset of concavity) the offset has little effect.

Overall, these results show that, in the first pass of spinning, the tool force distribution is sensitive to z_0, z_2 and n, unlike the foldback angle which is insensitive. The maximum thinning tends to grow with tool forces. Shape deviation – a form of springback – appears to be determined more by the increasing stiffness of the workpiece with increasing aggressiveness of the pass (z_2) and the concavity (n), than by the increases in tool force (which would normally result in larger springback). The tendency to wrinkle increases with z_2 but decreases slightly with n as the toolpath becomes more concave.

7.2.2 Forward pass late in the process

In contrast to the trials early in the process, the trials later in the process are conducted after the workpiece has increased geometric stiffness: the 3 dimensional shape of the workpiece allows it to withstand larger forces with the same deformation, and this is reflected by the comparable forces seen in Figure 7-5b compared to Figure 7-5a, but with lower values of z_2. Accordingly the mechanics of spinning are quite different for this more rigid workpiece.

Increasing the overall aggressiveness of the pass, z_2, increases the forces and maximum thinning, although before this pass, maximum thinning had already reached 35-36% from the work of creating the cone. Increasing z_2 decreases the shape deviation, without changing its form, and eventually this becomes negative. This suggests that as the tool moves further along the meridian of the workpiece the inner regions (lower s) may continue to deform, under bending about the blending roller. This may be because of the larger forces, but could also be because of the increased stiffness of the edge of the workpiece as foldback also increases. Increasing z_2 initially results in an increase in wrinkling, but after some limit further increases appear to *reduce* the amplitude of wrinkles. This is contrary to experience that suggests that increasing tool aggressiveness results in larger wrinkles, and challenges the assumption in chapter 6 that there is only an *upper* limit to the tool aggressiveness, but it may be related to the increase in foldback angle: when the tool moves into the workpiece close to the base, the outer region of the workpiece folds outwards. This will relieve compressive stress and might help to straighten out wrinkles. This is consistent with a strategy used by craft spinners to eliminate existing wrinkles by using an aggressive forward toolpass combined with a back-stick to try to push out the edge of the workpiece in order to straighten out wrinkles. Further increases in z_2 might eventually lead to further wrinkling – but in the trials reported here increasing beyond 15mm resulted in tearing of the workpiece due to excessive thinning.

As z_0 increases, more of the workpiece is "locked on" to the mandrel. Later in the process, this does indeed seem to improve the stability slightly and reduce wrinkling but at the cost of a slight increase in maximum thinning – and with significant increases in thinning further along the meridian from the blend, as shown in Figure 7-7b, although masked in Figure 7-9a by an already larger amount of thinning around the blend. However, increasing z_0 too far results in such an aggressive deformation that foldback is eliminated, wrinkling increases, and ultimately further increases are limited by the force capacity of the machine axes.

As n increases from negative to positive (convex to concave), the tool force bulges in in the middle of the pass as expected as the tool moves further into the workpiece, leading to increased thinning and foldback. Wrinkling increases as n becomes either positive or negative, but tearing occurred as n increased beyond 5mm. Shape deviation increases as the toolpass becomes more convex. As a trade-off between wrinkling and thinning, a convex path with n=-10mm is chosen, and both thinning and wrinkling can then be reduced by shifting the convexity outwards to the perimeter (increasing d).

7.2.3 Backward pass late in the process

The mechanics of the backward pass contrast strongly with those of the forward pass late in the process. (The s axes of the force graphs are oriented identically so for Figure 7-5c, time moves from right to left, as the tool moves inwards.) z_2 is fixed by the end of the toolpath used to produce the cone, and the results show that as z_0 increases, the forces, the tendency to wrinkle and foldback grow quickly. In contrast to the forwards pass, a concave tool pass here leads to an increase in wrinkling, although to some extent this may be due to the sequencing approach to path design used in these experiments: once z_0 has been fixed, an increase in concavity on a backwards pass will have a similar effect to a further increase in z_0 (as is clear from looking at the toolpath designs in Figure 7-2c) – the results show that both changes would increase the tendency to wrinkle. In contrast to the forward passes, a concave toolpath leads to the largest positive shape deviation, as the inward motion of the tool causes large amounts of foldback. The shape deviation becomes significantly negative with a convex pass only because the tool leaves contact with the workpiece leaving a large gap between the toolpath and the workpiece shape.

The backwards pass causes little thinning, presumably because the inward direction of the tool is acting to draw material in towards the mandrel. The change of direction must drive increased compressive circumferential stresses in the workpiece, and it is these which drive the strong tendency towards wrinkling shown in Figure 7-9b. This corresponds with recommendations from skilled manual spinners, who use backwards passes only to "lock" some more material onto the mandrel, allowing further deformation in the next forward pass, with no further thinning – they do not typically use the backward pass to try to deform the unstable region of the workpiece further away from the mandrel.

7.2.4 Comparison between the three sets of trials

Comparing the forces of the forward passes of Figure 7-5a and b, the tool force associated with the preferred path is quite similar: a sharp increase in force as the tool begins to indent the workpiece, followed quickly by a drop in force (which is much more pronounced later in the process when the workpiece has more stiffness), then a period of approximately constant force (around 0.7-0.8kN in this case) followed by a reduction as the tool approaches the perimeter of the workpiece.

The tendency to wrinkle can be reduced by making the toolpass more concave, but at the cost of higher thinning. The effect of z_2 on wrinkling is complex due to an apparent trade-off between the instability introduced by the local effect of the tool, and the increased geometrical stiffness and stability introduced by aggressive toolpaths. The tendency towards foldback, which when sufficiently pronounced causes difficulty for later passes, is always present with a flat workpiece, and returns later in the process, particularly for aggressive (large z_2), concave toolpaths (positive n).

At first sight, the results suggest that in order to reduce maximum thinning, toolpath designers (manual or automatic) should reduce the aggressiveness of the toolpath by reducing z_0 and z_2. However, this leads to a less aggressive toolpath and reduced geometry change, so more passes would be needed in order to produce the same deformation – so it is unclear from these results whether using more of these less aggressive passes would lead to less thinning in the final product. Nevertheless, the results are consistent with those of Kawai and Hayama (1987) who suggests that a greater number of less aggressive passes reduces the thinning in the final product. The results also suggest that in general a convex pass reduces thinning and tool forces, and this is consistent with the results of Wang and Long (2011).

Contrasting the forwards and backwards passes, the typical force distribution for the successful backwards passes is quite different – dropping quickly to zero as the tool unloads the workpiece, rising again suddenly just as the tool approaches the mandrel and pushes some more material onto the mandrel. The backwards pass avoids thinning, but an overambitious deformation (too high z_0 or n), particularly if with a concave path, leads to a strong tendency towards wrinkling and foldback.

7.3 Analysis

The results of section 7.2 provide rich opportunities for further interpretation, and have been provided in full (and published in the CIRP Annals on Manufacturing Technology) to allow detailed comparison with future studies aiming at the same goal. Two tentative insights are drawn from the results here.

7.3.1 Force control of the toolpath

Several observations in section 7.2 related the maximum thinning to increases in the tool force distribution. Although the results did not show a correlation between maximum force and maximum

thinning (Figure 7-11 show only a weak correlation, with correlation coefficients of R=0.52 early in the process and R=0.41 later – anything above R=0.3 suggests a correlation, but closer to R=1 suggests a stronger one), Figure 7-12 shows that the maximum thinning in the forward pass was strongly correlated with the mean force during the pass (R=0.87 early in the process; R=0.73 later in the process). This suggests that, if thinning becomes an issue or failure by tearing becomes a concern, these problems could be countered by strategies to reduce the average force.

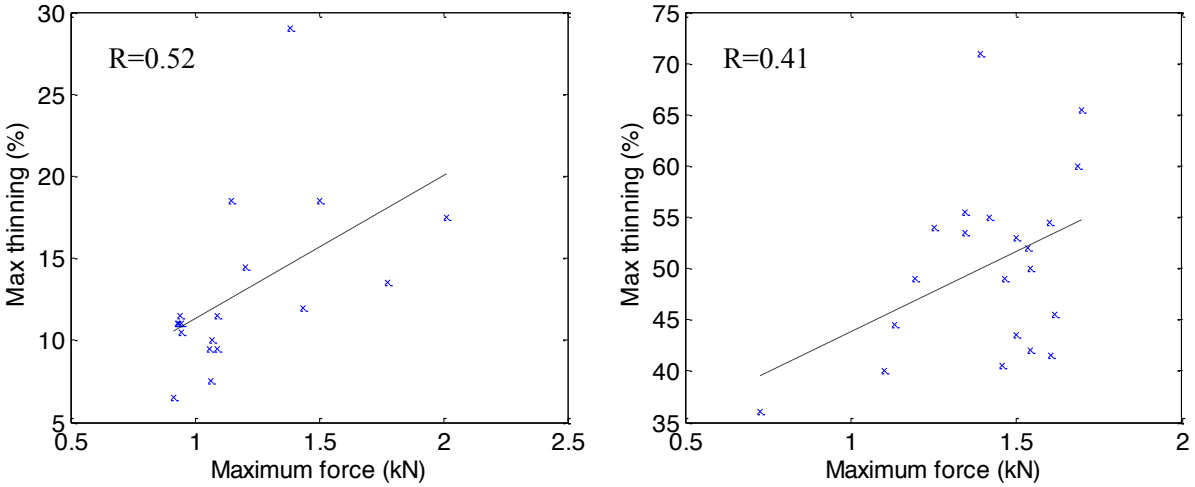

a) Early in process **b) Late in process**

Figure 7-11 - The maximum force and maximum thinning in each experiment

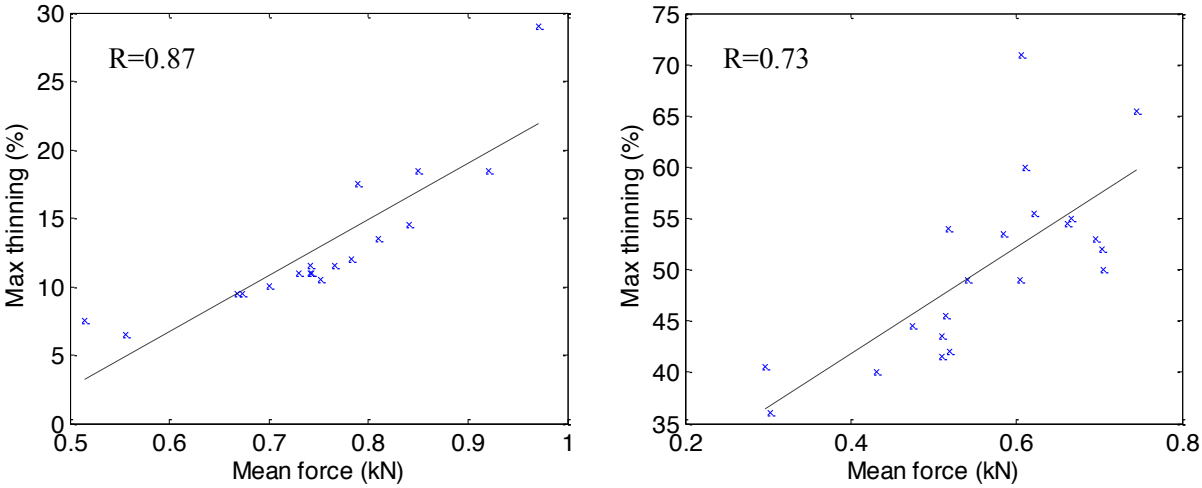

a) Early in process **b) Late in process**

Figure 7-12 - The mean force and maximum thinning in each experiment

7.3.2 Evolution of geometry of the workpiece

The tendency towards thinning and wrinkling during the forward pass was also dependant on the way that the workpiece changed shape during the pass.

Figure 7-13 shows "waterfall" plots to illustrate the evolution of the workpiece geometry through the forward pass in the process in experiments where the lowest and highest thinning was observed early

and late in the process. In those experiments where there was more thinning, the magnitude of the change in shape of the workpiece appears to be greater than those where there was less thinning – this is probably no surprise: that the larger mean forces that were shown to result in thinning in section 7.3.1 also result in a larger deformation.

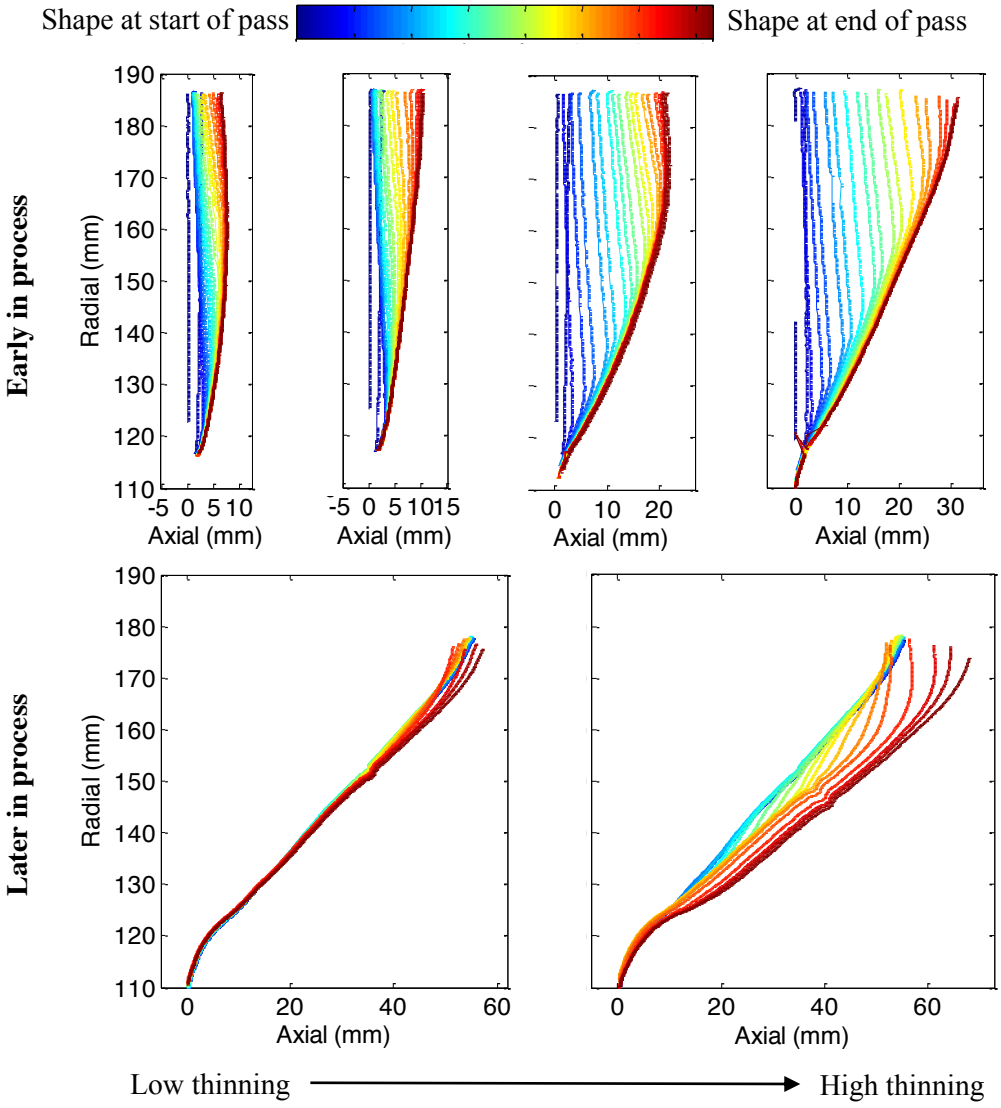

Figure 7-13 - The shape evolution of the workpiece for the experiments where the most and least thinning was measured (Each axis shows the shape of the workpiece at several points within a single experiment, with the left hand plots showing the experiments where the least thinning was observed, and the right hand plots showing those where the most thinning was observed)

In order to check that this is consistent across all of the experiments performed with a forward pass, a measure of the magnitude of deformation is defined. The distance between the workpiece shape at the start and end of the pass is calculated along the workpiece to give $h(s)$, as shown in Figure 7-14a. The magnitude of the deformation is then taken to be the mean value of h in the regions where the workpiece is not yet formed onto the mandrel. This is then plotted against thinning in Figure 7-15, showing a strong correlation (R=0.97 early, and R=0.85 late in the process).

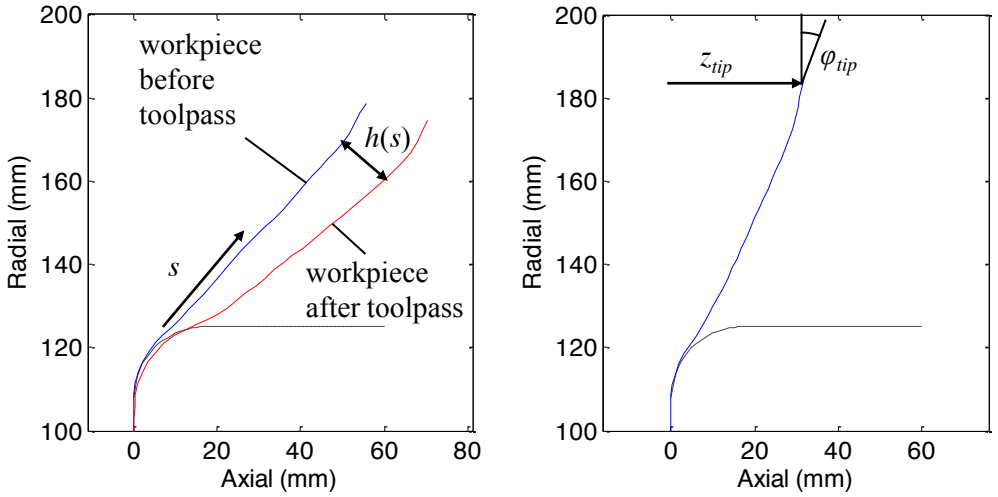

a) Distance between shapes **b) Tip angle measurement**

Figure 7-14 - Measurements for quantifying shape change

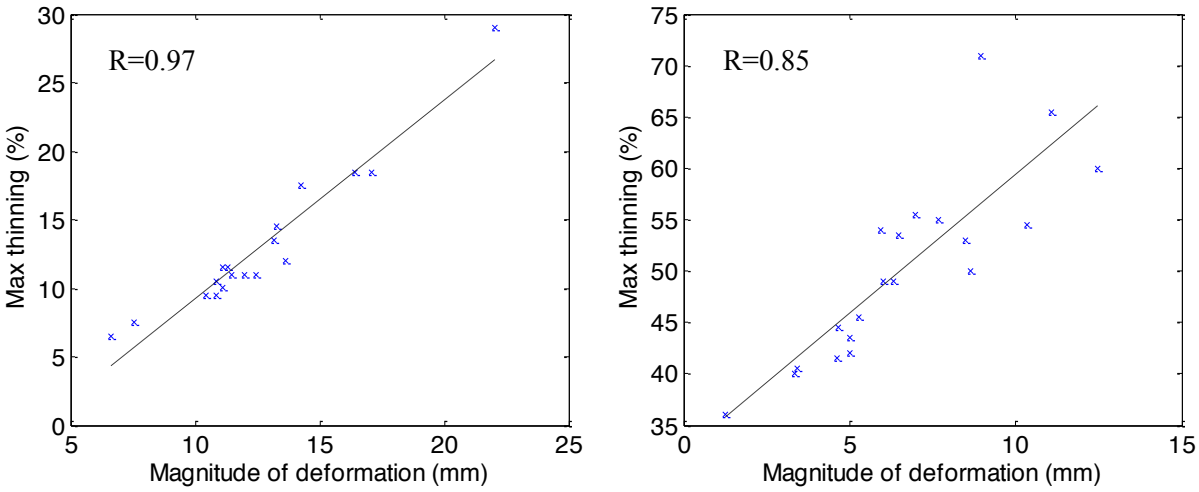

a) Early in process **b) Late in process**

Figure 7-15 - The magnitude of deformation and the maximum thinning in each experiment

Figure 7-16 shows similar waterfall plots to illustrate the evolution of the workpiece geometry through the forward pass early in the process in experiments where the lowest and highest wrinkle amplitudes were seen. In those with low wrinkle amplitude, the outer edge of the workpiece remains flat, pointing radially outwards. However, in those with higher wrinkle amplitude, the outer edge of the workpiece was bent forward or backwards. The consistency of this is checked by plotting the angle at the tip of the workpiece, normalised by the axial displacement of the tip from the blank (ϕ_{tip}/z_{tip} - Figure 7-14b), against the amplitude of wrinkles (Figure 7-17). This shows a quadratic trend with a minimum when the tip is straight – although with only a small number of data points with a negative angle at the tip. This suggests that, if wrinkling becomes a concern, the toolpath should be modified to straighten the edge of the workpiece.

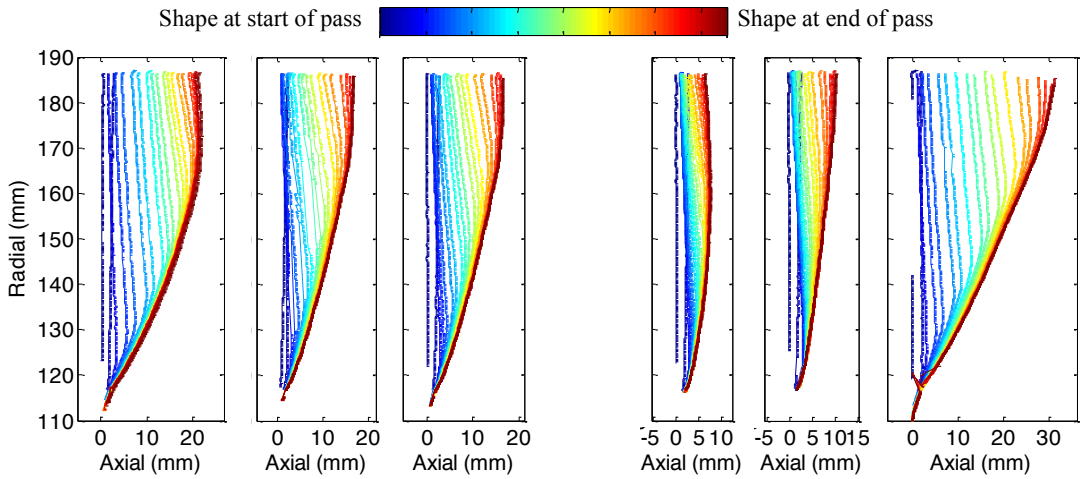

Figure 7-16 - The shape evolution of the workpiece for a) the three experiments early in the process with the lowest wrinkle amplitudes, and b) the three experiments early in the process with the highest amplitude of wrinkles (each axis shows the shape evolution for a single experiment)

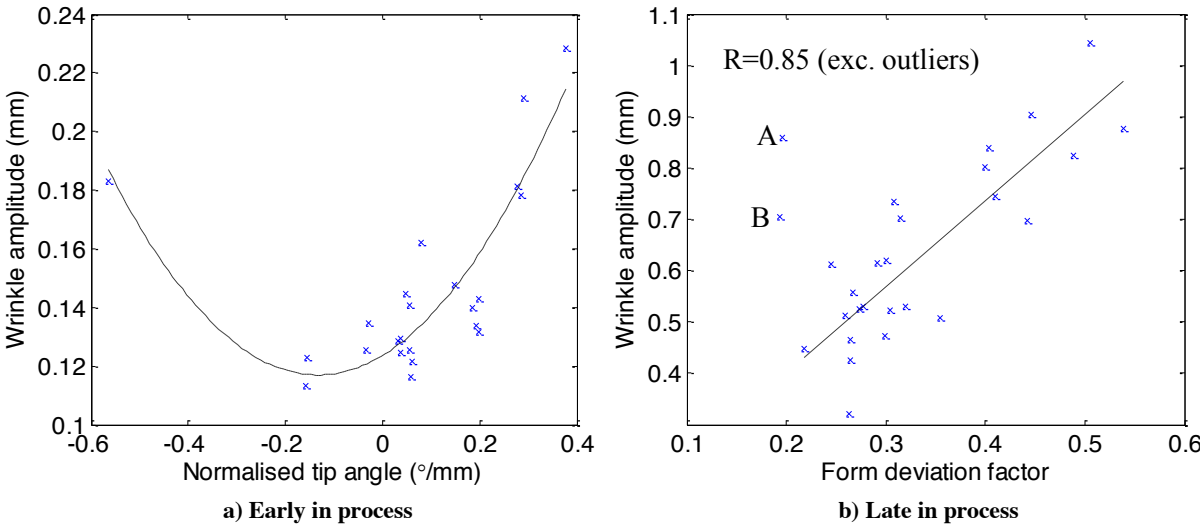

Figure 7-17 – The measure of shape deviation and wrinkle amplitude for each experiment

However, the edge of the workpiece must eventually bend forward in order to produce the target shape – for example, the 45° cone used as the starting point for the toolpaths later in the process. These trials give no suggestion as to how this could be done, but it might be that the edge should be bent forward only very gradually, perhaps allowing some asymmetry to build up, and then removed through further spinning later in the process.

Later in the process, the behaviour was slightly different: Figure 7-18 shows the workpiece geometry evolving in the forward pass of the 45° cone, in experiments where the lowest and highest amplitude of wrinkles was seen. They suggest that, in order to reduce wrinkles, the form of the region of the workpiece which has not yet been spun onto the mandrel should remain the same – the material not yet in contact with the mandrel should maintain the 45° cone shape, such that after each pass, the size of the remaining cone has reduced but its angle has not changed.

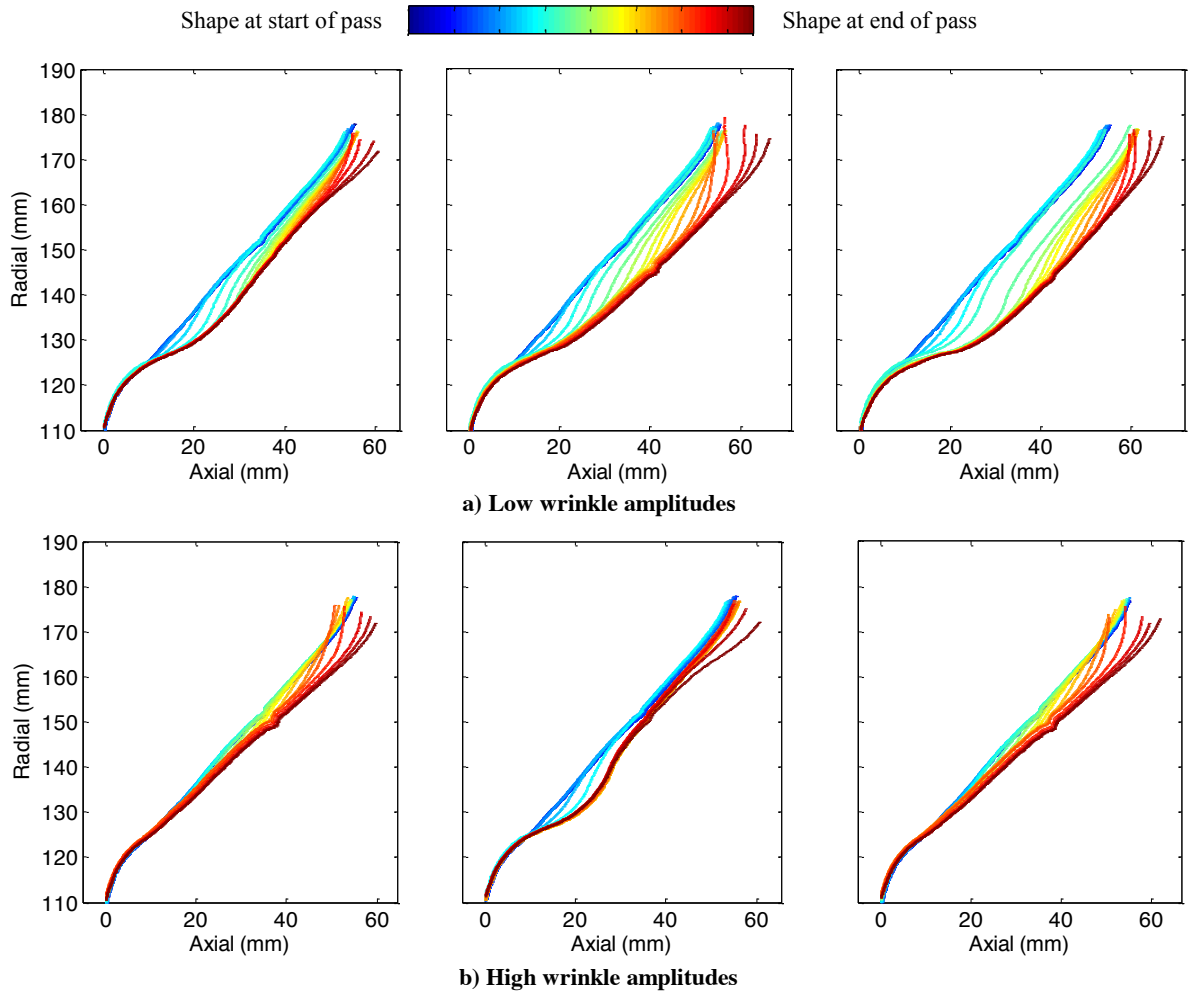

Figure 7-18 - The shape evolution of the workpiece for a) the three experiments late in the process with the lowest wrinkle amplitudes, and b) the three experiments late in the process with the highest amplitude of wrinkles (each axis shows the shape evolution for a single experiment)

In order to check that this is consistent, a form deviation factor is defined: The standard deviation of $h(s)$ is normalised by the mean value – this should give a large value where the form changes and $h(s)$ shows a large variation along the region of the workpiece not yet formed onto the mandrel; and a small value where the form remains the same and $h(s)$ is approximately constant along the meridian, s. The form deviation factor is plotted against the amplitude of wrinkles in Figure 7-17b, showing a good correlation (R=0.85), as predicted, between the form deviation factor and the amplitude of wrinkles, with two outliers labelled A and B in Figure 7-17b.

The shape evolution for these outliers is shown in Figure 7-19. For outlier A, it seems that the form deviation factor should be somewhat higher than it is – The shape of the flange has clearly changed from straight to a curve. This suggests that the measure of shape deviation used here is not perfect and could be further developed – but it is only intended to give an approximate yet quantitative measure of something which we have qualitatively described (a change in form).

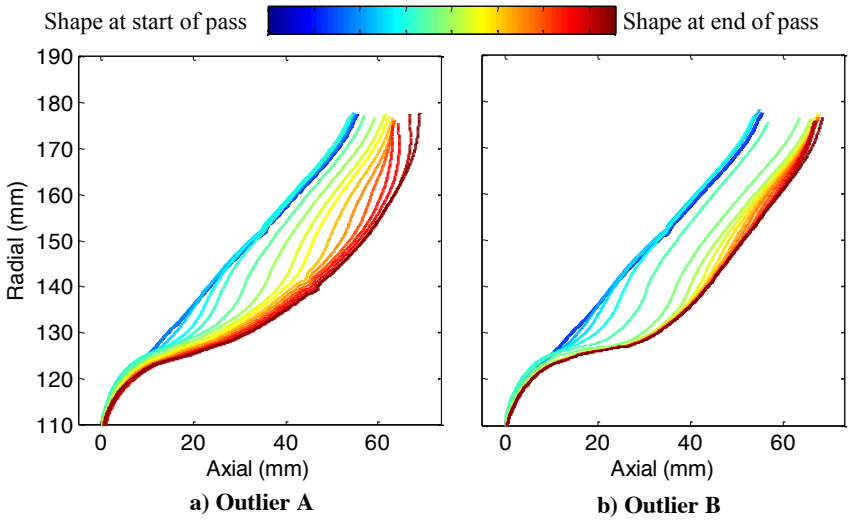

Figure 7-19 - The shape evolution of the workpiece for the two outlying experiments

For outlier B, the shape deviation factor is correctly low, but the shape evolution (Figure 7-19b) is different to that in the experiments with low amplitude of wrinkles. All of the deformation appears to occur early on, due to the toolpath being abnormally aggressive at the start of the workpiece (this experiment was with $z_0 = 25$, at the top of the range tried, and just before tearing occurred). In contrast, in the experiments with low wrinkle amplitude (Figure 7-18a), the edge of the workpiece lifted up and folded back very slightly before being flattened out towards the end of the pass – This would have contributed to a temporary increase in diameter of the workpiece, stretching the circumference and perhaps straightening out the workpiece.

These observations tentatively suggest that, in addition to the force control proposed in 7.3.1, a geometrical strategy could be taken also to control both thinning and wrinkling – with thinning being controlled by the *magnitude* of deformation, and wrinkling being controlled by the *distribution* of deformation. Furthermore, the understanding of shape deviation could potentially be used to transform a target workpiece shape after each pass into a toolpass shape.

7.4 Conclusion: Towards a set of rules for toolpath design

This investigation has shown that toolpath design in spinning involves balancing a trade-off between the need for deformation and the avoidance of failure by wrinkling, thinning or foldback. Craft workers have found means to navigate this trade-off by intuitive experience, but the results of these trials allow a tentative proposal for a set of rules that might form the basis of a future automatic toolpath design system, without requiring the unacceptable delay that would be caused by optimising paths with FE models or the inaccuracies from the fast approximate model in chapter 6.

1. The forward pass should aim to create an initial spike in the total tool force as the tool pushes material onto the mandrel (or support rollers in the case of FAS), followed by a steady force as the tool moves along the workpiece, tapering off as it reaches the edge of the tool.

2. If a target value of mean force is known – as it might be if the relationship between mean force and thinning is known - z_0 should be chosen to produce a higher value, and the rest of the pass should be designed to approach this mean force, but allow the force to taper off as the tool reaches the edge of the workpiece.
3. Early in the process, the perimeter of the workpiece should remain approximately perpendicular to the axis of rotation. However, some rotation of the perimeter must be allowed in order to ultimately reach the target shape. Once a stiff shape, such as the 45°cone used here, is established, the passes should proceed by maintaining this shape, as pass by pass more material is formed onto the mandrel.
4. The maximum deformation possible in a forwards pass (and therefore the maximum tool force) is limited by the maximum acceptable thinning.
5. Wrinkling can be reduced by using a concave toolpass early on, or a linear toolpath later, while a convex toolpass should be used to minimise thinning – creating a difficult trade-off.
6. Once the spun part has deformed sufficiently from its initial plane, backwards passes can be used to increase the rate of shape change without the risk of thinning. The tool-force on the backwards pass should drop to zero as the tool unloads the workpiece, and then increase quickly only as the tool approaches the target shape, in order to lock some more material onto the target shape in preparation for the next forward pass.

These tentative rules could be validated in future, both by interviews with skilled craft workers, and in automatic trials. At least some extensions are likely, as craft workers appear to have particular procedures for reacting to the early appearance of foldback or wrinkling. The trials in this chapter have also been limited to one workpiece material and geometry, so a wider range of trial products would be required in any serious validation.

A further limitation of this work is that it aims to optimise each toolpass individually. In order to optimise the whole toolpath, the effect of each toolpass on the outcome of the whole process should be considered. In particular, in order to understand the backward pass properly, it should be considered along with the next forward pass in order to answer the question: does the backward pass make the subsequent forward pass easier to design without wrinkling or thinning?

Chapter 8 - Conclusion and Further Work

The aim of this study was to automate the Flexible Asymmetric Spinning (FAS) machine developed and built by Music (2011). In particular, the focus has been on three aspects of the automation problem: automating the internal rollers; compensating for springback; and avoiding failure.

The process schedule could have been planned offline, using open-loop control. However, open-loop control generally requires a very accurate model of the process. Uncertainty in process models; disturbances in the process; and the limited controllability of the process, make automation in this way extremely difficult. Instead, closed-loop control of product properties was proposed as an online automation solution.

Closed-loop control of product properties still requires a model of the process, with the additional requirement that the process model needs to be very fast so that it can run online, in parallel with the process itself. The advantage, however, is that an approximate model can be used, and the closed-loop control system can compensate for any errors and still produce an accurate part. A literature review revealed that this approach has been successfully applied in 12 other manufacturing processes, including strip rolling, incremental sheet forming and roll forming, with significant improvements in product accuracy. However, it has not yet been applied in metal spinning, and a review of the literature revealed that fast models with enough detail to enable automated toolpath generation online do not yet exist.

In this chapter, a summary of the progress made in developing such models and applying closed-loop control of product properties to spinning will be presented, along with suggestions for future work.

8.1 Summary of contributions

With the goal to automate FAS, this thesis has contributed to knowledge in three areas: automation of the internal rollers; compensation for springback; and designing toolpaths to avoid failure.

Through extensive numerical modelling, validated against experiments, it was confirmed that, in general, three internal rollers are needed to replace the mandrel and recreate the mechanics of conventional spinning. However, in cases where the product has sufficient geometric stiffness, it may be possible to recreate, at least approximately, the mechanics of conventional spinning with just one internal roller. In these cases, experiments revealed that the product could be successfully created without overlap with the target shape (where the mandrel would be in conventional spinning) by positioning the internal roller at the point where the unloaded shape of the workpiece begins to diverge from the target shape. The roller should be positioned in real time on the first pass, but can be repositioned just twice per pass on subsequent passes.

This demonstrated that closed-loop control can be used to control supporting tools in metal forming, as well as working tools as many previous examples has shown. It could therefore be expanded to other metal forming processes where dedicated dies have been replaced by supporting tools, such as two-point incremental forming.

As has already been shown in several other metal forming processes, springback can be compensated in spinning with fast, approximate models within a closed-loop control system based on workpiece shape. In this thesis, we showed that using a simple 1D elastic cantilever model, calibrated online using laser measurements, to calculate and compensate for springback, could reduce errors in producing a 250mm diameter Aluminium cup by 75%, and also improve the stability and reduce the asymmetries in the final product. This was comparable to error reductions based on a part-by-part correction, but could reduce errors without wasting any additional material. This is yet another example of closed-loop control of product properties being used with fast, approximate models to improve product accuracy.

In designing toolpaths that prevent failure (wrinkling and thinning), it was tentatively shown that a finite horizon approach could be successful – designing the toolpath in 5 rotation increments, checking that failure did not occur for the increment. This was demonstrated using a very accurate, experimentally validated, FE model to create an FE-in-the-loop control system. However, to prevent tearing, this required the design of a thinning trajectory, as this is a progressive failure. It was found that this should allow more thinning at the start of the toolpass where large deformations should be allowed to occur to give the workpiece some stiffness; and then less thinning as the tool moves out towards the edge of the workpiece, where wrinkling will limit the tool motions.

Using an FE model online is too slow to run online to produce an industrial control system. However, the fast, approximate model developed in this thesis – using a linear elastic model to calculate the stresses, and a criterion based on the stresses at the edge of the workpiece becoming plastic – was too conservative and resulted in foldback problems so the final shape could not be successfully produced. A more detailed model, but one much faster than the FE model is therefore still needed to produce a successful online, automatic toolpath generator.

In order to explore the mechanics of the toolpath generation problem further, a series of trials were carried out with a parametric toolpath, revealing a set of rules for toolpath design. This confirmed some results already existing in the literature – for example that a convex toolpath results in larger forces and more thinning; while a concave toolpath can result in wrinkles. In addition, further analysis revealed some tentative new observations: that failure by wrinkling or thinning could be prevented by controlling the workpiece shape and the tool forces. Although these trials were limited to one material and geometry, this might provide a basis for a more general set of rules which could be the basis of a control system after a wider range of trials are performed.

8.2 Further work

Although the control systems in this thesis have been developed to be as general as possible, all of the experimental and modelling work has focused on a small range of products of diameters between 250mm and 500mm, and exclusively on a single alloy: commercially pure, half-hard, Aluminium (AA1050-H14). In industry, spinning is used to form a wide range of metals, from Aluminium and Steel to more challenging materials such as Stainless Steel, Magnesium and Titanium alloys. Therefore, in order to fully demonstrate the capabilities of the control systems developed in this thesis and the rules proposed in chapter 7, they would need to be tested on a wider range of materials and geometries – however, this would require an upgraded machine, as the current spinning machine was only designed to work with Aluminium and thinner sheets of Steel, and on parts of diameters 250-500mm.

Although the fast, elastic model of a concentrated force applied to an axisymmetric shell was not useful for toolpath generation, now that it has been created, it could be applied as a fast yet more advanced model than those used in this thesis to control the blending roller and to compensate for springback. Within blending roller control, it could be used as the model to calculate the unloaded shape from knowledge of the loaded shape and tool force, in order to position the blending roller in real time. It could also be used in positioning all three internal rollers: by looking at where the maximum overlap with the target shape is when the current shape is loaded by the working roller. If this works, it would complete the automation of all three internal rollers, enabling FAS to replace any conventional spinning machine.

Within springback control, it could be used to calculate the springback with more precision than the 1D cantilever shape. Although we showed a significant improvement in springback in this thesis, some of the errors are still more than the typical <0.1mm errors tolerated in industrial production, suggesting the use of this more advanced model might move us closer to industrial production. Without improvements in the model, industrial accuracy might require a combination of the cantilever based compensation *and* the part-by-part correction. Equally, some extensions of the 1D cantilever could be used: perhaps by replacing it with a 2D axisymmetric model, or by introducing some simple plasticity theory – but these would require some additional investment in model development.

However, to generate toolpaths which avoid failure by wrinkling or tearing online, a more advanced model is needed. The two models used for toolpath generation to avoid failure in this thesis were at two extremes of the speed-accuracy trade off: a slow but accurate FE model, and a fast but very approximate elastic model. In going from one to the other, assumptions were made: that wrinkling would happen when the yield occurred at the edge; that the stresses could be calculated using an elastic model with small displacements; that there were no residual stress, no work hardening, no thinning; and approximations in the boundary conditions applied by the working and support rollers.

Together, these assumptions create a toolpath which is too conservative and results in foldback, so further work is needed to explore which assumptions can still be made in order to produce a toolpath which works, but in a reasonable time.

Alternatively, a more advance control system could be explored: which treats the amplitude of wrinkles as a state variable to be minimised, rather than outright failure. Wrinkles can be measured online using the laser line scanner, and this information could be used online in order to calibrate the existing fast elastic model, for example by varying s_{step} throughout the process.

Perhaps a more promising approach, though, lies in the results of the parametric toolpath trials. Now that a set of rules have been tentatively proposed based on the workpiece shape to prevent wrinkling, a control system could be designed to use these rules – modifying a pre-determined toolpath online in order to create forms of workpiece that do not wrinkle, and reducing the magnitude of deformation if thinning becomes an issue. Such a control system would then need to be trialled for a range of geometries and materials in order to confirm that these rules apply universally, and not just to the Aluminium alloy used in this thesis, and to produce a full toolpath, not just a single toolpass.

References

Abaqus 6.13 Online Documentation., 2013.

Agrawal, A., Reddy, N. V., Dixit, P. M., 2007. Determination of optimum process parameters for wrinkle free products in deep drawing process. Journal of Materials Processing Technology, 191, 51–54.

Alberti, N., Cannizzaro, L., Lo Valvo, E., Micari, F., 1989. Analysis of Metal Spinning Processes by the ADINA code. Computers & Stuctures, 32, 517–525.

Allwood, J. M., Music, O., Raithathna, A., Duncan, S. R., 2009. Closed-loop feedback control of product properties in flexible metal forming processes with mobile tools. CIRP Annals - Manufacturing Technology, 58, 287–290.

Amano, T., Tamura, K., 1984. The Study of an Elliptical Cone Spinning Using Trial Equipment. Proceedings of the 3rd International Conference on Rotary Metalworking Processes, Kyoto, Japan, pp. 213–224.

Arai, H., 2003. Shear Spinning Using Force Feedback Control. Proceedings of the 2003 IEEE International Conference on Robotics and Automation, Taipei, Taiwan, pp. 3977–3983.

Arai, H., 2005. Robotic Metal Spinning − Forming Non-axisymmetric Products Using Force Control. Proceedings of the 2005 IEEE International Conference on Robotics and Automation, Barcelona, Spain, pp. 2691–2696.

Arai, H., 2006. Force-controlled metal spinning machine using linear motors. Proceedings 2006 IEEE International Conference on Robotics and Automation, Orlando, Florida, pp. 4031–4036.

Auer, C., Erdbrügge, M., Göbel, R., 2004. Comparison of multivariate methods for robust parameter design in sheet metal spinning. Applied Stochastic Models in Business and Industry, 20, 201–218.

Avitzur, B., Yang, C., 1960. Analysis of power spinning of cones. Journal of Engineering for Industry, 82, 231–245.

Awiszus, B., Meyer, F., 2005. Metal spinning of non-circular hollow parts. Proceedings of the 8th International Conference on Technology of Plasticity, Verona, Italy, pp. 9–13.

Blaich, C., Liewald, M., 2008. New Approach for Closed-Loop Control of Deep Drawing Processes. In M. Liewald (Ed.), New Developments in Sheet Metal Forming, Fellbach, Frankfurt, pp. 363–384.

Bravington, C. A., Barry, D. C., McClure, C. H., 1976. Design and development of a shape control system. The Metals Society Shape Conference, Chester, UK, pp. 82–88.

Chatti, S., Hermes, M., Weinrich, A., Ben-Khalifa, N., Tekkaya, a. E., 2009. New incremental methods for springback compensation by stress superposition. International Journal of Material Forming, 2, 817–820.

Chu, E., Xu, Y., 2004. Hydroforming of aluminum extrusion tubes for automotive applications. Part I: buckling, wrinkling and bursting analyses of aluminum tubes. International Journal of Mechanical Sciences, 46, 263–283.

Cubberly, W., Bakerjian, R., 1989. Tool and Manufacturing Engineers Handbook Desk Edition, Society of Manufacturing Engineers.

Desborough, L., Miller, R., 2002. Increasing Customer Value of Industrial Control Performance Monitoring — Honeywell's Experience. AlChE Symposium Series, 98, 169–189.

Duncan, S. R., 1989. The Cross Directional Control of a Web Forming Process, PhD Thesis, Imperial College of Science, Technology and Medicine, London, UK.

Duncan, S. R., 1995. The design of robust cross-directional control systems for paper making. Proceedings of the 1995 American Control Conference, Seattle, Washington, pp. 1800–1805.

Duncan, S. R., 1997. Estimating the response of actuators in a cross-directional control system. Pulp and Paper Canada, 98, 61–64.

Duncan, S. R., Allwood, J. M., Garimella, S. S., 1998. The analysis and design of spatial control systems in strip metal rolling. IEEE Transactions on Control Systems Technology, 6, 220–232.

Edwardson, S., Moore, A., Abed, E., McBridge, R., French, P., Hand, D., Dearden, G., et al., 2004. Iterative 3D laser forming of continuous surfaces. Proceedings of the 23rd International Congress of Applications of Lasers and Electro-Optics, San Francisco, California.

El-Khabeery, M. M., Fattouh, M., El-Sheikh, M. N., Hamed, O. A., 1991. On the conventional simple spinning of cylindrical aluminium cups. International Journal of Machine Tools and Manufacture, 31, 203–219.

Von Finckenstein, E., Dierig, H., 1990. CNC-Drucken. CIRP Annals - Manufacturing Technology, 39, 267–270.

Flugge, W., 1973. Stresses in Shells, Springer-Verlag (2nd ed.).

Gao, X. C., Kang, D. C., Meng, X. F., Wu, H. J., 1999. Experimental research on a new technology–ellipse spinning. Journal of Materials Processing Technology, 94, 197–200.

Geckeler, J., 1928. Plastisches Knicken der Wandung von Hohlzylindern und einige andere Faltungserscheinungen an Schalen und Blechen. Journal of Applied Mathematics and Mechanics/Zeitschrift für Angewandte Mathematik und Mechanik, 8, 341–352.

Gonçalves, R., Camotim, D., 2007. Thin-walled member plastic bifurcation analysis using generalised beam theory. Advances in Engineering Software, 38, 637–646.

Gross, E., Tomizuka, M., Messner, W., 1994. Cancellation of discrete time unstable zeros by feedforward control. ASME Journal of Dynamic Systems, Measurement, and Control, 116, 33–38.

Hao, W., Duncan, S. R., 2011. Optimization of tool trajectory for Incremental Sheet Forming using closed loop control. Proceedings of the 2011 IEEE International Conference on Automation Science and Engineering, Trieste, Italy, pp. 779–784.

Hardt, D. E., 1993. Modeling and control of manufacturing processes: getting more involved. ASME Journal of Dynamic Systems, Measurement, and Control, 115, 291–300.

Hardt, D. E., Fenn, R., 1993. Real-time control of sheet stability during forming. Journal of Engineering for Industry, 115, 299–308.

Hardt, D. E., Hale, M., 1984. Closed loop control of a roll straightening process. CIRP Annals-Manufacturing Technology, 33, 137–140.

Hardt, D. E., Roberts, M., Stelson, K., 1982. Closed-loop control in a roll bending process. ASME Journal of Dynamic Systems, Measurement, and Control, 104, 317–322.

Hardt, D. E., Webb, R., 1982. Sheet metal die forming using closed-loop shape control. CIRP Annals - Manufacturing Technology, 31, 165–169.

Hayama, M., 1981. Study on Spinnability of Aluminum and Its Alloys. Bulletin of the Faculty of Engineering, Yokohama National University, 30, 63–72.

Hayama, M., Kudo, H., Shinokura, T., 1970. Study of the Pass Schedule in Conventional Simple Spinning. Bulletin of JSME, 13, 1358–1365.

Hayama, M., Murota, T., 1963. On the Study of Metal Spinning. Bulletin of the Faculty of Engineering, Yokohama National University, 12, 53–88.

Hayama, M., Murota, T., Kudo, H., 1966. Deformation Modes and Wrinkling of Flange on Shear Spinning. Bulletin of JSME, 9, 423–433.

Hayama, M., Tago, A., 1968. Fracture of Cone-wall in Shear Spinning - Investigation into Spinnability of Aluminium Sheet. Bulletin of the Faculty of Engineering, Yokohama National University, 17, 93–103.

Henkenjohann, N., Göbel, R., Kleiner, M., Kunert, J., 2005. An Adaptive Sequential Procedure for Efficient Optimization of the Sheet Metal Spinning Process. Quality and Reliability Engineering International, 21, 439–455.

Hill, R., 1948. A Theory of the Yielding and Plastic Flow of Anisotropic Metals. Proceedings of the Royal Society A: Mathematical, Physical and Engineering Sciences, 193, 281–297.

Hill, R., 1958. A general theory of uniqueness and stability in elastic-plastic solids. Journal of the Mechanics and Physics of Solids, 6, 236–249.

Hosford, W., Caddell, R., 2007. Metal forming: mechanics and metallurgy, Cambridge University Press (3rd ed.).

Hutchinson, J., 1974. Plastic buckling. Advances in Applied Mechanics, 14, 67–144.

Hutchinson, J., Neale, K., 1985. Wrinkling of curved thin sheet metal. Plastic Instability, 71–78.

Kalpakcioglu, S., 1961. A Study of Shear-Spinnability of Metals. Journal of Engineering for Industry, 83, 478.

Kalpakjian, S., Schmid, S. R., 2008. Manufacturing processes for engineering materials, Pearson education (5th ed.).

Kang, D.-C., Gao, X.-C., Meng, X.-F., Wang, Z.-H., 1999. Study on the deformation mode of conventional spinning of plates. Journal of Materials Processing Technology, 91, 226–230.

Von Kármán, T., 1910. Untersuchungen über Knickfestigkeit, Springer Berlin Heidelberg.

Kawai, K., 1989. A fact data base on spinning technology. Rotary Forming, 59–62.

Kawai, K., Hayama, M., 1987. Roller Pass Programming in Conventional Spinning by NC Spinning Machine. Advanced Technology of Plasticity, 2, 711–718.

Kawai, K., Yang, L., Kudo, H., 2001. A flexible shear spinning of truncated conical shells with a general-purpose mandrel. Journal of Materials Processing Technology, 113, 28–33.

Kawai, K., Yang, L.-N., Kudo, H., 2007. A flexible shear spinning of axi-symmetrical shells with a general-purpose mandrel. Journal of Materials Processing Technology, 192-193, 13–17.

Kegg, R. L., 1961. A New Test Method for Determination of Spinnability of Metals. Journal of Engineering for Industry, 83, 119.

Kim, J. B., Yoon, J. W., Yang, D. Y., 2000. Wrinkling initiation and growth in modified Yoshida buckling test: Finite element analysis and experimental comparison. International Journal of Mechanical Sciences, 42, 1683–1714.

Kim, J. B., Yoon, J. W., Yang, D. Y., 2003. Investigation into the wrinkling behaviour of thin sheets in the cylindrical cup deep drawing process using bifurcation theory. International Journal for Numerical Methods in Engineering, 56, 1673–1705.

Kim, Y., Son, Y., 2000. Study on wrinkling limit diagram of anisotropic sheet metals. Journal of Materials Processing Technology, 97, 88–94.

Kleiner, M., Ewers, R., Kunert, J., Henkenjohann, N., Auer, C., 2005. Optimisation of the shear forming process by means of multivariate statistical methods. Technical Report, Universität Dortmund.

Kleiner, M., Göbel, R., Kantz, H., Klimmek, C., Homberg, W., 2002. Combined Methods for the Prediction of Dynamic Instabilities in Sheet Metal Spinning. CIRP Annals - Manufacturing Technology, 51, 209–214.

Kleiner, M., Tekkaya, A. E., Chatti, S., Hermes, M., Weinrich, A., Ben-Khalifa, N., Dirksen, U., 2009. New incremental methods for springback compensation by stress superposition. Production Engineering, 3, 137–144.

Kobayashi, S., 1963. Instability in the conventional spinning of cones. Journal of Manufacturing Science and Engineering, 85, 44–48.

Kollár, L., Dulácska, E., 1984. Buckling of shells for engineers. (G. R. Thomson, Ed.), Budapest: Ajadémiai Kiadó.

Lange, K., 1985. Handbook of metal forming, McGraw-Hill.

Li, M.-Z., Cai, Z.-Y., Liu, C., 2007. Flexible manufacturing of sheet metal parts based on digitized-die. Robotics and Computer-Integrated Manufacturing, 23, 107–115.

Li, Y., Wang, J., Lu, G., Pan, G., 2014. A numerical study of the effects of roller paths on dimensional precision in die-less spinning of sheet metal. Journal of Zhejiang University SCIENCE A, 15, 432–446.

Lim, Y., Venugopal, R., Ulsoy, A. G., 2008. Advances in the Control of Sheet Metal Forming. Proceedings of the 17th World Congress of The International Federation of Automatic Control, pp. 1875–1883.

Liu, J., Yang, H., Li, Y., 2002. A study of the stress and strain distributions of first-pass conventional spinning under different roller-traces. Journal of Materials Processing Technology, 129, 326–329.

Lu, H., Cheng, H. S., Cao, J., Liu, W. K., 2005. Adaptive enrichment meshfree simulation and experiment on buckling and post-buckling analysis in sheet metal forming. Computer Methods in Applied Mechanics and Engineering, 194, 2569–2590.

Luo, J. X., Joynt, D. L., Stelson, K., 1996. Control of the Fabrication of Long Slender Workpieces of Arbitrary Shape - Part II: Closed-loop Control of the Multi-Axis Bending Process. ASME Journal of Dynamic Systems, Measurement, and Control, 118, 549–556.

Maciejowski, J.M., 2000. Predictive Control with Constraints. Prentice-Hall.

Mori, K.-I., Nonaka, T., 2004. Simplified Three-Dimensional Finite Element Simulation of Shear Spinning Process Based on Axi-Symmetric Modeling. Journal of the Japan Society for Technology of Plasticity, 45, 34–38.

Music, O., 2011. Flexible Asymmetric Spinning, PhD Thesis, University of Cambridge.

Music, O., Allwood, J. M., 2010. A review of the mechanics of metal spinning. Journal of materials processing, 210, 3–23.

Music, O., Allwood, J. M., 2011a. Flexible asymmetric spinning. CIRP Annals-Manufacturing Technology, 60, 319–322.

Music, O., Allwood, J. M., 2011b. Tool-path Design for Metal Spinning. Proceedings of the 10th International Confernece on Technology of Plasticity, Aachen, Germany, pp. 542–547.

Music, O., Allwood, J. M., 2012. The use of spatial impulse responses to characterise flexible forming processes with mobile tools. Journal of Materials Processing Technology, 212, 1139–1156.

Music, O., Allwood, J. M., Kawai, K., 2010. A review of the mechanics of metal spinning. Journal of Materials Processing Technology, 210, 3–23.

Noyes, R. B., 1983. Forming Diagrams for Axisymmetric Sheet Metal Forming by Spinning. Sheet Metal Industries, 60, 264–265, 293.

Osakada, K., 2010. History of plasticity and metal forming analysis. Journal of Materials Processing Technology, 210, 1436–1454.

Polyblank, J. A., Allwood, J. M., 2014. Support Roller Control and Springback Compensation in Flexible Spinning. Procedia Engineering, 81, 2499–2504.

Prud'homme, C., Rovas, D. V., Veroy, K., Machiels, L., Maday, Y., Patera, A. T., Turinici, G., 2002. Reliable Real-Time Solution of Parametrized Partial Differential Equations: Reduced-Basis Output Bound Methods. Journal of Fluids Engineering, 124, 70.

Quigley, E., Monaghan, J., 2000. Metal forming: an analysis of spinning processes. Journal of Materials Processing Technology, 103, 114–119.

Quigley, E., Monaghan, J., 2001. Using a Finite Element Model to Study Plastic Strains in Metal Spinning. Proceedings of the Ninth International Conference on Sheet Metal, Leuven, Belgium, pp. 255–262.

Recker, D., Franzke, M., Hirt, G., 2011. Fast models for online-optimization during open die forging. CIRP Annals - Manufacturing Technology, 60, 295–298.

Reil, G., 1993. Process Control of Numerically Controlled Machines with Fuzzy Logic, Dr.-Ing. Thesis, Lehrstuhl für Umformende Fertigungsverfahren, Technische Universität Dortmund.

Sebastiani, G., Brosius, A., Homberg, W., Kleiner, M., 2007. Process Characterization of Sheet Metal Spinning by Means of Finite Elements. Proceedings of the 12th International Conference of Sheet Metal, Palermo, Italy, pp. 637–644.

Sekiguchi, A., Arai, H., 2012. Control of wall thickness distribution by oblique shear spinning methods. Journal of Materials Processing Technology, 212, 786–793.

Senior, B., 1956. Flange wrinkling in deep-drawing operations. Journal of the Mechanics and Physics of Solids, 4.

Shanley, F., 1947. Inelastic column theory. Journal of the Aeronautical Sciences, 14, 261–267.

Shi, F., Long, H., Zhan, M., Ou, H., 2014. Uncertainty analysis on process responses of conventional spinning using finite element method. Structural and Multidisciplinary Optimization, 49, 839–850.

Shima, S., Kotera, H., Murakami, H., 1997. Development of Flexible Spin-Forming Method. Journal of the Japan Society for Technology of Plasticity, 38, 814–818.

Siebel, E., Dröge, K. A., 1955. Forces and material flow in spinning. Werkstattstechnik und Maschinenbau, 45, 6–9.

Siegert, K., Häussermann, M., Haller, D., Wagner, S., Ziegler, M., 2000. Tendencies in presses and dies for sheet metal forming processes. Journal of Materials Processing Technology, 98, 259–264.

Sortais, H. C., 1963. Mechanics of conventional spinning. Journal of Engineering for Industry, 85, 346–350.

Sugita, Y., Arai, H., 2012. Development of Synchronous Multipath Metal-Spinning Method for Forming Nonaxisymmetric Shapes. Transactions of the Japan Society of Mechanical Engineers Series C, 78, 1004–1012.

Sugita, Y., Arai, H., 2015. Formability in synchronous multipass spinning using simple pass set. Journal of Materials Processing Technology, 217, 336–344.

Sun, W., Stelson, K., 1997. System identification and adaptive control of the multi-axis bending and twisting process. ASME Journal of Dynamic Systems, Measurement, and Control, 119, 782–790.

Timoshenko, S. P., Gere, J. M., 1961. Theory of elastic stability. McGraw-Hill, New York, McGraw-Hill (2nd ed.).

Timoshenko, S. P., Woinowsky-Krieger, S., 1959. Theory of Plates and Shells, McGraw-Hill (2nd ed.).

Wang, L., 2012. Analysis of Material Deformation and Wrinkling Failure in Conventional Metal Spinning Process, PhD Thesis, Durham University.

Wang, L., Long, H., 2011. A study of effects of roller path profiles on tool forces and part wall thickness variation in conventional metal spinning. Journal of Materials Processing Technology, 211, 2140–2151.

Wang, L., Long, H., 2013. Roller path design by tool compensation in multi-pass conventional spinning. Materials & Design, 46, 645–653.

Wang, L., Long, H., Ashley, D., Roberts, M., White, P., 2011. Effects of the roller feed ratio on wrinkling failure in conventional spinning of a cylindrical cup. Proceedings of the Institution of Mechanical Engineers, Part B: Journal of Engineering Manufacture, 225, 1991–2006.

Wang, X., Cao, J., 2000. On the prediction of side-wall wrinkling in sheet metal forming processes. International Journal of Mechanical Sciences, 42, 2369–2394.

Watson, M., Long, H., 2014. Wrinkling Failure Mechanics in Metal Spinning. Proceedings of the 2014 International Conference of the Technology of Plasticity, pp. 2391–2396.

Wellstead, P. E., Zarrop, M. B., Duncan, S. R., 2000. Signal processing and control paradigms for industrial web and sheet manufacturing. International Journal of Adaptive Control and Signal Processing, 14, 51–76.

Xia, Q., Shima, S., Kotera, H., Yasuhuku, D., 2005. A study of the one-path deep drawing spinning of cups. Journal of Materials Processing Technology, 159, 397–400.

Xia, Q., Xiao, G., Long, H., Cheng, X., Sheng, X., 2014. A Review of Process Advancement of Novel Metal Spinning. International Journal of Machine Tools and Manufacture, 85, 100–121.

Xiong, Z. Q., Xie, L. S., 2002. Study on the theory and application of the energy method for analyzing compressive instability in sheet forming. Journal of Materials Processing Technology, 129, 255–260.

Yang, M., Manabe, K., Nishimura, H., 1998. Development of an intelligent tool system for flexible L-bending process of metal sheets. Smart Materials and Structures, 7, 530–536.

Yu, T., Johnson, W., 1982. The buckling of annular plates in relation to the deep-drawing process. International Journal of Mechanical Sciences, 24, 175–188.

Yu, T. X., Johnson, W., 1984. A theoretical analysis of the bending into cylindrical dies of metal strips. Proceedings of the Institution of Mechanical Engineers, Part C: Mechanical Engineering Science, 198, 99–108.

Zhan, M., Yang, H., Zhang, J. H., Xu, Y. L., Ma, F., 2007. 3D FEM analysis of influence of roller feed rate on forming force and quality of cone spinning. Journal of Materials Processing Technology, 187-188, 486–491.

Zhan, M., Yang, H., Zhang, J., Xu, Y., Ma, F., 2006. Research on variation of stress and strain field and wall thickness during cone spinning. Proceedings of the 12th International Manufacturing Conference in China, Xi'an, China, pp. 149–152.

Appendix A – Boundary Conditions in MATLAB model

32 boundary conditions are required to solve equations 6.21-6.23 over four regions. These boundary conditions are:

Built in at spindle, s=0:

$$u_n^{(1)}(0) = 0 \tag{A1}$$

$$v_n^{(1)}(0) = 0 \tag{A2}$$

$$w_n^{(1)}(0) = 0 \tag{A3}$$

$$\left.\frac{dw_n^{(1)}}{ds}\right|_{s=0} = 0 \tag{A4}$$

No out-of-plane displacement at blending roller, s=b:

$$w_n^{(1)}(b) = 0 \tag{A5}$$

Compatibility at blending roller:

$$u_n^{(1)}(b) - u_n^{(2)}(b) = 0 \tag{A6}$$

$$v_n^{(1)}(b) - v_n^{(2)}(b) = 0 \tag{A7}$$

$$w_n^{(1)}(b) - w_n^{(2)}(b) = 0 \tag{A8}$$

$$\left.\frac{dw_n^{(1)}}{ds}\right|_{s=b} - \left.\frac{dw_n^{(2)}}{ds}\right|_{s=b} = 0 \tag{A9}$$

Equilibrium of N_s at blending roller:

$$\left(\frac{\partial v_n^{(1)}}{\partial s} + w_n^{(1)}k_1 + \nu\frac{nu_n^{(1)} + v_n^{(1)}\cos\phi + w_n^{(1)}\sin\phi}{r}\right)_{s=b-} - \left(\frac{\partial v_n^{(2)}}{\partial s} + w_n^{(2)}k_1 + \nu\frac{nu_n^{(2)} + v_n^{(2)}\cos\phi + w_n^{(2)}\sin\phi}{r}\right)_{s=b+} = 0 \tag{A10}$$

Equilibrium of $N_{s\theta}$ at blending roller:

$$\left(\frac{\partial u_n^{(1)}}{\partial s} - \frac{n v_n^{(1)} + u_n^{(1)} \cos\phi}{r}\right)_{s=b} - \left(\frac{\partial u_n^{(2)}}{\partial s} - \frac{n v_n^{(2)} + u_n^{(2)} \cos\phi}{r}\right)_{s=b} = 0 \quad \textbf{A11}$$

Equilibrium of M_s at blending roller:

$$\left[\frac{\partial^2 w_n^{(1)}}{\partial s^2} + \frac{\nu}{r}\left(-\frac{n^2}{r} w_n^{(1)} + \frac{\partial w_n^{(1)}}{\partial s}\cos\phi\right)\right]_{s=b} - \left[\frac{\partial^2 w_n^{(2)}}{\partial s^2} + \frac{\nu}{r}\left(-\frac{n^2}{r} w_n^{(2)} + \frac{\partial w_n^{(2)}}{\partial s}\cos\phi\right)\right]_{s=b} = 0 \quad \textbf{A12}$$

Compatibility at application of tool force, s=c:

$$u_n^{(2)}(c) - u_n^{(3)}(c) = 0 \quad \textbf{A13}$$

$$v_n^{(2)}(c) - v_n^{(3)}(c) = 0 \quad \textbf{A14}$$

$$w_n^{(2)}(c) - w_n^{(3)}(c) = 0 \quad \textbf{A15}$$

$$\left.\frac{dw_n^{(2)}}{ds}\right|_{s=c} - \left.\frac{dw_n^{(3)}}{ds}\right|_{s=c} = 0 \quad \textbf{A16}$$

Equilibrium of N_s at application of tool force:

$$\left(\frac{\partial v_n^{(2)}}{\partial s} + w_n^{(2)} k_1 + \nu\frac{n u_n^{(2)} + v_n^{(2)}\cos\phi + w_n^{(2)}\sin\phi}{r}\right)_{s=c-} - \left(\frac{\partial v_n^{(3)}}{\partial s} + w_n^{(3)} k_1 + \nu\frac{n u_n^{(3)} + v_n^{(3)}\cos\phi + w_n^{(3)}\sin\phi}{r}\right)_{s=c+} = 0 \quad \textbf{A17}$$

Equilibrium of $N_{s\theta}$ at application of tool force

$$\left(\frac{\partial u_n^{(2)}}{\partial s} - \frac{n v_n^{(2)} + u_n^{(2)} \cos\phi}{r}\right)_{s=c} - \left(\frac{\partial u_n^{(3)}}{\partial s} - \frac{n v_n^{(3)} + u_n^{(3)} \cos\phi}{r}\right)_{s=c} = 0 \quad \textbf{A18}$$

Equilibrium of M_s at application of tool force:

$$\left[\frac{\partial^2 w_n^{(2)}}{\partial s^2} + \frac{\nu}{r}\left(-\frac{n^2}{r} w_n^{(2)} + \frac{\partial w_n^{(2)}}{\partial s}\cos\phi\right)\right]_{s=c} - \left[\frac{\partial^2 w_n^{(3)}}{\partial s^2} + \frac{\nu}{r}\left(-\frac{n^2}{r} w_n^{(3)} + \frac{\partial w_n^{(3)}}{\partial s}\cos\phi\right)\right]_{s=c} = 0 \quad \textbf{A19}$$

Equilibrium of Q_s at application of tool force:

$$\left[r\frac{\partial^3 w_n^{(2)}}{\partial s^3}+\frac{\partial^2 w_n^{(2)}}{\partial s^2}\cos\phi+\frac{-n^2}{r}\frac{\partial w_n^{(2)}}{\partial s}+\frac{2n^2}{r^2}w_n^{(2)}\cos\phi-\frac{1}{r}\frac{\partial w_n^{(2)}}{\partial s}\cos^2\phi - \nu k_1\frac{\partial w_n^{(2)}}{\partial s}\sin\phi\right]_{s=c-} - \left[r\frac{\partial^3 w_n^{(3)}}{\partial s^3}+\frac{\partial^2 w_n^{(3)}}{\partial s^2}\cos\phi+\frac{-n^2}{r}\frac{\partial w_n^{(3)}}{\partial s}+\frac{2n^2}{r^2}w_n^{(3)}\cos\phi - \frac{1}{r}\frac{\partial w_n^{(3)}}{\partial s}\cos^2\phi-\nu k_1\frac{\partial w_n^{(3)}}{\partial s}\sin\phi\right]_{s=c+} = \begin{cases} -\frac{P}{2\pi K} \text{ for } n=0 \\ -\frac{P}{\pi K} \text{ for } n\geq 1 \end{cases} \quad \textbf{A20}$$

Where P is the magnitude of the tool force, which is set to 1 in the model to give the stress distribution and deformation for a unit force application.

Equilibrium of N_s at free edge:

$$\left[\frac{\partial v_n^{(3)}}{\partial s}+w_n^{(3)}k_1+\nu\frac{nu_n^{(3)}+v_n^{(3)}\cos\phi+w_n^{(3)}\sin\phi}{r}\right]_{s=d}=0 \quad \textbf{A21}$$

Equilibrium of $N_{s\theta}$ at free edge:

$$\left[\frac{\partial u_n^{(3)}}{\partial s}-\frac{nv_n^{(3)}+u_n^{(3)}\cos\phi}{r}\right]_{s=d}=0 \quad \textbf{A22}$$

Equilibrium of M_s at blending roller:

$$\left[\frac{\partial^2 w_n^{(3)}}{\partial s^2}+\frac{\nu}{r}\left(\frac{-n^2}{r}w_n^{(3)}+\frac{\partial w_n^{(3)}}{\partial s}\cos\phi\right)\right]_{s=d}=0 \quad \textbf{A23}$$

The final boundary condition at the free edge requires some explanation. Timoshenko and Woinowsky-Krieger (1959, pp. 84–87) showed that, at the free edge, the boundary condition on vertical force should be written as:

$$V_x=\left(Q_s+\frac{1}{r}\frac{\partial M_{\theta s}}{\partial\theta}\right)=0 \quad \textbf{A24}$$

$$\therefore \left[r\frac{\partial^3 w_n^{(3)}}{\partial s^3} + \frac{\partial^2 w_n^{(3)}}{\partial s^2}\cos\phi - 2\frac{n^2}{r}\frac{\partial w_n^{(3)}}{\partial s} + 3\frac{n^2}{r^2}w_n^{(3)}\cos\phi - \frac{1}{r}\frac{\partial w_n^{(3)}}{\partial s}\cos^2\phi \right.$$
$$\left. + \nu\left(-\frac{n^2}{r^2}w_n^{(3)}\cos\phi + \frac{n^2}{r}\frac{\partial w_n^{(3)}}{\partial s} - k_1\frac{\partial w_n^{(3)}}{\partial s}\sin\phi \right) \right]_{s=d} = 0 \qquad \textbf{A25}$$

Finally, the boundary conditions at interfaces where regions are split because of discontinuities, will look similar to equations A13-A20, at the appropriate value of s, and with the value of P set to zero, as no external force will be applied at these interfaces.